ҚАЗАҚСТАН РЕСПУБЛИКАСЫ
ҒЫЛЫМ ЖӘНЕ ЖОҒАРЫ БІЛІМ МИНИСТРЛІГІ

SATBAYEV UNIVERSITY
МЕТАЛЛУРГИЯ ЖӘНЕ КЕН БАЙЫТУ ИНСТИТУТЫ

ISSN 2616-6445 (Online)
ISSN 2224-5243 (Print)
DOI 10.31643/2018/166445

Минералдық шикізаттарды кешенді пайдалану

4(343)

Комплексное Использование Минерального Сырья

Complex Use of Mineral Resources

ҚАЗАН-ЖЕЛТОҚСАН 2027
OCTOBER-DECEMBER 2027
ОКТЯБРЬ-ДЕКАБРЬ 2027

ЖЫЛЫНА 4 РЕТ ШЫҒАДЫ
QUARTERLY JOURNAL
ВЫХОДИТ 4 РАЗА В ГОД

ЖУРНАЛ 1978 ЖЫЛДАН БАСТАП ШЫҒАДЫ
JOURNAL HAS BEEN PUBLISHING SINCE 1978
ЖУРНАЛ ИЗДАЕТСЯ С 1978 ГОДА

АЛМАТЫ - 2027

Редакция мекен жайы:
«Металлургия және кен байыту институты» АҚ
050010, Қазақстан Республикасы, Алматы қ., Шевченко к-сі, Уәлиханов к-нің қиылысы, 29/133,
Fax. +7 (727) 298-45-03, Tel. +7-(727) 298-45-02, +7 (727) 298-45-19
E mail: journal@kims-imio.kz, product-service@kims-imio.kz
http://kims-imio.com/index.php/main

«Минералдық шикізаттарды кешенді пайдалану» журналы ғылыми жұмыстардың негізгі нәтижелерін жариялау үшін Қазақстан Республикасы Білім және ғылым министірлігінің Білім және ғылым сапасын қамтамасыз ету комитеті ұсынған ғылыми басылымдар тізіміне енгізілген.
Меншік иесі: «Металлургия және кен байыту институты» АҚ

Журнал Қазақстан Республикасының Ақпарат және коммуникация министрлігінің Байланыс, ақпараттандыру және бұқаралық ақпарат құралдары саласындағы мемлекеттік бақылау комитетінде қайта тіркелген

2016 ж. 18 қазандағы № 16180-Ж Куәлігі

Address:
"Institute of Metallurgy and Ore Beneficiation" JSC
29/133 Shevchenko Street, corner of Ch. Valikhanov Street, Almaty, 050010, Kazakhstan
Fax. +7 (727) 298-45-03, Tel. +7-(727) 298-45-02, +7 (727) 298-45-19
E mail: journal@kims-imio.kz, product-service@kims-imio.kz
http://kims-imio.com/index.php/main

The Journal "Complex Use of Mineral Resources" is included in the List of publications recommended by the Committee for Control in the Sphere of Education and Science of the Ministry of Education and Science of the Republic of Kazakhstan for the publication of the main results of scientific activities.
Owner: "Institute of Metallurgy and Ore Beneficiation" JSC

The Journal was re-registered by the Committee for State Control in the Sphere of Communication, Information and Mass Media of the Ministry of Information and Communication of the Republic of Kazakhstan.

Certificate № 16180-Ж since October 18, 2016

Адрес редакции:
АО «Институт металлургии и обогащения»
050010, Республика Казахстан, г. Алматы, ул. Шевченко, уг. ул. Валиханова, 29/133,
Fax. +7 (727) 298-45-03, Tel. +7 (727) 298-45-02, +7 (727) 298-45-19
E mail: journal@kims-imio.kz, product-service@kims-imio.kz
http://kims-imio.com/index.php/main

Журнал «Комплексное использование минерального сырья» включен в Перечень изданий, рекомендуемых Комитетом по контролю в сфере образования и науки Министерства образования и науки Республики Казахстан для публикации основных результатов научной деятельности.
Собственник: АО «Институт металлургии и обогащения»

Журнал перерегистрирован в Комитете государственного контроля в области связи, информатизации и средств массовой информации
Министерства информации и коммуникации Республики Казахстан
Свидетельство № 16180-Ж от 18 октября 2016 г.

Crossref
DOI: 10.31643/2027/6445.36
Metallurgy and Metallurgical Engineering

Thermodynamics of Evaporation of Liquid Magnesium - Tin Alloys

Volodin V.N., Trebukhov S.A., Mukangaliyeva A.O., *Linnik X.A., Nitsenko A.V., Burabayeva N.M.

Institute of Metallurgy and Ore Beneficiation JSC, Satbayev University, Almaty, Kazakhstan

** Corresponding author email: x.linnik@satbayev.university*

Received: *December 22, 2025*
Peer-reviewed: *December 29, 2025*
Accepted: *January 28, 2026*

ABSTRACT

Based on the values of the partial pressures of magnesium above dimagnesium stannide and melts with tin, determined by the boiling point method (isobaric and isothermal variants, respectively) and tin, calculated by numerical integration of the Gibbs - Duhem equation in accordance with known expressions, the thermodynamic functions were determined: changes in entropy, enthalpy, and free energy of evaporation. Methods to determine the vapor pressure of isobaric and isothermal variants of the boiling point method and calculate thermodynamic values are described. The dependences of the values of partial vapor pressure of magnesium and tin were determined, based on which the energy functions were determined. The measurement error was 7.07%. Data on the change in evaporation entropies are presented graphically. An increase in the partial entropies of evaporation of magnesium and tin was noted with a decrease in their content in the alloy (each) to less than 20 at. %. Extremes are noted: a maximum for magnesium and a minimum for tin at a concentration corresponding to the stoichiometric composition of dimagnesium stannide (60 at. % Mg). The latter indicates the presence of a dissociating compound in the liquid phase that affects evaporation. The values of the change in enthalpy and Gibbs free energy of evaporation are tabulated. It was established that the values of partial and integral enthalpies and Gibbs free energy of vaporization monotonically increase from Mg to Sn in accordance with second-degree dependencies on the concentration of components in the alloy and linearly (Gibbs energy) with temperature. The very small change in the integral value of the free energy of evaporation of magnesium (0.03 ± 0.002 kJ/mol) at 1373 K (1100 °C) indicates a practical coincidence with the boiling point of magnesium. The energy functions of evaporation of magnesium-tin melts will supplement the thermodynamic database and can be used for thermal engineering calculations in the design of distillation processes and apparatus.

Keywords: magnesium, tin, dimagnesium stannide, thermodynamics, entropy, enthalpy, Gibbs energy.

Information about authors:

Volodin Valeriy Nikolaevich
Doctor of Technical Sciences, Professor, Chief Researcher of the Vacuum Processes Laboratory of the Institute of Metallurgy and Ore Beneficiation JSC, Satbayev University, 050010, Shevchenko str., 29/133, Almaty, Kazakhstan. Email: volodinv_n@mail.ru; ORCID ID: https://orcid.org/0000-0003-0116-1423

Trebukhov Sergey Anatolyevich
Candidate of Technical Sciences, Professor, Leading Researcher of the Laboratory of Vacuum Processes, Institute of Metallurgy and Ore Beneficiation JSC, Satbayev University, 050010, Shevchenko str., 29/133, Almaty, Kazakhstan. Email: s.trebukhov@satbayev.university; ORCID ID: https://orcid.org/0000-0001-9708-0307

Mukangaliyeva Arailym Omirzakkyzy
Master of Technical Sciences, Engineer of the Laboratory of Titanium and Rare Refractory Metals, Institute of Metallurgy and Ore Beneficiation JSC, Satbayev University, 050010, Shevchenko str. 29/133, Almaty, Kazakhstan. Email: a.mukangaliyeva@satbayev.university; ORCID ID: https://orcid.org/0000-0001-7032-1764

Linnik Xeniya Alexandrovna
Master of Technical Sciences, Junior Researcher of the Vacuum Processes Laboratory of the Institute of Metallurgy and Ore Beneficiation JSC, Satbayev University, 050010, Shevchenko str., 29/133, Almaty, Kazakhstan. Email: x.linnik@satbayev.university, xenija_linnik@mail.ru; ORCID ID: https://orcid.org/0000-0002-0683-1409

Nitsenko Alina Vladimirovna
Candidate of Technical Sciences, Head of the Vacuum Processes Laboratory of the Institute of Metallurgy and Ore Beneficiation JSC, Satbayev University, 050010, Shevchenko str., 29/133, Almaty, Kazakhstan. Email: alina.nitsenko@gmail.com; ORCID ID: https://orcid.org/0000-0001-6753-0936

Burabayeva Nurila Muratovna
Candidate of Technical Sciences, Senior Researcher of the Vacuum Processes Laboratory of the Institute of Metallurgy and Ore Beneficiation JSC, Satbayev University, 050010, Shevchenko str. 29/133, Almaty, Kazakhstan. Email: nuri_eng@mail.ru; ORCID ID: https://orcid.org/0000-0003-2183-2239

Introduction

Magnesium and its alloys are widely used in various industries [[1], [2], [3], [4], [5], [6], [7], [8]]. In recent years, researchers have paid great attention to the production of biodegradable magnesium alloys that have a minimal negative impact on the human body.

Along with the expansion of the range of magnesium-based alloys, problems have arisen with the processing of the wide variety of waste and secondary raw materials based on it. However, to date, no rational technology has been developed for the processing of biodegradable magnesium secondary raw materials containing tin, silver, and other metals, as well as defective products. One promising method to process such alloys may be vacuum distillation, with magnesium being transferred to the vapor phase and impurities being concentrated in the still bottom. However, no data on the energy characteristics of the evaporation of liquid magnesium–tin alloys have been found. In this regard, there is a need to determine the thermodynamic characteristics of Mg – Sn melt evaporation, which are necessary to calculate the energy costs of the distillation process. This can be done on the basis of experimental studies to determine the saturated vapor pressure values of the components that make up the system.

Magnesium and tin form alloys with unlimited solubility in the liquid state and the presence of a congruent melting compound Mg_2Sn at 778 °C [[9], [10]].

Quite a few papers [[11], [12], [13], [14], [15], [16], [17], [18], [19], [20]] are devoted to the study of the thermodynamic properties of magnesium–tin system melts. In studies [[11], [12]], using the method of electromotive forces of concentration chains, the thermodynamic functions of the system at temperatures of 650 °C and 800 °C were determined over the entire range of liquid alloy concentrations, and large negative deviations from ideal behavior were found. In paper [13], the saturated vapor pressure of magnesium, the thermodynamic functions of liquid alloys, and the liquidus lines of the phase diagram were determined using the isopyestic method at 990 and 1290 K.

The authors of [[14], [15]] determined the thermodynamic functions, thermal stability, and other physical properties of the Mg_2Sn condensed phase.

In the study [16], the partial pressure of saturated magnesium vapor for alloys containing 10–60 at. % Sn was determined using the boiling point method at temperatures of 1154–1385 K (881–1112 °C).

In papers [[17], [18]], data from previous studies were introduced into a double system model using a modified quasi-chemical model, which allowed for very good agreement with published experimental data.

Excess thermodynamic functions and activity coefficients, based on which the saturated vapor pressure can be determined for magnesium-tin alloy components at a temperature of 1073 K (800 °C), are given in publications [[19], [20]].

Other studies have investigated the physical properties and structure of magnesium alloys containing tin [[21], [22], [23]], as well as the effect of alloying additives on them [24]. No other information on vapor pressures, thermodynamic properties, or the thermodynamics of evaporation of the Mg – Sn system has been found in available sources.

This paper aims to determine the partial and integral thermodynamic functions of evaporation of the molten magnesium – tin system.

Materials, research methods, and calculations

Materials. The determination of the thermodynamic functions of evaporation of magnesium–tin alloys is based on the pressure values of the metals that make up the system.

Alloys containing 85.44, 73.18, 60.00, 47.12, and 32.81 at. % (58.18, 35.85, 23.50, 15.43, and 09 wt. %) tin were prepared for experiments to determine the saturated vapor pressure of the components.

To prepare the alloys, tin (99.99 wt. %) and double-distilled magnesium with a content of 99.99 wt.% of the main element were used for the preparation of alloys. The alloy was prepared in an alundum crucible placed in a steel retort at an argon pressure of 500 kPa and a temperature of 800–1100 °C, depending on the composition. Increased pressure was used to prevent magnesium evaporation. The initial components in the crucible were heated to the specified temperature, held for 5 hours, and then cooled by immersion in water.

An alloy with a content of 60.0 at. % Mg and 40.0 at. % Sn corresponds to the composition of the intermetallic compound Mg_2Sn – dimagnesium stannide. Analysis of the phase composition of the obtained sample, performed on a Bruker D8 Advance diffractometer with copper radiation

$\lambda_{k\alpha}$ = 0.154051 nm with a graphite monochromator, showed the presence of 97.8 % Mg_2Sn and 2.8 % Sn.

There is no information on the evaporation or decomposition of Mg_2Sn. In the case of congruent evaporation of the compound, the system should be considered as two quasi-binary systems: Sn–Mg_2Sn and Mg_2Sn–Mg with corresponding thermodynamic characteristics.

Determination of vapor pressure and vapor composition of Mg_2Sn. In this regard, the pressure and composition of the Mg_2Sn vapor were first determined. The boiling point method (isobaric variant) was used to determine the vapor pressure. The experiments were carried out on a continuous weighing setup, which is described in detail in [25]. The determination procedure was as follows. A sample of the Mg_2Sn alloy was placed in a quartz crucible and suspended on scales in a quartz retort filled with argon. Then, by throttling the inlet of the vacuum pump, the pressure specified by the experimental conditions was set and the crucible was lowered into the shaft furnace. The crucible with the sample was placed in a predefined isothermal zone of the furnace. After that, the furnace was heated at a constant rate. At the same time, the mass loss (Δm) and the corresponding temperature in the system were recorded. The temperature at which a sharp increase in the rate of mass loss was observed at a given pressure was considered equal to the vapor pressure of dimagnesium stannide or its decomposition components.

The composition of the vapor was judged by the composition of the condensate after the evaporation of Mg_2Sn in a vacuum at a temperature of 850 °C and a pressure of 0.67 kPa in a horizontal retort furnace.

Determination of the vapor pressure of magnesium over its alloys with tin. The saturated vapor pressures of magnesium and tin differ by several orders of magnitude – at the boiling point of magnesium (1373 K), the saturated vapor pressure of tin is 0.1 Pa [26]. In this regard, the isothermal boiling point method was chosen to determine the values of magnesium vapor pressure above its alloys with tin. The experiments were performed on a setup described in paper [25].

The determination method was as follows. A sample of the alloy was placed in a crucible, which was suspended in a retort outside the heating zone. The retort was evacuated twice using a vacuum pump and then filled with argon. After this, the lower part of the retort was placed in the isothermal zone of a preheated electric furnace. The retort was heated under an overpressure of 2–5 kPa with an open inert gas supply system to suppress the evaporation of components and compensate for the pressure increase in the retort due to gas expansion during heating. Once the sample reached the target temperature, argon evacuation from the retort volume was initiated while maintaining a constant sample temperature (isothermal mode). At the same time, the loss of the sample in mass and the change in pressure were simultaneously recorded. The pressure at which a sharp increase in the evaporation rate (weight loss) was observed was considered to be equal to the pressure of magnesium vapor above the alloy.

The values of the partial pressures of saturated magnesium vapor of alloys of the same concentration at different temperatures were described by the equation: $\ln\bar{p}_{Mg} = B + A \times T^{-1}$, then the dependence of each of the coefficients *A* and *B* was determined as a function of the magnesium concentration in the initial alloy. As a result, the temperature-concentration dependence of the magnesium vapor pressure $\ln\bar{p}_{Mg} = f(T, x_{Mg})$ was obtained.

The partial pressure of tin vapor above the magnesium–tin alloy was determined as: $\bar{p}_{Sn} = p^o_{Sn} \times a_{Sn} = p^o_{Sn} \times \gamma_{Sn} \times x_{Sn}$, where p^o_{Sn} is the saturated vapor pressure above elemental tin; a_{Sn} is the activity of tin in the alloy; γ_{Sn} is the activity coefficient of tin; x_{Sn} is the concentration of tin in the alloy, equal to $x_{Sn} = 1 - x_{Mg}$. Here x_{Mg} is the concentration of magnesium in the initial alloy.

The activity coefficient of tin was calculated by numerical integration of the Gibbs-Duhem equation, using an auxiliary function $\alpha_{Mg} = \ln\gamma_{Mg} / x^2_{Sn}$, proposed by Darken [27]. After transformation [28] and substitution into the equation: $\ln\gamma_{Sn} = -\int_{\ln\gamma_{Mg\ at\ x_{Mg}=1}}^{\ln\gamma_{Mg\ at\ x_{Mg}}} \frac{x_{Mg}}{x_{Sn}} d\ln\gamma_{Mg}$, this function relates $\ln\gamma_{Mg}$ and $\ln\gamma_{Sn}$ in a form convenient for numerical integration:

$$\ln\gamma_{Sn} = -\frac{\ln\gamma_{Mg} \times x_{Mg} \times x_{Sn}}{x^2_{Sn}} + \int_{x_{Mg}=0}^{x_{Mg}} \frac{\ln\gamma_{Mg}}{(1 - {}_{Mg})} dx_{Mg}.$$

Determination of energy characteristics. The values of the partial evaporation functions were determined in accordance with the dependence: $\Delta\bar{G}^V_{Mg(Sn)} = -RT\ln\bar{p}_{Mg(Sn)}$, where $\Delta\bar{G}^V_{Mg(Sn}$ is the partial Gibbs energy of evaporation of magnesium or tin;

$\bar{p}_{Mg(Sn)}$ is the partial pressure of saturated magnesium or tin vapor in their alloys. Hence: $\left(\frac{\partial \Delta \bar{G}^V_{Mg(Sn}}{\partial T}\right)_P = -\Delta \bar{S}^V_{Mg(Sn}$, $\Delta \bar{H}^V_{Mg(Sn)} = \Delta \bar{G}^V_{Mg(Sn)} + T \times \Delta \bar{S}^V_{Mg(Sn)}$, where $\Delta \bar{S}^V_{Mg(Sn}$ and $\Delta \bar{H}^V_{Mg(Sn)}$ are the partial entropy and enthalpy of evaporation of magnesium or tin.

The integral values of the entropy and enthalpy of evaporation were calculated by summing the fractions of the partial functions in the initial alloy: $\Delta S^V_{Mg-Sn} = x_{Mg}\Delta \bar{S}^V_{Mg} + x_{Sn}\Delta \bar{S}^V_{Sn}$ and $\Delta H^V_{Mg-Sn} = x_{Mg}\Delta \bar{H}^V_{Mg} + x_{Sn}\Delta \bar{H}^V_{Sn}$.

The change in Gibbs integral free energy (ΔG^V_{Mg-Sn}) is determined by the formula: $\Delta G^V_{Mg-Sn} = \Delta H^V_{Mg-Sn} - T\Delta S^V_{Mg-Sn}$.

Results and Discussion

The total error in the determination the vapor pressure of dimagnesium stannide is calculated as the sum of the errors in independent measurements, %: temperature – 1; weighing – 0.1; pressure 0.5; approximation of experimental data – 7.74, equal to 9.34%.

The values of the decomposition pressure – dissociation of dimagnesium stannide (p^D) depending on temperature were approximated by the expression: $\ln p^D[atm] = -21{,}250 \times T^{-1} + 15.169$. The complete dissociation temperature at atmospheric pressure corresponds to 1401 K = 1128 °C.

The enthalpy of magnesium dissociative evaporation, calculated from the equation of magnesium vapor pressure dependence on temperature, is 176.7 ± 16.5 kJ/mol, entropy – 126.1 ± 11.8 J/(mol×K).

Mg_2Sn undergoes decomposition into constituent metals during dissociative evaporation. Decomposition process of the compound at a temperature of 850 °C and a pressure of 0.67 kPa was performed using an installation to confirm such decomposition.

X-ray phase analysis of the condensate sample revealed 91.6 % Mg, 1.52 % Mg_2Sn, and 6.95 % SiO_2 (figure 1). X-ray fluorescence analysis revealed 95.35 % magnesium, 0.25 % tin, and 4.84 % silicon (figure 2). The presence of Mg_2Sn can be explained by entrainment of the initial alloy by the magnesium vapor flow formed during compound dissociation. As a result of the experiment to determine the composition of the vapor condensate, a significant number of spherical granules was found, indicating the fusion of tin droplets after the evaporation of magnesium from the alloy. The presence of SiO_2 is apparently due to its entry into the condensate sample when it was removed from the condenser.

The total measurement error in determining the values of magnesium vapor pressure above tin alloys was found to be equal to the errors of independent measurements: temperature – 1 %, weighing – 0.1 %, pressure 0.5 %, approximation of experimental data – 5.47 %, equal to 7.07 %.

We approximated the values of partial pressure of saturated magnesium vapor ($\bar{p}_{Mg}$) over alloys with tin by the dependence (1):

$$\ln \bar{p}_{Mg}[atm] = (-259{,}546x^4_{Mg} + 642{,}802x^3_{Mg} - 554{,}808x^2_{Mg} + 202{,}550x_{Mg} - 47{,}344) \times T^{-1} + 210.75x^4_{Mg} - 524.42x^3_{Mg} + 452.67x^2_{Mg} - 160.55x_{Mg} + 33.453 + \ln x_{Mg} \quad (1)$$

where: x_{Mg} – atomic fraction of magnesium in the alloy; T – temperature, K.

The saturated vapor pressure above elemental magnesium corresponds to the equation (2):

$$\ln p^o_{Mg}[atm] = -16{,}346 \times T^{-1} + 11.903 \quad (2)$$

The partial pressure of saturated tin vapor in the Mg–Sn system, was calculated by us by numerical integration of the Gibbs–Duhem equation and corresponds to the dependence (3):

$$\ln \bar{p}_{Sn}[atm] = (-259{,}546x^4_{Sn} + 741{,}443x^3_{Sn} - 776{,}751x^2_{Sn} + 384{,}200x_{Sn} - 125{,}543 - 16{,}884\ln x_{Sn}) \times T^{-1} + 210.75x^4_{Sn} - 599.58x^3_{Sn} + 621.78x^2_{Sn} - 302.35x_{Sn} + 81.96 + 15.53\ln x_{Sn} \quad (3)$$

The dependence of the vapor pressure above metallic tin was taken from [26] and converted by us to the form (4):

$$\ln p^o_{Sn}[atm] = -36{,}197 \times T^{-1} + 12.56 \quad (4)$$

The decomposition pressure of dimagnesium stannide (1401 ± 131 K), determined by the boiling point method (isobaric variant) within the limits of the determination errors, coincides with the boiling point of the melt (1494 ± 105 K), determined by the same method (isothermal variant).

The partial and integral entropies of evaporation are shown in Figure 3, and the enthalpies of evaporation of alloys calculated by us using the above equations are summarized in Table 1.

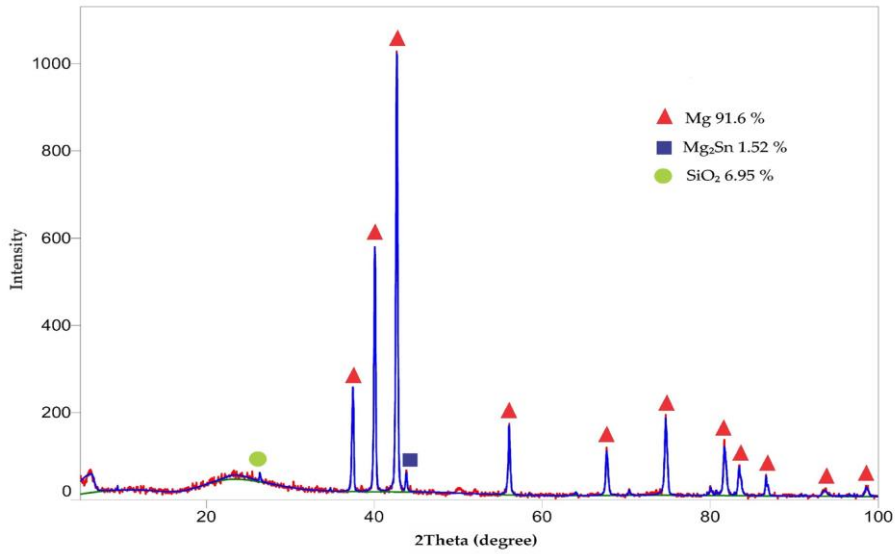

Figure 1 - X-ray diffraction pattern of the obtained magnesium condensate

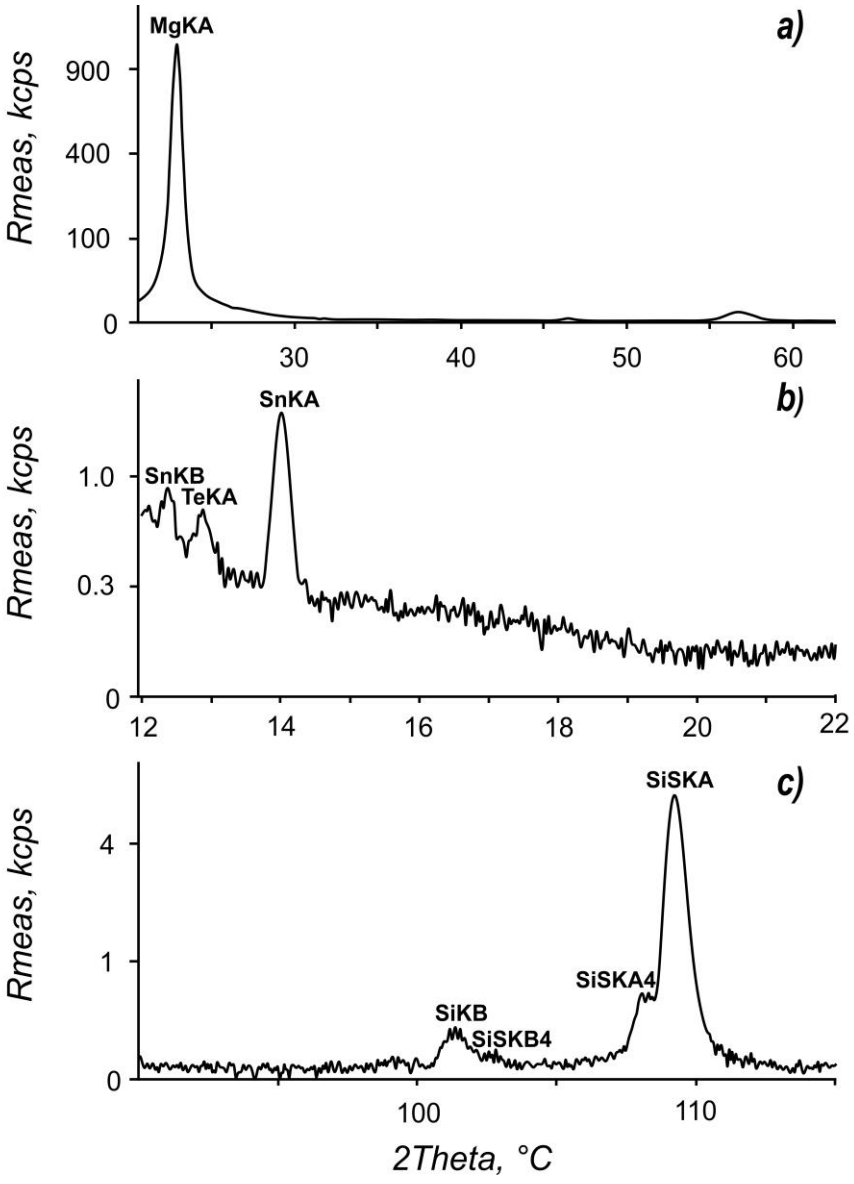

Figure 2 - Sections of the spectrogram of magnesium condensate obtained on different crystals (a - PX1; b - LiF200; c - PE) using the X-ray fluorescence wave-dispersive analysis method

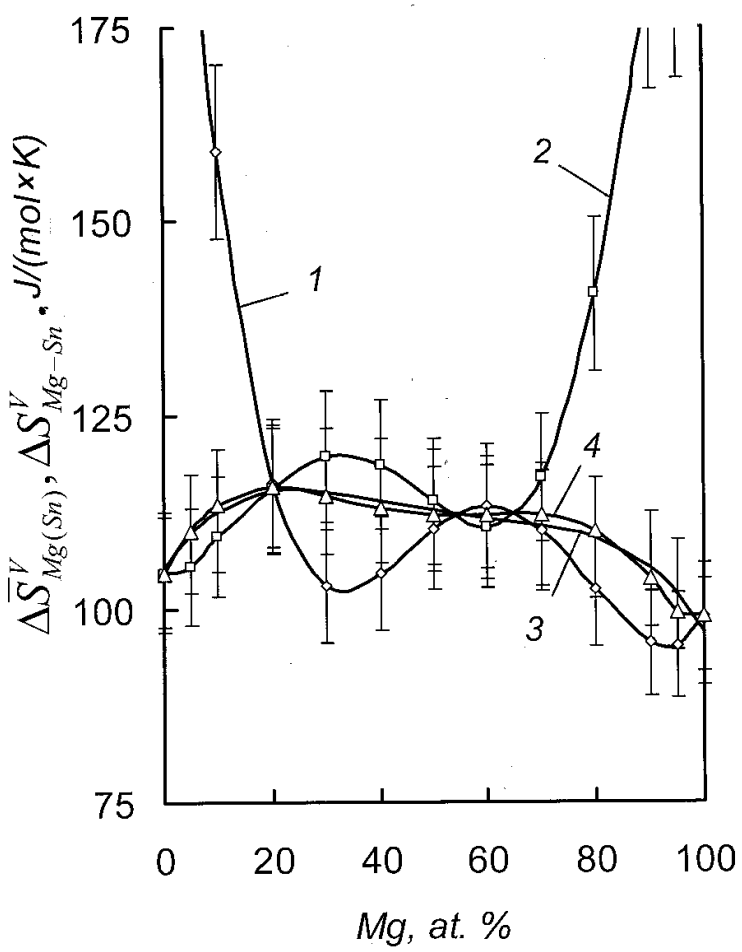

Figure 3 - Change in the entropies of evaporation of magnesium-tin alloys: 1 – change in the partial entropy of evaporation of magnesium; 2 – the same for tin; 3 – change in the integral entropy; 4 – calculated change in the integral entropy

The data shown in Figure 3 predictably indicate an increase in the partial entropies of evaporation of magnesium and tin when their content in the alloy (each) decreases to less than 20 at. %. Extremes are noted: a maximum for magnesium and a minimum for tin at a concentration corresponding to the stoichiometric composition of dimagnesium stannide (60 at. % Mg). The latter indicates the presence of a dissociating compound in the liquid phase that affects evaporation.

Based on the data we obtained, the change in the integral entropy of evaporation within the limits of measurement errors is approximated by the expression (5). In turn, the change in the integral enthalpy of evaporation can be determined by the formula (6), which was obtained by processing our experimental data.

$$\Delta S_{Mg-Sn}[J/(mol \times K)] = -255.29x_{Mg}^4 + 522.5x_{Mg}^3 - -383.48x_{Mg}^2 + 108.08\ _{Mg} + 105.14 \quad (5)$$

$$\Delta H_{Mg-Sn}[kJ/mol] = -134.3x_{Mg}^2 - 30.96x_{Mg} + 302.18 \quad (6)$$

The values of the change in Gibbs integral free energy (ΔG^V_{Mg-Sn}) in the liquid phase region up to the boiling point of magnesium at atmospheric pressure (1100 °C) are determined by us by the formula $\Delta G^V_{Mg-Sn} = \Delta H^V_{Mg-Sn} - T\Delta S^V_{Mg-Sn}$ and summarized in Table 2.

It can be seen, when analyzing the change in the values of partial and integral enthalpies and Gibbs free energy of vaporization, that the functions increase monotonically from Mg to Sn in accordance with the second-degree dependencies on the concentration of components in the alloy and linearly (Gibbs energy) with temperature. The very small change in the integral value of the free energy of evaporation of magnesium (0.03 ± 0.002 kJ/mol) at 1373 K (1100 °C) indicates a practical coincidence with the boiling point of magnesium.

Table 1 - Change in the partial and integral enthalpy of evaporation of magnesium-tin alloys

Composition of alloys, at. %		$\Delta\bar{H}^V_{Mg}$, kJ/mol	$\Delta\bar{H}^V_{Sn}$, kJ/mol	$\Delta\bar{H}^V_{Mg-Sn}$, kJ/mol
Mg	**Sn**			
100	0	135.91 ± 9.61	-	135.91 ± 9.61
95	5	132.32 ± 9.36	478.94 ± 33.86	149.65 ± 10.58
90	10	134.10 ± 9.48	459.77 ± 32.51	166.59 ± 11.78
80	20	146.14 ± 10.33	391.46 ± 27.68	195.20 ± 13.00
70	30	160.06 ± 11.32	348.75 ± 24.66	216.67 ± 15.32
60	40	169.09 ± 11.95	331.45 ± 23.43	234.03 ± 16.54
50	50	171.63 ± 12.13	328.17 ± 23.20	249.90 ± 17.67
40	60	171.26 ± 12.11	328.55 ± 23.23	265.63 ± 18.78
30	70	176.75 ± 12.50	325.87 ± 23.04	281.14 ± 19.88
20	80	202.03 ± 14.28	317.87 ± 22.47	294.70 ± 20.83
10	90	266.23 ± 18.82	307.09 ± 21.71	303.00 ± 21.42
5	95	320.31 ± 2264	302.80 ± 21.41	303.68 ± 21.47
0	100	-	301.03 ± 21.28	301.03 ± 21.28

Table 2 - Values of the change in Gibbs free energy of evaporation

Composition of alloys, at. %		ΔG^V_{Mg-Sn} (kJ/mol) at temperature, K:							
Mg	**Sn**	673	773	873	973	1073	1173	1273	1373
100	0	-	-	49.51 ± 3.50	39.62 ± 2.80	29.72 ± 2.10	19.83 ± 1.40	9.93 ± 0.70	0.03 ± 0.002
90	10	-	-	75.87 ± 5.36	65.48 ± 4.63	55.09 ± 3.89	44.70 ± 3.16	34.31 ± 2.43	23.92 ± 1.69
80	20	-	-	-	88.12 ± 6.23	77.12 ± 5.45	66.11 ± 4.67	55.11 ± 3.90	44.10 ± 3.12
70	30	-	-	-	-	96.33 ± 6.81	85.11 ± 6.02	73.90 ± 5.22	62.68 ± 4.43
60	40	-	-	-	-	113.73 ± 8.04	102.52 ± 7.23	91.30 ± 6.45	80.09 ± 5.66
50	50	-	-	-	-	129.62 ± 9.16	118.42 ± 8.37	107.21 ± 7.58	96.00 ± 6.79
40	60	-	-	-	155.71 ± 10.99	144.42 ± 10.21	133.12 ± 9.41	121.82 ± 8.61	110.53 ± 7.81
30	70	-	-	181.06 ± 12.80	169.60 ± 11.99	158.14 ± 11.18	146.67 ± 1.37	135.21 ± 9.6	123.75 ± 8.75
20	80	-	205.31 ± 14.52	193.74 ± 13.70	182.18 ± 12.88	170.61 ± 12.06	159.05 ± 11.24	147.48 ± 10.43	135.92 ± 9.61
10	90	226.68 ± 16.03	215.34 ± 15.22	204.00 ± 14.42	192.66 ± 13.62	181.31 ± 12.82	169.97 ± 12.02	158.63 ± 11.22	147.29 ± 10.41
0	100	230.75 ± 16.31	220.30 ± 15.58	209.86 ± 14.84	199.42 ± 14.10	188.97 ± 13.36	178.53 ± 12.62	168.09 ± 11.88	157.65 ± 11.15

Conclusions

Thus, as a result of the research, the values of partial pressure of magnesium and tin were determined, which served as the basis for determining the energy functions: changes in entropy, enthalpy and free energy of evaporation. As the content of each component in the alloy decreases to less than 20 at.%, the partial entropies of evaporation of magnesium and tin increase.

Extrema were established: a maximum for magnesium and a minimum for tin, which correspond to the dimagnesium stannide compound containing stoichiometrically 60 at. % Mg. It was found that the values of the partial and integral enthalpies, as well as the Gibbs free energy of evaporation, increase monotonically from magnesium to tin, with their concentration dependences described by second-degree polynomials, and the temperature dependence of the Gibbs free energy being linear. It was shown that the change in the integral value of the free energy of evaporation of elemental magnesium corresponds to 0.03±0.002 kJ/mol at 1373 K and indicates almost complete coincidence with the boiling point of magnesium. Thermodynamic functions of evaporation of magnesium-tin melts, determined on the basis of the values of vapor pressure of the system components, supplement the base of physical and chemical data and can be used for heat engineering calculations in the design of distillation processes and equipment.

Conflicts of interest. The corresponding author declare that there is no conflict of interest.

CRediT author statement: **V. Volodin**: Data Curation, Writing – original draft preparation, Conceptualization, Visualization, Investigation, Project administration; **S. Trebukhov, A. Nitsenko, A. Mukangaliyeva, X. Linnik, N. Burabayeva**: Data curation, Methodology, Writing – original draft preparation, Writing – Review & Editing. All authors have read and agreed to the published version of the manuscript.

Funding. The research was funded by the Science Committee of the Ministry of Science and Higher Education of the Republic of Kazakhstan (Grant AP 26196623).

Cite this article as: Volodin VN, Trebukhov ST, Mukangaliyeva AO, Linnik XA, Nitsenko AV, Burabayeva NM. Thermodynamics of Evaporation of Liquid Magnesium - Tin Alloys. Kompleksnoe Ispolzovanie Mineralnogo Syra = Complex Use of Mineral Resources. 2027; 343(4):5-15. https://doi.org/10.31643/2027/6445.36

Сұйық магний-қалайы қорытпаларының булануының термодинамикасы

Володин В.Н., Требухов С.А., Мұқанғалиева А.Ө., Линник К.А., Ниценко А.В, Бурабаева Н.М.

Металлургия және кен байыту институты АҚ, Сәтбаев университеті, Алматы, Қазақстан

Мақала келді: *22 желтоқсан 2025*
Сараптамадан өтті: *29 желтоқсан 2025*
Қабылданды: *28 қаңтар 2026*

ТҮЙІНДЕМЕ

Магнийдің қайнау температурасы әдісімен (сәйкесінше изобарлық және изотермиялық нұсқалар) анықталатын димагний станниді мен қалайы балқымасына және қалайыға парциалды қысымының мәндерін негізге ала отырып, термодинамикалық функциялар, энтропияның, энтальпияның және буланудың бос энергиясының өзгеруі белгілі өрнектерге сәйкес сандық интегралдау арқылы есептелген Гиббс-Дюгем теңдеуі арқылы анықталды. Қайнау температурасы әдісінің изобарлық және изотермиялық нұсқаларының бу қысымын анықтау және термодинамикалық шамаларды есептеу әдістері сипатталған. Магний мен қалайының парциалды бу қысымының мәндерінің тәуелділіктері анықталып, олардың негізінде энергетикалық функциялар анықталды. Өлшеудегі қателік 7,07 % болды. Булану энтропиясының өзгеруі туралы мәліметтер графикалық түрде берілген. Қорытпадағы магний мен қалайының үлесі (әрқайсысының) 20 ат. %-дан азайған кезде олардың булану энтропияларының артуы байқалды Экстремумдар белгіленді:: магний үшін максимум және қалайы үшін минимум димагний станнидінің (60 ат.% Mg) стехиометриялық құрамына сәйкес келетін концентрацияда Соңғысы сұйық фазада булануға әсер ететін диссоциацияланатын қосылыстың болуын көрсетеді. Энтальпияның өзгеру мәндері және Гиббс бос булану энергиясы кестеде келтірілген. Парциалды және интегралды энтальпиялардың және Гиббстің булануының еркін энергиясының мәндері Mg-ден Sn-ге қарай қорытпадағы компоненттер концентрациясынан екінші дәрежелі тәуелділікке сәйкес монотонды түрде артады және температураға байланысты сызықтық түрде (Гиббс энергиясы) артады. Магнийдің еркін булану энергиясының интегралдық мәндерінің өте аз мөлшердегі өзгерістері (1373 К (1100 °С) температурада 0,03±0,002 кДж/моль) магнийдің қайнау температурасымен іс жүзінде сәйкес келетінін көрсетеді. Магний-қалайы жүйесінің балқымаларының булануының энергетикалық функциялары термодинамикалық мәліметтер қорын толықтырады және дистилляция процестері мен аппараттарын жобалау кезінде жылу техникасының есептеулері үшін пайдаланылуы мүмкін.

Түйін сөздер: магний, қалайы, димагний станниді, термодинамика, энтропия, энтальпия, Гиббс энергиясы.

Володин Валерий Николаевич	***Авторлар туралы ақпарат:*** *Техника ғылымдарының докторы, профессор, Вакуумдық процестер зертханасының бас ғылыми қызметкері, Металлургия және кен байыту институты АҚ, Сәтбаев университеті, 050010, Шевченко көш., 29/133, Алматы, Қазақстан. Email: volodinv_n@mail.ru; ORCID ID: https://orcid.org/0000-0003-0116-1423*
Требухов Сергей Анатольевич	*Техника ғылымдарының докторы, профессор, Вакуумдық процестер зертханасының бас ғылыми қызметкері, Металлургия және кен байыту институты АҚ, Сәтбаев университеті, 050010, Шевченко көш., 29/133, Алматы, Қазақстан. Email: s.trebukhov@satbayev.university; ORCID ID: https://orcid.org/0000-0001-9708-0307*
Мұқанғалиева Арайлым Өмірзаққызы	*Техника ғылымдарының магистрі, Титан және сирек отқа төзімді металдар зертханасының инженері, Металлургия және кен байыту институты АҚ, Сәтбаев университеті, 050010, Шевченко көш., 29/133, Алматы, Қазақстан. Email: a.mukangaliyeva@satbayev.university; ORCID ID: https://orcid.org/0000-0001-7032-1764*
Линник Ксения Александровна	*Техника ғылымдарының магистрі, Вакуумдық процестер зертханасының кіші ғылыми қызметкері, Металлургия және кен байыту институты АҚ, Сәтбаев университеті, 050010, Шевченко көш., 29/133, Алматы, Қазақстан. Email: x.linnik@satbayev.university, xenija_linnik@mail.ru; ORCID ID: https://orcid.org/0000-0002-0683-1409*
Ниценко Алина Владимировна	*Техника ғылымдарының кандидаты, Вакуумдық процестер зертханасының меңгерушісі, Металлургия және кен байыту институты АҚ, Сәтбаев университеті, 050010, Шевченко көш., 29/133, Алматы, Қазақстан. Email: alina.nitsenko@gmail.com; ORCID ID: https://orcid.org/0000-0001-6753-0936*
Бурабаева Нурила Муратовна	*Техника ғылымдарының кандидаты, Вакуумдық процестер зертханасының аға ғылыми қызметкері, Металлургия және кен байыту институты АҚ, Сәтбаев университеті, 050010, Шевченко көш., 29/133, Алматы, Қазақстан. Email: nuri_eng@mail.ru; ORCID ID: https://orcid.org/0000-0003-2183-2239*

Термодинамика испарения жидких сплавов магния с оловом

Володин В.Н., Требухов С.А., Мукангалиева А.О., Линник К.А., Ниценко А.В. Бурабаева Н.М.

АО Институт металлургии и обогащения, Satbayev University, Алматы, Казахстан

Поступила: *22 декабря 2025*
Рецензирование: *29 декабря 2025*
Принята в печать: *28 января 2026*

АННОТАЦИЯ

На основании величин парциальных давлений магния над станнидом димагния и расплавами с оловом, определенные методом точек кипения (изобарический и изотермический вариант соответственно) и олова, рассчитанного численным интегрированием уравнения Гиббса-Дюгема в соответствии с известными выражениями определены термодинамические функции: изменения энтропии, энтальпии и свободной энергии испарения. Описаны методики определения давления пара изобарического и изотермического вариантов метода точек кипения и расчета термодинамических величин. Определены зависимости величин парциального давления пара магния и олова, на основании которых определены энергетические функции. Погрешность измерения составила 7,07 %. Данные об изменении энтропий испарения представлены графически. Отмечено увеличение парциальных энтропий испарения магния и олова при уменьшении их содержания в сплаве (каждого) менее 20 ат. %. Отмечены экстремумы: максимум для магния и минимум для олова при концентрации, соответствующей стехиометрическому составу станнида димагния (60 ат. % Mg). Последнее свидетельствует о наличии диссоциирующего соединения в жидкой фазе, влияющего на испарение. Величины изменения энтальпий и свободной энергии испарения Гиббса табулированы. Величины парциальных и интегральных энтальпий и свободной энергии испарения Гиббса монотонно увеличиваются от Mg к Sn в соответствии с зависимостями второй степени от концентрации компонентов в сплаве и линейно (энергия Гиббса) с температурой. Весьма малая величина изменения интегральной величины свободной энергии испарения магния (0,03±0,002 кДж/моль) при 1373 К (1100 ° С) свидетельствует о практическом совпадении с температурой кипения магния. Энергетические функции испарения расплавов системы магний – олово пополнят базу термодинамических данных, и могут быть использованы для теплотехнических расчетов при проектировании дистилляционных процессов и аппаратов.

Ключевые слова: магний, олово, станнид димагния, термодинамика, энтропия, энтальпия, энергия Гиббса.

Володин Валерий Николаевич	***Информация об авторах:*** *Доктор технических наук, профессор, главный научный сотрудник лаборатории вакуумных процессов, АО Институт металлургии и обогащения, Satbayev University, 050010, ул. Шевченко, 29/133, Алматы, Казахстан. Email: volodinv_n@mail.ru; ORCID ID: https://orcid.org/0000-0003-0116-1423*
Требухов Сергей Анатольевич	*Доктор технических наук, профессор, главный научный сотрудник лаборатории вакуумных процессов, АО Институт металлургии и обогащения, Satbayev University, 050010, ул. Шевченко, 29/133, Алматы, Казахстан. Email: s.trebukhov@satbayev.university; ORCID ID: https://orcid.org/0000-0001-9708-0307*

Мукангалиева Арайлым Омирзаковна	*Магистр технических наук, инженер лаборатории титана и редких тугоплавких металлов, АО Институт металлургии и обогащения, Satbayev University, 050010, ул. Шевченко, 29/133, Алматы, Казахстан. Email: a.mukangaliyeva@satbayev.university; ORCID ID: https://orcid.org/0000-0001-7032-1764*
Линник Ксения Александровна	*Магистр технических наук, младший научный сотрудник лаборатории вакуумных процессов, АО Институт металлургии и обогащения, Satbayev University, 050010, ул. Шевченко, 29/133, Алматы, Казахстан. Email: x.linnik@satbayev.university, xenija_linnik@mail.ru; ORCID ID: https://orcid.org/0000-0002-0683-1409*
Ниценко Алина Владимировна	*Кандидат технических наук, заведующая лабораторией вакуумных процессов, АО Институт металлургии и обогащения, Satbayev University, 050010, ул. Шевченко, 29/133, Алматы, Казахстан. Email: alina.nitsenko@gmail.com; ORCID ID: https://orcid.org/0000-0001-6753-0936*
Бурабаева Нурила Муратовна	*Кандидат технических наук, старший научный сотрудник лаборатории вакуумных процессов, АО Институт металлургии и обогащения, Satbayev University, 050010, ул. Шевченко, 29/133, Алматы, Казахстан. Email: nuri_eng@mail.ru; ORCID ID: https://orcid.org/0000-0003-2183-2239*

References

[1] Molaei M, Izadi M, Dikici B. Fattah-alhosseini A. Advances in green inhibitors for corrosion protection of magnesium and its alloys: A comprehensive review. Journal of Alloys and Compounds. 2025; 1038:182690. https://doi.org/10.1016/j.jallcom.2025.182690

[2] Yuan Y, Chen X, Xiong X, Li K, Tan J, Yang Y, Peng X, Chen X, Chen D, Pan F. Research advances of magnesium and magnesium alloys globally in 2024. Journal of Magnesium and Alloys. 2025; 13(10):4689-4732. https://doi.org/10.1016/j.jma.2025.09.034

[3] Volodin VN, Abdulvaliyev RA, Trebukhov SA, Nitsenko AV, Linnik XA. Recycling of beryllium, manganese, and zirconium from secondary alloys by magnesium distillation in vacuum. Kompleksnoe Ispolzovanie Mineralnogo Syra = Complex Use of Mineral Resources. 2024; 331(4):90-100. https://doi.org/10.31643/2024/6445.42

[4] Ablakatov IK, Ismailov MB, Mustafa LM, Sanin AF. Investigation of the Technology of Introducing Li, Mg and Zr Alloys into Aluminum Alloy. Kompleksnoe Ispolzovanie Mineralnogo Syra = Complex Use of Mineral Resources. 2023; 327(4):32-40. https://doi.org/10.31643/2023/6445.37

[5] Setiawan D, Lee H, Pyun J, Nimkar A, Shpigel N, Sharo D, Hong S, Aurbach D, Chae MS. Magnesium alloys as alternative anode materials for rechargeable magnesium-ion batteries: Review on the alloying phase and reaction mechanisms. Journal of Magnesium and Alloys. 2024; 12(9):3476-3490. https://doi.org/10.1016/j.jma.2024.09.018

[6] He M, Chen L, Yin M, Xu S, Liang Z. Review on magnesium and magnesium-based alloys as biomaterials for bone immobilization. Journal of Materials Research and Technology. 2023; 23:4396-4419. https://doi.org/10.1016/j.jmrt.2023.02.037

[7] Nitsenko A, Linnik X, Volodin V, Burabayeva N, Trebukhov S. Pyrolysis of copper telluride in a water vapour atmosphere. Kompleksnoe Ispolzovanie Mineralnogo Syra = Complex Use of Mineral Resources. 2025; 340(1):106–116. https://doi.org/10.31643/2027/6445.11

[8] Volodin V, Trebukhov S, Nitsenko A, Linnik X, Tuleutay F. Thermodynamics of antimony—selenium alloys formation and evaporation. Kompleksnoe Ispolzovanie Mineralnogo Syra = Complex Use of Mineral Resources. 2023; 330(3):13–21. https://doi.org/10.31643/2024/6445.24

[9] Nayeb-hashemi AA, Clark JB. The Mg – Sn (magnesium – tin) system. Bulletin of Alloy Phase Diagrams. 1984; 5(5):466-476.

[10] Lyakishev N.P., editor. Phase Diagrams of Binary Metallic Systems: Reference Book. Moscow: Mashinostroenie. 2001; 3(1):872.

[11] Yeremenko VN, Lukashenko GM. Thermodynamic Parameters of Melts in the Magnesium – Tin System. Ukrainian Chemical Journal. 1963; 29(9):896-900.

[12] Eckert CA, Irwin RB, Smith JS. Thermodynamic Activity of Magnesium in Several Highly-Solvating Liquid Alloys. Metallurgical Transactions B. 1983; 14(3):451-458. https://doi.org/10.1007/BF02654364

[13] Eldridge JM, Miller E, Komarek KL. Thermodynamic Properties of Magnesium – Tin Alloys by an Improved Isopiestic Method. Transactions of the Metallurgical Society of AIME. 1966; 236(1):114-121.

[14] Beardmore P, Howlett BW, Lichter BD, Bever MB. Thermodynamic Properties of Compounds of Magnesium and Group IVB Elements. Transactions of the Metallurgical Society of AIME. 1966; 236(1):102-108.

[15] Zheng B, Zhao L, Hu XB, Dong SJ, Li H. First-principles studies of $Mg_{17}Al_{12}$, Mg_2Al_3, Mg_2Sn, $MgZn_2$, Mg_2Ni и Al_3Ni. Physica B: Condensed Matter. 2019; 569:255-260. https://doi.org/10.1016/j.physb.2018.11.067

[16] Glazov VM, Pavlova LM, Poyarkov KB. P – T – x Diagrams of Binary Systems Mg - BIV (BIV - Si, Ge, Sn). Proceedings of the Academy of Sciences of the USSR. Inorganic Materials. 1983; 19(9):1465-1469.

[17] Glazov VM, Pavlova LM. Chemical Thermodynamics and Phase Equilibria (Binary Metallic and Semiconductor Systems). Moscow: Metallurgiia. 1981, 336.

[18] Ghosh P, Mezbahul-Islam M, Medraj M. Critical assessment and thermodynamic modeling of Mg – Zn, Mg – Sn, Sn – Zn and Mg – Sn – Zn systems. Calphad. 2012; 36:28-43. https://doi.org/10.1016/j.calphad.2011.10.007

[19] Dai YN, Bing Y. Vacuum Metallurgy of Non-Ferrous Metals. Beijing: Metallurgical Ind. Press. 2000; 3:547.

[20] Kubaschewski O, Alcock CB. Metallurgical Thermochemistry. Moscow: Metallurgiia. 1982, 390.

[21] Mesbah MB, Rashed HMMA. Effect of Sn on microstructure and tensile properties in a binary Mg-1Ca alloy. Results in Materials. 2025; 26:100697. https://doi.org/10.1016/j.rinma.2025.100697

[22] Castillo-Hernandez G, Yasseri M, Klobes B, Ayachi S, Müller E, de Boor J. Room and high temperature mechanical properties of Mg_2Si, Mg_2Sn and their solid solutions. Journal of Alloys and Compounds. 2020; 845:156205. https://doi.org/10.1016/j.jallcom.2020.156205

[23] Tani L, Kido H. Impurity doping into Mg2Sn: A first-principles study. Physica B: Condensed Matter. 2012; (407)17:3493-3498. https://doi.org/10.1016/j.physb.2012.05.008

[24] Han Y, Zhou R, Tong Y, Zhu L. Development of biodegradable in situ Zn-Mg_2Sn composites for bone implant application. Materials Letters. 2023; 333:133569. https://doi.org/10.1016/j.matlet.2022.13356919

[25] Kenzhalivev B, Trebukhov S, Volodin V, Nitsenko A, Linnik X, Ospanov Ye, Shakhalov A. Energy characteristics of the molten selenium-tellurium system. Scientific Reports. 2025; 15:36820. https://doi.org/1.1038/s41598-025-22206-9

[26] Malyshev VP, Turdukozhayeva AM, Ospanov EA, Sarkenov B. Vaporizability and boiling of simple substances. Moscow: Scientific World. 2010, 304.

[27] Darken LS, Gurry RW. Physical chemistry of Metals; McGraw-Hill Book Company INC: New York, Toronto, London. 1953, 570.

[28] Morachevsky AG. Thermodynamics of molten metal and salt systems. Moscow: Metallurgiia. 1987, 240.

Crossref
DOI: 10.31643/2027/6445.37
Metallurgy and Metallurgical Engineering

Deposition Methods of Multilayer Hard Coatings for Improving Tribological Performance: A Mini-Review

[1]Bakhytuly N., [1,2*]Smailov K.M., [1]Kenzhegulov A.K., [2]Kudabayeva M.A., [1]Yessengaziyev A.M., [1]Karim D.D., [1]Arynbayev T.M.

[1] Institute of Metallurgy and Ore Beneficiation JSC, Satbayev University, Almaty, Kazakhstan
[2] Al Farabi Kazakh National University, Almaty, Kazakhstan

** Corresponding author email: k.smailov@satbayev.university*

Received: *January 20, 2026*
Peer-reviewed: *January 27, 2026*
Accepted: *January 29, 2026*

ABSTRACT

Multilayer hard coatings remain among the most effective engineering solutions for reducing friction and wear and for extending the service life of components operating under high contact loads. However, their practical performance is governed not by multilayering per se, but by the extent to which the selected deposition technology enables reproducible control over three key parameters: layer density and defectiveness, adhesion to the substrate and/or interlayers, and architectural tunability through interface quality. This mini-review systematizes deposition approaches relevant to tribological applications and proposes a generalized classification comprising chemical processes (sol–gel, chemical vapor deposition (CVD), atomic layer deposition (ALD), hydrothermal synthesis, electrodeposition, anodization, and electroless coatings), physical vacuum techniques of the PVD family (magnetron sputtering, cathodic arc deposition, hollow cathode discharge (HCD) ion plating, ion beam assisted deposition (IBAD), among others), as well as hybrid and functional solutions (PVD+CVD, composite, self-lubricating, and nanocomposite systems). It is demonstrated that the selection of a deposition process for multilayer architectures must be based on technological constraints that directly affect interface stability and coating durability, including the deposition temperature window and conformality, interfacial diffusion-induced boundary blurring, residual stresses, and critical defects such as porosity, macroparticles, and growth-related imperfections. Practical guidelines are formulated for correlating "architecture–deposition regime–microstructure–tribological behavior," and key directions for future research are identified, including interface and defect engineering, targeted hybridization of deposition processes to compensate for intrinsic limitations (conformality, density, adhesion, and interface stability), and the use of predictive modeling validated by comparable tribological testing.

Keywords: multilayer hard coatings, CVD, PVD, magnetron sputtering, transition metal nitrides.

Information about authors:

Bakhytuly Nauryzbek — *PhD, Head of Laboratory of Physical Methods of Analysis of the Institute of Metallurgy and Ore Beneficiation JSC, Satbayev University, 050010, Shevchenko str., 29/133, Almaty, Kazakhstan. Email: n.bakhytuly@satbayev.university*

Smailov Kenzhegali Mamanovich — *Doctoral student, Al Farabi Kazakh National University; Junior Researcher at the Chemical Analytical Laboratory of the Institute of Metallurgy and Ore Beneficiation JSC, Satbayev University, 050010, Shevchenko str., 29/133, Almaty, Kazakhstan. Email: k.smailov@satbayev.university*

Kenzhegulov Aidar Karaulovich — *PhD, Head of Metal Science Laboratory of the Institute of Metallurgy and Ore Beneficiation JSC, Satbayev University, 050010, Shevchenko str., 29/133, Almaty, Kazakhstan. Email: a.kenzhegulov@satbayev.university*

Kudabayeva Madina Amirbekovna — *Doctoral student, senior lecturer at Al-Farabi Kazakh National University, 050040, Al-Farabi Ave., 71, Almaty, Kazakhstan. Email: madina.kudabayeva@kaznu.edu.kz*

Yessengaziyev Azamat Muratovich — *Ph.D., Head of the Laboratory of Titanium and Rare Refractory Metals of the Institute of Metallurgy and Ore Beneficiation JSC, Satbayev University, 050010, Shevchenko str., 29/133, Almaty, Kazakhstan. Email: a.yessengaziyev@satbayev.university*

Karim Diana Dauletovna — *Engineer at the Chemical Analytical Laboratory of the Institute of Metallurgy and Ore Beneficiation JSC, Satbayev University, 050010, Shevchenko str., 29/133, Almaty, Kazakhstan. Email: d.karim@satbayev.university*

Arynbayev Talgat Maratuly — *Engineer at the Laboratory of Physical Methods of Analysis of the Institute of Metallurgy and Ore Beneficiation JSC, Satbayev University, 050010, Shevchenko str., 29/133, Almaty, Kazakhstan. Email: arynbayev.talgat@mail.ru*

Introduction

In mechanical systems, friction and wear inevitably arise at interfaces where components move relative to one another under direct contact, leading to significant energy losses and premature equipment failure [[1],[2]]. To address these challenges, researchers have developed a wide range of innovative approaches aimed at reducing friction and mitigating wear [[3],[4]]. Among them, the application of protective coatings remains one of the most reproducible and technologically mature engineering solutions, as coating properties can be purposefully tailored through the selection of material composition and architectural design.

Multilayer hard coatings have moved to the foreground as deposition technologies and surface-engineering strategies mature. Their performance is now dictated not only by chemical composition, but by the layer architecture itself and the way it is manufactured [[5],[6]]. In tribological service, two variables dominate: the quality of interfaces and the characteristic architectural length scales. Interfaces control barrier behavior, redistribute stresses, and impede crack propagation. Shrinking the multilayer period, in turn, is typically coupled with structural hardening and a shift in the prevailing damage mechanisms. A third factor cannot be treated as secondary: protective tribofilm formation at the sliding contact often sets the boundary conditions for friction and wear, and therefore directly shapes the measured tribological response [[7], [8], [9]].

At the same time, “multilayering” is not a performance guarantee. In practice, the ceiling is frequently imposed by structure-formation parameters of the chosen process rather than by the concept of layering itself. Deposition temperature and conformality, diffusion-driven interfacial smearing, defect population, and residual-stress state repeatedly emerge as the controlling limitations [10]. For that reason, we treat the deposition route as part of coating-architecture engineering, not as an afterthought. The selected process must deliver sharp interfaces, reproducible layer thickness, and a controllable defect spectrum for the specific substrate and component geometry under consideration.

In this mini-review, we systematize deposition technologies for multilayer coatings (MLCs) aimed at friction and wear reduction and compare them through a single set of capability–limitation criteria. Chemical routes are examined first (sol–gel, chemical vapor deposition (CVD), atomic layer deposition (ALD), hydrothermal synthesis, electrodeposition, anodization, and electroless coatings). We then analyze physical vacuum approaches from the PVD family, including magnetron sputtering, cathodic arc deposition, hollow cathode discharge (HCD) ion plating, ion beam assisted deposition (IBAD), and related variants. Finally, hybrid and functional solutions are discussed – PVD+CVD combinations, composite architectures, self-lubricating systems, and nanocomposites. On this basis, we formulate practical guidelines for selecting deposition technologies to match the target architecture and service conditions, and we delineate research priorities centered on interface engineering, process hybridization, and predictive modeling of tribological response.

Market Overview of Multilayer Coating Deposition Technologies

Demand for hard protective coatings is shaped by engineering use-cases rather than by academic curiosity. Industry asks for measurable outcomes: higher wear resistance, lower friction coefficient, longer fatigue life, and stronger corrosion tolerance in parts that see high contact stresses and/or elevated temperatures. In this context, multilayer architectures function as a design lever. By tuning interface density and layer periodicity, engineers adjust the residual-stress state, raise crack tolerance, and steer the tribochemical response of the coating through controlled interfacial phenomena.

Specialized market reports place the global hard-coatings market at roughly USD 1.72–1.73 billion in 2025, forecast it to reach USD 1.84–1.85 billion in 2026, and project USD 2.98–3.01 billion by 2033; these trajectories correspond to a CAGR of about 7.0–7.2% [[11], [12], [13]]. These numbers should be read for what they are: outputs of market-research models rather than experimentally validated scientific measurements. We cite them here for one purpose only – to justify the technological relevance of those market segments where multilayer coatings (MLCs) are deployed.

Segmentation by End-Use Applications

Figure 1 summarizes how hard protective coatings are allocated across industrial sectors (2025 baseline with forecast estimates for 2026). The demand profile is skewed toward applications in which the coating operates as a functional reliability layer rather than a purely decorative finish. The

strongest pull comes from heavily loaded transportation and aerospace components, followed by medical devices and electronic systems, where service integrity is tightly coupled to surface performance.

For multilayer coatings, the commercial value therefore extends beyond hardness metrics. It is set by manufacturing discipline: whether interfaces can be reproduced with minimal drift, whether friction and wear remain stable over long service intervals, and whether the defect population can be held within controlled bounds from batch to batch at production scale.

Figure 1 maps hard-coating demand across industrial sectors. The largest portion is tied to heavily loaded engineering domains, where coatings must satisfy concurrent constraints: high wear resistance, thermal stability, and a tribological response that remains predictable over prolonged service intervals.

Segmentation by Coating Material Type

Figure 2 compiles the material-type breakdown of hard coatings using aggregated statistics for 2023–2025. In this dataset, nitride-based coatings form the largest group (31.5%). Oxides follow at 19.3%, then carbides at 15.1%. Carbon-based coatings account for 11.2%, borides for 8.0%, and multicomponent systems for 14.9%.

The ranking aligns with the engineering rationale of multilayer design. Nitrides are routinely selected as load-bearing and/or diffusion-barrier layers. Carbides and carbon-containing phases are introduced when the architecture must deliver lower friction and/or higher chemical resistance. Multicomponent compositions, by contrast, offer a practical route to stack several functions—hardness, oxidation resistance, and friction control–while preserving adhesion and maintaining thermal stability.

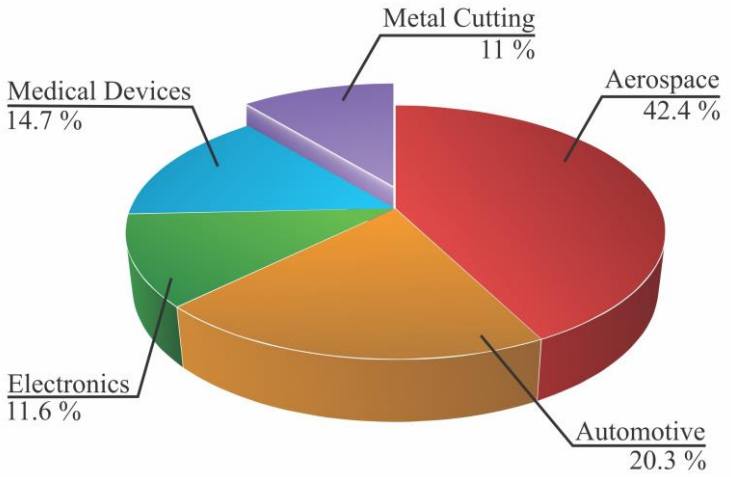

Figure 1 - Distribution of end-use application sectors for hard protective coatings (2025 estimates with forecast values for 2026; aggregated from marketing review data) [11]

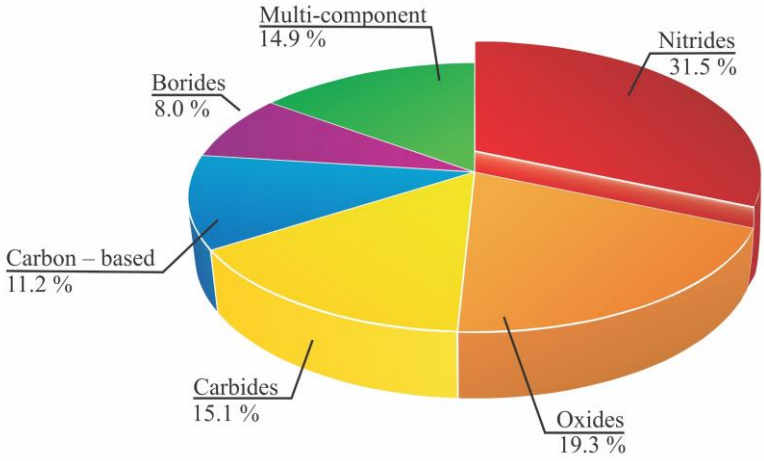

Figure 2 - Material-type distribution of hard coatings (aggregated data for 2023–2025) [11]

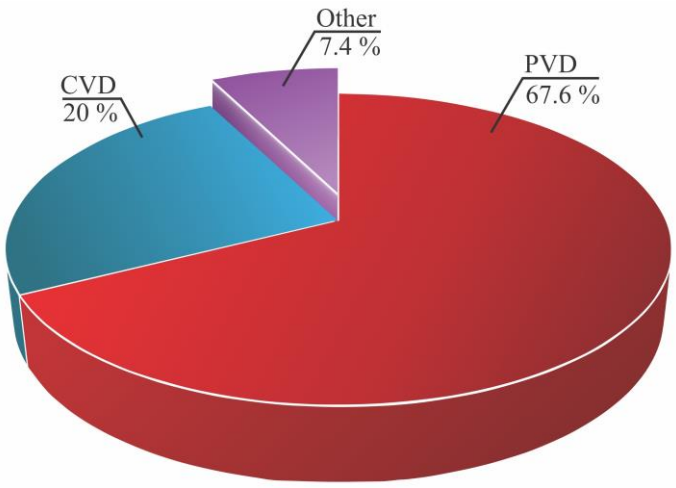

Figure 3 - Distribution of hard coating deposition technologies (2025 data; aggregated from marketing review sources) [11]

As summarized in Figure 2, nitride-based systems occupy the largest share of the dataset. This prevalence is consistent with their processing flexibility in PVD routes and with their practical role in multilayer periodic architectures, where stable growth conditions enable tight control over interface formation.

Segmentation by Deposition Technology.

Figure 3 compares deposition routes used for hard coatings. The dataset is clearly PVD-weighted: physical vapor deposition accounts for ≈67.5% of reported technologies, CVD contributes roughly 20%, and the balance is distributed among other methods. This dominance matters for multilayer systems. PVD routes typically allow tighter metrology-level control over individual layer thickness and preserve interface sharpness – two parameters that govern whether interface-mediated strengthening and crack-arrest mechanisms can be reliably activated in service.

CVD retains a distinct niche. When the application prioritizes high thermal stability and/or strong conformality, CVD often provides the required film continuity on complex geometries. That advantage has a cost: the thermal budget intrinsic to CVD narrows the set of compatible substrates and constrains which multilayer architectures can be implemented without substrate degradation or interfacial smearing.

Figure 3 makes the market's technological base unambiguous: hard coatings are produced predominantly by PVD routes, and this positioning effectively turns PVD into the main industrial platform for multilayer coatings (MLCs). CVD still occupies a sizeable fraction, yet its wider deployment is curtailed by the admissible deposition-temperature window and by substrate compatibility constraints.

The same segmentation points to a pragmatic selection criterion. Industry favors technologies that scale without losing reproducibility, i.e., routes that can hold layer periodicity, interface integrity, and defect population within controlled bounds while staying within an acceptable cost envelope. As a result, the deposition method is not chosen solely based on peak coating performance. Process robustness, the breadth of the workable parameter space, and batch-to-batch tolerances for property scatter carry comparable weight in decision-making.

Classification of Multilayer Coating Deposition Methods

Deposition routes for multilayer coatings (MLCs) are best treated as an engineering toolbox: each process expands certain capabilities while simultaneously setting hard constraints on the properties that can be realized. In tribological practice, three control targets repeatedly determine success. The first is layer compactness together with the defect landscape (porosity, droplets/particles, columnar boundaries). The second is adhesion – both to the substrate and, where relevant, across interlayers. The third is functional response, which in multilayer systems is inseparable from the ability to reproduce the intended architecture (period, thickness ratios, and interface integrity).

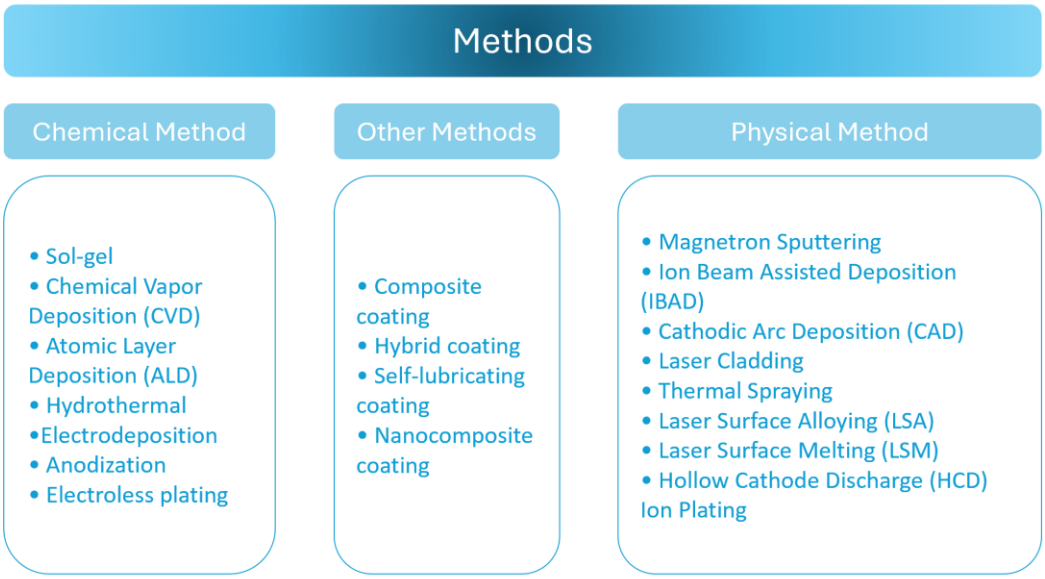

Figure 4 - Classification of multilayer coating deposition methods

With these requirements in view, we organize the deposition methods discussed in this review into three generalized groups. This classification provides a practical basis for selecting deposition routes intended to optimize coating performance, rather than treating deposition as a secondary processing step.

As illustrated in Figure 4, the methods are classified into three blocks: chemical methods, in which coating formation is governed by reactive transformations in the gas and/or liquid phase; hybrid and functional approaches that combine elements of chemical and physical processes to produce multifunctional layers; and physical methods, predominantly of the vacuum-based class, which enable controlled microstructure development and precise engineering of interlayer interfaces.

Chemical methods comprise processes in which coating growth is governed by reaction-controlled transformations and mass transport in the gas and/or liquid phase. This group includes sol–gel processing, chemical vapor deposition (CVD), atomic layer deposition (ALD), hydrothermal synthesis, electrodeposition, anodization, and electroless plating. From an engineering perspective, these approaches are typically regarded as effective routes for producing uniform and conformal layers on a wide range of substrates at moderate process temperatures, making them particularly suitable for forming individual functional layers and/or process stages where coating continuity is critical. At the same time, when applied to multilayer architectures, a specific limitation emerges: diffusion – and reaction-driven phenomena at interfaces may lead to interlayer boundary blurring and, consequently, to reduced reproducibility of the intended architectural effects.

Hybrid and functional approaches are considered as a separate category, as they represent not a single deposition technique but rather a class of solutions in which the targeted tribological functionality is achieved through the combination of multiple processes and/or materials. As shown in Figure 4, this group includes composite, hybrid, self-lubricating, and nanocomposite coatings. From a practical standpoint, such solutions are employed to integrate properties that are difficult to achieve within a single process or material system–for example, low friction while maintaining load-bearing capacity and resistance to degradation. Accordingly, the key issue for this category is not the enumeration of composite variants, but rather reproducibility criteria, including controllability of phase/component distribution and interface stability within multilayer systems during scale-up.

Physical routes include vacuum evaporation and sputtering, along with allied processes in which coating outcome is set primarily by plasma/particle flux characteristics and by growth kinetics during film formation. In the scheme summarized in Figure 4, this class covers physical vapor deposition (PVD), magnetron sputtering, ion beam assisted deposition (IBAD), cathodic arc deposition (CAD), laser cladding, thermal spraying, laser surface alloying (LSA), laser surface melting (LSM), and hollow cathode discharge (HCD) ion plating. For multilayer coatings, these methods offer a practical advantage: they give

the operator comparatively direct leverage over microstructure and interface integrity. Layer thickness can be metered with high precision, and interface sharpness can be preserved – both are prerequisites for activating architecture-driven mechanisms that raise wear resistance.

This category, however, is not uniform. It spans fundamentally different process families and distinct engineering purposes. At one end sit vacuum thin-film techniques that enable nanometer-scale control of periodicity; at the other, localized deposition or surface-modification routes intended for thick coatings and repair scenarios. Such breadth forces a different comparison logic: we cannot rank technologies by name alone. Instead, we evaluate the constraints each process places on component geometry, defect generation, adhesion, and – crucially – the reproducibility of multilayer architectures.

Figure 4 therefore, functions as the organizing scaffold for the present mini-review. It allows us to compare deposition methods against three operational criteria – layer density/defectiveness, adhesion, and functional performance coupled with architectural controllability – and to select deposition routes that match specific tribological requirements.

Chemical methods

Chemical methods for the formation of multilayer coatings (MLCs) are based on reaction-controlled layer growth in the gas and/or liquid phase and are applied where conformality, uniformity, and/or the formation of functional barrier or interlayers within the architecture are required. Chemical approaches include sol–gel processing, chemical vapor deposition (CVD), atomic layer deposition (ALD), hydrothermal synthesis, electrodeposition, anodization, and electroless plating.

For tribological applications, chemical methods can be rationally viewed as tools for addressing two practical tasks: (1) the fabrication of a continuous functional layer with a predefined chemical nature; and (2) the integration of this layer into a hybrid architecture with vacuum-based methods, where compatibility in terms of adhesion and interface stability is required.

CVD enables the deposition of dense coatings (reported to exceed 95% of the theoretical density) with high adhesion strength ($\sigma_{(adh)}$ > 50 MPa), including coatings on internal surfaces. However, its applicability to multilayer architectures is constrained by the process window, notably high deposition temperatures (T 1173 K), precursor toxicity, and the risk of diffusion-induced interfacial blurring.

ALD is described as a self-limiting process with atomic-scale growth control and is particularly relevant for nanolaminates and thin functional interlayers, where reproducibility and nanometer-level thickness control are critical.

Sol–gel processing is characterized by low-temperature synthesis (293–423 K) and the capability to conformally coat complex geometries. Nevertheless, for tribological applications, key limitations summarized in Table 1 must be considered, including shrinkage during thermal treatment (up to 30%), porosity (>10%), and hydration. Consequently, sol–gel approaches are well-suited for forming oxide-based functional layers (e.g., SiO_2, TiO_2); however, when designing wear-resistant multilayer systems, the effects of porosity and shrinkage on mechanical integrity and interface stability must be carefully accounted for.

Hydrothermal and solution-based processes are employed to form specific functional layers. Hydrothermal synthesis is conducted in aqueous solutions under elevated pressure and is described as an approach that promotes crystallization of oxide structures without the use of organic solvents. Electrodeposition and electroless plating enable the formation of metallic layers at near-room temperature, but require strict control of pH and electrolyte composition due to the risk of hydrogen embrittlement. Anodization produces porous oxide films and is inherently limited to valve metals.

A critical limitation of chemical methods in multilayer coatings is interfacial diffusion, which can lead to boundary blurring and reduced mechanical integrity of the multilayer system. To mitigate these effects, post-treatments aimed at improving interface quality are often required. Consequently, in tribological multilayer coatings, chemical methods typically function as part of a broader technological route–often at early stages of graded structure formation–and/or as elements of hybrid schemes, where their combination with physical methods is considered a means to enhance resistance to tribological degradation.

Comparative characteristics of chemical methods, including temperature windows, risks of porosity and shrinkage, interfacial blurring, and typical application domains, are summarized in Table 1.

Table 1 - Chemical methods

Method	Advantages	Limitations	Scientific Applications	References
Sol–gel	Low-temperature synthesis (293–423 K); molecular homogeneity; conformal coating of complex topologies	Shrinkage during heat treatment (up to 30%); porosity (>10%); hydration	Formation of amorphous oxide matrices (SiO_2, TiO_2) for biocompatible implants and optical coatings	[[14], [15]]
Chemical Vapor Deposition (CVD)	High density (>95% of theoretical); excellent adhesion ($\sigma_{(adh)}$ > 50 MPa); capability to coat internal surfaces	High thermal load (T > 1173 K); diffusion-induced interface blurring ($D>10^{-18}$ m^2/s^{-1}); toxic precursors	Thermal barrier coatings (YSZ); monolithic carbide layers on WC–Co	[[16,[17], [18]]
Atomic Layer Deposition (ALD)	Self-limiting growth (0.1–0.3 Å/$cycle^{-1}$); conformality >99%; atomic-scale thickness control	Low deposition rate (1–5 nm/min); high precursor cost ($TiCl_4$, TMA); vacuum requirements	Nanolaminates (Al_2O_3/TiN); barrier layers in microelectronics; polymer protection	[[19],[20]]
Hydrothermal synthesis	Crystallization at moderate temperatures (373–573 K); environmentally benign; solvent-free organic chemistry	Restricted to aqueous systems; low kinetics (hours–days)	Nanostructured oxide synthesis (ZnO, TiO_2) for photocatalysis and sensors	[[21], [22]]
Electrodeposition	Room-temperature processing; scalability; low cost	Limited to conductive substrates; hydrogen embrittlement risk	Electrochemical deposition of Ni–P, Cu for corrosion protection	[[23], [24]]
Anodization	Local strengthening; formation of porous oxides (pore diameter 20–200 nm)	Restricted to valve metals (Ti, Al, Ta); thickness <50 µm	Anodized Ti_6Al_4V for osteointegration and biomedical implants	[[25], [26], [27]]
Electroless plating	Deposition on dielectrics; high thickness uniformity (±5%)	Bath instability; phosphorus-induced embrittlement	Ni–P coatings on polymers and printed circuit boards	[[28], [29]]

Table 1 indicates that chemical methods can be rationally regarded as tools for forming functional layers with high uniformity, albeit with fundamentally different technological trade-offs. Sol–gel processing offers advantages in terms of temperature window and cost, but is limited by shrinkage and porosity; CVD provides high density and strong adhesion, yet requires elevated temperatures and toxic precursors; ALD delivers the highest level of thickness control at the nanometer-scale, but is primarily suited for thin layers and localized architectural tuning; solution-based methods (hydrothermal synthesis, electrodeposition, electroless plating, and anodization) are advantageous under low thermal loads, while imposing constraints related to process chemistry, risks of hydrogen embrittlement, and/or substrate material compatibility.

Other / Hybrid Methods

In this work, the group of Other Methods is treated as a separate category, as it does not represent an additional deposition technique per se, but rather a set of engineering solutions aimed at multifunctionality, in which the desired tribological response is achieved through combinations of phases and structures and/or through the integration of multiple technological routes. The main variants within this group include composite, hybrid (PVD+CVD), self-lubricating, and nanocomposite coatings; their comparative characteristics are summarized in Table 2.

Composite coatings exploit dispersed functional phases to couple two targets that often compete: high hardness and low friction. Table 2 lists representative performance benchmarks (H > 40

GPa, μ < 0.2) and provides example formulations used in cutting-tool service, including nc-TiN/a-Si_3N_4 architectures with MoS_2 additives. The approach remains sensitive to microstructural stability. Phase segregation and the practical difficulty of metering dispersion quality and spatial distribution limit repeatability; in multilayer systems, that variability translates directly into scatter of measured properties.

Hybrid PVD+CVD schemes address a different constraint set and are typically adopted as a process-level compromise. Here, PVD supplies nanostructuring capability, whereas CVD is used to achieve high layer density. Table 2 illustrates this route with TiCN/TiN coatings deposited on cemented carbide inserts. Two obstacles recur in industrial deployment: high capital cost and the emergence of thermal gradients. Both factors complicate scale-up and can erode architectural stability when the process is pushed to production throughput.

Self-lubricating coatings pursue friction reduction through the in situ generation and/or controlled release of lubricious species. Table 2 highlights a MoS_2-based system that undergoes transformation to MoO_3 and reports friction coefficients as low as μ < 0.1 under vacuum – conditions characteristic of dry-friction assemblies, including space mechanisms. Their weakness is equally clear. Oxidative degradation limits operation at elevated temperature (Table 2 indicates constraints above T > 673 K), and service life is finite, which must be accounted for when defining operating windows and when selecting multilayer architectures.

Nanocomposite coatings exploit nanoscale phase dispersion to achieve a combination of superhardness and fracture toughness. Table 2 reports representative benchmarks (H > 40 GPa, $K_{(IC)}$ > 5 MPa·$m^{1/2}$) and example systems (nc-TiC/a-C, nc-WC/DLC) intended for extreme loading conditions. The primary technological risk is nanoparticle agglomeration and the complexity of synthesis and dispersion control, which can lead to property scatter and reduced coating strength.

Across all Other Methods, a common bottleneck is the controllability of phase dispersion and the stability of interphase and interlayer boundaries. The manuscript explicitly notes that difficulties in dispersion control promote nanoparticle agglomeration and, in multilayer systems, phase segregation; compared to physical methods, these approaches often exhibit inferior density unless additional post-treatment is applied. Consequently, their use in tribological multilayer coatings is primarily justified in applications where adaptability (self-lubrication and multifunctionality) is required and where increased process complexity is acceptable, including hybridization with vacuum-based methods to improve interface quality.

Table 2 indicates that Other Methods provide enhanced functionality–such as friction reduction, adaptive lubricating phases, and the combination of high hardness with fracture toughness–but require substantially stricter structural control. The key risks are associated with phase segregation and agglomeration, thermal stability limitations (particularly for self-lubricating systems at T > 673 K), and the technological complexity inherent to hybrid PVD+CVD routes.

Table 2 - Other/Hybrid Methods

Method	Advantages	Limitations	Scientific Applications	References
Composite coatings	Synergistic strengthening (H > 40 GPa) with reduced friction (μ < 0.2); adaptive response	Phase segregation; difficulty in dispersion control	nc-TiN/a-Si_3N_4 + MoS_2 for cutting tools	[[30], [31]]
Hybrid coatings (PVD + CVD)	Combined microstructure: PVD-induced nanostructuring and CVD-derived high density	High capital cost; thermal gradients complicating scale-up	TiCN/TiN coatings on cemented carbide inserts	[32]
Self-lubricating coatings	In situ formation of lubricious phases (MoS_2 → MoO_3); μ < 0.1 in vacuum	Oxidative degradation at T > 673 K; limited lifetime	Space mechanisms; dry-friction systems	[[33], [34]]
Nanocomposite coatings	Superhardness (H > 40 GPa); high fracture toughness ($K_{(IC)}$ > 5 MPa·$m^{1/2}$)	Nanophase agglomeration; synthesis complexity	nc-TiC/a-C, nc-WC/DLC for extreme loading conditions	[[35], [36], [37]]

Physical PVD Methods

Physical deposition methods for multilayer coatings (MLCs), primarily those belonging to the PVD family, remain the core technology for tribological systems, as they offer high adhesion, microstructural control, and architectural reproducibility under vacuum conditions and at moderate process temperatures. As summarized in Table 3, the key processes in this class–magnetron sputtering, HCD ion plating, IBAD, CAD, as well as laser cladding, thermal spraying, and LSA/LSM – differ mainly in terms of achievable density and defect levels, adhesion strength, controllability of layer thickness, and technological constraints (vacuum requirements, deposition rate, and growth-related defects).

Relative to chemical routes, physical processes preserve interface sharpness more reliably and allow tighter defect management through plasma tuning and/or ion bombardment. That capability matters for MLCs subjected to abrasive wear and contact-fatigue loading, where interfacial integrity and defect population often set the failure threshold. The same vacuum-based PVD family carries a structural drawback: most techniques are intrinsically line-of-sight. Uniform coverage on complex geometries therefore degrades unless the process is supported by compensatory технологические решения (fixturing, motion strategies, plasma configuration, and related measures).

For multilayer tribological coatings, magnetron sputtering remains the workhorse for building periodic stacks and functionally graded designs under controlled plasma conditions. Reported characteristics include a high ionization degree (up to 70%), dense columnar growth (ρ > 98% of the theoretical value), and high adhesion strength ($\sigma_{(adh)}$ > 80 MPa) when substrate ion bombardment is applied. The method also enables nanoscale metering of layer thickness (0.1–5 nm per layer) with an indicated accuracy of ±2%. The limitations are largely technological: stringent vacuum requirements are cited (ultra-high vacuum, $P < 10^{-4}$ Pa), and the geometry dependence typical of PVD persists due to the line-of-sight nature of the flux.

HCD ion plating is characterized by an even higher ionization fraction (>90%) and strong adhesion (>60 MPa), combined with a highly dense columnar microstructure (ρ > 99%). The constraints here are practical rather than conceptual. A more complex plasma source and higher ion energies demand tighter control of substrate bias and of interlayer boundary formation; if these variables drift, defect generation and residual-stress buildup become increasingly likely.

IBAD and CAD can both be positioned as routes for interface strengthening and/or throughput gains, but they reach that goal through different compromises. IBAD delivers ion-induced interfacial reinforcement (E > 10 keV) and is associated with reduced residual stresses. Deposition rate, however, is extremely low (<1 $nm \cdot s^{-1}$), which limits industrial use for thick coatings and large production batches. CAD moves in the opposite direction: deposition rates can reach 100 $nm \cdot s^{-1,}$ and adhesion remains high, yet macroparticles (d > 1 μm) represent a critical defect class. If filtration and defect control are insufficient, these inclusions become failure initiation sites and can partially erode the advantages expected from multilayer architectures.

A separate class comprises technologies intended for thick coatings and localized repair or modification. Laser cladding enables localized deposition and alloying with thicknesses exceeding 1 mm and allows the formation of graded properties; however, it is constrained by the risk of thermal cracking and porosity (>5%), which imposes strict requirements on thermal cycling and surface preparation. Thermal spraying provides high productivity (coating thicknesses of 50–500 μm), but is characterized by significant porosity (5–15%) and relatively low adhesion; consequently, it is more commonly applied as a thick protective solution under abrasive wear conditions rather than as a method for precise interface engineering. LSA and LSM are surface modification techniques affecting the near-surface layer (up to 1 mm) and promoting microstructural homogenization; nevertheless, the risk of martensitic transformation–i.e., undesirable structural changes in the substrate and heat-affected zone–must be considered, as it can be critical for component service life.

Overall, most physical methods share two systemic limitations: (1) geometric directionality (line-of-sight), which reduces coating uniformity on complex three-dimensional components; and (2) the need for separate optimization of adhesion and defect populations, including issues related to macroparticles in arc-based processes and porosity in thick-coating technologies.

Table 3 - Physical Methods (PVD-Based)

Method	Advantages	Limitations	Scientific Applications	References
Magnetron sputtering	High plasma ionization (up to 70%); dense columnar structures (ρ > 98%); excellent adhesion ($\sigma_{(adh)}$ > 80 MPa); nanometer-scale thickness control (0.1–5 nm/layer^{-1}, ±2%); absence of macroparticles (CFUBMS); suitability for complex 3D geometries	Line-of-sight limitation; requirement for ultra-high vacuum (P < 10^{-4} Pa)	Functionally graded TiN/TiCN/TiC multilayers for cutting tools and biomedical implants	[[38], [39], [40]]
HCD ion plating	Ionization degree >90%; dense columns (ρ > 99%); high adhesion (>60 MPa)	Complex plasma source; high ion energy requiring strict process control	TiC/$TiC_{0.5}N_{0.5}$/TiN multilayers on high-speed steel	[41]
IBAD	Interface strengthening via ion bombardment (E > 10 keV); reduced residual stresses	Very low deposition rate (<1 nm/s^{-1})	Functionally graded interlayers	[42]
Cathodic Arc Deposition (CAD)	Very high deposition rate (up to 100 nm/s^{-1}); excellent adhesion	Macroparticles (d > 1 μm); requires filtration	TiN, CrN coatings on cutting edges	[[43], [44]]
Laser cladding	Local alloying; thickness >1 mm; gradient properties	Thermal cracking; porosity (>5%)	Turbine blade repair	[45]
Thermal spraying	High productivity; thick coatings (50–500 μm)	Porosity (5–15%); relatively low adhesion	Protection against abrasive wear	[46]
LSA / LSM	Near-surface modification (up to 1 mm); microstructural homogenization	Risk of martensitic transformation	Surface strengthening of high-speed steels	[[47], [48], [49], [50], [51], [52], [53], [54], [55], [56], [57], [58]]

Table 3 captures a key practical insight: physical processes–primarily those of the PVD family–provide the highest level of control over multilayer architectures at the nanometer scale, including bilayer thickness, interface sharpness, coating density, and adhesion; however, the selection of a specific process is governed by characteristic trade-offs. Magnetron sputtering represents the baseline option for dense, functionally graded multilayer systems under stringent vacuum requirements; HCD ion plating is preferred where high ionization and strong adhesion are critical; IBAD is employed for interface engineering under constraints on deposition rate; CAD is selected for high productivity, provided that macroparticle suppression is ensured; and laser cladding, thermal spraying, and LSA–LSM are suitable for thick coatings and localized strengthening or repair, albeit with typical risks of porosity and thermally induced defects.

Physical routes are generally favored for multilayer coatings (MLCs) because they offer the highest reproducibility in defining interlayer boundaries and bilayer thickness, while keeping interdiffusion within a limited range. This consideration motivates a shift from the broad классификационного обзора to process-specific discussion. We therefore narrow the scope in the following section and examine PVD methods in detail, treating them as the baseline industrial platform for fabricating thin-film multilayer systems. PVD processes are inherently designed for controlled sputtering/evaporation under vacuum conditions and for precise tuning of particle flux and plasma parameters, which directly determine coating density, growth-related defect populations, and interface quality.

Within the PVD category, the most promising methods are subsequently identified and discussed in sequence–cathodic sputtering, plasma spraying, and magnetron sputtering–since these processes constitute the practical and technological backbone of most industrial solutions. They differ in the mechanisms of ionized flux generation, particle

energy, deposition rate, and characteristic defect formation, i.e., the parameters that ultimately define the achievable limits of friction and wear performance as well as the operational stability of multilayer architectures.

Cathodic Sputtering

Cathodic sputtering is a fundamental PVD deposition technique in which material transport to the coating is driven by ion bombardment of a target under low-pressure discharge conditions. The method is technologically straightforward in implementation, yet highly sensitive to discharge parameters and the gas environment, as these factors govern the sputtering rate, particle energy at the substrate, layer density and defectiveness, and the reproducibility of interlayer boundaries during multilayer coating formation.

Figure 5 presents a schematic representation of a typical cathodic sputtering setup in a vacuum chamber. After evacuation, an inert gas–most commonly argon (Ar) – is introduced into the chamber, initiating a glow discharge between the cathodic target and the anode component of the system. Within the plasma, positively charged inert gas ions are generated and accelerated by the electric field toward the target surface. As a result of momentum transfer, atoms or clusters of the target Materials are sputtered; the resulting flux of sputtered species is transported through the gas phase and condenses on the substrate mounted on a holder, thereby forming the coating.

The scheme also illustrates the reactive sputtering mode: upon the introduction of an active gas (e.g., N_2, O_2, CH_4), sputtered atoms react either in the gas phase and/or on the substrate surface, resulting in the formation of compounds such as nitrides, oxides, or carbides. In this configuration, two process variables dominate the outcome: the active-gas flow balance and discharge stability. Both directly govern the chemistry of the growing layer, the defect population, and the integrity of interlayer interfaces within multilayer architectures.

From an engineering standpoint, cathodic sputtering remains a workhorse for depositing metallic and compound layers when the key targets are reproducible thickness control and sufficiently sharp interfaces. The method, however, inherits the line-of-sight constraint typical of vacuum deposition routes, which degrades thickness uniformity on complex geometries. Reactive sputtering adds another layer of sensitivity. When gas delivery or discharge parameters drift, layer stoichiometry shifts and property scatter increases; in multilayer stacks, this manifests as poorer reproducibility of interlayer boundaries and a broader spread in tribological response.

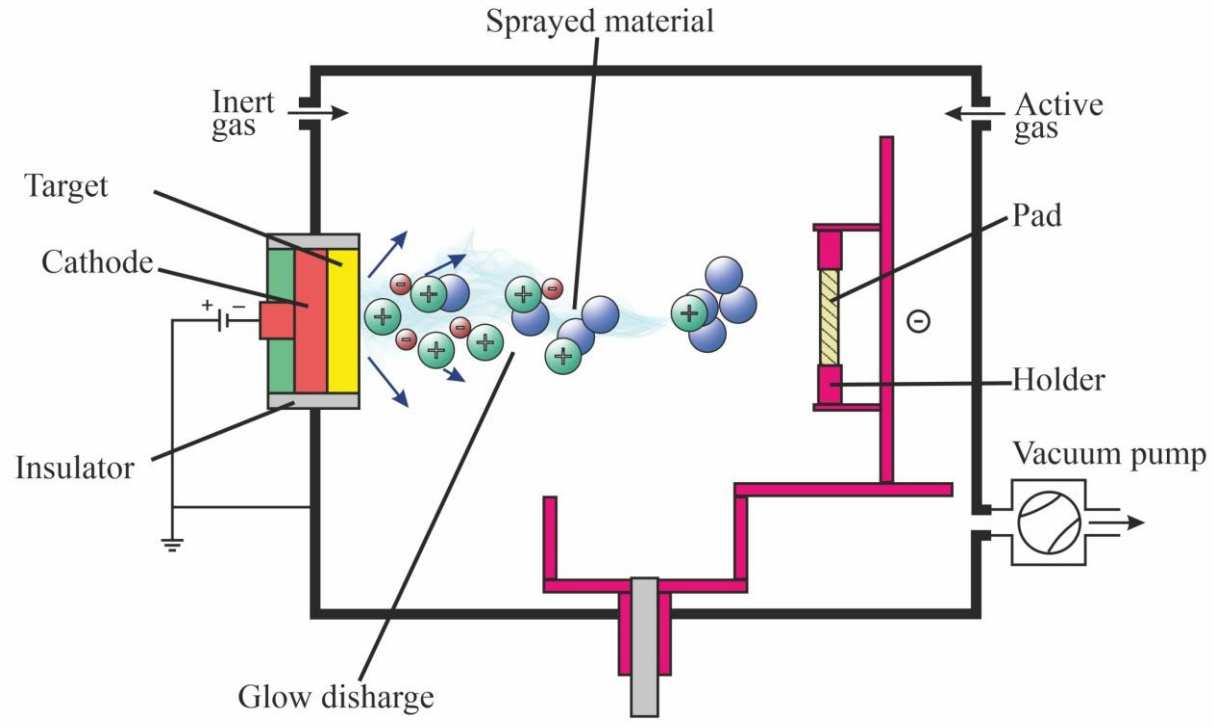

Figure 5 - Schematic diagram of cathodic sputtering in a glow discharge under inert/reactive gas atmospheres

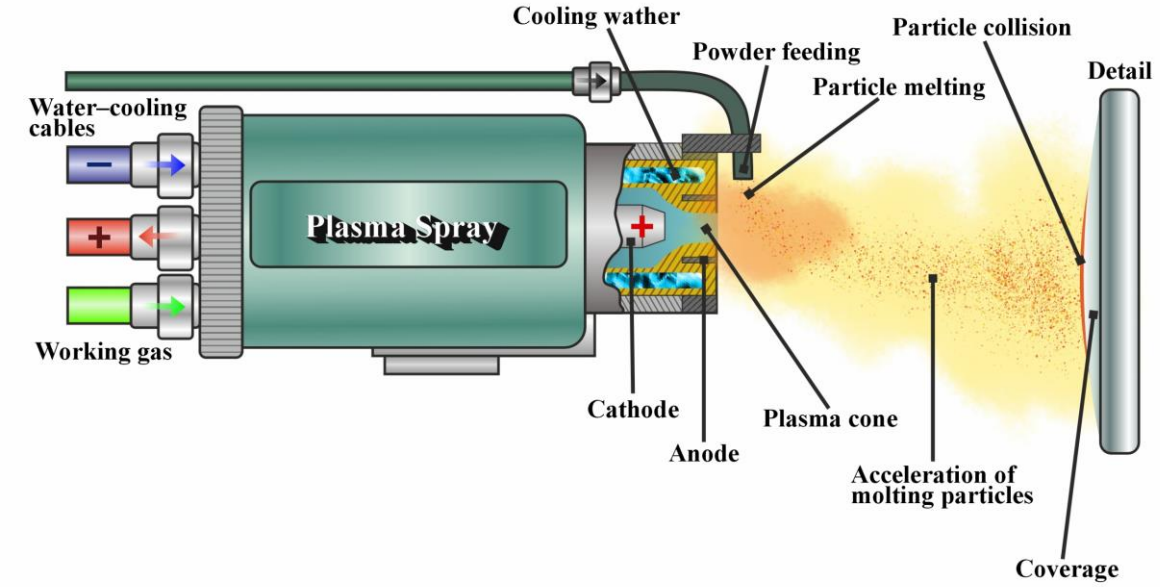

Figure 6 - Schematic representation of the plasma spraying process: powder feeding into the plasma torch, particle melting/acceleration, and coating formation on the component

Plasma Spraying

Plasma spraying is a thermal deposition route in which the feedstock arrives at the surface as molten or partially molten particles. This mechanism separates it sharply from cathodic or magnetron sputtering. Under sputtering, an atomic or ionic flux evolves in a vacuum environment and builds the film atom by atom; in plasma spraying, powder particles are heated, accelerated, and driven into the substrate, and coating growth proceeds through successive particle impacts. The resulting microstructure therefore tracks particle dynamics – temperature, velocity, and flight path – together with impact deformation and lamella formation/closure, rather than being dictated solely by plasma discharge settings.

Figure 6 schematically depicts the plasma-spraying setup. The process gas enters the torch, and an electric discharge between the cathode and anode sustains a high-enthalpy plasma jet (plasma cone). Water-cooling circuits protect the torch hardware, as indicated by the cooling lines. The powder feedstock is injected into the plasma region; particles heat to molten or semi-molten states while the gas stream accelerates them toward the workpiece. Collisions within the jet can occur, producing a spread in particle temperature and velocity before impact. On contact with the surface, molten particles flatten and solidify on short timescales, generating the coating. Layer continuity and thickness uniformity are then governed by spray distance, jet energy, and powder-feed conditions.

From the perspective of multilayer systems, plasma spraying is best regarded as a method for producing thick functional layers (tens to hundreds of micrometers or more), in which architectural control is implemented at the macroscale, while interface quality is governed by pass repeatability, thermal cycling, and the stability of particle kinetics. In tribological applications, this makes the method practical for protective coatings operating under abrasive wear, erosion, and high-temperature degradation conditions; however, it is not a direct analogue of PVD in terms of nanometer-scale control over interlayer boundaries and defect populations.

Magnetron Sputtering

Magnetron sputtering represents an advanced form of cathodic sputtering in which a magnetic field is employed to stabilize and intensify the discharge by confining electrons near the target surface. As a result, the degree of working gas ionization increases, plasma density is enhanced, and sputtering efficiency improves at lower operating pressures. In practice, this translates into two outcomes that matter for multilayer tribological coatings. First, the process offers high deposition repeatability together with tight metering of individual layer thickness. Second, once the parameter window is properly tuned, it suppresses defect formation and promotes coating densification.

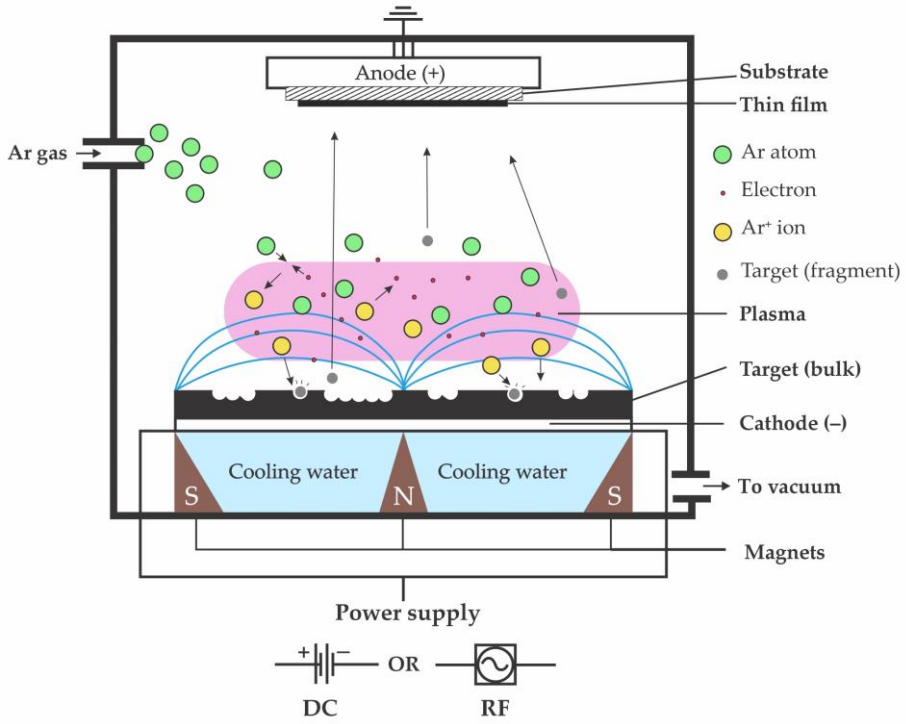

Figure 7 - Schematic of magnetron sputtering: plasma localization by a magnetic field near the target, Ar^+ bombardment, and deposition of sputtered material onto the substrate (DC/RF modes)

Figure 7 schematically outlines magnetron sputtering. Argon is admitted into the evacuated chamber, and a plasma is then sustained between the cathodic target (target, cathode −) and the anode/substrate assembly (anode +, substrate). A magnet set placed behind the target establishes closed magnetic field lines that trap electrons near the cathode surface; the local electron confinement raises plasma density in the region immediately above the target. Ar^+ ions accelerate toward the cathode and bombard the target, ejecting atoms (or target-derived fragments). These species traverse the chamber and condense on the substrate, where they coalesce into a thin film. The schematic also indicates that power can be supplied in either DC or RF mode, thereby extending the applicability of the method to different target materials and deposition regimes.

From an engineering perspective, magnetron sputtering is the primary PVD tool for constructing multilayer structures with high reproducibility, as it enables stable process operation in regimes that provide a favorable balance between deposition rate and coating quality. For multilayer architectures, a key advantage is the controlled formation of layers with predefined thicknesses and relatively sharp interlayer boundaries, as well as the capability to operate in reactive modes (with the introduction of N_2, O_2, etc.) for the deposition of nitride and oxide layers. The limitations are predominantly technological in nature, including geometric dependence (line-of-sight), the need to control substrate heating and plasma stability, and–in reactive sputtering–the sensitivity to active gas flow rates and discharge conditions, which directly affect the composition and defect density of the growing layer.

Conclusions

This review demonstrates that the effectiveness of multilayer coatings in tribological applications is governed not by multilayering per se, but by the extent to which the selected deposition method provides reproducible control over three key parameters: layer density and defect population, adhesion to the substrate and/or interlayers, and architectural controllability through interface quality. Accordingly, the deposition technology should be regarded as a limiting factor for the attainable coating properties. Chemical processes are well-suited for conformal functional and barrier layers, yet are sensitive to interfacial blurring; hybrid and functional solutions enable multifunctionality at the cost of stricter requirements for structural reproducibility; and physical vacuum-based methods–particularly those of the PVD family–remain the foundational platform, as they offer

superior control over microstructure and interlayer boundaries, which constitute the primary mechanism underlying genuine architectural effects.

Future developments are expected to shift from merely expanding the range of coating materials toward interface and defect engineering. Key priorities include controlling interface sharpness and intermixing, mitigating critical defects (macroparticles, porosity, and growth-related imperfections), and managing residual stresses, all of which govern coating lifetime under contact fatigue and abrasive wear. Of particular practical relevance are targeted hybrid process routes, in which the deliberate combination of deposition methods compensates for specific limitations (conformality, density, adhesion, and interface stability), as well as the integrated framework linking "architecture–deposition regime–microstructure–tribological behavior," validated by comparable tribological testing and, where appropriate, supported by multiphysics modeling.

Conflicts of interest. On behalf of all authors, the corresponding author states that there is no conflict of interest.

CRediT author statement: **N. Bakhytuly**: Supervision, Investigation, Data curation; **K. Smailov**: Conceptualization, Writing draft preparation, Reviewing and Editing; **A. Kenzhegulov**: Conceptualization, Supervision; Validation, Data curation; **M. Kudabayeva**: Investigation, Data curation, Software. **A. Yessengaziyev**: Supervision; Validation, Data curation; **D. Karim**: Data curation, Visualization, Software; **T. Arynbayev**: Conceptualization, Data curation.

Acknowledgements. This research was funded by the Science Committee of the Ministry of Science and Higher Education of the Republic of Kazakhstan (Grant No. AP27511437).

Cite this article as: Bakhytuly N, Smailov KM, Kenzhegulov AK, Kudabayeva MA, Yessengaziyev AM, Karim DD, Arynbayev TM. Deposition Methods of Multilayer Hard Coatings for Improving Tribological Performance: A Mini-Review. Kompleksnoe Ispolzovanie Mineralnogo Syra = Complex Use of Mineral Resources. 2027; 343(4):16-33. https://doi.org/10.31643/2027/6445.37

Трибологиялық сипаттамаларды жақсартуға арналған көпқабатты қатты жабындарды тұндыру әдістері: шағын шолу

[1]Бахытұлы Н., [1,2*]Смаилов К.М., [1]Кенжеғұлов А.К., [2]Құдабаева М.А., [1]Есенғазиев А.М., [1]Карим Д.Д., [1]Арынбаев Т.М.

[1] Металлургия және кен байыту институты АҚ, Сәтбаев университеті, Алматы, Қазақстан
[2] Әл-Фараби атындағы Қазақ Ұлттық университеті, Алматы, Қазақстан

Мақала келді: *20 қаңтар 2026*
Сараптамадан өтті: *27 қаңтар 2026*
Қабылданды: 2*9 қаңтар 2026*

ТҮЙІНДЕМЕ

Көпқабатты қатты жабындар жоғары жанасу жүктемелері кезінде жұмыс істейтін бөлшектердің үйкелісі мен тозуын азайту сонымен қатар қызмет ету мерзімін ұзарту үшін ең тиімді инженерлік шешімдердің бірі болып табылады. Дегенмен, олардың практикалық тиімділігі көп қабаттылықтың өзіне емес, таңдалған тұндыру технологиясының үш негізгі параметрлері – қабат тығыздығы мен ақаулары, негізге және/немесе аралық қабаттарға адгезия, сондай-ақ интерфейстердің сапасы арқылы архитектураны басқару мүмкіндігін – қаншалықты тұрақты қамтамасыз ететініне байланысты болады. Бұл шағын шолуда трибологиялық қолданбалар үшін өзекті тұндыру әдістері жүйеленіп, олардың жалпыланған жіктемесі ұсынылған: химиялық процестерді қамтитын (sol–gel, газ фазасынан химиялық тұндыру (CVD), атомдық-қабаттық тұндыру (ALD), гидротермалдық синтез, электролиттік тұндыру, анодтау және электролитсіз тұндыру), PVD тобына жататын физикалық вакуумдық әдістер (магнетронды тозаңдату, катодты-доғалық тұндыру, құыс катодты разрядтағы иондық тұндыру (HCD), ион-сәулелік көмекші тұндыру (IBAD) және т.б.), сондай-ақ гибридті және функционалдық шешімдер (PVD+CVD, композиттік, өздігінен майланатын және нанокомпозиттік жүйелер). Көпқабатты архитектуралар үшін тұндыру әдісін таңдау интерфейстердің тұрақтылығы мен жабынның ұзақ мерзімділігіне тікелей әсер ететін технологиялық шектеулерге негізделуі тиіс екені көрсетілген, оның ішінде тұндыру температурасының диапазоны мен конформдылығы, диффузиялық араласу салдарынан шекаралардың бұлыңғырлануы, қалдық кернеулер және кеуектілік, макробөлшектер мен өсу ақаулары сияқты критикалық кемшіліктер бар. «Архитектура – тұндыру режимі – микроқұрылым – трибологиялық сипаттама» байланысын үйлестіруге арналған практикалық бағдарлар ұсынылып, әрі қарайғы зерттеулердің негізгі бағыттары анықталды, соның ішінде

	интерфейстер мен ақаулар инженериясы, ішкі шектеулерді (конформдылық, тығыздық, адгезия және интерфейстердің тұрақтылығы) өтеу үшін тұндыру процестерін мақсатты гибридтеу және салыстырмалы трибологиялық сынақтармен расталған болжамды модельдеуді қолдану ұсынылған.
	Түйін сөздер: көпқабатты қатты жабындар, CVD, PVD, магнетрондық тозаңдату, ауыспалы металдардың нитридтері.
Бахытұлы Наурызбек	***Авторлар туралы ақпарат:*** *PhD, Физикалық әдіспен талдау зертханасының меңгерушісі, Металлургия және кен байыту институты АҚ, Сәтбаев университеті, 050010, Шевченко көш., 29/133, Алматы, Қазақстан. Email: n.bakhytuly@satbayev.university*
Смаилов Кенжеғали Маманұлы	*Докторант, Әл-Фараби атындағы Қазақ Ұлттық университеті; Аналитикалық химия зертханасының кіші ғылыми қызметкері, Металлургия және кен байыту институты АҚ, Сәтбаев университеті, 050010, Шевченко көш., 29/133, Алматы, Қазақстан. Email: k.smailov@satbayev.university*
Кенжеғұлов Айдар Қарауылұлы	*PhD, Материалтану зертханасының меңгерушісі, Металлургия және кен байыту институты АҚ, Сәтбаев университеті, 050010, Шевченко көш., 29/133, Алматы, Қазақстан. Email: a.kenzhegulov@satbayev.university*
Құдабаева Мадина Әмірбекқызы	*Докторант, аға оқытушы, әл-Фараби атындағы Қазақ ұлттық университеті, 050040, Әл-Фараби даңғ., 71, Алматы, Қазақстан. Email: madina.kudabayeva@kaznu.edu.kz*
Есенғазиев Азамат Муратұлы	*PhD, Титан және сирек қиын балқитын металдар зертханасының меңгерушісі, Металлургия және кен байыту институты АҚ, Сәтбаев университеті, 050010, Шевченко көш., 29/133, Алматы, Қазақстан. Email: a.yessengaziyev@satbayev.university*
Карим Диана Дәулетқызы	*Аналитикалық химия зертханасының инженері, Металлургия және кен байыту институты АҚ, Сәтбаев университеті, 050010, Шевченко көш., 29/133, Алматы, Қазақстан. Email: d.karim@satbayev.university*
Арынбаев Талғат Маратұлы	*Физикалық талдау әдістері зертханасының инженері, Металлургия және кен байыту институты АҚ, Сәтбаев университеті, 050010, Шевченко көш., 29/133, Алматы, Қазақстан. Email: arynbayev.talgat@mail.ru*

Методы осаждения многослойных твёрдых покрытий для улучшения трибологических характеристик: мини-обзор

[1]Бахытулы Н., [1,2*]Смаилов К.М., [1]Кенжегулов А.К., [2]Кудабаева М.А., [1]Есенгазиев А.М., [1]Карим Д.Д., [1]Арынбаев Т.М.

[1] АО Институт металлургии и обогащения, Satbayev University, Алматы, Казахстан
[2] Казахский национальный университет им. аль-Фараби, Алматы, Казахстан

Поступила: *20 января 2026*
Рецензирование: *27 января 2026*
Принята в печать: *29 января 2026*

АННОТАЦИЯ

Многослойные твёрдые покрытия остаются одним из наиболее эффективных инженерных решений для снижения трения и износа, а также для увеличения срока службы деталей, работающих при высоких контактных нагрузках. Однако их практическая эффективность определяется не самой многослойностью, а тем, насколько выбранная технология осаждения обеспечивает воспроизводимый контроль трёх ключевых параметров: плотности и дефектности слоя, адгезии к подложке и/или межслоевым прослойкам, а также управляемости архитектуры через качество интерфейсов. В данном мини-обзоре систематизированы методы осаждения, релевантные для трибологических применений, и предложена их обобщённая классификация, включающая химические процессы (sol–gel, химическое осаждение из газовой фазы (CVD), атомно-слоевое осаждение (ALD), гидротермальный синтез, электроосаждение, анодирование и безэлектролитное осаждение), физические вакуумные методы семейства PVD (магнетронное распыление, катодно-дуговое осаждение, ионное осаждение в разряде с полым катодом (HCD), ионно-лучевое ассистированное осаждение (IBAD) и др.), а также гибридные и функциональные решения (PVD+CVD, композитные, самосмазывающиеся и нанокомпозитные системы). Показано, что выбор метода осаждения для многослойных архитектур должен основываться на технологических ограничениях, напрямую влияющих на стабильность интерфейсов и долговечность покрытия, включая температурное окно и конформность осаждения, диффузионное размывание границ, остаточные напряжения и критические дефекты, такие как пористость, макрочастицы и дефекты роста. Сформулированы практические ориентиры согласования «архитектура – режим осаждения – микроструктура – трибологическое поведение», а также обозначены ключевые направления дальнейших исследований, включая инженерию интерфейсов и дефектов, целенаправленную гибридизацию процессов осаждения для компенсации присущих ограничений (конформность, плотность, адгезия и стабильность интерфейсов) и использование прогностического моделирования, подтверждённого сопоставимыми трибологическими испытаниями.

Ключевые слова: многослойные твёрдые покрытия, CVD, PVD, магнетронное распыление, нитриды переходных металлов.

Бахытулы Наурызбек	***Информация об авторах:*** *PhD, заведующий Лабораторией физических методов анализа, АО Институт металлургии и обогащения, Satbayev University, 050010, ул. Шевченко, 29/133, Алматы, Казахстан. Email: n.bakhytuly@satbayev.university*
Смаилов Кенжегали Маманович	*Докторант, Казахский национальный университет им. аль-Фараби; Младший научный сотрудник Химико-аналитической лаборатории, АО Институт металлургии и обогащения, Satbayev University, 050010, ул. Шевченко, 29/133, Алматы, Казахстан. Email: k.smailov@satbayev.university*
Кенжегулов Айдар Караулович	*PhD, заведующий Лабораторией металловедения, АО Институт металлургии и обогащения, Satbayev University, 050010, ул. Шевченко, 29/133, Алматы, Казахстан. Email: a.kenzhegulov@satbayev.university*
Кудабаева Мадина Амирбековна	*Докторант, старший преподаватель, Казахский национальный университет им. аль-Фараби, 050040, пр. Аль-Фараби, 71, Алматы, Казахстан. Email: madina.kudabayeva@kaznu.edu.kz*
Есенгазиев Азамат Муратович	*PhD, заведующий Лабораторией титана и редких тугоплавких металлов, АО Институт металлургии и обогащения, Satbayev University, 050010, ул. Шевченко, 29/133, Алматы, Казахстан. Email: a.yessengaziyev@satbayev.university*
Карим Диана Даулетовна	*Инженер Химико-аналитической лаборатории, АО Институт металлургии и обогащения, Satbayev University, 050010, ул. Шевченко, 29/133, Алматы, Казахстан. Email: d.karim@satbayev.university*
Арынбаев Талгат Маратович	*Инженер Лаборатории физических методов анализа, АО Институт металлургии и обогащения, Satbayev University, 050010, ул. Шевченко, 29/133, Алматы, Казахстан. Email: arynbayev.talgat@mail.ru*

References

[1] Yan W, Zhang Z, Zhang Y, Chen L, Zhang X, Liao B, Ying, M. Research on Ti-GLC/TiCN/TiN Composite Multilayer Coating with Ultra-Low Friction Coefficient in Various Environments. Surfaces and Interfaces. 2021; 26:101426. https://doi.org/10.1016/j.surfin.2021.101426

[2] Mamayeva A, Kenzhegulov A, Panichkin A, Kshibekova B, Bakhytuly N. Deposition of Carbonitride Titanium Coatings by Magnetron Sputtering and Its Effect on Tribo-Mechanical Properties. Kompleksnoe Ispolzovanie Mineralnogo Syra = Complex Use of Mineral Resources. 2022; 321(2):65-78. https://doi.org/10.31643/2022/6445.19

[3] Muradova S, Negim E-S, Makhmetova A, Ainakulova D, Mohamad N. An Overview of the Current State and the Advantages of Using Acrylic Resins as Anticorrosive Coatings. Kompleksnoe Ispolzovanie Mineralnogo Syra = Complex Use of Mineral Resources. 2023; 327(4):90–98. https://doi.org/10.31643/2023/6445.44

[4] Khamseh S, Alibakhshi E, Mahdavian M, Saeb MR, Vahabi H, Lecomte J-S, Laheurte P. High-Performance Hybrid Coatings Based on Diamond-Like Carbon and Copper for Carbon Steel Protection. Diamond and Related Materials. 2017; 80:84–92. https://doi.org/10.1016/j.diamond.2017.10.008

[5] Jehn HA. Multicomponent and Multiphase Hard Coatings for Tribological Applications. Surface and Coatings Technology 2000; 131(1–3):433–440. https://doi.org/10.1016/S0257-8972(00)00783-0

[6] Bakhytuly N, Kenzhegulov A, Nurtanto M, Aliev A, Kuldeev E. Microstructure and Tribological Study of TiAlCN and TiTaCN Coatings. Kompleksnoe Ispolzovanie Mineralnogo Syra = Complex Use of Mineral Resources. 2023; 327(4):99–110. https://doi.org/10.31643/2023/6445.45

[7] Ryaguzov A, Nemkayeva R, Guseinov N, Kudabayeva M. Nanocomposite Materials Based on Amorphous SiC-Containing DLC Structures Modified with Rhodium Nanoparticles. Diamond and Related Materials. 2024; 144:111034. https://doi.org/10.1016/j.diamond.2024.111034

[8] Yessengaziyev A, Mukangaliyeva A, Toishybek A, Yersaiynova A, Bakhytuly N. Studies the Crucial Role of Selection of Extractant to Extract Niobium from Sulfuryl Fluoride Solution and Optimization of Extraction Conditions. Acta Metallurgica Slovaca 2024; 30(3):120–126. https://doi.org/10.36547/ams.30.3.2060

[9] Ospanov K, Smailov K, Nuruly Y. Patterns of Non-Traditional Thermodynamic Functions ΔrG0/n and ΔfG0(Averaged) Changes for Cobalt Minerals. Chemical Bulletin of Kazakh National University 2020; 96:22–30. https://doi.org/10.15328/cb1005

[10] Serdiuk IV, Petrushenko SI, Stolbovyi VO, Fijalkowski M. Influence of Technological Parameters of Deposition on Physical and Mechanical Properties of Vacuum-Arc Multilayer Nitride Coatings Based on Chromium and Niobium. Metallofizika i Noveishie Tekhnologii = Metallophysics and Advanced Technologies. 2024; 46(1):23–46. https://doi.org/10.15407/mfint.46.01.0023

[11] Grand View Research. Hard Coatings Market Size, Share & Growth Report, 2030. Available online: https://www.grandviewresearch.com/industry-analysis/hard-coatings-market-report (accessed on 6 January 2026).

[12] ConsaInsights. Hard Coatings Market Size, Market Share, Companies & Forecast Up To 2033. Available online: https://www.consainsights.com/reports/hard-coatings-market (accessed on 6 January 2026).

[13] Market Data Forecast. Global Hard Coatings Market—By Material Type (Nitrides, Oxides), By Application (Cutting Tools, Decorative Coatings), By Deposition Technique (PVD and CVD), By End-Use (General Manufacturing, Transportation) & By Region—Global Industry Analysis, Size, Share, Growth, Investment & Forecast. Available online: https://www.marketdataforecast.com/market-reports/hard-coatings-market (accessed on 6 January 2026).

[14] Bobzin K. High-Performance Coatings for Cutting Tools. CIRP Journal of Manufacturing Science and Technology. 2017; 18:1-9. https://doi.org/10.1016/j.cirpj.2016.11.004

[15] Matthews A, Eskildsen SS. Engineering Applications for Diamond-Like Carbon. Diamond and Related Materials. 1994; 3:902-911. https://doi.org/10.1016/0925-9635(94)90297-6

[16] Kawata K, Sugimura H, Takai O. Characterization of (Ti,Al)N Films Deposited by Pulsed D.C. Plasma-Enhanced Chemical Vapor Deposition. Thin Solid Films. 2001; 386(2):271-275. https://doi.org/10.1016/S0040-6090(00)01672-2

[17] Fang T-H, Jian S-R, Chuu D-S. Nanomechanical Properties of TiC, TiN and TiCN Thin Films Using Scanning Probe Microscopy and Nanoindentation. Applied Surface Science. 2004; 228:365–372. https://doi.org/10.1016/j.apsusc.2004.01.053

[18] Dubar M, Dubois A, Dubar L. Wear Analysis of Tools in Cold Forging: PVD versus CVD TiN Coatings. Wear. 2005; 259:1109–1116. https://doi.org/10.1016/j.wear.2005.01.006

[19] Springer RW, Hosford, C.D. Characterization of Aluminum–Aluminum Nitride Coatings Sputter Deposited Using the Pulsed Gas Process. J. Vac. Sci. Technol. 1982; 20:462–465. https://doi.org/10.1116/1.571334

[20] Ståhl J-E. Metal Cutting: Theories and Models; Lund University: Lund, Sweden. 2012, 580. ISBN 978-9163713361.

[21] Ataibis V, Taktak S. Characteristics and Growth Kinetics of Plasma Paste Borided Cp–Ti and Ti6Al4V Alloy. Surface and Coatings Technology. 2015; 279:65-71. https://doi.org/10.1016/j.surfcoat.2015.08.023

[22] Mareus R, Mastail C, Anğay F, Brunetière N, Abadias G. Study of Columnar Growth, Texture Development and Wettability of Reactively Sputter-Deposited TiN, ZrN and HfN Thin Films at Glancing Angle Incidence. Surface and Coatings Technology. 2020; 399:126130. https://doi.org/10.1016/j.surfcoat.2020.126130

[23] Aiso T, Wiklund U, Kubota M, Jacobson S. Effect of Si and Al Additions to Carbon Steel on Material Transfer and Coating Damage Mechanism in Turning with CVD Coated Tools. Wear. 2016; 368–369:379–389. https://doi.org/10.1016/j.wear.2016.10.011

[24] Leyland A, Bin-Sudin M, James AS, Kalantary MR, Wells PB, Matthews A, Housden J, Garside B. TiN and CrN PVD Coatings on Electroless Nickel-Coated Steel Substrates. Surface and Coatings Technology. 1993; 60:474–479. https://doi.org/10.1016/0257-8972(93)90135-B

[25] Lautenschlager EP, Monaghan P. Titanium and Titanium Alloys as Dental Materials. International Dental Journal. 1993; 43(3):245–253. PMID: 8406955.

[26] Yan H, Wang J, Cai M, Wang X, Song S, Zhang L, Li H, Li W Fan X, Zhu M. Towards Long-Term Corrosion and Wear Protection of Al Alloy: Synergy of Ti3C2Tx Flake and Micro-Arc Oxidation Coating. Corrosion Science. 2020; 174:108813. https://doi.org/10.1016/j.corsci.2020.108813

[27] Wang J, Pan Ya, Feng R, Cui H, Gong B, Zhang L, Gao Z, Cui X, Zhang H, Jia Zh. Effect of electrolyte composition on the microstructure and bio-corrosion behavior of micro-arc oxidized coatings on biomedical Ti6Al4V alloy. Journal of Materials Research and Technology. 2020; 9(2):1477-1490. https://doi.org/10.1016/j.jmrt.2019.11.073

[28] Yang S, Wiemann E, Teer DG. The Properties and Performance of Cr-Based Multilayer Nitride Hard Coatings Using Unbalanced Magnetron Sputtering and Elemental Metal Targets. Surface and Coatings Technology. 2004; 188–189:662–668. https://doi.org/10.1016/j.surfcoat.2004.07.032

[29] Bin-Sudin M, Leyland A, James AS, Matthews A, Housden J, Garside B. Substrate Surface Finish Effects in Duplex Coatings of PAPVD TiN and CrN with Electroless Nickel-Phosphorus Interlayers. Surface and Coatings Technology. 1996; 81:215–224. https://doi.org/10.1016/0257-8972(95)02529-4

[30] Shtansky DV, Kiryukhantsev-Korneev PV, Bashkova IA, Sheveiko AN, Levashov EA. Multicomponent Nanostructured Films for Various Tribological Applications. International Journal of Refractory Metals and Hard Materials. 2010; 28:32–39. https://doi.org/10.1016/j.ijrmhm.2009.07.014

[31] Saba F, Kabiri E, Vahdati Khaki J, Haddad Sabzevar M. Fabrication of Nanocrystalline TiC Coating on AISI D2 Steel Substrate via High-Energy Mechanical Alloying of Ti and C. Powder Technology. 2016; 288:76–86. https://doi.org/10.1016/j.powtec.2015.10.030

[32] PalDey S, Deevi SC. Single Layer and Multilayer Wear Resistant Coatings of (Ti,Al)N: A Review. Materials Science and Engineering: A. 2003; 342:58–79. https://doi.org/10.1016/S0921-5093(02)00259-9

[33] Martin JM, Pascal H, Donnet C, Le Mogne T, Loubet JL, Epicier T. Superlubricity of MoS2: Crystal Orientation Mechanisms. Surface and Coatings Technology. 1994; 68–69:427–432. https://doi.org/10.1016/0257-8972(94)90197-X

[34] Yang S, Cooke K, Sun H, Li X, Lin K, Dong H. Development of Advanced Duplex Surface Systems by Combining CrAlN Multilayer Coatings with Plasma Nitrided Steel Substrates. Surface and Coatings Technology. 2013; 236:2–7. https://doi.org/10.1016/j.surfcoat.2013.07.017

[35] Mi P, He J, Qin Y, Chen K. Nanostructure Reactive Plasma Sprayed TiCN Coating. Surface and Coatings Technology. 2017; 309:1–5. https://doi.org/10.1016/j.surfcoat.2016.11.033

[36] Musil J. Hard Nanocomposite Coatings: Thermal Stability, Oxidation Resistance and Toughness. Surface and Coatings Technology. 2012; 207:50–65. https://doi.org/10.1016/j.surfcoat.2012.05.073

[37] Liu S, Yang Y, Ji R, Zeng XT, Clegg WJ. AlN/CrN Multilayer Structures with Increased Thermal Stability. Scripta Materialia. 2017; 130:242–246. https://doi.org/10.1016/j.scriptamat.2016.12.020

[38] Saoula N, Madaoui N, Tadjine R, Erasmus RM, Shrivastava S, Comins JD. Influence of Substrate Bias on the Structure and Properties of TiCN Films Deposited by Radio-Frequency Magnetron Sputtering. Thin Solid Films. 2016; 616:521–529. https://doi.org/10.1016/j.tsf.2016.08.047

[39] Komarov FF, Konstantinov VM, Kovalchuk AV, Konstantinov SV, Tkachenko HA. The Effect of Steel Substrate Pre-Hardening on Structural, Mechanical, and Tribological Properties of Magnetron Sputtered TiN and TiAlN Coatings. Wear. 2016; 352–353:92–101. https://doi.org/10.1016/j.wear.2016.02.007

[40] Warcholiński B, Gilewicz A, Kukliński Z, Myśliński P. Arc-Evaporated CrN, CrN and CrCN Coatings. Vacuum. 2008; 83:715–718. https://doi.org/10.1016/j.vacuum.2008.05.005

[41] Kanda K, Takehana S, Yoshida S, Watanabe R, Takano S, Ando H, Shimakura F. Application of Diamond-Coated Cutting Tools. Surface and Coatings Technology. 1995; 73:115–120. https://doi.org/10.1016/0257-8972(94)02370-0

[42] Zhu F, Zhu K, Hu Y, Ling Y, Wang D, Peng H, Xie Z, Yang R, Zhang Z. Microstructure and Young's Modulus of ZrN Thin Film Prepared by Dual Ion Beam Sputtering Deposition. Surface and Coatings Technology. 2019; 374:997–1005. https://doi.org/10.1016/j.surfcoat.2019.06.094

[43] Vetter J, Burgmer W, Dederichs HG, Perry AJ. The Architecture and Performance of Multilayer and Compositionally Gradient Coatings Made by Cathodic Arc Evaporation. Surface and Coatings Technology. 1993; 61:209–214. https://doi.org/10.1016/0257-8972(93)90227-F

[44] Rousseau AF, Partridge JG, Mayes ELH, Toton JT, Kracica M, McCulloch DG, Doyle ED. Microstructural and Tribological Characterisation of a Nitriding/TiAlN PVD Coating Duplex Treatment Applied to M2 High Speed Steel Tools. Surface and Coatings Technology. 2015; 272:403–408. https://doi.org/10.1016/j.surfcoat.2015.03.034

[45] Yan H, Cai M, Wang J, Zhang L, Li H, Li W, Fan X, Zhu M. Insight into Anticorrosion/Antiwear Behavior of Inorganic–Organic Multilayer Protection System Composed of Nitriding Layer and Epoxy Coating with Ti3C2Tx MXene. Applied Surface Science. 2021; 536:147974. https://doi.org/10.1016/j.apsusc.2020.147974

[46] Zhu L, He J, Yan D, Xiao L, Dong Y, Zhang J, Liao H. Synthesis and Microstructure Observation of Titanium Carbonitride Nanostructured Coatings Using Reactive Plasma Spraying in Atmosphere. Applied Surface Science. 2011; 257:8722–8727. https://doi.org/10.1016/j.apsusc.2011.05.056

[47] Liu Y, Yu S, Shi Q, Ge X, Wang W. Multilayer Coatings for Tribology: A Mini Review. Nanomaterials. 2022; 12:1388. https://doi.org/10.3390/nano12091388

[48] Kenzhaliyev B, Koizhanova A, Fischer D, et al. Study of Efficiency of Organic Activator Application to Process Difficult-to-Beneficiate Polymetallic Ridder Ores. Transit. Met. Chem. 2025. https://doi.org/10.1007/s11243-025-00637-7

[49] Kenzhaliyev B, Fischer D, Temirova S, Ultarakova A, Baltabekova Z, Bakhytuly N, Smailov K. Removal of Hexavalent Chromium Ions from Industrial Effluents Using Natural and Modified Diatomite, Taurite, Lewatit M500, and Activated Carbon. Processes. 2025; 13:997. https://doi.org/10.3390/pr13040997

[50] Abdulvaliev RA, Surkova TY, Baltabekova Z, Yessimova DM, Stachowicz M, Smailov KM, Dossymbayeva ZD, Ainur B. Effect of Amino Acids on the Extraction of Copper from Sub-Conditional Raw Materials. Kompleksnoe Ispolzovanie Mineralnogo Syra = Complex Use of Mineral Resources. 2024; 335(4):50–58. https://doi.org/10.31643/2025/6445.39

[51] Kenzhaliyev B, Surkova T, Berkinbayeva A, Baltabekova Z, Smailov K, Abikak Y, Saulebekkyzy S, Tolegenova N, Omirbek T, Dosymbaeva Z. Innovative Methods for Intensifying the Processing of Zinc Clinker: Synergy of Microwave Treatment and Ultrasonic Leaching. Metals. 2025; 15:246. https://doi.org/10.3390/met15030246

[52] Kenzhaliyev B, Berkinbayeva A, Baltabekova Z, Moldabayeva G, Smailov K, Saulebekkyzy S, Tolegenova N, Karim D, Omirbek T. Investigation of Phase Transformations in Technogenic Raw Materials Under Microwave Treatment for Enhanced Zinc Leaching. Processes. 2025; 13:1099. https://doi.org/10.3390/pr13041099

[53] Kenzhaliyev B, Berkinbayeva A, Smailov K, Baltabekova Z, Saulebekkyzy S, Tolegenova N, Yessengaziyev A, Bakhytuly N, Tugambay S. Microwave Pre-Treatment for Efficient Zinc Recovery via Acid Leaching. Materials. 2025; 18:2496. https://doi.org/10.3390/ma18112496

[54] Berkinbayeva A, Saulebekkyzy S, Kenzhaliyev B, Smailov K, Yessengaziyev A, Nurtazina N, Karim D, Birlikzhan Y. Sodium Percarbonate for Eco-Efficient Cyanide Detoxification in Gold Mining Tailings. Metals. 2025; 15(10):1162. https://doi.org/10.3390/met15101162

[55] Kenzhaliyev B, Surkova T, Yessimova D, Baltabekova Z, Abikak Y, Abdikerim B, & Dosymbayeva Z. Extraction of Noble Metals from Pyrite Cinders. ChemEngineering. 2023; 7(1):14. https://doi.org/10.3390/chemengineering7010014

[56] Koizhanova A, Kenzhaliyev B, Magomedov D, Kamalov E, Yerdenova M, Bakrayeva A, & Abdyldayev N. Study of Factors Affecting the Copper Ore Leaching Process. ChemEngineering. 2023; 7(3):54. https://doi.org/10.3390/chemengineering7030054

[57] Koizhanova AK, Berkinbayeva AN, Sedelnikova GV, Kenzhaliyev BK, Azlan MN, & Magomedov DR. Research of biochemical gold recovery method using high-arsenic raw materials. Metalurgija. 2021; 60(3-4):423-426.

[58] Khadem M, Penkov OV, Yang HK, et al. Tribology of Multilayer Coatings for Wear Reduction: A Review. Friction. 2017; 5:248–262. https://doi.org/10.1007/s40544-017-0181-7

Crossref
DOI: 10.31643/2027/6445.38
Metallurgy and Metallurgical Engineering

Investigation of synthesized carbon nanofilaments by reactive magnetron reactive sputtering methane decomposition

[1]Shaidalina D.R., [1*]Baitimbetova B.A., [2]Astemessova K.S., [2]Turlybekova G.K., [3]Topanov B.G., [4]Bukhvalov D.V., [5]Chuchvaga N.A, [5]Mit' K.A., [6]Serikkanov A.S.

[1]Mining and Metallurgical Institute, Satbayev University, Almaty, Kazakhstan
[2]Institute of Energy and Mechanical Engineering, Satbayev University, Almaty, Kazakhstan
[3]The Institute of Combustion Problems Committee of Science of the Ministry of Education and Science of the Republic of Kazakhstan, Almaty
[4]College of Science, Institute of Materials Physics and Chemistry, Nanjing Forestry University, Nanjing, China
[5]Institute of Physics and Technology LLP, Satbayev University, Almaty, Kazakhstan
[6]National Academy of Sciences of the Republic of Kazakhstan under the President of the Republic of Kazakhstan, Almaty

[*]Corresponding author email: baitim@physics.kz

Received: *September 25, 2025*
Peer-reviewed: *November 17, 2025*
Accepted: *February 23, 2026*

ABSTRACT

This work presents the synthesis of carbon nanofilaments obtained through the decomposition of graphite in methane plasma with argon admixture. The resulting nanostructures exhibit an amorphous configuration and remain transparent across the visible spectrum, making them attractive candidates for optical and optoelectronic applications. Atomic force microscopy revealed that the filaments form a compact, vertically oriented network on the substrate surface, while Raman spectroscopy provided information on their local bonding environment. Morphologically, the carbon filaments display flattened, ribbon-like forms, and their densely packed columnar structures reach an average length of ~36 nm. The optical transmission spectrum showed transmittance of ~65% near 400 nm, ~75% within the visible region, and nearly 80% in the near-infrared range, gradually increasing toward longer wavelengths. This degree of transparency in the visible spectrum is sufficient for practical device applications. When the incident light wavelength is comparable to or smaller than the inter-filament spacing (100–500 nm), light propagation occurs through reflections from the filament walls. The optical band gap of the structures was determined to be ~2.85 eV. Overall, the analysis of structural and optical properties confirms the successful fabrication of amorphous carbon nanofilaments, highlighting their strong potential for integration into advanced optoelectronic systems.

Keywords: reactive magnetron sputtering, nanofilaments, methane gas, thin film, nanostructure.

Information about authors:

Shaidalina Damira — *PhD student, Master of Engineering and Technology, Mining and Metallurgical Institute, Satbayev University, Satpayev str. 22, 050013, Almaty, Kazakhstan. Email: Shaidalina.D@stud.satbayev.university; ORCID ID: https://orcid.org/0009-0003-4734-170X*

Baitimbetova Bagila — *Candidate of Physical and Mathematical Sciences, Associate Professor, Mining and Metallurgical Institute, Satbayev University, Satpayev str. 22, 050013, Almaty, Kazakhstan. Email: baitim@physics.kz; ORCID ID: https://orcid.org/0000-0002-3728-2430*

Astemessova Kalamkas — *Doctor of PhD, Head of Department, Institute of Energy and Mechanical Engineering, Satbayev University, Satpayev str. 22, 050013, Almaty, Kazakhstan. Email: k.astemessova@satbayev.university; ORCID ID: https://orcid.org/0000-0002-4143-6084*

Turlybekova Gulzhan — *Candidate of technical sciences, Associate professor, Institute of Energy and Mechanical Engineering, Satbayev University, Satpayev str. 22, 050013, Almaty, Kazakhstan. Email: g.turlybekova@satbayev.university; ORCID ID: https://orcid.org/0000-0001-5522-4931*

Topanov Bolat — *Senior Research Scientist, The Institute of Combustion Problems Committee of Science of the Ministry of Education and Science of the Republic of Kazakhstan, 050012, Bogenbai Batyr str. 172, Almaty, Kazakhstan. Email: topikbotat@mail.ru; ORCID ID: https://orcid.org/0009-0008-7872-1437*

Danil Boukhvalov — *Candidate of Physical and Mathematical Sciences, College of Science, Institute of Materials Physics and Chemistry, Nanjing Forestry University, Nanjing, 210037, China. Email: danil@njfu.edu.cn; ORCID ID: https://orcid.org/0000-0002-2286-3443*

Chuchvaga Nikolay — *Doctor of PhD, Deputy Director of Institute for Scientific Work, Institute of Physics and Technology LLP, Satbayev University, 050032, Ibragimov Street str. 11, Almaty, Kazakhstan. Email: n.chuchvaga@satbayev.university; ORCID ID: https://orcid.org/0000-0003-4417-4996*

Kostya Mit' — *Candidate of Physical and Mathematical Sciences, Institute of Physics and Technology, Satbayev University, 050032, Ibragimov Street str. 11, Almaty, Kazakhstan. Email: k.mit@sci.kz; ORCID ID: https://orcid.org/0000-0002-0078-6723*

Serikkanov Abay — *Candidate of Physical and Mathematical Sciences, Professor, National Academy of Sciences of the Republic of Kazakhstan under the President of the Republic of Kazakhstan, 050010, Shevchenko street str.28, Almaty, Kazakhstan. Email: a.serikkanov@gmail.com; ORCID ID: https://orcid.org/0000-0001-6817-9586*

Introduction

In recent years, humanity has faced new challenges in organizing social and economic relations. History demonstrates that economic revolutions are frequently accompanied by scientific breakthroughs, where a qualitative shift emerges after the gradual accumulation of knowledge. Within the framework of our research, one of the tasks was to study carbonaceous residues obtained during experiments performed by reactive magnetron sputtering [1]. A review of the literature, combined with optical characterization of these residues, suggested that they represent heterogeneous carbon formations containing nanofibers. To properly follow the logic of this investigation, it is necessary to refer to relevant earlier studies [2].

The main aim of this work is to synthesize and investigate carbon nanofilaments of various architectures for different practical applications. In particular, we focused on amorphous carbon nanofilaments with broad optical transparency covering both the visible and near-infrared regions, which makes them promising for optoelectronic devices. Owing to their topology, carbon nanostructures often exhibit properties of quantum-size systems and are therefore of considerable scientific and technological interest. The nanofilament concept is widely applied across materials science, nanotechnology, and device engineering. For instance, nanofilaments can serve as fundamental elements in nanoscale electronics, such as nanowire transistors, where their unique nanoscale electronic properties can be fully exploited [[3], [4]].

Several studies have emphasized the fabrication of advanced nanostructures [5], including patterned metasurfaces [5] and the integration of ZnO nanofilaments into one-dimensional TiO_2 structures [6]. These publications primarily concentrate on synthesis techniques and subsequent analysis [6].

Reference [7] provides a comprehensive overview of how carbon nanofilaments have been integrated into cementitious composites. It also reports recent experimental results demonstrating improvements in the mechanical performance of CNF-reinforced cements [8].

There are three main approaches to fabricating such carbon nanostructures: arc discharge [[9], [10], [11], [12]], laser ablation [[10], [11], [12]], and chemical vapor deposition (CVD) [11]. For example, in [[10], [11], [12]], CNTs and CNFs were synthesized on an aluminum substrate pre-coated with nickel, which acted as a catalyst (approximately 5 wt.%). Key parameters such as carrier gas composition, reaction temperature, and growth duration were shown to significantly affect the resulting morphology [12].

In another study, a ternary catalyst system consisting of NiO, CuO, and Al_2O_3 was designed with three distinct regions for the synthesis of CNTs and carbon nanosheets (CNSs). The process relied on thermal CVD with acetylene as the precursor [[10], [11], [12], [13]]. Reference [14] investigated carbon nanotubes and nanofilaments synthesized via catalytic acetylene decomposition over Pd/Al_2O_3 catalysts. At 700 °C, the products were predominantly CNFs with diameters in the 9–26 nm range, while at 800 °C, multiwalled CNTs with a layered morphology were formed. Under other conditions, amorphous carbon with diverse geometries was also observed.

One strategy to prevent aggregation of CNTs and CNFs is to anchor their ends, enabling the formation of stable hierarchical structures. A common approach involves growing CNTs directly on micron-sized carbon fibers. For example, CNTs have been deposited on both polyacrylonitrile- (PAN-) and pitch-based fibers using hot-filament CVD with H_2 and CH_4 as feed gases. In this case, nickel clusters electrodeposited onto the fiber surface served as catalysts, producing uniform coatings of multi-walled CNTs with smooth walls and low impurity levels [15].

Carbon nanofilaments and nanotubes show strong potential in enhancing the performance of fiber-reinforced polymer (FRP) composites by improving both mechanical behavior and multifunctionality. Direct dispersion of nanofilaments into the polymer matrix, however, has drawbacks. A promising alternative involves growing large volumes of aligned CNFs directly on

fiber surfaces before composite processing. The so-called *graphitic structures by design* (GSD) approach makes use of fuel mixtures and nickel catalysts, and has been shown to produce nanofilament coatings on commercial PAN-based fibers at 550 °C using ethylene as the carbon source [16].

The pyrolysis of methane, acetylene, and benzene has been extensively studied. Methane, unlike CO, does not easily decompose at low temperatures, which favors the growth of single-walled CNTs with fewer amorphous carbon impurities. Various activation methods have been tested, including external gas heating, plasma excitation (microwave plasma, glow discharge, etc.),

hot-filament techniques, and laser heating. The most common plasma synthesis route employs methane diluted with hydrogen [17].

Magnetron sputtering is also an important method in plasma nanotechnology, enabling the deposition of graphite films, nanotubes, and related carbon nanostructures [18]. Owing to their high strength and stiffness, CNFs/CNTs are regarded as effective reinforcements for cementitious materials [19]. Nevertheless, their direct incorporation presents practical challenges.

Catalytic methane decomposition (CDM) offers a CO_2-free hydrogen production pathway while yielding CNFs as valuable by-products. Studies have applied thermogravimetric screening to identify suitable catalysts by measuring carbon yield in CDM [20]. For example, Ni–Cu–Mg–Al catalysts have been tested, where Cu content was shown to affect both filament morphology and catalyst particle size [20]. Beyond catalytic methods, other synthesis approaches such as graphene growth and template-assisted methods are also employed [[21], [22]].

In [22], nanofilaments were synthesized directly on carbon fiber surfaces using GSD techniques, while liquid-phase carbonization with anodic alumina templates produced porous carbon structures. Samples annealed at 1000 °C exhibited higher electrochemical capacity compared to those treated at higher temperatures. Other works demonstrated multiscale growth of nanofilaments using Pd catalysts from ethylene/oxygen mixtures at 550 °C, producing filaments whose diameters corresponded to catalyst particle size [23]. These fibers showed potential for improving strength, ductility, and energy absorption in composite systems.

High-pressure synthesis of sp^3-hybridized hydrogenated carbon nanofilaments remains an active field. Such materials are expected to possess superior strength due to their dense packing and strong covalent bonding. In one study, mechano-chemical synthesis was used to transform benzene into crystalline bundles of sp^3-carbon nanofilaments under uniaxial compression, with the resulting fibers demonstrating ease of exfoliation and high energy density [24]. Raman spectroscopy, XRD, SEM, and TEM analyses were used to study their structure and growth mechanisms.

The relationship between catalyst properties and filament texture was also reported in [25], where CNTs and CNFs were synthesized on Ni–Cu–Mg–Al catalysts via vapor-phase deposition. It was established that the graphene orientation and crystalline domains in the filaments are directly correlated with the morphology and dimensions of the catalyst particles.

In the present work, we focus on amorphous, columnar carbon nanofilaments synthesized by plasma-assisted methane decomposition with argon addition. Their structural features, including transparency and vertical alignment, make them suitable for optoelectronic applications.

Experimental part

A. Method of magnetron sputtering

In this study, direct-current magnetron sputtering of a graphite target was employed under varying working gas pressures at room temperature. Magnetron sputtering is a widely used physical vapor deposition technique for producing thin films on a substrate. In this method, the target material, which simultaneously acts as the cathode, undergoes erosion under the influence of a magnetron plasma discharge. The process initiates with the generation of plasma within the chamber above the target surface, where accelerated electrons collide with inert gas atoms, typically argon, leading to ionization.

In the case of reactive magnetron sputtering, an additional reactive gas, methane, is introduced. This gas interacts with the sputtered atomic species during deposition, thereby facilitating the formation of a compound thin film. Depending on the process conditions, reactions may occur either directly on the target surface or predominantly at the substrate. When the partial pressure of the reactive gas is high, reactions take place at the target surface, producing compounds that are subsequently transported and deposited on the substrate. Conversely, at lower pressures, the interaction in the gas phase is limited, and the reactions primarily occur on the substrate surface as solid-phase processes.

During sputtering, positively charged argon ions generated within the plasma are accelerated toward the graphite cathode, impacting its surface and ejecting carbon atoms and clusters. These liberated species travel through the plasma toward the substrate, where they condense and form thin films. The high plasma current enhances decomposition, excitation, and ionization of methane molecules, resulting in a flux of energetic species, including free atoms with sufficient kinetic energy to surpass the activation barrier for diffusion and nucleation. As a

consequence, stable thin films of the desired material are formed on the substrate surface.

B. Carbon Nanofilaments fabrication

The coating deposition was carried out under fixed process conditions: the gas mixture consisted of 25% methane and 75% argon. The discharge parameters were maintained at a voltage of U = 500 V and a current of I = 30 mA, corresponding to a discharge power of P = 15 W. The pressure inside the working chamber was kept at 6×10^{-3} Torr, while the vacuum lamp operated at a voltage of U = 2.4 mV. The sputtering duration was 15 minutes, and the substrate temperature was stabilized at 230 °C. Quartz substrates were employed for the deposition process.

C. Physical methods

The synthesized carbon nanofilaments were examined using a set of complementary physical characterization techniques, including X-ray diffraction (XRD), scanning electron microscopy (SEM), and Raman spectroscopy. Optical transmission spectra of the samples were recorded with SF-256 UVI and Shumasu spectrophotometers over a spectral range of 160–1100 nm**.** The phase composition was analyzed using a PANalytical X'Pert MPD PRO X-ray diffractometer equipped with Cu-Kα radiation, and the obtained patterns were identified by comparison with the JCPDS reference database.

Electron microscopy investigations were conducted on an MT-MDT Integra Prima system and a Jeol SPM 5200 scanning probe microscope fitted with NSC 37 AlBS cantilevers. Raman measurements were performed on an MT-MDT Integra Spectra spectrometer at room temperature. A 473 nm semiconductor laser (2.62 eV) with a 2 µm spot size was used to excite the spectra, ensuring sufficient illumination of the thin-film surface. The accuracy of phonon frequency determination was within ±4 cm^{-1}**,** with an exposure time of 30 seconds. To minimize local heating and irradiation effects from the 1.5 mW laser, the measurements were performed in scanning mode at a velocity of approximately 10 µm/s**.**

Results and Discussion

Atomic force microscopy (AFM) is a highly effective technique for investigating the surface structure of thin films, as it enables the determination of surface roughness from several micrometers down to fractions of a nanometer. AFM micrographs of the synthesized samples demonstrated that the carbon nanofilaments grow in a densely packed arrangement, oriented almost perfectly perpendicular to the substrate surface (Figure 1a). Morphologically, the filamentous carbon structures resemble flattened, ribbon-like forms. The average length of the vertically aligned, columnar nanofilaments was measured to be approximately 36 nm (Figure 1b).

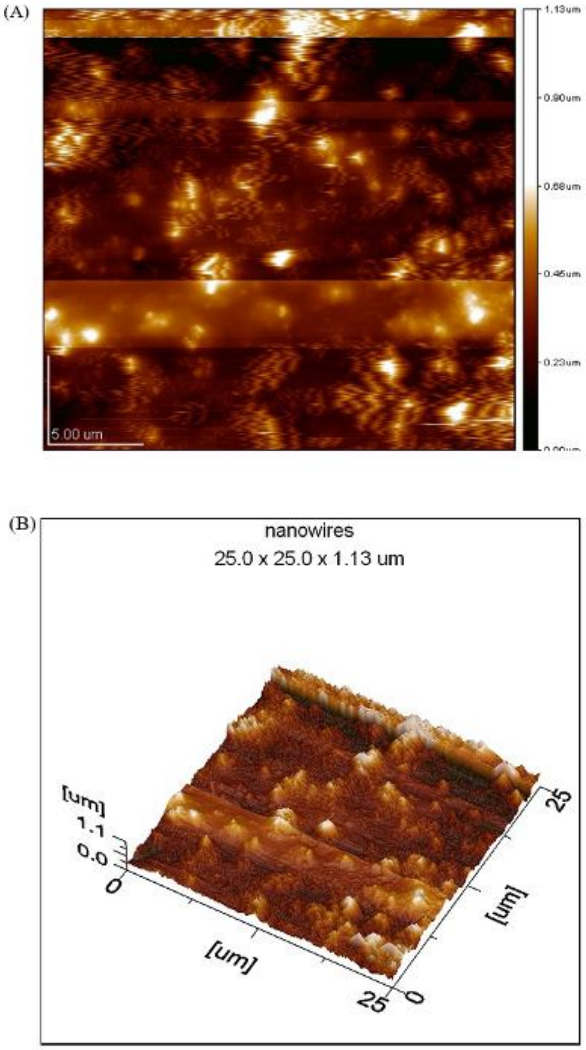

Figure 1 - AFM image of the nanofilament: (A) structure is a growth of densely packed nanofilaments strictly vertical to the substrate surface: (B) the columnar densely packed carbon nanofilament

The thickness of the deposited films was measured by comparing the cantilever displacement at regions without coating and at regions covered with the film. The height difference provided the film thickness, which was found to vary between 0.3 µm and 1 µm**.** The synthesized nanofilaments reached lengths of up to 300 nm, with diameters ranging from 10 to 68 nm (Figure 2).

Initially, some uncertainty arose regarding the accuracy of these measurements. To ensure

reliability, AFM imaging was performed in two independent laboratories, using different instruments and specialized cantilevers designed for structures of this scale, thereby minimizing noise and measurement artifacts.

In order to study the optical characteristics of the nanocarbon structures, transmittance was measured with incident light directed perpendicularly to the sample surface. The obtained transmission spectrum, recorded within the 160–1100 nm range, is presented in Figure 3.

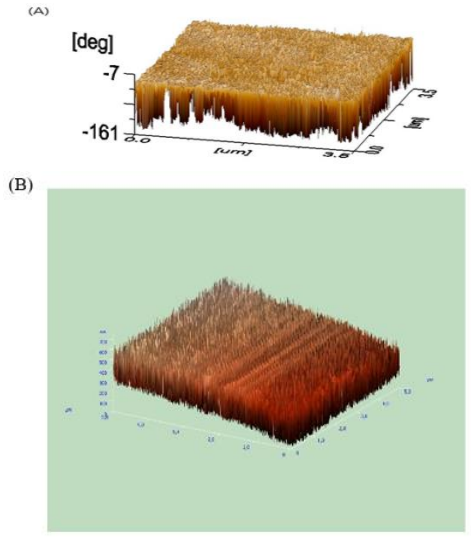

Figure 2 - Micrographs of carbon nanofilaments obtained in methane plasma, obtained by different atomic force microscopes:
(A) Growth of carbon nanofilaments,
(B) Arrays of vertically oriented carbon nanofilaments on quartz substrates.

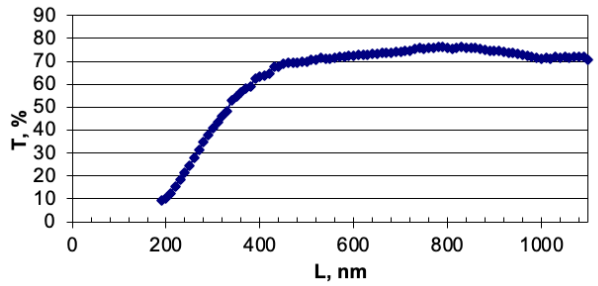

Figure 3 - Transmission spectrum of carbon nanofilaments

The transmission spectrum revealed that at a wavelength of approximately 400 nm (short-wavelength region), the transmittance reached about 65%. Within the visible range, the transparency remained around 75%, while in the near-infrared region it increased to nearly 80%, continuing to rise gradually with longer wavelengths. Such a level of optical transparency in the visible spectrum is sufficient to enable the application of carbon nanofilaments in optoelectronic devices.

When the incident light wavelength is comparable to, or smaller than, the spacing between individual nanofilaments (100–500 nm), photons are able to propagate through the structure owing to multiple reflections from the filament walls. The optical band gap of the carbon nanofilaments was estimated to be approximately E = 2.85 eV**.** (Figure 4).

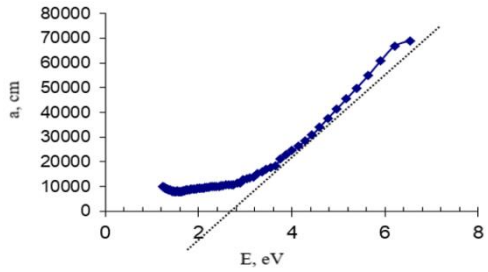

Figure 4 - Optical characteristics of the sample: dependence of a, on photon energy

The optical band gap of a bulk film, assumed to be homogeneous in mass, can be evaluated using the Bouguer–Lambert–Beer law, which defines the exponential relationship between light absorption and the electromagnetic wavelength [26]. For practical application, this general law can be reformulated into the following expression (1.1):

$$a = -\frac{ln(\frac{\tau}{100})}{thickness}(1/cm) \qquad (1.1)$$

Thickness ≈ 1000E-7 cm

Raman spectroscopy is a highly informative technique for analyzing the vibrational modes and local structural environment of carbon-based materials, making it indispensable in their characterization. Disordered carbon films typically exhibit two characteristic features in their Raman spectra: the D-band (Disordered) in the range of 1350–1400 cm^{-1}, and the G-band (Graphitic) between 1575–1600 cm^{-1}. Variations in the relative intensities and frequency positions of these two peaks provide valuable insight into the degree of C–C bond hybridization and the evolution of allotropic modifications in the synthesized carbon films.

For crystalline graphite, Raman scattering generally produces two main bands: the G peak at ~1582 cm^{-1}, attributed to the doubly degenerate E_2g phonon mode within the graphene plane, and a low-

frequency feature near 42 cm^{-1}, associated with lattice vibrations involving sp^2-hybridized carbon bonds [27]. Even slight disruptions of the graphite lattice can induce noticeable shifts in the G-band position. It has been reported [28] that when graphite crystallite sizes decrease to about 25 Å**,** the G peak broadens and shifts to higher frequencies, up to 1593 cm^{-1}. In carbon nanostructures and nanotubes, multiple discrete vibrational modes may be detected within the G-band region (e.g., 1571, 1585, 1586, 1587, and 1593 cm^{-1}). For hollow carbon systems such as nanotubes of various morphologies, the Raman response becomes more complex, with additional peaks corresponding to different bonding environments.

The D-band, typically at 1341–1350 cm^{-1}, arises from phonon modes near the M and K points of the Brillouin zone and is strongly correlated with structural disorder. These modes are particularly sensitive to lattice imperfections and are indicative of defect-induced vibrations. The G-band, spanning 1550–1594 cm^{-1}, reflects the degree of order in graphitic materials and is used as a marker for structural organization in nanotubes and related systems. In contrast, the *2D (D) band**, observed in the 2500–2900 cm^{-1} region, originates from second-order resonant scattering involving two phonons of equal energy and opposite momentum near the K point. The intensity and profile of this band provide insight into the stacking and three-dimensional arrangement of graphene layers [[29], [30], [31], [32]].

The Raman spectra obtained for our carbon nanofilament samples are shown in Figure 5. The three most prominent lines typically observed in carbon materials were detected. The G peak at 1590 cm^{-1} corresponds to tensile vibrations of hexagonal carbon rings, associated with sp^2 bonding [35]. In amorphous carbon films, the G peak is often broadened and may shift within the 1500–1630 cm^{-1} range due to disordered bonding environments [34]. The D peak arises from breathing modes of hexagonal carbon units and is indicative of lattice disorder, influenced by phonons near the K point [[33], [34]]. Its absence suggests a lack of ring structures, as in pyrolytic graphite [[31], [32], [33], [34], [35], [36]].

The Raman spectrum of our samples (Figure 6) showed a dominant G peak at ~1588 cm^{-1} with an associated shoulder in the low-frequency range, characteristic of amorphous carbon produced by reactive methane magnetron sputtering. The D line at 1350 cm^{-1} confirmed the presence of numerous defects. The 2D band (2600–2710 cm^{-1}) was also detected, associated with two-phonon resonant scattering. The enhanced intensity of this band in certain regions suggests partial structural ordering within the amorphous carbon matrix.

For quantitative analysis, spectral deconvolution was carried out. Owing to the overlapping nature of the D and G peaks (1000–1800 cm^{-1}), Lorentzian fitting was employed, with additional verification using the Voigt function—a convolution of Lorentzian and Gaussian distributions. The fitting reliability exceeded 0.999, confirming the accuracy of the decomposition [[35], [36], [37]].

The structural classification of the films can thus be deduced from Raman spectral features. Narrow line widths (20–40 cm^{-1}) and the presence of both G and 2D peaks suggest a high degree of graphitization in certain domains, consistent with CNT-like regions. Furthermore, the intensity ratio I_D/I_G is strongly correlated with the lateral crystallite size (La), providing an estimate of the degree of disorder or graphitization in the films [[38], [39]]. The authors [[38], [39]] empirically derived the expression (1.2):

$$L_a\ (\text{nm}) = 4.5R = 4.5 \cdot I_G / I_D \qquad (1.2)$$

The lateral crystallite size (La) serves as an indicator of the structural type of carbon present in the sample. When La > 20 nm, the material exhibits predominantly graphitic characteristics. At La ≈ 10 nm, the structure is classified as semi-graphitic, whereas values of La ≤ 5 nm correspond to amorphous carbon domains.

Raman scattering also provides the possibility to analyze spectra at different distances from the substrate surface, enabling the monitoring of structural variations along the vertical axis of the nanofilament array. In this study, it was demonstrated that the Raman response of vertically aligned nanofilaments exhibits noticeable changes depending on the position of the probing laser beam along their height, thereby reflecting spatial variations in structural ordering within the array.

Such an approach makes it possible to trace the structural evolution of nanofilaments throughout their vertical growth within the array. Recognizing these spectral variations provides a basis for controlling both the degree of ordering and the morphological profile of the synthesized nanofilaments, which is essential for tailoring their fabrication to specific applications. In this study, the key aspects of interpreting Raman spectra of light scattering from vertically aligned carbon nanofilament arrays have been outlined.

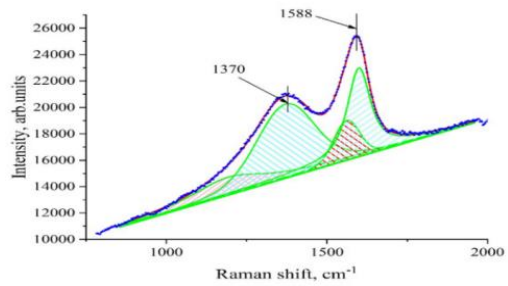

Figure 5 - Raman spectra of light scattering of the sample using the Voigt profile (Gaussian and Lorentz decomposition), carbon nanofilaments

Among the most informative techniques for characterizing crystalline structures, including nanostructured materials, is X-ray phase and structural analysis, which offers direct insight into lattice ordering and interplanar spacings. (Figure 6).

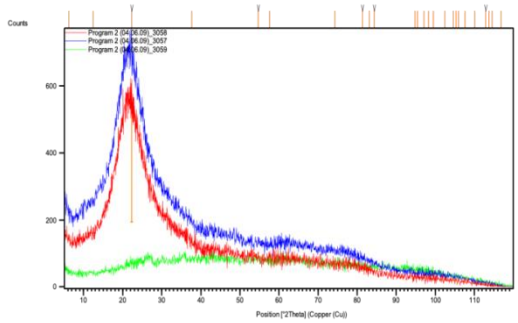

Figure 6- General view of the X-ray image of the nanofilament. a): Blue line by Bragg-Brentano method. Red line according to the sliding X-ray method. Green line by small angle X-ray scattering. Red line carbon on substrate quartz

The diffraction parameters of the carbon films deposited on quartz substrates—including the Bragg angles (2θ) of the X-ray reflections, line intensities (I), full width at half maximum (FWHM) of the peaks, and corresponding interplanar spacings (d)—are summarized in Table 1.

Based on the analysis of the X-ray peak broadening, the average size of amorphous crystallites was estimated to be approximately L = 1.2 Å, with an interplanar distance of d = 3.98 Å **(**Table 1). The dominant reflection, observed at 2θ = 22.28°, exhibited an integral intensity value of 100, confirming the presence of carbonaceous deposits within the sample.

A distinct category of nanostructured materials includes amorphous–crystalline systems and cluster-type metals and alloys, where crystalline domains are embedded within an amorphous matrix. In such cases, the characteristic dimensions of the crystalline inclusions do not exceed 100 nm for amorphous–crystalline materials, while for cluster systems, the size of ordered regions is typically below 2 nm. Within the amorphous film matrix, these crystalline inclusions manifest as nanocrystals, thereby imparting unique structural and functional properties to the material [[40], [41]].

Table 1 - X-ray data of carbon nanofilaments

Pos. [°2Th.]	*d-spacing Å]*	*I, Int. [%]*	*FWHM [°2Th.]*
6.1907	14.26544	4.8	0.3
12.4479	7.10513	2.55	0.3
22.2838	3.98624	100	1.2
37.6532	2.38701	4.5	0.3
54.6909	1.67692	2.07	0.48
57.5956	1.59906	4.86	0.36
74.3308	1.27508	2.28	0.3
81.3617	1.18172	1.19	0.48
83.1549	1.16073	3.43	0.36
84.4011	1.14674	1.53	0.3
94.784	1.0466	2.61	0.36
95.491	1.04071	2.17	0.36
97.0905	1.02778	3.86	0.36
98.2354	1.01884	2.68	0.36
99.4839	1.00938	2.78	0.36
102.3854	0.9885	1.47	0.3
104.5484	0.97389	2.18	0.36
105.2722	0.96918	1.91	0.36
105.9447	0.96487	2.24	0.3
107.5544	0.95485	2.27	0.36
110.0735	0.93994	1.58	0.36
112.8789	0.92439	1.5	0.36
113.6632	0.92024	1.95	0.36
114.5307	0.91573	1.1	0.36
116.8588	0.90411	0.97	0.48

Conclusions

Carbon nanofilaments were successfully synthesized via reactive magnetron sputtering in a methane atmosphere. Raman spectroscopy revealed a distinct G-band at 1588 cm^{-1} for nanofilaments deposited on quartz substrates. Atomic force microscopy confirmed the formation of vertically aligned nanofilaments with diameters reaching up to 68 nm. X-ray diffraction analysis indicated that the average crystallite size was approximately L = 1.2 Å, with an interplanar distance

of d = 3.98 Å, and an integral peak intensity of 100 at 2θ = 22.28°.

Optical transmission measurements demonstrated a transmittance of about 65% at 400 nm, approximately 75% across the visible region, and nearly 80% in the near-infrared range, showing a gradual increase at longer wavelengths. Such transparency within the visible spectrum is a critical property, highlighting the suitability of carbon nanofilaments for optoelectronic applications. Their ability to transmit visible light with minimal absorption or scattering is a key advantage for device integration.

Furthermore, a correlation was observed between the dimensions of nanofilaments composed of sp^2 nodes, the optical band gap, and the XRD results. The favorable conductivity of these structures, particularly in the direction perpendicular to the sputtering plane, suggests their potential use in perovskite solar cells. Specifically, they may serve as an intermediate layer preventing direct contact between silver electrodes and the p-layer of the perovskite absorber. As noted in [39], future advances in heterojunction photovoltaics are expected to exploit materials with quantum-dimensional effects, such as quantum wells and quantum barriers. In this context, the relative ease of fabricating carbon nanostructures could make them an attractive candidate for further development in heterostructure-based solar technologies.

Conflict of Interest. The authors have no conflicts to disclose.

CRediT author statement: **D. Shaidalina:** Formal analysis, Data curation; **B. Baitimbetova:** Conceptualization, Methodology, Validation, Supervision, Investigation; **K.Astemessova:** Reviewing and Editing; **G.Turlybekova:** Data curation; **B. Topanov:** Methodology, Validation; **D. Bukhvalov:** Investigation, Formal analysis; **N. Chuchvaga:** Visualization, Writing, Reviewing and Editing; **Mit':** Investigation; **A. Serikkanov:** Visualization.

Acknowledgments. This research was supported by the Research Grant from the Ministry of Science and Higher Education of the Republic of Kazakhstan.

Formatting of funding sources. AP32728461 - Development of technology for producing two-dimensional films based on graphene-containing structures and chalcogenide compounds for wide practical application, and BR28712683 – Development of a Technology for Reducing Energy Consumption and Waste Without Compromising Efficiency in the Recycling of Lithium-Ion Batteries.

Cite this article as: Shaidalina DR, Baitimbetova BA, Astemessova KS, Turlybekova GK, Topanov BG, Bukhvalov DV, Chuchvaga NA, Mit' KA, Serikkanov AS. Investigation of synthesized carbon nanofilaments by reactive magnetron reactive sputtering methane decomposition. Kompleksnoe Ispolzovanie Mineralnogo Syra = Complex Use of Mineral Resources. 2027; 343(4):34-45. https://doi.org/10.31643/2027/6445.38

Метанның ыдырауы кезінде реактивті магнетронды тозаңдату арқылы синтезделген көміртекті наноталшықтарды зерттеу

[1] Шайдалина Д.Р., [1]Байтимбетова Б.А., [2]Астемесова К.С., [2]Турлыбекова Г.К., [3]Топанов Б.А., [4]Бухвалов Д.В., [5]Чучвага Н.А., [5]Мить К.А., [6]Серикканов А.С.

[1] Тау-кен-металлургия институты, Сәтбаев университеті, Алматы, Қазақстан
[2]Энергетика және машина жасау институты, Сәтбаев университеті, Алматы, Қазақстан
[3]Қазақстан Республикасы Білім және ғылым министрлігі Ғылым комитетінің Жану проблемалары институты, Алматы
[4]Ғылым колледжі, Материалдар физикасы және химия институты, Нанкин орман шаруашылығы университеті, Нанкин, Қытай
[5]ЖШС Физика-техникалық институты, Сәтбаев университеті, Алматы, Қазақстан
[6]Қазақстан Республикасы Президентінің жанындағы Қазақстан Республикасының Ұлттық ғылым академиясы

ТҮЙІНДЕМЕ

Бұл жұмыста графиттің метан плазмасында аргон енгізілуі арқылы ыдырауы нәтижесінде алынған көміртекті наноталшықтарды зерттеу нәтижелері келтірілген. Алынған наноталшықтардың аморфты құрылымы бар және көрінетін спектр аймағында мөлдірлігімен ерекшеленеді, бұл оларды оптикалық қолданбалар үшін болашағы бар екендігіне дәлел. Атомдық-күштік микроскопия көмегімен наноталшықтардың астар бетінде тығыз тік тор түзетіні анықталды. Үлгілердің жергілікті құрылымы Раман спектроскопиясы арқылы зерттелді. Морфологиялық тұрғыдан көміртекті талшық тәрізді құрылымдар жалпақ

Мақала келді: *25 қыркүйек 2025*
Сараптамадан өтті: *17 қараша 2025*
Қабылданды: *23 ақпан 2026*

таспа тәрізді түзілімдерге ұқсайды. Тығыз орналасқан колонна тәрізді көміртекті наноталшықтардың ұзындығы шамамен 36 нм құрайды. Тарату спектрі 400 нм шамасындағы қысқа толқынды аймақта тарату шамамен 65%-ға, көрінетін диапазонда шамамен 75%-ға жететінін, ал жақын инфрақызыл диапазонда ұзын толқын ұзындықтарында біртіндеп артуымен шамамен 80%-ға дейін артатынын көрсетеді. Көрінетін диапазондағы мөлдірліктің бұл деңгейі оптоэлектрондық құрылғыларда көміртекті наноталшықтарды пайдалану үшін жеткілікті. Түскен жарықтың толқын ұзындығы наноталшықтар арасындағы қашықтықпен (100–500 нм) немесе одан да қысқарақ болса, жарық олардың қабырғаларынан шағылысу арқылы олардың арасында тарай алады. Көміртекті талшықтың жолақ аралығы E=2,85 эВ. Сипаттама нәтижелерін талдағаннан кейін, көміртекті наноталшықтардың аморфты құрылымдармен тиімді синтезделгені туралы қорытынды жасауға болады, бұл олардың әлеуетін көрсетеді.

Түйін сөздер: реактивті магнетронды шашырату, нано талшықтар, метан газы, жұқа қабықша, наноқұрылым.

Авторлар туралы ақпарат:

Шайдалина Дамира — *PhD докторанты, Техника және технологиялар магистрі, Тау-кен-металлургия институты, Сәтбаев университеті, Сәтбаев к-сі 22, 050013, Алматы, Қазақстан. Email: Shaidalina.D@stud.satbayev.university; ORCID ID: https://orcid.org/0009-0003-4734-170X*

Байтимбетова Бағила — *Физика-математика ғылымдарының кандидаты, қауымдастырылған профессор, Тау-кен-металлургия институты, Сәтбаев университеті, Сәтбаев к-сі 22, 050013, Алматы, Қазақстан. Email: baitim@physics.kz; ORCID ID: https://orcid.org/0000-0002-3728-2430*

Астемесова Каламкас — *PhD докторы, Кафедра меңгерушісі, Энергетика және машина жасау институты, Сәтбаев университеті, Сәтбаев к-сі 22, 050013, Алматы, Қазақстан. Email: k.astemessova@satbayev.university; ORCID ID: https://orcid.org/0000-0002-4143-6084*

Турлыбекова Гулжан — *Техникалық ғылымдар кандидаты, қауымдастырылған профессор, Энергетика және машина жасау институты, Сәтбаев университеті, Сәтбаев к-сі 22, 050013, Алматы, Қазақстан. Email: g.turlybekova@satbayev.university; ORCID ID: ORCID ID: https://orcid.org/0000-0001-5522-4931*

Топанов Болат — *Аға ғылыми қызметкер, Қазақстан Республикасы Білім және ғылым министрлігі Ғылым комитетінің Жану проблемалары институты, 050012, Бөгенбай батыр к-сі 172, Алматы, Қазақстан. Email: topikbotat@mail.ru; ORCID ID: https://orcid.org/0009-0008-7872-1437*

Бухвалов Данил — *Физика-математика ғылымдарының кандидаты, Ғылым колледжі, Материалдар физикасы және химия институты, Нанкин орман шаруашылығы университеті, 210037, Нанкин, Қытай. Email: danil@njfu.edu.cn; ORCID ID: https://orcid.org/0000-0002-2286-3443*

Чучвага Николай — *PhD докторы, директордың ғылыми жұмыс жөніндегі орынбасары, Физика-техникалық институты ЖШС, Сәтбаев университеті, Ибрагимова к-сі 11, Алматы, Қазақстан. Email: n.chuchvaga@satbayev.university; ORCID ID: https://orcid.org/0000-0003-4417-4996*

Мить Костя — *Физика-математика ғылымдарының кандидаты, Физика-техникалық институты ЖШС, Сәтбаев университеті, Ибрагимова к-сі 11, Алматы, Қазақстан. Email: k.mit@sci.kz; ORCID ID: https://orcid.org/0000-0002-0078-6723*

Серикканов Абай — *Физика-математика ғылымдарының кандидаты, профессор, Қазақстан Республикасы Президентінің жанындағы Қазақстан Республикасының Ұлттық ғылым академиясы, 050010, Шевченко к-сі 28, Алматы, Қазақстан. Email: a.serikkanov@gmail.com; ORCID ID: https://orcid.org/0000-0001-6817-9586*

Исследование синтезированных углеродных нановолокон методом реактивного магнетронного распыления при разложении метана

[1] Шайдалина Д.Р., [1]Байтимбетова Б.А., [2]Астемесова К.С., [2]Турлыбекова Г.К., [3]Топанов Б.А., [4]Бухвалов Д.В., [5]Чучвага Н.А., [5]Мить К.А., [6]Серикканов А.С.

[1] Горно-металлургический институт, Satbayev University, Алматы, Казахстан
[2]Институт энергетики и машиностроения, Satbayev University, Алматы, Казахстан
[3] Институт проблем горения Комитета науки Министерства образования и науки Республики Казахстан, Алматы
[4]Научный колледж, Институт физики и химии материалов, Нанкинский лесотехнический университет, Нанкин, Китай
[5]ТОО Физико-технический институт, Satbayev University, Алматы, Казахстан
[6]Национальная академия наук Республики Казахстан при Президенте Республики Казахстан

Поступила: *25 сентября 2025*
Рецензирование: *17 ноября 2025*
Принята в печать: *23 февраля 2026*

АННОТАЦИЯ

В данной работе представлены результаты получения углеродных нановолокон путем разложения графита в метановой плазме с введением аргона. Полученные нановолокна имеют аморфную структуру и прозрачность в видимой области спектра, что делает их перспективными для оптических применений. Атомно-силовая микроскопия показала, что нановолокна образуют плотную вертикальную сетку на поверхности подложки. Локальная структура образцов была исследована с помощью рамановской спектроскопии. Морфологически углеродные нитевидные структуры напоминают плоские лентообразные

	образования. Длина столбчатых, плотно упакованных углеродных нановолокон составляет около 36 нм. Спектр пропускания показывает, что в области коротких волн около 400 нм пропускание достигает около 65%, в видимом диапазоне — около 75%, а в ближнем инфракрасном диапазоне оно увеличивается до почти 80% с постепенным ростом на более длинных волнах. Такой уровень прозрачности в видимом диапазоне достаточен для применения углеродных нановолокон в оптоэлектронных устройствах. Когда длина волны падающего света сопоставима с расстоянием между нанофиламентами (100–500 нм) или меньше его, свет может распространяться между ними за счет отражения от их стенок. Ширина запрещенной зоны углеродного нити составляет E = 2,85 эВ. После анализа результатов характеристики можно сделать вывод, что углеродные нанонити были эффективно синтезированы с аморфными структурами, что свидетельствует об их потенциале.
	Ключевые слова: реактивное магнетронное распыление, нано-нити, метановый газ, тонкая плёнка, наноструктура.
Шайдалина Дамира	***Информация об авторах:*** *PhD докторант, Магистр техники и технологии, Горно-металлургический институт, Satbayev University, 050013, ул.Сатпаева 22, Алматы, Казахстан. Email: Shaidalina.D@stud.satbayev.university; ORCID ID: https://orcid.org/0009-0003-4734-170X*
Байтимбетова Багила	*Кандидат физико-математических наук, ассоциированный профессор, Горно-металлургический институт, Satbayev University, 050013, ул. Сатпаева 22, Алматы, Казакстан. Email: baitim@physics.kz; ORCID ID: https://orcid.org/0000-0002-3728-2430*
Астемесова Каламкас	*Доктор PhD, Заведующая кафедрой, Институт энергетики и машиностроения, Satbayev University, 050013, ул. Сатпаева 22, Алматы, Казакстан. Email: k.astemessova@satbayev.university; ORCID ID: https://orcid.org/0000-0002-4143-6084*
Турлыбекова Гулжан	*К.э.н., ассоциированный профессор, Институт энергетики и машиностроения, Satbayev University, 050013, ул. Сатпаева 22, Алматы, Казахстан. Email: g.turlybekova@satbayev.university; ORCID ID: https://orcid.org/0000-0001-5522-4931*
Топанов Болат	*Ведущий научный сотрудник, Институт проблем горения Комитета науки Министерства образования и науки Республики Казахстан, 050012, ул. Богенбай батыра, 172, Алматы, Казахстан. Email: topikbotat@mail.ru; ORCID ID: https://orcid.org/0009-0008-7872-1437*
Бухвалов Данил	*Кандидат физико-математических наук, Научный колледж, Институт физики и химии материалов, Нанкинский лесотехнический университет, 210037, Нанкин, Китай. Email: danil@njfu.edu.cn; ORCID ID: https://orcid.org/0000-0002-2286-3443*
Чучвага Николай	*Доктор PhD, Заместитель директора по научной работе, ТОО Физико-технический институт, Satbayev University,, 050013, ул. Ибрагимова 11, Алматы, Казахстан. Email: n.chuchvaga@satbayev.university; ORCID ID: https://orcid.org/0000-0003-4417-4996*
Мить Костя	*Кандидат физико-математических наук, ТОО Физико-технический институт, Satbayev University, 050013, ул. Ибрагимова 11, Алматы, Казахстан. Email: k.mit@sci.kz; ORCID ID: https://orcid.org/0000-0002-0078-6723*
Серикканов Абай	*Кандидат физико-математических наук, профессор, Национальная академия наук Республики Казахстан при Президенте Республики Казахстан, 050010, ул. Шевченко 28, Алматы, Казахстан. Email: a.serikkanov@gmail.com; ORCID ID: https://orcid.org/0000-0001-6817-9586*

References

[1] Baitimbetova BA, Vermenichev BM, Ryabikin YuA, Mansurov ZA, Abdikasova AA. Study of graphene formed in the atmosphere of vapors of aromatic hydrocarbons. Russian Physics Journal. 2015; 58(3):347-353. https://doi.org/10.1007/s11182-015-0513-x

[2] Babu Naidu ChK, Kumar SN, Banerjee P. A review on the origin of nanofibers/nanorods structures and applications. Journal of Materials Science: Materials in Medicine. 2021; 32(6):68. https://doi.org/10.1007/s10856-021-06513-4

[3] Torres-Costa V. Nanostructures for photonics and optoelectronics. Nanomaterials. 2022; 12:1820. https://doi.org/10.3390/nano12101820

[4] Husain Z. (ed.). Emerging Trends in Nanotechnology. Springer Nature Singapore. 2021. https://doi.org/10.1007/978-981-15-9904-0

[5] Huo D, Ma X, Su H, Wang C, Zhao H. Broadband absorption based on thin refractory titanium nitride patterned film metasurface. Nanomaterials. 2021; 11:1092. https://doi.org/10.3390/nano11051092

[6] Liang Y, Zhao W. Crystal growth and design of disk/filament ZnO-decorated 1D TiO_2 composite ceramics for photoexcited device applications. Nanomaterials. 2021; 11:667. https://doi.org/10.3390/nano11030667

[7] Baytimbetova BA, Ryabikin YuA. Issledovanie uglerodnykh nanostruktur metodom spektroskopii v karbonizovannom ferrokhromovom spinele [The study by spectroscopy method of carbon nanostructure in carbonized ferrochromic spinel]. Spectroscopy Letters. 2008; 41:9-14. (in Russ.). https://doi.org/10.1080/00387010801905219

[8] Sobolev K, Shah SP. Nanotechnology in Construction. Proceedings of the 5th International Symposium on Nanotechnology in Construction (NICOM5). 2015.

[9] Sharma R, Sharma AK, Sharma V. Synthesis of carbon nanotubes by arc-discharge and chemical vapor deposition method with analysis of its morphology, dispersion and functionalization characteristics. Cogent Engineering. 2015; 2:1-14. https://doi.org/10.1080/23311916.2015.1061726

[10] Chrzanowska J, Hoffman J, Małolepszy A, Mazurkiewicz M, Stobiński L. Synthesis of carbon nanotubes by the laser ablation method: Effect of laser wavelength. Physica Status Solidi (b). 2015; 252(8):1860-1867. https://doi.org/10.1002/pssb.201552017

[11] Song L, Holleitner WA, Qian H, Hartschuh A. A carbon nanofilament-bead necklace. Journal of Physical Chemistry C. 2008; 112(26):9644-9649. https://doi.org/10.1021/jp801608r

[12] Zhao N, Zhang Q, Wang J, Tian L, Qi Z, He F, Li Y. Synthesis of carbon nanostructures with different morphologies by CVD of methane. Materials Science and Engineering A. 2007; 460-461:255-260. https://doi.org/10.1016/j.msea.2007.01.121

[13] Sivamaran VV, Balasubramanian M, Gopalakrishnan V, Viswabaskaran A. Combined synthesis of carbon nanospheres and carbon nanotubes using thermal chemical vapor deposition process. Chemical Physics Impact. 2022; 4:100072. https://doi.org/10.1016/j.chphi.2022.100072

[14] Torres D, Pinilla JL, Suelves I. Screening of Ni-Cu bimetallic catalysts for hydrogen and carbon nanofilaments production via catalytic decomposition of methane. Applied Catalysis A: General. 2018; 559:10-19. https://doi.org/10.1016/j.apcata.2018.04.004

[15] Lee SY, Yamada M, Miyake M. Synthesis of carbon nanotubes and carbon nanofilaments over palladium supported catalysts. Science and Technology of Advanced Materials. 2005; 6(4):420-426. https://doi.org/10.1016/j.stam.2005.02.004

[16] Tehrani M, Boroujeni AY, Luhrs C, Phillips J, Al-Haik MS. Hybrid composites based on carbon fiber/carbon nanofilament reinforcement. Materials. 2014; 7(6):4182-4195. https://doi.org/10.3390/ma7064182

[17] Zhao S, Hong R, Luo Z, Lu H, Yan B. Carbon nanostructures production by AC arc discharge plasma process at atmospheric pressure. Journal of Nanomaterials. 2011; 2011:346206. https://doi.org/10.1155/2011/346206

[18] Yazdanbakhsh A, Grasley Z, Tyson B, Al-Rub RKA. Challenges and benefits of utilizing carbon nanofilaments in cementitious materials. Journal of Nanomaterials. 2012; 2012:371927. https://doi.org/10.1155/2012/371927

[19] Dussault L, Pinilla JL, Suelves I, Moliner R, Lázaro MJ. New Ni–Cu–Mg–Al-based catalysts preparation procedures for the synthesis of carbon nanofibers and nanotubes. Journal of Physics and Chemistry of Solids. 2006; 67(5-6):1162-1167. https://doi.org/10.1016/j.jpcs.2006.01.022

[20] Luhrs CC, Garcia D, Tehran M, Al-Haik M, Taha MR, Phillips J. Generation of carbon nanofilaments on carbon fibers at 550 °C. Carbon. 2009; 47(13):3071-3078. https://doi.org/10.1016/j.carbon.2009.06.019

[21] Baitimbetova BA, Ryabikin YA. & Mukashev BN. Correction to: Study of Paramagnetic Properties of Graphene Structures Obtained from Pure Graphite in Organic Reagents Exposed to Ultrasound. Russ Phys J. 2021; 64:1582. https://doi.org/10.1007/s11182-021-02494-0

[22] Xiang L, Zhang L, Xu T, Ding F, Yang W, Xu Y, et al. Mechanochemical synthesis of carbon nanothread single crystals. Journal of the American Chemical Society. 2017; 139(45):16343-16349. https://doi.org/10.1021/jacs.7b08176

[23] Lee TW, Lee GH. Interstitial nanofilament pathway reduces energy consumption in memristors. Nat. Nanotechnol. 2025; 20:1552–1553. https://doi.org/10.1038/s41565-025-02014-y

[24] Zeng Z, Natesan K. Relationship between the growth of carbon nanofilaments and metal dusting corrosion. Chemistry of Materials. 2005; 17(15):3794-3801. https://doi.org/10.1021/cm050333a

[25] Monthioux M, Charlier JC, Masin F, Flahaut E, Razafinimanana M, Capria E, et al. Texturizing and structuring mechanisms of carbon nanofilaments during growth. Journal of Materials Chemistry. 2007; 17(46):4611-4623. https://doi.org/10.1039/b708354a

[26] Sivukhin DV. Absorption of light and broadening of spectral lines. In: General course of physics. Moscow: Fizmatlit. 2005, 582-583. (in Russ.).

[27] Nemanich RJ, Solin SA. First- and second-order Raman scattering from finite-size crystals of graphite. Physical Review B. 1979; 20(2):392-401. https://doi.org/10.1103/PhysRevB.20.392

[28] Reich S, Thomsen C. Raman spectroscopy of graphite. Philosophical Transactions of the Royal Society A. 2004; 362(1824):2271-2288. https://doi.org/10.1098/rsta.2004.1454

[29] Casimir D, Alghamdi H, Ahmed IY, Misra P. Raman spectroscopy of graphene, graphite and graphene nanoplatelets. In: Wongchoosuk Ch, Seekaew Y. (editors). 2D Materials. London: IntechOpen. 2019. https://doi.org/10.5772/intechopen.85711

[30] Ni Zh, Wang Y, Yu T, Shen Z. Raman spectroscopy and imaging of graphene. Nano Research. 2008; 1(4):273-291. https://doi.org/10.1007/s12274-008-8036-1

[31] Mohiuddin TMG, Lombardo A, Nair RR, Bonetti A, Savini G, Jalil R, Bonini N, Basko DM, Galiotis C. Uniaxial strain in graphene by Raman spectroscopy: G peak splitting, Grüneisen parameters, and sample orientation. Physical Review B. 2009; 79(20):205433. https://doi.org/10.1103/PhysRevB.79.205433

[32] Ferrari AC, Meyer JC, Scardaci V, Casiraghi C, Lazzeri M, Mauri F, et al. Raman spectrum of graphene and graphene layers. Physical Review Letters. 2006; 97(18):187401. https://doi.org/10.1103/PhysRevLett.97.187401

[33] Robertson J. Diamond-like carbon (DLC) coatings: classification, properties, and applications. In: Rajak KD, Kumar A, Behera A. (eds). Applied Sciences. 2021; 11:4445. https://doi.org/10.3390/app11104445

[34] Ferrari AC, Robertson J. Interpretation of Raman spectra of disordered and amorphous carbon. Physical Review B. 2000; 61(20):14095-14107. https://doi.org/10.1103/PhysRevB.61.14095

[35] Ferrari AC, Robertson J. Resonant Raman spectroscopy of disordered, amorphous, and diamondlike carbon. Physical Review B. 2001; 64(7):075414. https://doi.org/10.1103/PhysRevB.64.075414

[36] Ryaguzova AP, Nemkayeva RR, Guseinova NP. Vliyanie uslovii sinteza i nanostruktur olova na svoistva a-C:H<Sn> kompozitnykh plenok [Influence of the synthesis conditions and tin nanoparticles on the structure and properties of a-C:H<Sn> composite thin films]. Semiconductors. 2018; 52(10):1327-1333. (in Russ.). https://doi.org/10.1134/S1063782618100182

[37] Bukunov KA, Vorobyeva EA, Chechenin NG. Osobennosti ramanovskikh spektral'nykh kharakteristik v massive vertikal'no orientirovannykh mnogosloinykh uglerodnykh nanotrubok [Features of Raman spectra of light scattering in an array of vertically oriented multi-walled carbon nanotubes]. BMU. Series 3. Physics. Astronomy. 2022; 49-54. (in Russ.).

[38] Heise HM, Lampen P, Kiefer W, Hildebrandt P, Janotta M, et al. Characterisation of carbonaceous materials using Raman spectroscopy: a comparison of carbon nanotube filters, single- and multi-walled nanotubes, graphitised porous carbon and graphite. Journal of Raman Spectroscopy. 2009; 40(3):344-353. https://doi.org/10.1002/jrs.2145

[39] Murae T, Kagi H, Masuda A. Structure and chemistry of carbon in meteorites. In: Oya H. (ed). Primitive Solar Nebula and Origin of Planets. Tokyo: Terra Scientific Publishing Company. 1993.

[40] Alemasova NV, Bugorskaya DI, Burkhovetsky VV, Volkova GK, Glazunova VA, Burkhovetsky MYu, Zelensky MY, Savoskin MV. Grafit oksid: osobennosti issledovaniya materiala fizicheskimi metodami [Graphite oxide: peculiarities of material investigation by physical methods]. Experimental Studies of Nanoparticles, Nanosystems and Nanomaterials. Physical and Chemical Aspects of the Study of Clusters. Nanostructures and Nanomaterials. 2023; 15:8. (in Russ.).

[41] Ryabov AV, Okishev KY. New metallic materials and methods of their production: textbook. Chelyabinsk: South Ural State University Publishing House. 2007.

[42] Chuchvaga N, Kireev V, et al. Development of hetero-junction silicon solar cells with intrinsic thin layer: A review. Coatings. 2023; 13(4):796. https://doi.org/10.3390/coatings13040796

Crossref
DOI: 10.31643/2027/6445.39
Metallurgy and Metallurgical Engineering

Device for automatic control of non-roundness and eccentricity of small rotating parts

[1*]Atalykova A.K., [1] Yeleukulov Ye.O., [2] Muslimov A.P.

[1] Almaty University of Power Engineering and Telecommunications, Almaty, Kazakhstan
[2] Kyrgyz State Technical University, Bishkek, Kyrgyz Republic

** Corresponding author email: a.atalykova@aues.kz*

Received: *July 14, 2025*
Peer-reviewed: *August 25, 2025*
Accepted: *February 26, 2026*

ABSTRACT
In the field of mechanical engineering, one of the key tasks is quality control of manufactured products. Particular attention should be paid to quality control of small parts used in precision devices, metalworking machines, and equipment for the metallurgical and defense industries that operate at high rotational speeds. The aim of this study is to develop a device for controlling the out-of-roundness and eccentricity of rollers weighing up to 10 g. The paper proposes a device using a new method of free rotation of cylindrical products with a radius of r = 4 mm on support rollers rotating at a speed of up to 15000 rpm. The advantage of this work is that the geometric and kinematic parameters of the device were determined depending on the mass-geometric characteristics of the controlled products in the absence of radial displacement of the center of mass: e=0. Five products with a conditional displacement of the center of mass e=4; 6; 8; 12; 15 µm, artificially created by removing a certain amount of material from the average outer surface. The mass of the product before and after removal was determined on analytical scales. The number of measurements of one product at each roller rotation speed was n=12. Based on the data obtained, the average angle of product breakage from the rollers was calculated, which can be used to judge the quality of the controlled products: as the eccentricity increases, the angle at which the product breaks from the rollers decreases. The measurement accuracy of the device was evaluated for the case when measurements were taken for a product with e=8 µm at n_r=9000 rpm.

Keywords: small products, non-roundness of products, inspection accuracy, eccentricity, inspection device.

Information about authors:

Atalykova Alfiya Kenesovna — *Senior Lecturer, Department of Automation and Control, Almaty University of Power Engineering and Telecommunications, Baytursynov str., 126/1, 050013, Almaty, Kazakhstan. Email: a.atalykova@aues.kz; ORCID ID: https://orcid.org/0000-0001-7517-2438*

Yeleukulov Yerlan Onlanovich — *Professor of Practice, Department of Electronic Engineering, Almaty University of Power Engineering and Telecommunications, Baytursynov str., 126/1, 050013, Almaty, Kazakhstan. Email: e.eleukulov@aues.kz; ORCID ID: https://orcid.org/0000-0001-6866-3941*

Muslimov Annas Poyasovich — *Doctor of Technical Sciences, Professor, Department of Automation and Robotics, Kyrgyz State Technical University, Ch. Aitmatov str., 66, 720044, Bishkek, Kyrgyz Republic. Email: map.muslimov@mail.ru; ORCID ID: https://orcid.org/0000-0001-7819-8510*

Introduction

Rapidly rotating products are widely used in various applications such as machinery and instrumentation, machine tools, metallurgical and defence equipment, and bearing systems. The quality of low mass and small size rotating body type products has an important influence on the accuracy, performance and service life of equipment. As soon as cracks, scratches, rust [[1], [2]] or material defects [[3], [4]] appear on their surface, the quality and performance of, for example, a bearing [5] will be significantly impaired and even lead to major accidents. Therefore, the quality of products such as bodies of rotation must be fully checked before leaving the factory in order to fulfil the reliability requirements of the entire mechanical system [6].

Parts of the body of rotation type, for example, steel balls [[7], [8], [9]] are manufactured by various processes, including cold drawing, melting and heat treatment, crushing, grinding and rough (fine) lapping [10]. Due to this, various kinds of defects may occur at each stage of the manufacturing process. It is quite difficult to inspect these defects due to the curved and shiny surface of these balls.

As a result, manual visual inspection is still widely used in current inspection of steel balls. The inspector takes a sample of the entire batch of parts and compares it with a control sample. Although this method requires less investment and does not require high-precision equipment, however, it is difficult to improve production efficiency due to the large testing error [[11], [12]]. Moreover, the quality of visual inspection is easily influenced by personal factors, which leads to uneven testing quality of steel balls because the checker works under bright light for a long time, besides visual inspection can only detect obvious spots, cracks, etc., but cannot detect surface micro-cracks and subsurface cracks. For this reason, it cannot meet the needs of automatic defect detection with large batch, high accuracy [[13],[14], [15]] and high reliability [[16], [17], [18]].

The quality of small rotating bodies operating at high speeds is determined by the degree of eccentricity, i.e., the radial displacement of the center of mass. The displacement of the center of gravity from the geometric axis occurs due to material heterogeneity and manufacturing inaccuracies. The dynamic characteristics of rotating bodies are radial and axial displacements of the center of mass, misalignment of surfaces, and product shape errors (out-of-roundness), which create unbalanced forces and moments during operation, causing dynamic imbalance.

Currently, the machines used worldwide to determine dynamic imbalance are mainly designed for large and heavy rotating bodies (weighing from 20 g to 200 g), such as machine spindles, motor rotors, and car wheel hubs. In contrast, cylindrical rollers, which have a smaller volume and mass, pose a problem when determining dynamic imbalance. The development of high-tech equipment requires appropriate precision measurement technologies that can measure the inevitable micro-insignificant residual imbalance of cylindrical bearing rollers, which seriously affects the performance and service life of high-speed precision rolling bearings. A tiny cylindrical roller is a shaftless rotor that cannot be mounted directly on rotary bearing systems, and the vibration response excited by micro-imbalance is difficult to detect and easily confused with background noise. This article describes a device for controlling the quality of cylindrical roller manufacturing to determine eccentricity from 4 μm, which is equivalent to a microdynamic imbalance of 18.1 mg*μm. This device solves problems associated with detecting eccentricity in cylindrical rollers with a radius of $4*10^{-3}$ m, thus offering a new solution for detecting dynamic imbalance in other micro- and small rotating components.

Experimental part

To control non-roundness and the value of radial centre of mass displacement (RCMD), a method of free rotation of the product on support rolls [19] and an automatic control device based on it were developed.

Structurally, the inspection device in Figure 1 consists of a frame with rotating rolls and a drive of rotating rolls.

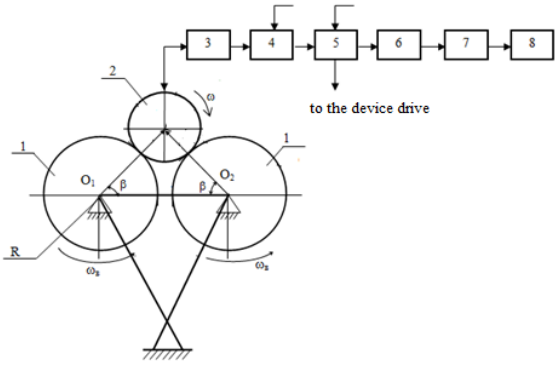

1 - rotating rollers, 2 - controlled product,
3 - speed sensor, 4 - amplifier, 5 - comparator,
6 - second pulse generator, 7 - pulse counter,
8 - digital indicator

Figure 1 - Functional diagram of the device

Controlled products are loaded onto rotating rollers using a piece-by-piece dispensing mechanism, thus starting the rotation of these products with simultaneous measurement of their rotation speed and acceleration time to the set speed. Cylindrical products with a radius of r=4 mm and a length of l=18 mm were used as the controlled parts. Eccentricity was artificially created by removing a certain amount of material from the middle of the outer surface. The drilling pattern is shown in Figure 2. The mass of the drilled-out material is calculated using the formula:

$$m = \pi r_0^2 h \sigma, \quad (1)$$

where r_0 is the radius of the drilled hole; h is the drilling depth; σ is the specific weight of the material.

From Figure 2, the following equation can be derived:

$$2 r l \sigma e = \pi r_0^2 h \sigma. \quad (2)$$

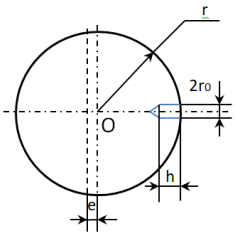

Figure 2 – Drilling diagram for the part

Then the eccentricity will be equal to:

$$e = \frac{\pi r_0^2 h}{2rl}, \qquad (3)$$

where r and l are the radius and length of the part being examined.

Then, for a given value of e=4 μm (device sensitivity), the mass of the drilled material should be:

$$m = \pi r_0^2 h\sigma = 3{,}14 * 0{,}00018344 * 7{,}85$$

$$m = 0{,}00452 \ \text{g}.$$

The measurement method is based on the following physical principle: when accelerating the product to a set speed, additional energy is required due to the need to overcome the momentum from inertial forces due to the radial displacement of the centre of mass.

To develop a method for calculating the center of mass displacement and other errors in cylindrical products, we will justify the choice of certain characteristics of the device and its main parameters.

Required initial data for calculation: r – radius of the controlled product, m; f – coefficient of sliding friction between the roller surface and the surface of the support rolls; e_{max} – maximum permissible eccentricity, m; e_{min} – specified sensitivity of the device to the minimum displacement of the center of mass, m. The maximum angular velocity of rotation of the product (roller) from the surfaces rotating it when the displacement of the center of mass is less than the maximum permissible value $e \le e_{max}$. At $e \ge e_{max}$, the roller will vibrate on the rolls with periodic detachment from their surface. The maximum angular velocity of the roller is calculated using the formula:

$$\omega_r \le \sqrt{\frac{g}{e_{max}} \cdot \frac{(\cos\beta - f\sin\beta)}{\sqrt{1+f^2}}}, \qquad (4)$$

where g –acceleration due to gravity, m/s^2;

β - angle determining the postion of center of rotation on the rolls and calculated using the formula the roller's:

$$\beta = \arccos\frac{R + \delta/2}{R + r}, \qquad (5)$$

where R is the roller radius, m; δ is the gap between rollers, m. Parameters R and δ are specified by design.

Angular velocity of roller rotation

$$\omega_R = \frac{r}{R} \cdot \omega_r \qquad (6)$$

and the rotational speed

$$n = (\omega/2\pi) \cdot 60, \ \text{min}^{-1} \qquad (7)$$

required to accelerate the product to its maximum angular velocity with zero center of mass displacement

$$t_r = \frac{R \cdot \omega_r (1+f^2)\sin\beta}{2f \cdot g}. \qquad (8)$$

The maximum angular speed of the frame rotation is determined by the condition of continuous movement of the product from the roller, which can be represented as

$$g\left[\cos(\varphi+\beta) + f \cdot \sin(\varphi+\beta)\right] \ge \rho \cdot \omega_p^2(\cos\beta + f \cdot \sin\beta)$$
$$+ e(\omega_f + \omega_r)^2\left[\cos(\beta-\gamma) + f \cdot \sin(\beta-\gamma)\right], \qquad (9)$$

where φ is the angle of rotation of the frame from its initial position, degrees; ρ - distance from the center of the product to the axis of rotation of the frame (specified by design), m; γ - angle of rotation of the product, degrees.

It can be shown that the right-hand side (9) is maximal when

$$\gamma = \beta - \text{arctg } f. \qquad (10)$$

The displacement of the center of mass of the product is assumed to be equal to the sensitivity of the device $e=e_{min}$. The maximum angle of rotation of the frame is determined by its design and is assumed to be equal to:

$$\varphi = \varphi_{max} \le 90 - \beta \qquad (11)$$

Taking into account (10) and (11), expression (9) determines the maximum angular velocity of

the frame rotation at which the product with the eccentricity value at the sensitivity limit of the device will break when the frame rotates to the maximum angle. As the value of *e* increases, the breakaway angle will decrease, and at the value of e_{max}, the product will break away at a frame rotation angle of zero.

Results and Discussion

Experimental verification of the method was carried out on the developed device, the photo of which is shown in Figure 3.

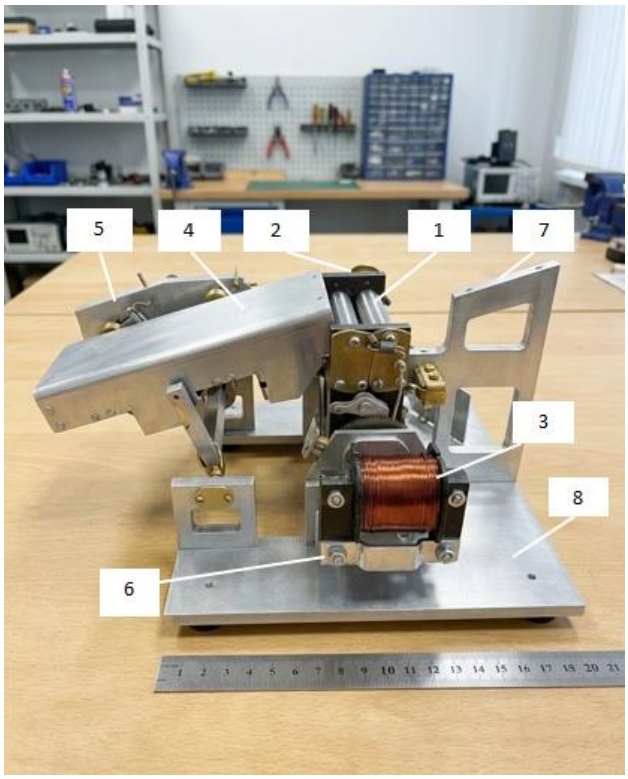

1 - rotating rollers, 2 - rotating frame, 3 - DC drive motor, 4 - guide chute, 5 - angle gauge, 6 - toggle switch, 7 - tray bracket, 8 - base of the device

Figure 3 - Non-roundness control device and RCMD

The process of product control consists of the following: switch on toggle switch 6, during 10 minutes the device starts to work only in idle mode to stabilise the speed mode. Then the controlled product with radius r=4 mm, length l=18 mm is placed manually on the support rollers 1 and accelerated to nominal speed. After that the frame 2 is rotated, the controlled product is torn off the rolls and at the moment of product tearing off the angle of inclination of the plane of rolls axes to the horizon is marked by the angle meter 5. Depending on a certain interval of the tear-off angle, the flap in the guide chute 4 is opened and the product falls into one of two or three hoppers under the chute, the frame is returned to the initial position for control of the next product. Cylindrical products, which have passed the inspection, fall into the hoppers of sorting by quality groups depending on the interval of the tear-off angle α_{sa} from the rotating rolls. In the experiment there were three hoppers for sorting the products by quality, corresponding to α_{sa}: 1 hopper – $0^0 \div 15^0$, 2 hopper – $15^0 \div 26^0$ and 3 hopper – 26^0 and above.

The experiments were carried out in the following volume: the number of products - 5 pieces with RCMD e=4, 6, 8, 12, 15 µm, the speed of rotation of rolls n_r - 3000, 6000, 9000, 12000, 15000 rpm, the number of measurements of one product at each speed of rotation n=12. After the experiment, the average stall angle $\overline{\alpha}_{sa}$ for the products was calculated and a graph of the average stall angle as a function of RCMD was constructed using regression fitting (Figure 4).

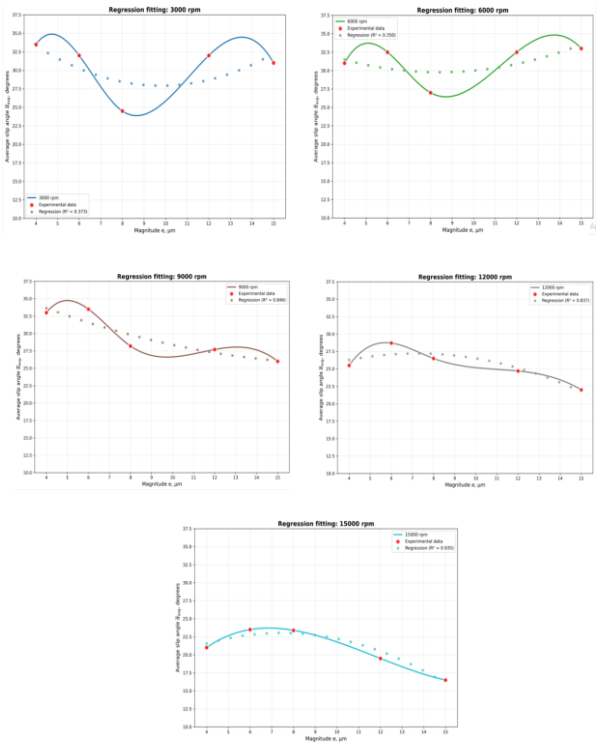

Figure 4 - Dependence of stall angle on RCMD

To evaluate the accuracy of the device measurements, 30 tests were carried out on the product with unbalance e=8 µm at roll rotation speed n_r=9000 rpm. The arithmetic mean was taken as the mathematical expectation of the mean stall angle $\overline{\alpha}_{sa} = 20{,}433^{\circ}$. The point estimate of the standard deviation was [20]:

$$\sigma_{\bar{\alpha}_{sa}} = \sqrt{\frac{1}{n-1}\sum_{i=1}^{30}(\alpha_{sai} - \bar{\alpha}_{sa})^2} = \\ = \sqrt{\frac{41{,}367}{29}} = 1{,}194^{\circ} \quad (12)$$

The value of the point estimate obtained in formula (12) satisfies the requirements of the experiment quite well.

The developed control device has the following design features. The base is made on height-adjustable legs. Support rollers are made of textolite and are mounted with their centre holes on freely rotating balls (one on each side). The support rolls rotate at a constant speed. In the initial position of the frame, the plane of the roll axes is horizontal. The workpiece is placed on the rolls and accelerated to nominal speed. After that the measurement is made: the frame is rotated around the axis and at the moment when the product comes off the rolls the angle of inclination of the planes to the horizon is noted on the angle scale. Then the frame is returned to the initial position to check the next product. The greater the unbalance of the product and therefore the influence of unbalanced forces, the smaller the limiting angle at which the product comes off the rolls. The measured value of the breakaway angle is converted into the value of the product quality parameter according to the calibration chart. Preliminary calibration is carried out using reference products with specified unbalance values.

For testing, real products were selected, whose imbalance was measured on analytical scales and conditionally expressed as the displacement of the center of mass from the geometric axis of the product (e=4; 6; 8; 12; 15 μm). Before taking measurements, the device was adjusted to compensate for the drift of the controlled product along its axis at high roll speeds.

It was found that at speed n_r=9000 rpm, this method of control of products allows sorting them into 2-3 quality groups. One and the same controlled product (for example, with RCMD e=8 μm) behaves differently at different speeds of rotation. The observed deterioration in the rotational stability of the product with e = 8 μm at low speeds (n_R = 9000 rpm) is explained by the influence of shape error (out-of-roundness), which is smoothed out at high speeds, giving way to the influence of imbalance. The mathematical justification for this effect is that imbalance causes inertial force:

$$F = m\omega^2 e \quad (13)$$

where m is the mass of the product, e is the eccentricity, and ω is the angular velocity of rotation of the product. Thus, the product has a significant moment of inertia, which prevents instantaneous changes in the trajectory of the center of mass in response to microdefects on the surface. The experiment clearly shows that in the presence of imbalance, even ideal geometry leads to early failure of the product from the support rolls, and vice versa—at high speeds, imbalance suppresses the influence of minor manufacturing defects.

To date, certain results in measuring microimbalance have been obtained by researchers at Henan University of Science and Technology, who have developed a dynamic imbalance detection system with V-shaped supports. The results are shown in Table 1 below [[21], [22]]:

Table 1 – Parameters of prepared test rollers

Roller name	m (g)	m_0 (g)	e (m)	Length (m)	Diame-ter (m)
Standard	3.091	≈0	≈0	$8*10^{-3}$	$8*10^{-3}$
Unbalan-ced	3.077	$14*10^{-3}$	$3*10^{-3}$	$8*10^{-3}$	$8*10^{-3}$

According to Table 1, the developed device detects a roller imbalance equal to 42 mg*mm.

The results of the experiments obtained by the authors of the article are presented in Table 2:

Table 2 – Parameters test rollers by the authors

Roller name	m (g)	m_0 (g)	e (m)	Length (m)	Diame-ter (m)
Standard	7.098	≈0	≈0	$18*10^{-3}$	$8*10^{-3}$
Unbalan-ced	7.093	$4.52*10^{-3}$	$4*10^{-6}$	$18*10^{-3}$	$8*10^{-3}$

According to the results of experiments conducted on the developed device, the detected imbalance is equal to 18.1 mg*μm.

The sensitivity of this method for determining the stall angle in a separately conducted experiment with sample cylindrical products with given values of unbalance is 4÷6 μm of the conditional displacement of the centre of mass, which agrees well with theoretical calculations.

Conclusions

For experimental verification of the method of quality control of products, a prototype of the device was manufactured. The following main conclusions can be drawn from the testing of the prototype device:

- the method is simple in realisation and according to the above formulas it is possible for engineers and technicians to calculate geometric and kinematic parameters of the drive depending on mass-geometric characteristics of the controlled product;

- increasing values of non-circularity and eccentricity of the product lead to an increase in the time of acceleration of the product to a steady speed when rotating the product on the rolls;

- according to the angle of product breakage from the rotating rolls, it is possible to judge the quality of controlled products and sort them into quality groups;

- the device is recommended for control of fast-rotating small products of metalworking machines, equipment of metallurgical and defence industry.

Conflicts of interest. On behalf of all authors, the corresponding author states that there is no conflict of interest.

CRediT author statement: A**. Atalykova**: Investigation, Writing – Review & Editing, Visualization, Software; **Ye. Yeleukulov**: Validation, Formal analysis, Data curation, Writing – Original Draft; A**. Muslimov**: Conceptualization, Methodology, Supervision.

Acknowledgements. This research did not receive any specific grant from funding agencies in the public, commercial, or not-for-profit sectors.

Cite this article as: Atalykova AK, Yeleukulov YeO, Muslimov AP. Device for automatic control of non-roundness and eccentricity of small rotating parts. Kompleksnoe Ispolzovanie Mineralnogo Syra = Complex Use of Mineral Resources. 2027; 343(4):46-53. https://doi.org/10.31643/2027/6445.39

Ұсақ айналмалы бұйымдардың дөңгелек еместігін және эксцентриситет шамасын бақылауға арналған құрылғы

[1*] Аталыкова А.К., [1] Елеукулов Е.О., [2] Муслимов А.П.

[1] Алматы энергетика және байланыс университеті, Алматы, Қазақстан
[2] Қырғыз мемлекеттік техникалық университеті, Бишкек, Қырғыз Республикасы

Мақала келді: *14 шілде 2025*
Сараптамадан өтті: *25 тамыз 2025*
Қабылданды: *26 ақпан 2026*

ТҮЙІНДЕМЕ

Машина жасау саласында негізгі міндеттердің бірі – өндірілген өнімнің сапасын бақылау. Жоғары айналу жылдамдығымен жұмыс істейтін дәл құрылғыларда, металл өңдеу машиналарда, металлургия және қорғаныс өнеркәсібінің жабдықтарында қолданатын ұсақ бұйымдардың сапасын бақылау ерекше назар аударуды талап етеді. Осы зерттеудің мақсаты салмағы 10г. дейінгі роликтердің дөңгелектігі мен эксцентриситетін бақылауға арналған жаңа құрылғыны әзірлеу болып табылады. Бұл жұмыста 15000 айн/мин жылдамдықпен айналатын тірек роликтерінде радиусы r = 4 мм цилиндрлік бұйымдарды еркін айналдыру әдісін қолданатын құрылғы ұсынылған. Бұл жұмыстың артықшылығы құрылғының геометриялық және кинематикалық параметрлері бақыланатын бұйымдардың масса-геометриялық сипаттамаларына байланысты, e=0 масса центрінің радиалды орын ығысуы болмаған жағдайда анықталды. Тәжірибеге масса центрінің шартты ығысуы e=4; 6; 8; 12; 15 мкм болатын бес бұйымдар қойылды, бұл ығысу сыртқы ортаңғы беттен белгілі бір мөлшерде материалды алып тастау арқылы жасанды түрде жасалған. Материалды алып тастағанға дейін және кейін бұйымның массасы дәл аналитикалық таразыларда анықталды. Әрбір бұйым үшін біліктердің әр айналу жылдамдығында өлшеулер саны n=12 болды. Алынған деректер негізінде бұйымдардың біліктерден ажырау бұрышы есептелді, бұл бақыланатын бұйымдардың сапасын бағалауға мүмкіндік береді: эксцентриситет артқан сайын ажырау бұрышы азаяды. Алайда, төмен айналу жылдамдықтарында эксцентриситеті бар бұйымдар e=8 мкм пішін дәлсіздігіне байланысты тұрақсыз болады, бұл жоғары жылдамдықтарда тегістеліп, эксцентриситеттің әсеріне ұшырайды. Құрылғының өлшеу дәлдігі бұйым үшін e=8 мкм болған жағдайда, $n_б$=9000 айн/мин жылдамдықта жүргізілген өлшеулер негізінде бағаланды.

Түйін сөздер: ұсақ бұйымдар, бұйымдардың дөңгелек еместігі, бақылаудың дәлдігі, эксцентриситет, бақылауға арналған құрылғы.

Аталыкова Альфия Кенесовна	***Авторлар туралы ақпарат:*** *Автоматтандыру және басқару кафедрасының аға оқытушысы, Алматы энергетика және байланыс университеті, Байтурсынұлы көш., 126/1, 050013, Алматы, Қазақстан. Email: a.atalykova@aues.kz; ORCID ID: https://orcid.org/0000-0001-7517-2438*
Елеукулов Ерлан Онланович	*Профессор-практик, Электрондық инженерия кафедрасы, Алматы энергетика және байланыс университеті, Байтурсынұлы көш., 126/1, 050013, Алматы, Қазақстан. Email: e.eleukulov@aues.kz; ORCID ID: https://orcid.org/0000-0001-6866-3941*
Муслимов Аннас Поясович	*Техника ғылымдарының докторы, профессор, Көлік және робототехника институтының Автоматика және мехатроника кафедрасы, Қырғыз мемлекеттік техникалық университет, Ш. Айтматов көш., 66, 720044, Бишкек, Қырғыз Республикасы. Email: map.muslimov@mail.ru; ORCID ID: https://orcid.org/0000-0001-7819-8510*

Устройство для контроля некруглости и эксцентриситета мелких вращающихся изделий

[1*] Аталыкова А.К., [1] Елеукулов Е.О., [2] Муслимов А.П.

[1] Алматинский университет энергетики и связи, Алматы, Казахстан
[2] Кыргызский гостударственный технический университет, Бишкек, Кыргызская Республика

Поступила: *14 июля 2025*
Рецензирование: *25 августа 2025*
Принята в печать: *26 февраля 2026*

АННОТАЦИЯ

В сфере машиностроения одной из ключевых задач является контроль качества изготовляемых изделий. Особое внимание требует контроль качества мелких изделий, применяемых в точных устройствах, металлообрабатывающих станках, оборудовании металлургической и оборонной промышленности, работающих с высокими скоростями вращения. Целью настоящего исследования является разработка нового устройства для контроля некруглости и эксцентриситета роликов массой до 10г. В работе предложено устройство с применением метода свободного вращения цилиндрических изделий радиусом r=4 мм. на опорных валках, вращающихся со скоростью до 15000 об/мин. Преимущество настоящей работы заключается в том, что геометрические и кинематические параметры устройства были определены в зависимости от массо-геометрических характеристик контролируемых изделий при отсутствии радиального смещения центра масс: e=0. На эксперимент были поставлены пять изделий с условным смещением центра масс e=4; 6; 8; 12; 15 мкм, искусственно созданного путем удаления определенного количества материала со средней наружной поверхности. Масса изделия до и после удаления определялась на точных аналитических весах. Количество измерений одного изделия на каждой скорости вращения валков составило n=12. По полученным данным был вычислен средний угол срыва изделий с валков, по которому можно судить о качестве контролируемых изделий: с увеличением эксцентриситета уменьшается угол, при котором происходит срыв изделия с валков. Точность измерений устройства была оценена для случая, когда измерения проводили для изделия с e=8 мкм при $n_в$=9000 об/мин.

Ключевые слова: мелкие изделия, некруглость изделий, точность контроля, эксцентриситет, устройство для контроля.

Аталыкова Альфия Кенесовна	***Информация об авторах:*** *Старший преподаватель, кафедра Автоматизация и управление, Алматинский университет энергетики и связи, ул. Байтурсынова, 126/1, 050013, Алматы, Казахстан. Email: a.atalykova@aues.kz; ORCID ID: https://orcid.org/0000-0001-7517-2438*
Елеукулов Ерлан Онланович	*Профессор-практик, кафедра Электронная инженерия, Алматинский университет энергетики и связи, ул. Байтурсынова, 126/1, 050013, Алматы, Казахстан. Email: e.eleukulov@aues.kz; ORCID ID: https://orcid.org/0000-0001-6866-3941*
Муслимов Аннас Поясович	*Доктор технических наук, профессор, Институт транспорта и робототехники, кафедра Автоматизация и мехатроника, Кыргызский технический университет, ул.Ч. Айтматова, 66, 720044, Бишкек, Кыргызская Республика. Email: map.muslimov@mail.ru; ORCID ID: https://orcid.org/0000-0001-7819-8510*

References

[1] Zhang H, Ma L, Xie F. A method of steel ball surface quality inspection based on flexible arrayed eddy current sensor. Measurement. 2019; 144(7):192–202. https://doi.org/10.1016/j.measurement.2019.05.056

[2] Wang Y, Hadfield M. Failure modes of ceramic rolling elements with surface crack defects. Wear. 2004; 256(1-2):208–219. https://doi.org/10.1016/S0043-1648(03)00409-5

[3] Bhadeshia HKDH. Steels for bearings. Progress in Materials Science. 2012; 57(2):268–435. https://doi.org/10.1016/j.pmatsci.2011.06.002

[4] Pater Z, Tomczak J, Bartnicki J, Lovell MR. Experimental and numerical analysis of helical-wedge rolling process for producing steel balls. International Journal of Machine Tools and Manufacture. 2013; 67:1–7. https://doi.org/10.1016/j.ijmachtools.2012.12.006

[5] Chen Y-J, Deng Y, Pu Y, Tang B, Su Y, Tang J. A real-time surface inspection system for precision steel balls based on machine vision. Measurement Science and Technology. 2016; 27(7):1–9. https://doi.org/10.1088/0957-0233/27/7/074010

[6] Wang L, Snidle RW, Gu L. Rolling contact silicon nitride bearing technology. Wear. 2000; 246(1-2):159–173. https://doi.org/10.1016/S0043-1648(00)00504-4

[7] Kakimoto A. Detection of surface defects on steel ball bearings in production process using a capacitive sensor. Measurement. 1996; 17(1):51–57. https://doi.org/10.1016/0263-2241(96)00007-3

[8] Li G, Zhou Sh, Ma L, Wang Y. Research on dual wavelength coaxial optical fiber sensor for detecting steel ball surface defects. Measurement. 2019; 133:310–319. https://doi.org/10.1016/j.measurement.2018.10.026

[9] Wang Y, Yang Y, Geng Y., Zheng M. Kinematic analysis of detection of steel ball surface defect based on ADAMS. Advanced Materials Research. 2010; 102–104:82–87. https://doi.org/10.4028/www.scientific.net/AMR.102-104.83

[10] Abuazza A, Brabazon D, El-Baradie M.A. Multi-beam fibre-optic laser scanning system for surface defect recognition. Journal of Materials Processing Technology. 2004; 155–156:2065–2070. https://doi.org/10.1016/j.jmatprotec.2004.04.339

[11] Zhang Q, Wu XL, Yang XX, Li HB, Feng H. Failure analysis of steel ball in the brake operating cylinder of heavy launch vehicle. Engineering Failure Analysis. 2016; 60:353-362. https://doi.org/10.1016/j.engfailanal.2015.11.056

[12] Li Y, Wang G, Cui H, Cao Sh, Wang X. Dynamic characteristics and optimization research on PVDF piezoelectric film force censor for steel ball cold heading machine. Isa Transactions. 2019; 94:265-275. https://doi.org/10.1016/j.isatra.2019.04.021

[13] ISO 2014 ISO 3290–1:2014(E) Rolling Bearings – Balls – Part 1: Steel Balls. 2014; 11.

[14] Liu Qing. Detection and classification for surface defects of steel balls based on machine. Vision. 2013; 10:44-48.

[15] Chyla P, Pater Z, Tomczak J. Numerical analysis of a rolling process for producing steel balls using helical rolls. Archives of Metallurgy and Materials. 2016; 61(2):485–492. https://doi.org/10.1515/amm-2016-0085

[16] Yuhang Song, Zhong Wang, Fu Luhua, Jiang Meihua. Defection of surface defect on highly reflective curved surface using reflective fringe pattern. Mechanical Science and Technology for Aerospace Engineering. 2017; 36(8):1250-1254. https://doi.org/10.13433/j.cnki.1003-8728.2017.0817

[17] Peter Gloeckner, Sebald W. A new Method of Calcuating the Attainable Life and Reliability in Aerospace Bearings. European Journal of Engineering and Technology Research. 2020; 5(6):745-750. http://dx.doi.org/10.24018/ejeng.2020.5.6.1977

[18] Lazovic T, Marinkovic A, Atanasovska I, Sedak M, Stojanovic B. From Innovation to Standartization – A Century of Rolling Bearing Life Formula. Machines. 2024; 12(7):444. https://doi.org/10.3390/machines12070444

[19] Atalykova A. Kontrol velichiny disbalansa izdelii metodom vrashcheniia izdeliia na vrashchaiushchikhsia oporakh [Monitor the amount of product unbalance by rotating the product on rotating supports]. Promyshlennost Kazakhstana =Industry of Kazakhstan. 2018; 3(104):65–68. (In Russ.).

[20] Klyuyev VV. Mashinostroyeniye. Entsiklopediya [Mechanical engineering. Encyclopedia]. Moscow: Mechanical engineering. 1996, 464. (In Russ.).

[21] Wang X, Sui X, Xue Y, Li J, Ma W, Liu C. Investigation on measurement for micro unbalance of tiny cylindrical rollers of the high-speed precision rolling bearings. ICMCCE. 2017; 71-74.

[22] Sui X, Liu C, Li J, Xue Y, Yu Y, Cui Y. Laser-based measurement for micro-unbalance of cylindrical rollers of the high-speed precision rolling bearings. Cluster Computing. 2019; 22:9159-9167. https://doi.org/10.1007/s10586-018-2095-1

Crossref
DOI: 10.31643/2027/6445.40
Mining & Mineral Processing

Analysis of fragmentation results from limestone blasting activities at Semen Padang company

Syahida Al Adi Rahmattullah, *Suci Fitria Rahmadhani Z, Rizto Saliazakri, Norfohu Retongga

Mining Engineering, STTIND Padang, Padang City, Indonesia

** Corresponding author email: sucifitria1228@gmail.com*

Received: *January 5, 2026*
Peer-reviewed: *January 29, 2026*
Accepted: *February 27, 2026*

ABSTRACT

Semen Padang is a company engaged in the mining of limestone and silica rock as the main raw materials for cement production. The mining system used is open-pit mining. This study discusses the effect of geometry on rock fragmentation. The purpose of this study is to determine the blasting geometry and identify the causes of limestone block formation at the PT. Semen Padang site. The research focuses on fragmentation because fragmentation is a determining factor in the success of blasting activities. Fragmentation plays an important role in improving the company's targets, and the distribution of fragmentation must be optimal. To control fragmentation, blasting geometry is required as a parameter. Based on the results of the researcher's observations in the field, the size of rock chunks in the company that are larger than 80 cm is around 25%, so it is necessary to re-evaluate the blasting geometry. The purpose of this study is to determine the geometric design that produces the desired fragmentation, which is below 15% on an 80 cm sieve, so that production can be increased and a comparison can be made between the R.L Ash, C.J Konya, and ICI Explosive methods. The method used for the ideal blasting geometry design is the R.L Ash method with supporting theory using the Kuz-Ram theory. After data processing, the ideal geometry was obtained with a load value of 4.32 m, a distance of 5.18 m, stemming of 4.32 m, a blasting hole depth of 12.1 m, a filling column length of 7.78 m, and a blasting hole diameter of 5 inches, with a lump fragmentation percentage of around 15%.

Keywords: blast geometry, fragmentation, R.L Ash, Kuz-Ram, C.J Konya, ICI Explosive.

Information about authors:

Syahida Al-adi Rahmattullah — *Mining Engineering Class of 20, Padang Industrial Technology College, Jl. Hamka No. 121, Parupuak Tabing, Koto Tangah District, Padang City, Indonesia. Email: SyahidaAlhadid@gmail.com*

Suci Fitria Rahmadhani Z — *Mining Engineering Class of 20, Padang Industrial Technology College, Jl. Hamka No. 121, Parupuak Tabing, Koto Tangah District, Padang City, Indonesia. Email: sucifitria1228@gmail.com; ORCID ID: https://orcid.org/0000-0003-0714-3672*

Rizto Saliazikri — *Mining Engineering Class of 20, Padang Industrial Technology College, Jl. Hamka No. 121, Parupuak Tabing, Koto Tangah District, Padang City, Indonesia.*

Nofrohu Rettongga — *Mining Engineering Class of 20, Padang Industrial Technology College, Jl. Hamka No. 121, Parupuak Tabing, Koto Tangah District, Padang City, Indonesia. Email: nofrohu1198@gmail.com*

Introduction

Indonesia is one of the countries blessed with abundant natural resources, particularly as a source of energy and for community needs [1]. Natural resource management in Indonesia is generally managed through the mining sector. One of the mining companies in Indonesia that produces cement raw materials is PT Semen Padang. PT Semen Padang is engaged in limestone mining in the Bukit Karang Putih area, Indarung Village, Padang City, West Sumatra [2]. The limestone mining process is carried out using the blasting method. This is done because the rock layer has a high level of hardness [3].

Blasting is the process of breaking up large volumes of rock using explosives so that the rock mass is easier to excavate and transport [4]. The blasting process aims to break up the rock so that it is easier to excavate and load into transport vehicles, thereby enabling mining operations to run effectively and efficiently [5].

One of the factors that influences the success of blasting is the blasting geometry. The blasting geometry includes burden, spacing, stemming, subdrilling, blast hole depth, charge column length,

blast hole diameter, and bench height. Blasting geometry will affect the size of fragmentation and the success of blasting. Fragmentation in the mining sector is one of the important things that needs to be considered. Fragmentation is a measure that shows each piece of rock resulting from blasting [6].

The level of rock fragmentation is an important indicator in assessing the success of a blasting activity, where material with a uniform size is more desirable than material that contains many large pieces [7]. Fragmentation is a measure that shows each piece of rock resulting from blasting. Fragmentation resulting from blasting is often used as a problem in blasting activities [8]. The larger the fragmentation, the longer it will take to excavate the blasted material. Meanwhile, the better and more uniform the size of the fragmented rock, the easier it will be for the excavator to dig and load the rock. This will have an impact on the effectiveness of mining activities. Large fragmentation is influenced by a reduction in explosives, or it could also be because when charging explosives, in this case Ammonium Nitrate and Fuel Oil (ANFO), they do not enter the blast hole optimally [9].

The results of several blasting operations show that there is still uneven rock fragmentation and boulders larger than 80 cm (estimated to be around 25% of the total amount of rock excavated). The company expects the amount of blasted material larger than 80 cm to be less than 15%. With fragmentation larger than 80 cm, the company may encounter difficulties in the crushing process. The occurrence of such fragmentation risks, which cannot be predicted accurately, will affect the digging time. Therefore, it is necessary to have a fragmentation prediction model using software, one of which is Split Desktop 4.0 software.

The main raw material in cement production is limestone, which has a high level of hardness and therefore cannot be excavated directly by loading equipment such as excavators or power shovels. To break up the relatively hard limestone, drilling and blasting are carried out to ensure that mining operations are carried out effectively and efficiently. Next, the limestone material resulting from the blasting is handled through excavation and loading [10]. The limestone is obtained from the mining process at the Bukit Karang Putih quarry of PT. Semen Padang using the side hill type open pit mining system, which is an open pit mining system applied to mine rocks or industrial mineral deposits located on hillsides or deposits that form hills [11].

Experimental part

The study analyzes the fragmentation that occurs due to blasting activities. The data sources used consist of primary and secondary data. Primary data was obtained through direct measurements in the field and field documentation, including the actual geometry of the blasting, such as burden, spacing, stemming, subdrilling, blast hole depth, fill column length, blast hole diameter, and bench height, as well as documentation of the fragmentation resulting from the blasting. Secondary data is obtained from company archives, such as PT Semen Padang location maps, geological maps, research area condition maps, blasting geometry reports, and geological data on the research area.

Data collection techniques are obtained by conducting direct observations in the field, namely observations of geometry and fragmentation data, as well as literature studies and company documentation. The type of data collected was quantitative, in the form of actual geometric data of the blasting in the field. For data analysis, the fragmentation in the field was processed using Split Desktop 4.0 software. This application was carried out by taking photos of the fragmentation results of the blasting using a 38 cm rubber ball as a reference, then analyzing them using the software. The average fragmentation results from the geometry obtained based on the theories of R.L Ash, C.J Konya, ICI Explosive, and the Kuz-Ram equation can be compared with the fragmentation size obtained in the field using Split Desktop 4.0 software after being processed manually.

Blasting Geometry R.L. Ash

The parameters used in the blasting geometry design use R.L. Ash's theory [12], namely burden (B), spacing (S), blast hole depth (L), subdrilling (J), bench height (H), stemming (T), and number of explosive charges (PC).

Blasting Geometry C.J. Konya

Konya and Walter [13] explain the parameters used in blasting geometry design, namely burden (B), spacing (S), stemming (T), subdrilling (J), blast hole depth (H), bench height (L), amount of explosive charge (PC), and loading density (de).

ICI-Explosive Blasting Geometry

ICI-Explosive blasting geometry design is a way to design blasting geometry through trial and error or the rule of thumb. The parameters calculated are bench height (H), burden (B), spacing (S), subgrade (J), stemming (T), and powder factor (PF).

Kuz-Ram Method

The larger the size of the resulting fragmentation, the longer the time required by the loading equipment to excavate the blasted material, and vice versa. If the resulting fragmentation is smaller, the faster the time required by the loading equipment to excavate the blasted material. The level of rock fragmentation is the level of material breakage as a result of the blasting process. To estimate the average size of rock fragmentation resulting from blasting, the Kuznetsov [14] equation can be used. The Kuz-Ram method pays close attention to the size distribution of rock fragmentation resulting from blasting, whereas the image analysis method does not pay much attention to the size distribution of rock fragmentation, but rather directly to the degree of uniformity of rock fragmentation [15].

Split Desktop 4.0

The Split Desktop 4.0 program can present size distributions in three formats, namely ISO standard, UK standard, and custom standard. In addition, the percentage [16].

Results and Discussion

Blasting is a demolition activity that uses explosives to break up the overburden, thereby facilitating excavation by mechanical equipment [17]. In general, the blasting pattern shows the sequence or sequence of explosions from several blast holes. There are several factors that influence the blasting pattern, including the delay time in blasting activities [18]. The actual blasting geometry in ten blasts was obtained with an average burden (B) of 3.13 m, spacing (S) of 3.17 m, subdrilling (J) of 0.94 m, bench height (L) of 10.1 m, blast hole depth (H) of 11.03 m, stemming (T) of 4 m, powder column (PC) of 7 m, and hole diameter (De) of 5 inches can be seen in Table 1 below.

Limestone is an industrial mineral composed of calcium carbonate (CaCO3) and other elements, including magnesium. One important thing to note in analyzing limestone is the presence of Ca and Mg elements. If the Ca content is high and the Mg content is low, the quality is good. Conversely, if the Ca content is low and the Mg content is high, the quality is poor. High Mg content will interfere with the hardening process, because Mg cannot bind with other elements in cement. Limestone containing more than 50% CaO (by weight) is excellent for use as a building material in the form of cement. Limestone generally originates from the shells of mollusks, foraminifera, coelenterates, and carbonate sediments [19].

Blasting geometry can be defined as the relationship between various types of dimensions used in blasting planning [20]. Stemming that is too deep or long can cause chunks to form because the force generated is not strong enough to destroy the rock. Meanwhile, short stemming can cause small rock fragments and fly rock [21].

Table 1 - Actual Blasting Geometry Data in the Field

No	Date	B (m)	S (m)	J (m)	L (m)	H (m)	T (m)	PC (m)	De (inc)
1	23 Nov 2024	3.2	3	0.96	10.04	11	4	7	5
2	2 Dec 2024	3.2	3.2	0.96	10.34	11.3	4	7	5
3	6 Dec 2024	3	3.2	0.90	9.40	10.3	4	7	5
4	9 Dec 2024	3.2	3.3	0.96	10.04	11	4	7	5
5	10 Dec 2024	3.2	3.3	0.96	10.34	11.3	4	7	5
6	11 Dec 2024	3.1	3.1	0.93	10.17	11.1	4	7	5
7	12 Dec 2024	3	3	0.90	10.40	11.3	4	7	5
8	13 Dec 2024	3	3	0.90	10.10	11	4	7	5
9	16 Dec 2024	3.4	3.6	1.02	9.98	11	4	7	5
10	18 Dec 2024	3	3	0.90	10.10	11	4	7	5
	Total	31.3	31.7	9.39	100.91	110.3	40	70	50
	Mean	3.13	3.17	0.94	10.1	11.03	4	7	5

Figure 1 - Results of Limestone Blasting

Table 2 - Geometric Calculation Results According to R.L Ash

B (m)	S (m)	J (m)	L (m)	H (m)	T (m)	PC (m)	De (inchi)
4.32	5.18	0.86	11.24	12.1	4.32	7.78	5

Table 3 - Geometric Calculation Results According to C.J Konya

B (m)	S (m)	J (m)	L (m)	H (m)	T (m)	PC (m)	De (inchi)
3.51	4.91	1.05	10.2	11.25	2.46	8.79	5

Table 4 - Geometric Calculation Results According to ICI Explosive

B (m)	S (m)	J (m)	L (m)	H (m)	T (m)	PC (m)	De (inchi)
3.81	4.76	1.27	11.43	12.7	3.18	9.52	5

The highest variation in this data occurred on December 16, 2024, when the Burden (3.4 m) and Spacing (3.6 m) values were at their highest compared to other days. Conversely, on December 6, 2024, the hole depth (L) was recorded at its shallowest at 9.40 meters. Overall, the blasting operations in the field showed a high degree of consistency, particularly in terms of hole diameter and fill column, with minor adjustments to the burden and spacing distances depending on the specific daily conditions in the field.

From Table 2 above, the blast geometry design is obtained with a burden (B) of 4.32 m, spacing (S) of 5.18 m, stemming (T) of 4.32 m, subdrilling (J) of 0.86 m, bench height (L) 11.24 m, Blast Hole Depth (H) 12.1 m, Filling Column Length (PC) 7.78 m, Blast Hole Diameter (De) 5 inches.

In the observations to be conducted, there are several blast geometry parameters that determine the fragmentation of the blast results according to [22]. From Table 3 above, the blast geometry design is obtained with a burden (B) of 3.51 m, spacing (S) of 4.91 m, stemming (T) of 2.46 m, subdrilling (J) of 1.05 m, bench height (L) of 10.2 m, blast hole depth (H) of 11.25 m, Filling Column Length (PC) of 8.79 m, and Blast Hole Diameter (De) of 5 inches.

Fragmentation is a general term used to indicate the size of rock fragments resulting from blasting [23]. Blasting fragmentation can be predicted in various ways, one of which is by using the Kuz-ram equation. The Kuznetsov equation is used to determine the average fragmentation size, and the Rosin-Rammler equation is used to determine the percentage of material. From Table 4 above, the designed blasting geometry was obtained with a burden (B) of 3.81 m, spacing (S) of 4.76 m, stemming (T) of 3.18 m, subdrilling (J) of 1.27 m, bench height (L) 11.43 m, Blast Hole Depth (H) 12.7 m, Filling Column Length (PC) 9.52 m, Blast Hole Diameter (De) 5 inches.

Table 5 - Percentage of Actual Geometric Fragmentation Size Using the Kuz-Ram Formula

Size (cm)	*Kuz-Ram*	
	Held back (%)	Pass (%)
10	91	9
20	80	20
30	58	42
40	68	32
50	48	52
60	39	61
70	31	69
80	25	75
90	20	80
100	16	84

Table 6 - Percentage of Fragmentation Size of R.L Ash's Method Using the Kuz-Ram Formula

Size (cm)	*Kuz-Ram*	
	Held back (%)	Pass (%)
10	87	13
20	72	28
30	58	42
40	45	55
50	34	66
60	26	74
70	19	81
80	15	85
90	11	89
100	8	92

Table 7 - Percentage of Fragmentation Size in C.J. Konya's Method Using the Kuz-Ram Formula

Size (cm)	*Kuz-Ram*	
	Held back (%)	Pass (%)
10	81	19
20	60	40
30	42	58
40	29	71
50	20	80
60	13	87
70	8	92
80	5	95
90	3	97
100	2	98

Table 8 - Percentage of Fragmentation Size of ICI Explosive Design Method Using the Kuz-Ram Formula

Size (cm)	*Kuz-Ram*	
	Held back (%)	Pass (%)
10	79	21
20	59	41
30	41	59
40	28	72
50	18	82
60	11	89
70	7	93
80	5	95
90	3	97
100	2	98

Table 9 - Comparison of Actual and Design Geometry

Geometry	B (m)	S (m)	T (m)	J (m)	L (m)	H (m)	PC (m)
Actual	3.13	3.17	0.94	10.1	11.03	4	7
R.L Ash	4.32	5.18	0.86	11.24	12.1	4.32	7.78
C.J Konya	3.51	4.91	1.05	10.2	11.25	2.46	8.79
ICI Explosive	3.81	4.76	1.27	11.43	12.7	3.18	9.52

From the percentage of fragmentation size in Table 5, it was found that 75% of fragments measuring 80 cm passed through the sieve, marked in red, while fragments measuring < 80 cm that passed through the sieve were marked in green.

From the percentage of fragmentation size in Table 6, it was found that 85% of fragments measuring 80 cm passed through the sieve, marked in red, while fragments measuring < 80 cm that passed through the sieve were marked in green. From the percentage of fragmentation size in Table 7, it was found that 95% of fragments measuring 80 cm passed through the sieve, marked in red, while fragments measuring < 80 cm that passed through the sieve were marked in green.

From the percentage of fragmentation size in Table 8, it was found that 95% of fragments measuring 80 cm passed through the sieve, marked in red, while fragments measuring < 80 cm that passed through the sieve were marked in green. After calculating the actual geometry and the design geometry, the following is a comparison of the actual geometry with the design geometry, as shown in Table 9 and Figure 1 below.

From the table above, it can be seen that from a comparison of actual geometric data, R.L Ash, C.J Konya, and ICI Explosive obtained the ideal blasting geometry, namely R.L Ash.

The actual blasting geometry data in the field above was collected during 10 blasts. From November 23 to December 2, there were several days when blasting activities were not carried out due to visits to check the explosives warehouse, so there were no blasting activities on those days. The actual blasting geometry in ten blasts was obtained with an average burden (B) of 3.13 m, spacing (S) of 3.17 m, subdrilling (J) of 0.94 m, bench height (L) of 10.1 m, blast hole depth (H) of 11.03 m, stemming (T) of 4 m, Powder Column (PC) of 7 m, and hole diameter (De) of 5 inches.

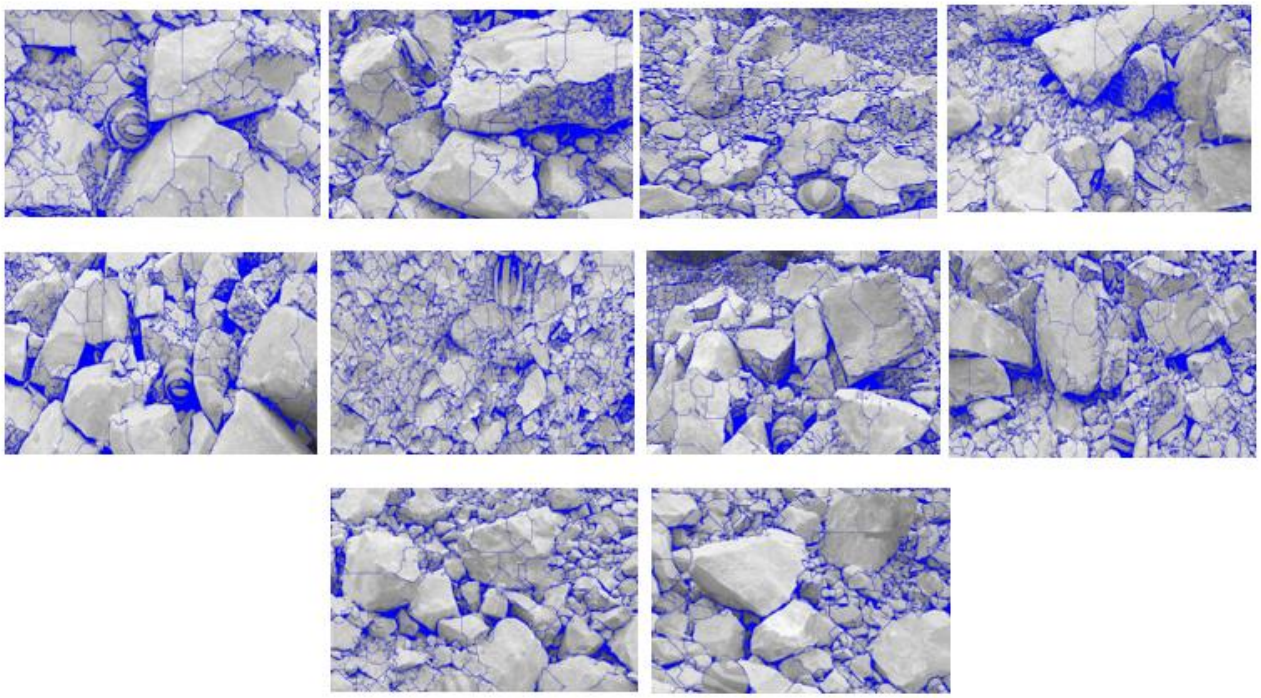

Figure 2 - Actual Fragmentation

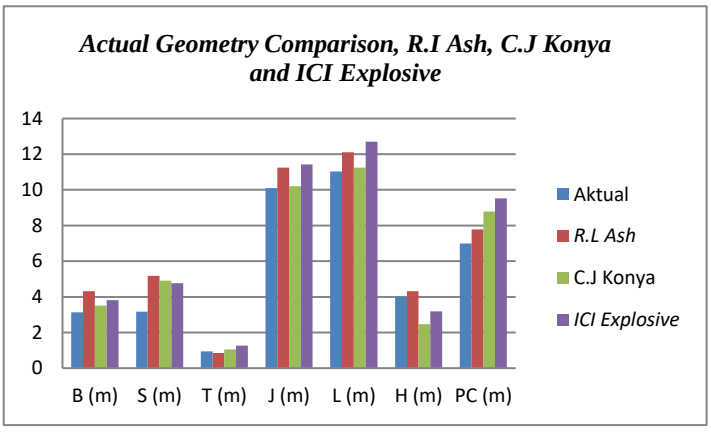

Figure 3 - Comparison Chart of Actual and Design Geometry

Table 10 - Comparison of Actual and Design Geometric Fragmentation Percentages

Size (cm)	Pass rate comparation %			
	Aktual	*R.L Ash*	*C.J Konya*	*ICI.Explosive*
10	9	13	19	21
20	20	28	40	41
30	42	42	58	59
40	32	55	71	72
50	52	66	80	82
60	61	74	87	89
70	69	81	92	93
80	75	85	95	95
90	80	89	97	97
100	84	92	98	98

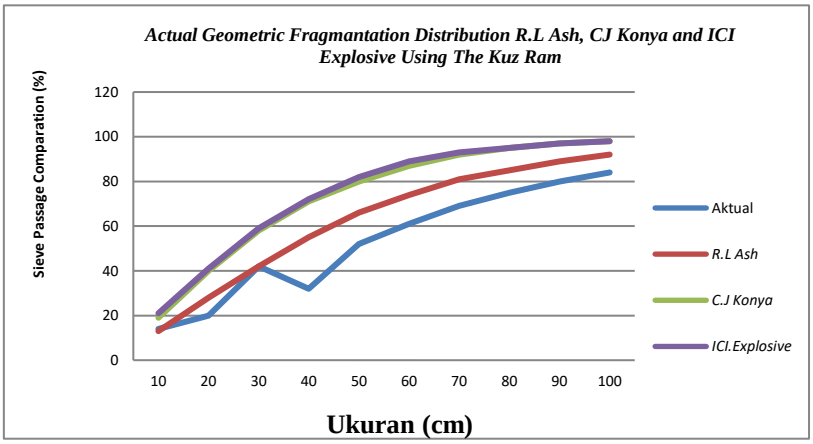

Figure 4 - Actual Geometric Fragmentation Distribution Graph, RL. Ash, C.J Konya, ICI Explosive Using the Kuz-Ram Method

As the blasting geometry increases, the fragmentation results decrease, and as the blasting geometry decreases, the fragmentation results increase. A comparison of the actual fragmentation results with the design processed using the Kuz-Ram method can be seen in Table 10 and Figure 2 below.

From the comparison results above, which passed with a size of < 80 cm, it can be concluded that the geometric design results using R.L Ash's theory are better than the actual geometry.

This can also be seen based on the Powder Factor values, where the Powder Factor value for R.L Ash is 0.44 kg/m3, C.J Konya is 0.76 kg/m3, and ICI Explosive is 0.47 kg/m3. It can be seen that the R.L. Ash method produces a smaller Powder Factor value than C.J. Konya and ICI Explosive, thus supporting the ideal geometric design using the R.L. Ash method as being better than C.J. Konya and ICI Explosive.

Conclusions

The results of the study show that the cause of boulders larger than 80 cm is due to improper blasting geometry, which prevents the company from achieving its targets. The geometry measured or obtained in the field differs from the geometry obtained by the company; it is necessary to evaluate the blasting geometry in order to achieve these targets. The actual blasting geometry of PT. Semen Padang has an average burden value of 3.13 m, spacing of 3.17 m, subdrilling of 0.94 m, bench height of 10.1 m, blast hole depth of 11.03 m, stemming of 4 m, filling column length of 7 m, and blast hole diameter of 5 inches, resulting in boulders > 80 cm amounting to 25%. The results of the actual fragmentation distribution in the field and using the R.L Ash, C.J Konya, and ICI Explosive methods, which use the Kuz-Ram method, each show a fragmentation size of 80 cm that passes through the sieve, namely, actual 75%, RL Ash 85%, C.J Konya 95%, and ICI-Explosive 95%. Based on the Powder Factor value, the R.L Ash method produced a smaller Powder Factor value compared to the C.J Konya and ICI Explosive methods, where the Powder Factor value for R.L Ash was 0.44 kg/m3, C.J Konya was 0.76 kg/m3, and ICI Explosive was 0.47 kg/m3. Using the R.L. Ash blasting geometry, the company's target of having boulders (>80 cm) at <15% can be achieved.

Conflicts of interest. If you agree, you should not delete this statement: On behalf of all authors, the corresponding author states that there is no conflict of interest.

CRediT author statement: **Syahida Al-adi Rahmattullah**: Conceptualization, Methodology, Software, visualization, Investigation; **Suci Fitria Rahmadhani Z:** Data curation, Writing draft preparation, visualization, Investigation; **Rizto Saliazikri:** Supervision. **Nofrohu Rettongga**: Validation.

Acknowledgements. We would like to express our gratitude to PT Semen Padang for permitting us and providing us with research opportunities, as well as to other institutions that have supported this research.

This research was conducted without any funding other than that provided by the researchers themselves. This research did not receive any special grants from funding agencies in the public, commercial, or non-profit sectors.

Cite this article as: Syahida Al Adi Rahmattullah, Suci Fitria Rahmadhani Z, Rizto Saliazakri, Norfohu Retongga. Analysis of fragmentation results from limestone blasting activities at semen padang company. Kompleksnoe Ispolzovanie Mineralnogo Syra = Complex Use of Mineral Resources. 2027; 343(4):54-64. https://doi.org/10.31643/2027/6445.40

Semen Padang кәсіпорнында әктасты өндіру бойынша жарылыс жұмыстары кезіндегі фрагменттеу нәтижелерін талдау

Syahida Al Adi Rahmattullah, *Suci Fitria Rahmadhani Z, Rizto Saliazakri, Norfohu Retongga

Тау-кен инженериясы, STTIND Padang, Падаң, Индонезия

Мақала келді: *5 қаңтар 2026*
Сараптамадан өтті: *29 қаңтар 2026*
Қабылданды: *27 ақпан 2026*

ТҮЙІНДЕМЕ

Semen Padang - цемент өндірісі үшін негізгі шикізат ретінде әктас пен және кварц жыныстарын өндірумен айналысатын компания. Тау-кен өндіру жүйесі ашық тәсілмен пайдаланылады. Бұл зерттеуде геометрияның тау жыныстарының фрагментациясына әсері талқыланады. Осы зерттеудің мақсаты.жарылыс жұмыстарының геометриясын анықтау және PT Semen Padang кен орнында әктасты блоктардың пайда болу себептерін анықтау болып табылады. Зерттеу фрагменттеуге бағытталған, өйткені фрагменттеу жарылыс қызметінің табысты болуының анықтаушы факторы болып табылады. Фрагменттеу компанияның мақсаттарын жақсартуда маңызды рөл атқарады және фрагменттеуді бөлу оңтайлы болуы тиіс. Параметр ретінде фрагменттеуді бақылау үшін құм ағынымен өңдеу геометриясы талап етіледі. Зерттеушінің осы саладағы бақылауларының нәтижелерін негізге ала отырып, компанияда 80 см-ден асатын жыныс кесектерінің көлемі шамамен 25% -ды құрайды, сондықтан жарылыс жұмыстарының геометриясын қайта бағалау қажет. Бұл зерттеудің мақсаты 80 см ұяшық өлшемімен елеуіште 15% -дан кем болатын, ұяшықтың қажетті деңгейін қамтамасыз ететін геометриялық құрылымды анықтау болып табылады, бұл өнімділікті арттыруға R.L Ash, C.J Konya және ICI Explosive әдістерін салыстыруға мүмкіндік береді. Жарылыстың идеалды геометриясын жобалау үшін Куз-Рам теориясын қолдана отырып, Р.Л. Эш әдісі пайдаланылды. Деректерді өңдегеннен кейін, жүктеме мәні 4,32 м, қашықтық 5,18 м, кенжардың ұзындығы 4,32 м, жарылыс ұңғымасының тереңдігі 12,1 м, толтыру бағанасының ұзындығы 7,78 м және жарылыс ұңғымасының диаметрі 5 дюйм, бөлшектеу пайызы шамамен 15% болатын мінсіз геометрия алынды.

Түйін сөздер: жарылыс геометриясы, фрагментация, Р.Л. Эш, Куз-Рам, К.Дж. Конья, ICI жарылғыш заты.

Авторлар туралы ақпарат:

Syahida Al-adi Rahmattullah
20 класс тау-кен инженериясы, Падаң өнеркәсіптік технологиялық колледжі, Jl. Хамка №121, Парупуак Табинг, Кото Танга ауданы, Падаң қаласы, Индонезия. Email: SyahidaAlhadid@gmail.com

Suci Fitria Rahmadhani Z
20 класс тау-кен инженериясы, Падаң өнеркәсіптік технологиялық колледжі, Jl. Хамка №121, Парупуак Табинг, Кото Танга ауданы, Падаң қаласы, Индонезия. Email: sucifitria1228@gmail.com; ORCID ID: https://orcid.org/0000-0003-0714-3672

Rizto Saliazikri
20 класс тау-кен инженериясы, Падаң өнеркәсіптік технологиялық колледжі, Jl. Хамка №121, Парупуак Табинг, Кото Танга ауданы, Падаң қаласы, Индонезия.

Nofrohu Rettongga
20 класс тау-кен инженериясы, Падаң өнеркәсіптік технологиялық колледжі, Jl. Хамка №121, Парупуак Табинг, Кото Танга ауданы, Падаң қаласы, Индонезия. Email: nofrohu1198@gmail.com

Анализ результатов фрагментации при взрывных работах по добыче известняка на предприятии Semen Padang.

Syahida Al Adi Rahmattullah, *Suci Fitria Rahmadhani Z, Rizto Saliazakri, Norfohu Retongga

Горное дело, STTIND Padang, Падаң, Индонезия

Semen Padang –компания, занимается добычей известняка и кварцевой породы в качестве как основного сырья для производства цемента. Горнодобывающая система используется открытым способом. В этом исследовании обсуждается влияние геометрии на фрагментацию пород. Цель данного исследования является определение геометрии взрывных работ и выявление причин образования известняковых блоков на месторождении PT. Semen Padang. Исследование сосредоточено на фрагментации, потому что фрагментация является определяющим фактором успеха взрывной деятельности. Фрагментация играет

Поступила: *5 января 2026*
Рецензирование: *29 января 2026*
Принята в печать: *27 февраля 2026*

важную роль в улучшении целей компании, и распределение фрагментации должно быть оптимальным. Для контроля фрагментации в качестве параметра требуется геометрия пескоструйной обработки. Основываясь на результатах наблюдений исследователя в этой области, размер кусков породы в компании, которые превышают 80 см, составляет около 25%, поэтому необходимо переоценить геометрию взрывных работ. Цель данного исследования является определение геометрической конструкции, обеспечивающую желаемый уровень фрагментации, составляющий менее 15% на сите с размером ячейки 80 см, что позволит увеличить производительность и провести сравнение методов Р.Л. Эша, К.Дж. Конья и ICI Explosive. Для проектирования идеальной геометрии взрыва использовался метод Р.Л. Эша с применением теории Куз-Рама. После обработки данных была получена идеальная геометрия со значением нагрузки 4,32 м, расстоянием 5,18 м, длиной забоя 4,32 м, глубиной взрывной скважины 12,1 м, длиной заполняющей колонны 7,78 м и диаметром взрывной скважины 5 дюймов, с процентом фрагментации куском около 15%.

Ключевые слова: Геометрия взрыва, фрагментация, Р.Л. Эш, Куз-Рам, К.Дж. Конья, ICI Explosive.

Информация об авторах:

Syahida Al-adi Rahmattullah
20-й класс горного дела, Падангский колледж промышленных технологий, Jl. Хамка № 121, Парупуак Табинг, район Кото Танга, город Паданг, Индонезия. Email: SyahidaAlhadid@gmail.com

Suci Fitria Rahmadhani Z
20-й класс горного дела, Падангский колледж промышленных технологий, Jl. Хамка № 121, Парупуак Табинг, район Кото Танга, город Паданг, Индонезия. Email: sucifitria1228@gmail.com; ORCID ID: https://orcid.org/0000-0003-0714-3672

Rizto Saliazikri
20-й класс горного дела, Падангский колледж промышленных технологий, Jl. Хамка № 121, Парупуак Табинг, район Кото Танга, город Паданг, Индонезия.

Nofrohu Rettongga
20-й класс горного дела, Падангский колледж промышленных технологий, Jl. Хамка № 121, Парупуак Табинг, район Кото Танга, город Паданг, Индонезия. Email: nofrohu1198@gmail.com

References

[1] Rachmat A N. Indonesia in the vortex of global energy politics. Indonesian Perspective. 2018; 3(1):66-78.

[2] Fadhila F, Dwinagara B, AMRI NA, & Rauf A. Technical Study of Blasting Geometry to Meet Fragmentation Targets at the Limestone Mining Site of PT Semen Padang. Yogyakarta. 2022; 8(1):36-44.

[3] Aulia MR, Irvani I, & Oktarianty H. Analysis of Distance On Ground Vibration at Around Residential Areas in PT Semen Padang Indarung West Sumatera Province. MINERAL. 2020; 5(1):31-36.

[4] Kramadirata S. Education and Training for Mining Explosives Operators. Bandung: DESM Mineral and Coal Technology Training Center. 2004.

[5] Rinaldo R, Heriyadi B, and Prabowo H. Analysis of the influence of rock geomechanical parameters on blasting activities at the A2 mining front at CV. Triarga Nusatama, Lareh Sago Halaban District, Lima Puluh Kota Regency, West Sumatra. Jurnal Bina Tambang. 2018; 3(3):1163–1173.

[6] Bozic B. Monitoring to Evaluate Blasting Quality and the Prediction of Fragmentation. Int. Engineering Modelling Journal. 2001; 14:61-71.

[7] Oktaviani N. Analysis of the powder factor value of blasting to obtain the target rock fragmentation in the main ridge pit of PT. J Resources Bolaang Mongondow, Bakan Site, North Sulawesi (Bachelor's thesis, Faculty of Science and Technology, Syarif Hidayatullah State Islamic University Jakarta). 2019.

[8] Safarudin S, Purwanto P, & Djamaluddin D. Analysis of the Effect of Blasting Geometry on Fragmentation and Digging Time of Blasting Material. Journal of Engineering Research. 2016; 20(2):54-62.

[9] Bhandari S. Engineering rock blasting operations. Rotterdam: AA Balkema, Mukhlis IT. Technical Study of Blasting Geometry Using the Rl Ash Combine Ved Method to Achieve a Productivity Target of 2000 Tons/Hour for Cat 3060 Bh Excavators in the Pnbp Area at Pt. Semen Padang. University of Jambi. 1997.

[10] Ridho M, and Gusman M. Technical study of the effect of blasting fragmentation at PT. Semen Padang, Bina Tambang Journal. 2019; 4(1):424–434.

[11] Samanlangi AI. Mining Systems. First Edition. Edited by E. Risanto. Yogyakarta: Andi Publishers. 2016.

[12] Ash RL. Design of blasting rounds, in BA Kennedy (ed.) Surface Mining. 2nd Edition. Colorado: Society for Mining, Metallurgy, and Exploration, Inc. 1990, 565–583.

[13] Konya CJ, and Walter EJ. Surface blast design. Prentice Hall. 1990.

[14] Kuznetsov VM. The mean diameter of the fragments formed by blasting rock, Soviet mining science. 1973; 9(2):144–148. https://doi.org/10.1007/BF02506177

[15] Harukadol T, and Kopa R. Evaluation of blasting geometry design to optimize blasting results in andesite mining at PT. Bintang Sumatera Pacific Pangkalan Koto Baru, 50 Kota Regency, West Sumatra Province. Jurnal Bina Tambang. 2021; 6(1):24–36.

[16] Hexagon - Split Engineering. Split Engineering. 2023.

[17] Mukhlis IT. Technical Study of Blasting Geometry Using the Rl Ash Combine Ved Method to Achieve a Productivity Target of 2000 Tons/Hour for Cat 3060 Bh Excavators in the Pnbp Area at Pt. Semen Padang. University of Jambi. 2022.

[18] Hidayatullah, Rachmat, & Salmani. Blasting Techniques. Poliban Press. 2019.

[19] Alfarizi Y, Budiadi E, & Trisnaning PT. Analisis geokimia xrf untuk menentukan kualitas batugamping di bukit tarjarang Pt. semen padang, Indarung, kec. Lubuk Kilagan, Padang, Sumatra Barat. Geoda. 2020; 1(2):19-28.

[20] Prayoga Harris. Prediction of Ground Vibrations Caused by Blasting Activities at the Pt Kaltim Jaya Bara Mine in Berau Regency, East Kalimantan. UIN Syarif Hidayattullah Jakarta. 2020.

[21] Adji AE. Analysis of Blasting Geometry to Obtain Optimal Fragmentation and Digging Time Results at the North Pit Cover of PT. SIS site Adaro (PT. Adaro Indonesia). UIN Syarif Hidayatullah. 2019.

[22] Konya CJ, & Walter EJ. Rock blasting and overbreak control (No. FHWA-HI-92-001; NHI-13211). United States. Federal Highway Administration. 1991.

[23] Dhiyauddin SH. Observation and Analysis Techniques for Andesite Rock Blasting Results at the PT Gunung Mas Jaya Abadi Mine. UIN Syarif Hidayatullah Jakarta. 2022.

Crossref
DOI: 10.31643/2027/6445.41
Mining & Mineral Processing

Reduction of Fluoride in Central Kyzylkum Phosphate Waste in an Acidic Environment: Experimental and Mathematical Study Based on the Langmuir Model

[1]Kurayazov Z., [1*]Ollaberganova A., [2]Jabbarov M., [3]Matnazarov U., [1]Babajanova R.

[1]Urgench State University named after Abu Rayhon Biruni, Uzbekistan
[2]Mamun university, Uzbekistan
[3]Urgench State Pedagogical Institute, Uzbekistan

**Corresponding author email: shamuratovsx@gmail.com*

Received: *December 15, 2025*
Peer-reviewed: *December 25, 2025*
Accepted: *March 3, 2026*

ABSTRACT
Below is a scientific article explaining the results of a comprehensive study on the desorption of fluoride from mineralized waste (MM) of the Central Kyzylkum phosphate deposits in an acidic environment, studied by experiments and mathematical modeling. The interaction between fluorapatite present in MM and acidic wastewater (AWW) was studied in detail. Acidic components in AWW, mainly free fatty acids, promote the decomposition of fluoride in MM through ion exchange mechanisms. Experiments were performed at 333 K with 30 minutes of mixing for different AWW: MM mass ratios from 100:10 to 100:40. The initial pH of the MM samples was close to neutral, while the pH of the AWW was 2.2; therefore, the pH in the mixtures was acidic. Values of q_e (fluoride adsorbed per unit mass) and C_e (equilibrium fluoride concentration) were calculated for each mixture. Using these data, a regression graph was plotted according to the Langmuir adsorption model. A linear equation obtained from the graph gave q_{max} = 7.48 mg/g and K_L = 0.027 L/mg. An R^2 value of 0.93484 obtained from the Langmuir equation showed that the model and experimental results are in good correlation. Fluoride ions in AWW can be converted into HF gas by strong acids and released into the atmosphere. The identification of reaction products allowed them to propose a mechanism of decomposition. Two different streams of industrial wastes, MM and AWW, were combined in the current work, and this combination allowed the development of new technological solutions.

Keywords: Phosphate waste, Central Kyzylkum, fluoride, acidic environment, acidic wastewater, Langmuir model, fluorapatite, mathematical modeling.

Information about authors:

Kurayazov Zaripbay — *Doctor of Philosophy in Technical Sciences, Associate Professor at the Faculty of Chemical Technology, Urgench State University named after Abu Rayhon Beruni, 220100, H. Olimjon Street 14, Urgench, Uzbekistan. Email: zaripboy.q@urdu.uz; ORCID ID: https://orcid.org/0000-0002-9217-0669*

Ollaberganova Aziza — *Doctor of Philosophy in Technical Sciences, Associate Professor at the Faculty of Chemical Technology, Urgench State University named after Abu Rayhon Beruni, 220100, H. Olimjon Street 14, Urgench, Uzbekistan. Email: shamuratovsx@gmail.com*

Jabbarov Majidbek — *Non-government Educational Institution Mamun University, Khiva, Uzbekistan. Email: jabbarovmajidbek2@gmail.com; ORCID ID: https://orcid.org/0009-0001-5987-0057*

Matnazarov Uktam — *Candidate of Pedagogical Sciences in the Faculty of Natural and Applied Sciences, Urgench State Pedagogical Institute, 220100, Gurlan str, 1-A, Urgench city, Uzbekistan. Email: shamuratovsx@gmail.com*

Babajanova Rimajon — *Doctor of Philosophy in Technical Sciences, Associate Professor at the Faculty of Chemical Technology, Urgench State University named after Abu Rayhon Beruni, 220100, H. Olimjon Street 14, Urgench, Uzbekistan. Email: sanjar.sh@urdu.uz*

Introduction

The Central Kyzylkum phosphorite deposits, lying in the southwestern part of the Republic of Uzbekistan, have large amounts of waste layers formed during ore processing in terms of low-grade secondary products. The waste layers have accumulated over a rather long-time span during mining and processing of phosphorus ores using advanced separation technology. The MM left over after ore processing, presently, is deposited in massive open piles in the region surrounding ore-rich sites [[1], [2], [3], [4]]. The leachable constituents of these piles, such as P_2O_5, CaO, F, and others, have suitable reactive chemistry. Of major interest, however, is a high content level of fluoride,

which is a major ecological factor. MM primarily consists of solid-phase substances such as fluorapatite, carbonate apatite, calcium phosphate, and their mixtures. Fluoride is primarily present in MM in $Ca_5(PO_4)_3F$ form. Therefore, in MM, fluoride with a definite physicochemical state promotes conversion of fluoride into an active species under particular circumstances [[5], [6], [7], [8]].

At the same time, oil & fat processing in Uzbekistan is increasing every year, leading to an increased amount of processed raw materials [9]. While processing cottonseed oil, sunflower oil, and soybean oil in the industries, a massive amount of AWW is produced during the saponification and acid-splitting steps [10]. Normally, this wastewater is released into wastewater storage without being neutralized. The oil & fat industry in Uzbekistan processes 1.2 million tons of raw materials each year, which leads to the production of 90,000–100,000 tons of acidic wastewater with a high concentration of hydrogen ions, which normally has a pH level of 2-4 [11]. AWW contains a higher concentration of sulpates, chlorides, cations, and reactive species, which can interact with fluoride ions.

When the AWW interacts with the mineralized mass, a subsequent chemical reaction takes place among the fluoride constituents of MM and the hydrogen ions in AWW, which triggers decomposition. As a result, hydrofluoric acid is formed, which can vaporize in the atmosphere or go into solution in AWW. Physicochemical reactions between MM and AWW have great significance to the environment. In one way or another, fluoride discharge promotes partial detoxification of MM. Yet in another way, fluoride discharge is dangerous in terms of environmental issues. Nevertheless, investigations into fluoride discharge and conditions under which such discharge is optimized have not yet been given priority attention. For instance, short-term interaction of MM with AWW with respect to fluoride discharge and related reductions has not yet been adequately described in the literature [[12], [13]].

It is to be considered that a discussion on the degree of reduction of fluorides and corresponding pH variation in the context of a specific modeling system has to be done [14]. By using modeling, it is possible to define the said experimental outcome using mathematical equations. Regarding this context, the mathematical definition of the reduction of fluorides using the Langmuir adsorption model may be considered to be a credible scientific method to define the said reduction dynamics of fluorides. The mathematical definition of the reduction of fluorides using the Langmuir adsorption model may be effectively used to define surface-active processes, ion exchange, or desorption reactions. Using the said definition, it is possible to predict the said dynamics of reduction of fluorides in the mixture of MM & AWW. Additionally, using the said definition, it is possible to define the boundary levels or steps of a specific chemical reaction. Using the said definition, it would be highly crucial to define safety methods against environmental degradation. Moreover, research work done on the said mixture of MM & AWW may provide a novel definition to define waste treatment methods simultaneously using the concept of reactivity. Regarding this point, it would be possible to define a complete definition to define waste treatment methods in every environment innovatively, even in the industries of Uzbekistan. Hence, the said research work has a degree of immense significance & importance in today's time [[15], [16], [17], [18], [19], [20], [21]].

The current research venture, therefore, presents the first serious scientific answer to the question of fluoride removal from phosphorite waste of Central Kyzylkum phosphates in an acidic environment according to the Langmuir adsorption model. Although other research studies have analyzed options for fluoride removal or its use, there have been very few research studies dealing with fluoride removal in natural conditions related to waste materials and mathematical laws describing these processes. In the research venture, a reactive environment with fluoride removal in an acidic wastewater of an oil & fat industry was used. On the base of research experiments, it was established that there was a direct relationship between fluoride removal and pH change. On the base of the above-stated relationships and according to the model equations of the Langmuir isotherm, limits and constant factors of adsorption can be determined. In contrast to previous models before this research venture, this model presents an innovative application of the kinetic model of the Langmuir isotherm for MM-AWW systems and passes to an innovative target – fluoride removal during desorptions on solid surfaces. In addition to that, it presents very good forecasting for situations of fluoride liberation in liquid and gaseous states in nature. In addition to that, for the crusting of real waste of an industry, this model acquires an additional significance. Therefore, this research venture leads to an innovative research path and an

innovative model in an industry waste treatment process [[22], [23], [24], [25]].

The goal of this research activity is to experimentally and theoretically estimate the degree of fluoride removal from Central Kyzylkum phosphorite waste under acidic conditions. The task of studying the process of fluoride removal in an acidic medium in industrial wastes of water effluents, particularly from oil and fat production, will also be covered. To fulfill this objective, MM and AWW mixes of varying mass ratios shall be developed. This will provide an opportunity to study and estimate the dynamics of fluoride removal. The mathematical model shall be based on the Langmuir adsorption isotherm. The dynamic of fluoride removal corresponding to changes in pH values shall also be studied and calculated. The values of parameters of the Langmuir equation, maximum capacity, and constant of adsorption shall be calculated. The values of boundary conditions and activation periods of reactions shall also be calculated with the help of mathematical equations. Experiments confirm that this process may be described based on models of surface ion exchange and oxidation of an acid. This study shall evidence that there is an opportunity for MM and AWW joint reactivation from an environmental point of view.

Experimental part

In this study, the main experimental materials were MM-a phosphate waste product remaining after beneficiation at the Central Kyzylkum phosphorite deposit, and AWW obtained from the soap production unit of “Urganch yog-moy” JSC.

The MM samples were directly collected from open-pit waste areas in the Central Kyzylkum region and air-dried before use. The chemical composition of the MM was determined as follows: assimilable phosphorus pentoxide (P_2O_5) – 15.09%, total P_2O_5 – 43.17%, CaO – 13.23%, Al_2O_3 – 1.22%, Fe_2O_3 – 1.34%, MgO – 1.21%, F – 1.70%, CO_2 – 14.01%, and SO_3 – 2.17%. Fluorine in the MM mainly exists in the form of fluorapatite, $Ca_5(PO_4)_3F$, which is sensitive to chemical attack under acidic conditions and thus represents a reactive phase [[26], [27], [28], [29], [30], [31]].

The AWW was collected directly from the acidic effluent reservoir of “Urganch Oil and Fat JSC” - the point where it is generated during saponification and acid hydrolysis of cottonseed oil. The composition of AWW was as follows: cations - H^+ (100 mg/L), Na^+ (43,158 mg/L), Ca^{2+} (300 mg/L), Mg^{2+} (1,824 mg/L), NH_4^+ (100 mg/L), Fe^{2+} (30 mg/L), and Fe^{3+} (0.3 mg/L), with a total cation equivalent concentration of 2148.08 mg-eq/L. Among anions, it consisted of Cl^- (38,116 mg/L), SO_4^{2-} (48,145 mg/L), NO_3^- (840 mg/L), and HCO_3^- (3,446 mg/L), while the total anion equivalent also equaled 2148.08 mg-eq/L, indicating an ion balance in the system. The high concentration of H^+ ions (87% eq.) sets a pH range of 2.5 to 4.5 for the wastewater, making it highly acidic and reactive [[6], [12]].

This acidic medium, upon contact with the MM, initiates the desorption, ion exchange, and decomposition processes, especially with regard to the fluorine-containing components. Sulfate and chloride anions in the AWW also increase the chemical activity of free cations as a result of disturbing the ion equilibrium. Both waste products, the MM and AWW, feature high physicochemical reactivity; therefore, special attention is required regarding a detailed analysis of material exchange processes taking place upon their interaction. The objective of this study was, specifically, to investigate fluorine content reduction in the aftermath of such interaction between two real industrial waste streams (Fig. 1).

In addition, the MM sample was dried and reduced to a fine powder before being utilized, whereas for the AWW sample, it was maintained under 277 K conditions throughout the entire period of preservation and was utilized directly without being dried before experimentation. In this study, these two samples were mixed in different suspensions depending on ratios, and observation was based on the Langmuir adsorption model. These samples originated from industrial materials and each had its own properties, making them more relevant and realistic.

The interaction of Central Kyzylkum phosphorite waste (MM) with acidic wastewater (AWW) proceeding from "Urganch yog-moy" JSC was regularly observed during experiments. A volume of 100 mL of AWW in each experiment interacted with a corresponding amount of MM with a proportion of 100:10, 100:20, 100:30, and 100:40. Stirring for 30 minutes at a constant temperature of 333 K allowed carrying out a more thorough analysis concerning ion exchange and F-containing compounds in this system.

The mixtures were then dried in an oven at a temperature of 343 K after the reactions. Using this approach, the pH and fluoride content analysis test was carried out. The different mass ratios of the conditions per group were documented with

averages processed to facilitate comparisons. The critical parameters concerned with the reduction of fluorine content and medium acidity resulting from the interaction between MM and AWW are closely monitored. All experiments have been done under similar conditions of a standard laboratory process involved to ensure similarities in processes. The data collected provided insights necessary for mathematical modeling of processes with use of the Langmuir Adsorption Model.

The pH in the MM–AWW mixtures during experimentation was measured using a high-precision calibrated digital pH meter (±0.01 pH units). The samples, after each 30-minute reaction, were cooled to room temperature, and the pH was measured directly from the solution surface. Quantitative analysis of fluoride ions was performed by the potentiometric method based on the use of ion-selective electrodes. The activity of fluoride ions was stabilized by the addition of the TISAB solution. The measurements were made in the pH range of 5.0-5.5. Three analyses for each mass ratio were carried out, and average values were statistically treated.

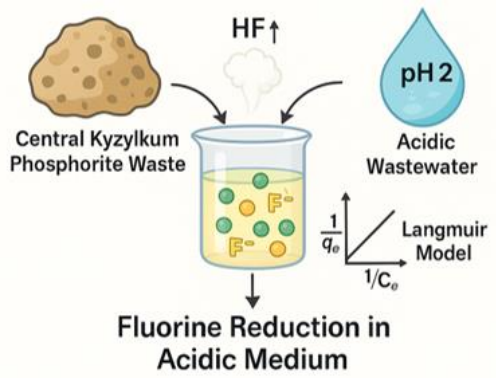

Fig. 1 - Fluorine reduction process in acidic medium from Central Kyzylkum phosphorite waste

With the increase in the values of the MM ratios, the pH levels of the mixture became closer to the neutral point, which indicated the neutralization of the H^+ ions in the acid environment due to the basic nature of the oxides of MM. With this approach, the levels of the fluoride ions increased to a point to be described by the conditions due to the interaction between the fluorapatite in the MM and the H^+ ions present in the solution, which resulted in the desorption of the fluoride ions in the mixture. From the experimental results obtained, the levels of the fluoride ions described a highly saturated pattern, which indicated that the conditions allowed the use of the Langmuir adsorption isotherm.

Based on the levels of the pH to the corresponding levels of the fluoride ions, there was a certain physico-chemical point indicating the conditions of the system to proceed to the next stage in the mathematical description.

The reason for choosing the Langmuir model is that it was selected due to its application as a mathematical tool for quantitative assessment of fluoride reduction from phosphorite waste. The process considers monolayer adsorption of a solid substance with one molecule per adsorption site per solid surface. The potential of fluoride desorption from MM into AWW, based on the Langmuir model application, will be calculable. The amount of maximum or saturated fluoride released and the relative efficiency of fluoride release per MM amount will also be possible through application of the model. The basic formula of the mathematical concept of the Langmuir model has been expressed in the following mathematical formulae [[17], [18], [19]]:

$$F(x) = \frac{F_{max} \cdot K \cdot x}{1 + K \cdot x}$$

Here, *F(x)* represents the amount of fluoride (mg/L) dissolved at a given mass ratio, *x* is the mass ratio of the AWW to MM in the mixture, F_{max} denotes the maximum amount of fluoride that can potentially be desorbed (mg/L), and *K* is the characteristic constant of the sorption process.

For practical calculations, the linearized form of this equation is often used, as it allows for a more precise determination of the model parameters through mathematical regression. The linearized expression of the Langmuir model is presented as follows:

$$\frac{1}{F(x)} = \frac{1}{F_{max}} + \frac{1}{F_{max} \cdot K} \cdot \frac{1}{x}$$

This linear form facilitates plotting $\frac{1}{F(x)}$ against $\frac{1}{x}$, from which the slope and intercept can be used to determine both F_{max} and *K* values accurately. In the corresponding linearized graph, the intercept represents $\frac{1}{F_{max}}$, while the slope corresponds to $\frac{1}{F_{max} \cdot K}$. Given the strong correlation between the experimental data and the Langmuir model, the reduction of fluoride from the MM in the acidic AWW environment was accurately described using this model. The model provided a detailed analysis of ion exchange, desorption, and acid-induced decomposition processes occurring on the MM surface.

The derived model parameters-namely, the maximum fluoride removal capacity *(F_{max})* and the Langmuir constant *(K)*-served as a scientific basis for developing environmentally sound recommendations for the MM–AWW system.

Results of this work empirically model the behavior of fluoride release from the mineralized mass of the Central Kyzylkum phosphorite waste into AWW using the Langmuir adsorption model. Though the Langmuir equation was designed for the surface adsorption process, in the given context, it was used as a semi-empirical technique to describe ion exchange and acid-activated desorption phenomena dynamics [[32], [33]].

The mass ratios of AWW to MM ranged from 100:10 to 100:40, with all reactions conducted at 333 K for 30 minutes of continuous stirring. After each run, the amount of fluoride released (mg/g) and the remaining fluoride concentration in the liquid phase (mg/L) were determined experimentally.

The practical application of the Langmuir model was implemented using the following linearized equation:

$$\frac{1}{q_e} = \frac{1}{q_{max}} + \frac{1}{K_L \cdot q_{max}} \cdot \frac{1}{C_e}$$

Here, q_e is denoted as the quantity of fluoride desorbed per gram of MM (mg/g), C_e is referred to as the concentration of fluoride in AWW at equilibrium (mg/L), q_{max} is termed as the maximum quantity of fluoride possible for desorption (mg/g), K_L is referred to as a constant of the Langmuir model representing the affinity of fluoride for desorption (L/mg).

Graph analysis involved plotting $\frac{1}{q_e}$ on the y-axis and $\frac{1}{C_e}$ on the x-axis. Equations for the trend line were used to establish values for the coefficients of y and x:

$$q_{max} = \frac{1}{\frac{angle\ of\ deflection}{intersection\ point}}; \qquad K_L =$$

Computational approaches were used to examine the sorption parameters quantitatively. Data analysis was conducted using OriginPro 2021 software. Linear regression analysis was obtained from charts, and it showed a good fit with an R^2 of 0.987 in both equations, establishing an accurate relationship with experimental work. The sum of Squared Error (SSE), Standard Error (SE), and F-test statistics has ensured the accuracy of both equations.

Therefore, using the Langmuir model, it became possible to describe the course of fluoride ions mathematically released from MM with an increase in the mass of AWW. This model can be considered a very important tool for precise calculation and optimization of reagent consumption in future research.

Results and Discussion

In this study, the decrease in fluoride content (1.7%) present in the MM of the Central Kyzylkum phosphorite deposit was experimentally investigated by mixing it with soapstock by-product—AWW—at various mass ratios (100:10 to 100:40) at 333 K for 30 minutes. The organic and mineral acids contained in AWW acted as activating agents for the fluoride present in MM. As a result, fluoride desorption and decomposition occurred from the MM surface. For each ratio, the initial fluoride mass, the remaining fluoride content at the end of the experiment (F_t), the amount of fluoride lost (ΔF), and the amount of fluoride lost per gram of MM (q_e) were calculated (Table 1).

Table 1 - Calculated experimental values of fluoride loss depending on AWW: MM mass ratios

AWW:MM	MM (g)	F_o (mg)	F_t (mg)	ΔF (mg)	q_e (mg/g)
100:10	10	170.00	107.00	63.00	6.30
100:15	15	255.00	174.00	81.00	5.40
100:20	20	340.00	253.00	87.00	4.35
100:25	25	425.00	355.00	70.00	2.80
100:30	30	510.00	417.00	93.00	3.10
100:35	35	595.00	491.50	103.50	2.96
100:40	40	680.00	544.00	136.00	3.40

*Note: F_o = 17 mg/g × MM (g); F_t = (Remaining fluoride, %) × MM × 10. For example: 1.07% × 10 g × 10 = 107.00 mg (for the 100:10 ratio case).

Table 2 - Values of q_e and C_e based on the Langmuir model and their linearized forms prepared for regression analysis

AWW:MM	F_t (mg)	C_e (mg/L)	q_e (mg/g)	$1/q_e$	$1/C_e$
100:10	107.00	1070.0	6.30	0.1587	0.000935
100:15	174.00	1160.0	5.40	0.1852	0.000862
100:20	253.00	1265.0	4.35	0.2299	0.000791
100:25	355.00	1420.0	2.80	0.3571	0.000704
100:30	417.00	1390.0	3.10	0.3226	0.000719
100:35	491.50	1404.3	2.96	0.3378	0.000712
100:40	544.00	1360.0	3.40	0.2941	0.000735

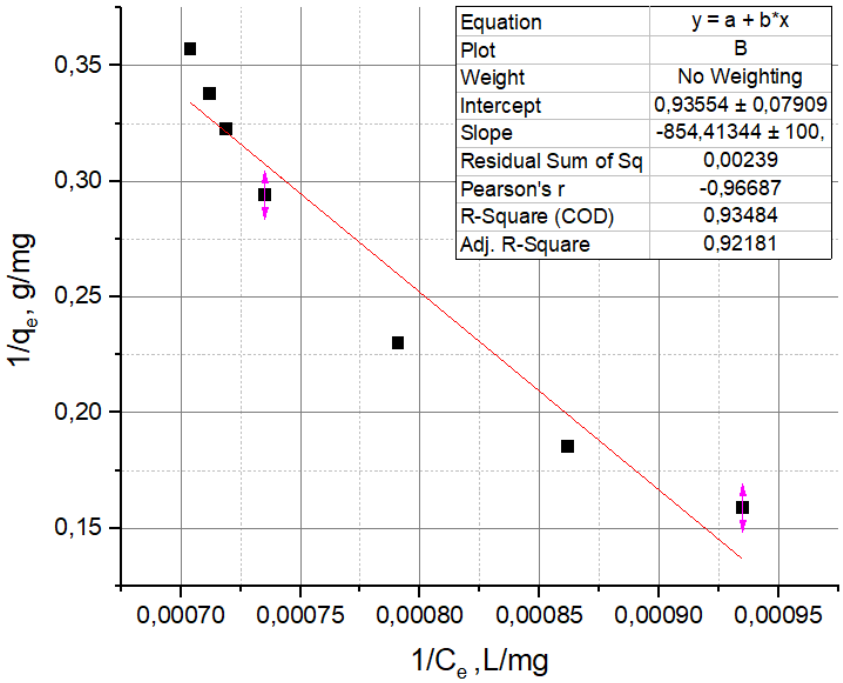

Fig. 2 - Linear regression of fluoride loss based on the Langmuir model

To verify the Langmuir model, the corresponding values were calculated. The results are presented in Table 2 and Figure 2.

As a result of the graphical analysis, the regression equation was derived in linear form, and the main model parameters, q_{max} and b, were determined. The R^2 value obtained was 0.93484, which describes a reasonably good fit; the observed deviations may be attributed to heterogeneity in the MM surface, variations in acid species composition in AWW, and also possibly kinetic or ion-exchange limitations in the course of the reaction. In particular, the presence of silicon, aluminum, and iron oxides in the MM may have formed passive surface zones that hindered fluoride desorption under acidic conditions.

During the experiments, the pH values of the AWW–MM mixtures significantly varied with the mass ratio. The original pH of the AWW was around 2.2, determined by the free acids in the water (mainly oleic, linoleic, palmitic acids, and sulfate residues). When MM was added, neutralization between those acids and basic oxides in the MM (like CaO, MgO, and Al_2O_3) gradually raised the pH. Experimental results can be seen in Table 3.

Table 3 - Variation in solution pH values and fluoride loss per 1 g of MM (q_e) depending on the mass ratios of AWW to MM

AWW:MM	pH	q_e (mg/g)
100:10	4.10	6.30
100:15	4.81	6.09
100:20	5.62	5.83
100:25	5.90	5.35
100:30	6.33	4.80
100:35	6.74	4.25
100:40	7.30	3.97

As shown in Table 3, with an increase in pH, a decrease in fluoride loss per gram of MM (q_e) can be observed. A negative relationship can be established using the graph plotted on q_e-pH co-ordinates, which depicts a non-linear graph. However, it is important to note that a higher fluoride loss occurred in samples with a pH of ≤5.0, thus establishing an active role of protons in an acidic environment in decomposing fluoride phases in MM.

The primary mechanism of this reaction is illustrated in Figure 3:

$$Ca_5(PO_4)_3F + 10H^+ \rightarrow 5Ca^{2+} + 3H_2PO_4^- + HF \uparrow$$

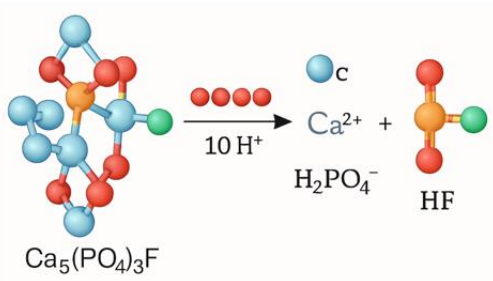

Fig. 3 - Decomposition of $Ca_5(PO_4)_3F$ (fluorapatite) in an acidic environment: mechanism of ion exchange and hydrolysis reaction with fluorine release

When the concentration of H^+ ions is high (i.e., at low pH values), the kinetic activity that promotes the release of fluoride in the form of *HF* into the atmosphere increases. Conversely, at pH values equal to or greater than 6.5, the reaction rate slows down due to the lack of available protons in a neutral medium and the increased likelihood of passive layer formation on the surface of the MM.

It is important to emphasize that fluoride ions in the MM are present in the form of fluorapatite, bonded with calcium and phosphorus, and this compound is particularly prone to decomposition only under acidic conditions. Experimental results demonstrated that the maximum value of equilibrium fluoride loss per gram of MM (q_e = *6.30 mg/g*) occurred at pH 4.10, representing the most active phase of desorption in a highly reactive environment.

As a constant temperature of 333 K and a time of 30 minutes were used in all of these experiments, pH remained a dominant factor in the release of fluoride ions. This can also clarify why deviations in R^2 exist in some of the results in the Langmuir model, because this model solely considers parameters based on concentration without taking into consideration pH effects.

Therefore, the correlation noted between pH and q^b in the experiments is a manifestation of the sensitivity of fluoride ion release to ion exchange, as well as hydrolytic reactions. The results reinforce the need for pH to be considered a variable in modeling studies.

Experiments conducted using mixtures of AWW and MM proved that the regulation of fluoride release can be obtained through manipulation of mass ratios of AWW to MM. Mass ratios were proven to be a very important factor. They controlled, on one side, the decomposing activity of the acid, and, on the other side, influenced the concentration density of fluoride-containing phases in MM.

During this study, AWW: MM ratios were varied from 100:10 to 100:40. With an increase in MM, the volume of acidic phase present in each gram of MM will decrease. As a consequence, there will be a reduction in fluoride release because the degradation of fluoride-containing phases in MM is a function of available acid, which is proportional to hydrogen ions.

As already shown, with the increase in pH from 4.10 to 7.30, a corresponding decrease in q_e from 6.30 mg/g to 3.97 mg/g occurred. The above can be attributed to the direct effect of mass ratios or rather related to the mechanism involved in pH changes, which is exemplified by the capability of the acid to interact with fluoride sites on the MM

Table 4 - Parameters of the Langmuir model and their calculation basis

№	Indicator	Designation	Value	Calculation formula
1	Linear regression slope	*m*	5.03	From the graph (slope)
2	y-intercept (point where a line crosses the y-axis)	*b*	0.1337	From the graph (intercept)
3	Maximum capacity	q_{max}	7.48 mg/g	$q_{max} = \frac{1}{b} = \frac{1}{0.1337}$
4	Langmuir constant	K_L	0.027 L/mg	$K_L = \frac{1}{m \cdot q_{max}}$
5	Modeling compatibility coefficient	R^2	0.93484	From the graph (R^2)

surface. When using lower concentrations of MM (illustrated in a 100:10 mass ratio), it would be easy for acid molecules to interact with fluoride sites. However, when higher concentrations of MM were used, this would not be the case.

Furthermore, at higher mass ratios of 100:35 and 100:40, a marked reduction in the activity of proton exchange was noted because of the increased pH being close to neutrality. The linear fit function in the Langmuir model with an R^2 value of 0.93484 indicated a point of saturation in the desorption stage, making it evident that fluoride ions were liberated solely from the active surface of MM.

Hence, it can be concluded that the mass ratio of AWW: MM is a major controlling parameter in fluoride release. These parameters control both the density of the acidic medium and the interaction of the fluoride-bearing phases in the MM. Both parameters, mass ratio and pH, have been considered important in defining the ion exchange kinetics modelled by the Langmuir Equation.

On the basis of linear regression, a graph of $1/q_e$ vs $1/C_e$ was plotted, which helped in finding the Langmuir parameters. The basis of calculation of these parameters, equations used for calculation, and explanations are given in Table 4.

The work described in this thesis involved an in-depth research study of fluoride removal in phosphorite waste deposited in the Central Kyzylkum area under an acidic environment and concentrated in MM, which accumulated in large quantities, and in AWW produced in the fat and oil industry. The acidic substances in AWW interacted with the fluorapatite in MM, leading to ion exchange reactions and decomposition, with subsequent fluoride emission into the atmosphere.

Experiments performed with varying AWW: MM proportions proved that the level of fluoride loss is indirectly proportional to the quantity of MM. That is, both 100:10 and 100:15 proportions presented higher q_e values. The pH level of the solutions ranged from 2.2 to 4.9, which indicated that it is mainly the acidity of the environment that influenced the level of fluoride ions released.

Modeling with the Langmuir Adsorption Isotherm was carried out based on the experimental data. Graphical analysis provided the parameters: q_{max} = 7.48mg/g, KL=0.027L/mg, and R^2=0.93484. Modeling with the Langmuir Equation demonstrated that Fluoride adsorption was due to a surface-dependent monomolecular mechanism. Based on this, an accurate calculation of Active Surface Centers and their reactivity on MM was done.

The trend in the decrease of q_e with an increase in mass ratio was due to surface saturation. Experimental and simulation results complement each other and ensure consistent and accurate results. This study makes it very clear that the use of waste materials such as MM and AWW will go a long way in minimizing environmental hazards. Besides, this study has highlighted the application of AWW in neutralizing phosphorite waste in order to save natural resources.

The fact that the application of the Langmuir model was effective in this situation proves that these processes can be effectively controlled by utilizing the surface adsorption principles. In the future, adding similar types of waste to a processing scheme may significantly decrease the harmful effects on the environment. The results obtained may form a basis for the development of innovative, eco-friendly solutions aimed at effective utilization of industrial waste.

Conclusion

The work described in this thesis involved an in-depth research study of fluoride removal in phosphorite waste deposited in the Central Kyzylkum area under an acidic environment and concentrated in MM, which accumulated in large

quantities, and in AWW produced in the fat and oil industry. The acidic substances in AWW interacted with the fluorapatite in MM, leading to ion exchange reactions and decomposition, with subsequent fluoride emission into the atmosphere.

Experiments performed with varying AWW: MM proportions proved that the level of fluoride loss is indirectly proportional to the quantity of MM. That is, both 100:10 and 100:15 proportions presented higher q_e values. The pH level of the solutions ranged from 2.2 to 4.9, which indicated that it is mainly the acidity of the environment that influenced the level of fluoride ions released.

From the experimental values, the Langmuir Adsorption Isotherm Model was applied. The values obtained from the graphical analysis for the Isotherm Model were: q_{max}= 7.48mg/g, KL= 0.027L/mg, and R^2= 0.93484. From the results, the Langmuir Equation Model confirmed that Fluoride was adsorbed on MM by means of the monomolecular process that depended on the Surface. For this purpose, the Active Surface Centers were.

The trend of a decrease in q_e with an increase in mass ratio can be attributed to surface saturation. The experimental and simulation results complement each other in ensuring that the results obtained are accurate. One thing this study confirms clearly is that utilizing waste materials such as MM and AWW will make a major contribution to controlling environmental hazards. Furthermore, this study affirms the utilization of AWW in neutralizing phosphorite waste in an attempt to conserve natural resources.

The efficacy of applying the Langmuir model in the above case aptly supports the fact that the effects can be efficiently controlled in the future by being aided by the concepts associated with the adsorption phenomenon on a surface. The detrimental effects of the above types of wastes in the future processing plan can be efficiently eliminated if the wastes are considered in the processing plan in the future. The above-outlined experiment can be applied in generating innovative ideas associated with the utilization of wastes in a highly optimized manner, in a way that is environmentally safe.

Conflicts of interest. On behalf of all authors, the corresponding author states that there is no conflict of interest.

CRediT author statement: **Z. Kurayazov:** Conceptualization, Methodology, Software; **A. Ollaberganova:** Data curation, Writing draft preparation; **M. Jabbarov:** Visualization, Investigation; **U. Matnazarov:** Supervision; **R. Babajanova:** Software, Validation, Reviewing, and Editing.

Formatting of funding sources. This research did not receive any specific grant from funding agencies in the public, commercial, or not-for-profit sectors.

Cite this article as: Kurayazov Z, Ollaberganova A, Jabbarov M, Matnazarov U, Babajanova R. Reduction of Fluoride in Central Kyzylkum Phosphate Waste in an Acidic Environment: Experimental and Mathematical Study Based on the Langmuir Model. Kompleksnoe Ispolzovanie Mineralnogo Syra = Complex Use of Mineral Resources. 2027; 343(4):65-76. https://doi.org/10.31643/2027/6445.41

Орталық Қызылқұм фосфат қалдықтарындағы фтор мөлшерін қышқыл ортада азайту: Ленгмюр моделі негізіндегі эксперименттік және математикалық зерттеу

[1]Құраязов З., [1]Оллаберғанова А., [2]Жаббаров М., [3]Матназаров У., [1]Бабажанова Р.

[1]Абу Райхон Беруни атындағы Ургенч мемлекеттік университеті, Өзбекстан
[2]Мамун университеті, Өзбекстан
[3]Ургенч мемлекеттік педагогикалық институты, Өзбекстан

АННОТАЦИЯ

десорбцияланuын зерттеуге арналған кешенді жұмыстың нәтижелері эксперименттік әдістер мен математикалық модельдеу негізінде баяндалған.

ММ құрамындағы фторапатиттің қышқылды ағынды сулармен (AWW) өзара әрекеттесуі жан-жақты зерттелді. AWW құрамындағы қышқыл компоненттер, негізінен бос май қышқылдары, ион алмасу механизмдері арқылы ММ-дегі фтордың ыдырауына ықпал етеді. Эксперименттер 333 К температурада 30 минут араластыру режимінде, AWW:ММ массалық қатынастары 100:10–100:40 аралығында жүргізілді. ММ үлгілерінің бастапқы pH көрсеткіші

Мақала келді: *15 желтоқсан 2025*
Сараптамадан өтті: *25 желтоқсан 2025*
Қабылданды: *3 наурыз 2026*

бейтарапқа жақын болды, ал AWW-дің pH мәні 2,2 болғандықтан, қоспалардағы орта қышқыл сипатта болды. Әрбір қоспа үшін q_e (масса бірлігіне адсорбцияланған фтор мөлшері) және C_e (фтордың тепе-теңдік концентрациясы) мәндері есептелді. Осы деректер негізінде Ленгмюр адсорбция моделіне сәйкес регрессиялық график тұрғызылды. Графиктен алынған сызықтық теңдеу максимал адсорбциялық сыйымдылықты q_{max} = 7,48 мг/г және Ленгмюр константасын K_L = 0,027 л/мг деп анықтауға мүмкіндік берді. Ленгмюр теңдеуінен алынған R^2 = 0,93484 детерминация коэффициентінің мәні модель мен эксперименттік нәтижелердің жақсы сәйкестігін көрсетеді. AWW құрамындағы фтор иондары күшті қышқылдардың әсерінен газ тәрізді HF-ке айналып, атмосфераға бөлінуі мүмкін. Реакция өнімдерін сәйкестендіру ыдырау механизмін ұсынуға мүмкіндік берді. Осы жұмыста ММ және AWW атты екі түрлі өнеркәсіптік қалдық ағындарын біріктіру жаңа технологиялық шешімдерді әзірлеуге жол ашты.

Түйін сөздер: Фосфат қалдықтары, Орталық Қызылқұм, фторид, қышқылды орта, қышқылды ағынды су, Ленгмюр моделі, фторапатит, математикалық модельдеу.

Авторлар туралы ақпарат:

Құраязов Зарипбай — *Техникалық ғылымдар бойынша философия докторы (PhD), Абу Райхон Беруни атындағы Ургенч мемлекеттік университетінің Химиялық технология факультетінің доценті, 220100, Х. Алимжон көшесі 14, Ургенч, Өзбекстан. Email: zaripboy.q@urdu.uz; ORCID ID: https://orcid.org/0000-0002-9217-0669*

Оллаберғанова Азиза — *Техникалық ғылымдар бойынша философия докторы (PhD), Абу Райхон Беруни атындағы Ургенч мемлекеттік университетінің Химиялық технология факультетінің доценті, 220100, Х. Алимжон көшесі 14, Ургенч, Өзбекстан. Email: shamuratovsx@gmail.com*

Жаббаров Мажидбек — *Мамун жеке білім беру мекемесі, Хива, Өзбекстан. Email: jabbarovmajidbek2@gmail.com; ORCID ID: https://orcid.org/0009-0001-5987-0057*

Матназаров Уктам — *Ургенч мемлекеттік педагогикалық институтының Жаратылыстану және қолданбалы ғылымдар факультетінің педагогика ғылымдарының кандидаты, 220100, Гурлан көшесі 1-А, Ургенч, Өзбекстан.*

Бабажанова Римажон — *Техникалық ғылымдар бойынша философия докторы (PhD), Абу Райхон Беруни атындағы Ургенч мемлекеттік университетінің Химиялық технология факультетінің доценті, 220100, Х. Алимжон көшесі 14, Ургенч, Өзбекстан. Email: sanjar.sh@urdu.uz*

Снижение содержания фтора в фосфатных отходах Центрального Кызылкума в кислой среде: экспериментальное и математическое исследование на основе модели Ленгмюра

[1]Кураязов З., [1]Оллаберганова А., [2]Джаббаров М., [3] Матназаров У., [1]Бабажанова Р.

[1]Ургенчский государственный университет имени Абу Райхона Беруни, Узбекистан
[2]Университет Мамун, Узбекистан
[3]Ургенчский государственный педагогический институт, Узбекистан

Поступила: *15 декабря 2025*
Рецензирование: *25 декабря 2025*
Принята в печать: *3 марта 2026*

АННОТАЦИЯ

В данной научной статье изложены результаты комплексного исследования, посвящённого десорбции фтора из минерализованных отходов (ММ) фосфатных месторождений Центрального Кызылкума в кислой среде, изученной с применением экспериментальных методов и математического моделирования. Взаимодействие фторапатита, содержащегося в ММ, с кислотными сточными водами (AWW) было подробно исследовано. Кислотные компоненты AWW, главным образом свободные жирные кислоты, способствуют разложению фтора в ММ за счёт ионно-обменных механизмов. Эксперименты проводились при температуре 333 K в течение 30 минут перемешивания при различных массовых соотношениях AWW:ММ в диапазоне 100:10–100:40. Начальное значение pH образцов ММ было близким к нейтральному, тогда как pH AWW составлял 2,2, вследствие чего среда в смесях была кислой. Для каждой смеси были рассчитаны значения q_e (количество фтора, адсорбированного на единицу массы) и C_e (равновесная концентрация фтора). На основе полученных данных была построена регрессионная зависимость в соответствии с моделью адсорбции Ленгмюра. Линейное уравнение, полученное из графика, позволило определить максимальную адсорбционную ёмкость q_{max} = 7,48 мг/г и константу Ленгмюра K_L = 0,027 л/мг. Значение коэффициента детерминации R^2 = 0,93484, полученное по уравнению Ленгмюра, свидетельствует о хорошем соответствии модели экспериментальным результатам. Ионы фтора в AWW под действием сильных кислот могут превращаться в газообразный HF и выделяться в атмосферу. Идентификация продуктов реакции позволила предложить механизм разложения. В рамках настоящей работы были объединены два различных потока промышленных отходов — ММ и AWW, что создало предпосылки для разработки новых технологических решений.

	Ключевые слова: Фосфатные отходы, Центральный Кызылкум, фторид, кислотная среда, кислотные сточные воды, модель Ленгмюра, фторапатит, математическое моделирование.
Кураязов Зарипбай	***Информация об авторах:*** *Доктор философии по техническим наукам (PhD), доцент факультета химической технологии Ургенчского государственного университета имени Абу Райхона Беруни, 220100, ул. Х. Алимджана 14, Ургенч, Узбекистан. Email: zaripboy.q@urdu.uz; ORCID ID: https://orcid.org/0000-0002-9217-0669*
Оллаберганова Азиза	*Доктор философии по техническим наукам (PhD), доцент факультета химической технологии Ургенчского государственного университета имени Абу Райхона Беруни, 220100, ул. Х. Алимджана 14, Ургенч, Узбекистан. Email: shamuratovsx@gmail.com*
Джаббаров Маджидбек	*Негосударственное образовательное учреждение Университет Мамун, Хива, Узбекистан. Email: jabbarovmajidbek2@gmail.com; ORCID ID: https://orcid.org/0009-0001-5987-0057*
Матназаров Уктам	*Кандидат педагогических наук факультета естественных и прикладных наук Ургенчского государственного педагогического института, 220100, ул. Гурлан, д. 1-А, Ургенч, Узбекистан.*
Бабажанова Римажон	*Доктор философии по техническим наукам (PhD), доцент факультета химической технологии Ургенчского государственного университета имени Абу Райхона Беруни, 220100, ул. Х. Алимджана 14, Ургенч, Узбекистан. Email: sanjar.sh@urdu.uz*

References

[1] Shamuratov S X, Baltayev U S, Alimov U K, Jabbarov M E, and Madaminov A E. Sigmoid Neutralization Response of Acidic Soapstock Waste by Mineralized Phosphorite Residues: A 4-Parameter Logistic Approach. Kompleksnoe Ispolzovanie Mineralnogo Syra = Complex Use of Mineral Resources. 2027; 342(3):80–89. https://doi.org/10.31643/2027/6445.32

[2] Bekzod Khoshimov, et al. Results of Physical and Chemical Research of Phosphorus Fertilizers and Problems in Certification. JournalNX. 2021; 7(10):96-100. https://doi.org/10.17605/OSF.IO/RZKE3

[3] Temirov U, Doniyarov N, Jurakulov B, Usanbaev N, Tagaev I, & Mamataliyev A. Obtaining complex fertilizers based on low-grade phosphorites. E3S Web of Conferences. 2021; 264. https://doi.org/10.1051/e3sconf/202126404009

[4] Doniyarov NA, Tagaev IA, Muratova MN, & Andriyko LS. New organic-mineral fertilizer based on low-grade phosphorites and microflora of activated sludge. NaAWWystems: Physics, Chemistry, Mathematics. 2021; 19(2):391–405.

[5] Tagaev IA, Doniyarov N A, Andriyko L S, Murodov I N, & Asrorov A A. Acid treatment as a beneficiation method for phosphorite waste of Kyzylkum Phosphorite Plant. Voprosy Khimii i Khimicheskoi Tekhnologii. 2022; 4:75–83. https://doi.org/10.32434/0321-4095-2022-143-4-75-83

[6] Bazhirova K, Zhantasov K, Bazhirov T, Kolesnikov A, Toltebaeva Z, & Bazhirov N. Acid-Free Processing of Phosphorite Ore Fines into Composite Fertilizers Using the Mechanochemical Activation Method. Journal of Composites Science. 2024; 8(5):165. https://doi.org/10.3390/jcs8050165

[7] Paat A, Majak J, Karu V, & Hitch M. Fuzzy analytical hierarchy process based environmental, social and governance risks assessment for the future phosphorite mining in Estonia. Extractive Industries and Society. 2024; 17:101438. https://doi.org/10.1016/j.exis.2024.101438

[8] Muxammatova U, Ruxsora R, Durdona A, Jurabek S, & Temirov U. Production of Complex Fertilizers from Phosphorite Waste of the Central Kyzylkum. Excellencia: International Multi-Disciplinary Journal of Education. 2024; 2(9):569-573.

[9] Shamuratov S, et al. Investigation of the Kinetics of Cotton Soapstock Saponification under Ultrasonic Illumination. Eurasian Chemico-Technological Journal. 2025; 27(4):323–335. https://doi.org/10.18321/ectj1679

[10] Boyjanov N, Radjabov M, Serkayev Q, Boyjanov I, & Yaxshimuradov N. Activation and comparison of indicators of bentonite clay of the Navbakhor deposit. E3S Web of Conferences. 2024; 563:02018. https://doi.org/10.1051/e3sconf/202456302018

[11] Climate Policy Watcher. (n.d.). Impacts on wastewater treatment processes. Climate Policy Watcher. Retrieved August 12, 2025.

[12] Iris Publishers. (n.d.). Agricultural activity and chemical water pollution. Annals of Advanced Agricultural Sciences. Retrieved August 12, 2025. https://irispublishers.com/aahds/fulltext/agricultural-activity-and-chemical-water-pollution.ID.000511.php

[13] Khalid S, Shahid M, Natasha Bibi I, Sarwar T, Shah A H, & Niazi N K. A Review of Environmental Contamination and Health Risk Assessment of Wastewater Use for Crop Irrigation with a Focus on Low and High-Income Countries. International Journal of Environmental Research and Public Health. 2018; 15(5):895. https://doi.org/10.3390/ijerph15050895

[14] Wikipedia. (n.d.). Nutrient pollution. In Wikipedia. Retrieved August 12, 2025. https://en.wikipedia.org/wiki/Nutrient_pollution

[15] Camargo JA. Fluoride toxicity to aquatic organisms: A review. Chemosphere. 2003; 50(3):251–264. https://doi.org/10.1016/S0045-6535(02)00498-8

[16] World Health Organization. Guidelines for drinking-water quality: Fourth edition incorporating the first addendum. Geneva: WHO. 2017. https://www.who.int/publications/i/item/9789241549950

[17] Jha S K, Mishra V K, Sharma D K, & Damodaran T. Fluoride in the environment and its metabolism in humans. In D. M. Whitacre (Ed.), Reviews of Environmental Contamination and Toxicology. 2011; 211:121–142. Springer. https://doi.org/10.1007/978-1-4419-8011-3_4

[18] Fawell J, Bailey K, Chilton J, Dahi E, Fewtrell L, & Magara Y. Fluoride in drinking-water. Geneva: World Health Organization. 2006. https://iris.who.int/handle/10665/43514

[19] Abbas H, Alrubaye S J, Al-Hussainy A F, Saadi B M, Gati M A, Hussein T K, Ilxomovich B N, & Muften N F. Role of carrageenan and health approach for adsorption of Safranin-T dye from aqueous solution by using polymer/CNT surface. Journal of Nanostructures. 2025; 15(4):1839-1848. https://doi.org/10.22052/JNS.2025.04.028

[20] Hussein U A-R, Alalwan D H K, Qabel H A, Abid F M, Hamza H H, Ilxomovich B N, Aljeboree A M, & Alkaim A F. Green synthesis and characterization of guar gum/polyacrylamide/activated carbon hydrogel for efficient methylene blue removal. Journal of Nanostructures. 2025; 15(4):1849-1860. https://doi.org/10.22052/JNS.2025.04.028

[21] Murphy OP, Mayank V, Palanisamy P, & Kumar KV. Adsorption isotherms and design calculations for the optimization of adsorbent mass and contact time. ACS Omega. 2023; 8(20):17407–17430. https://doi.org/10.1021/acsomega.2c08155

[22] Boyjanov NI, Rakhimov UB, Ataullaev ZM, Boltayev MA, Serkayev QP, Khamidova MO. Mathematical analysis of the linear increase in SIO2 content during the activation of Navbakhor alkaline bentonite with hydrochloric acid. Kompleksnoe Ispolzovanie Mineralnogo Syra = Complex Use of Mineral Resources. 2027; 342(3):90-99. https://doi.org/10.31643/2027/6445.33

[23] Ho Y S, & McKay G. Pseudo-second order model for sorption processes. Process Biochemistry. 1999; 34(5):451–465. https://doi.org/10.1016/S0032-9592(98)00112-5

[24] Chu K H, Hashim MA, Zawawi MH, & Bollinger J-C. The Weber–Morris model in water contaminant adsorption: Shattering long-standing misconceptions. Journal of Environmental Chemical Engineering. Elsevier BV. 2025. https://doi.org/10.1016/j.jece.2025.117266

[25] Weber WJ, & Morris JC. Kinetics of Adsorption on Carbon from Solution. Journal of the Sanitary Engineering Division. 1963; 89:31-59.

[26] Shamuratov Sanzharbek, Umid Baltaev, Umarbek Alimov, Namazov Shafoat, Sherzod Kurambaev, and Bazar Ibadullaev. Utilization Process Research of the Soap Industry Acid Waste Water with High Carbonate Phosphorite of Central Kyzylkum. E3S Web of Conferences. EDP Sciences. 2021. https://doi.org/10.1051/e3sconf/202126404079

[27] Shamuratov Sanjarbek, Umid Baltaev, Sanobar Achilova, Umarbek Alimov, Shafoat Namazov, and Najimuddin Usanbaev. Enhancement of Availability of High Calcareous Phosphorite by Neutralization of Acid Effluent and Composting of Cattle Manure. E3S Web of Conferences. EDP Sciences. 2023. https://doi.org/10.1051/e3sconf/202337703004

[28] Shamuratov Sanjarbek, Umid Baltaev, Olga Myachina, Umarbek Alimov, Elyor Atashev, and Tokhir Kuramboev. Agrochemical Efficiency of Slow Release Phosphate Fertilizers Derived on the Base of Phosphorite Activation. E3S Web of Conferences. EDP Sciences. 2023. https://doi.org/10.1051/e3sconf/202343403014

[29] Sotimboev Ilgizarbek, Umidbek Baltaev, Sanjarbek Shamuratov, Ruzimov Shamsiddin, Umarbek Alimov, and Mirzabek Saporboyev. Technical and Economic Efficiency of Processing Acidic Wastewater from the Oil and Fat Industry into Necessary Agricultural Products. E3S Web of Conferences. EDP Sciences. 2024. https://doi.org/10.1051/e3sconf/202456303072

[30] Turatbekova Aidai, Malokhat Abdukadirova, Sanjarbek Shamuratov, Bakhodir Latipov, Mirzabek Saporboyev, Jafar Shamshiyev, and Yusuf Makhmudov. Investigation of the Effect of Fertilizers on the Biochemical and Physical Characteristics of Carrots (Daucus Carota L.). E3S Web of Conferences. EDP Sciences. 2024. https://doi.org/10.1051/e3sconf/202456303074

[31] Yuldasheva A, Shamuratov S, Kurambayev S, & Radjabov M. Mathematical Analysis of CaO Content Variation in Acidic Wastewater and Mineralized Mass Mixture from Central Kyzylkum Phosphorite Based on Exponential Decay Model. Kompleksnoe Ispolzovanie Mineralnogo Syra = Complex Use of Mineral Resources. 2025; 339(4):79–86. https://doi.org/10.31643/2026/6445.42

[32] Atashev E. Decomposition of Magnesite-Sparing Waste in Sulfuric Acid with a High Concentration: Empirical Modeling and Determination of Optimal Conditions. Kompleksnoe Ispolzovanie Mineralnogo Syra = Complex Use of Mineral Resources. 2025; 339(4):71–78. https://doi.org/10.31643/2026/6445.41

[33] Baltayev U, Shamuratov S, Alimov U, Madaminov A, & Jabbarov M. Extraction of P_2O_5 from the mineralized mass of the Central Kyzylkum using acidic wastewater generated from cotton soapstock processing: scientific analysis based on equilibrium principles. Kompleksnoe Ispolzovanie Mineralnogo Syra = Complex Use of Mineral Resources. 2025; 341(2):83–96. https://doi.org/10.31643/2027/6445.20

Crossref
DOI: 10.31643/2027/6445.42
Mining & Mineral Processing

Phosphorus-humus fertilizers based on oxidized licorice meal and phosphate raw materials

[1] Orakbayev A., [2] Jumaewa O., [1] Usanbayev N., [2] Ataew H., [1] Namazov Sh., [1*] Alimov U., [2]Rejepowa M., [3]Shamuratov S.

[1]Institute of General and Inorganic Chemistry, Academy of Sciences of the Republic of Uzbekistan, Tashkent, Uzbekistan
[2]Institute of Chemistry, Academy of Sciences of Turkmenistan, Ashgabat, Turkmenistan
[3]Urgench State University named after Abu Rayhon Biruni, Urgench, Uzbekistan

Corresponding author email: umaralihonalimov@mail.ru

Received: *December 17, 2025*
Peer-reviewed: *January 10, 2026*
Accepted: *March 10, 2026*

ABSTRACT

Humus-containing organic and organo-mineral fertilizers play a key role in increasing soil fertility due to their high water-holding capacity, improved water permeability, and ability to reduce phosphorus fixation by calcium and magnesium ions in calcareous soils and by sesquioxides in acidic soils. Organic matter from livestock waste, peat, and brown coal can enrich fertilizers with humus. However, plant residues such as aspen bark, agricultural husks, and licorice root meal are among the most effective additives to produce organic fertilizers. The present study evaluates the synthesis of phosphorus-humus fertilizers in grain form using indicator phosphate rocks discovered in the Kyzylkum deposit, Turkmenistan, and oxidized licorice paste, treated with hydrogen peroxide and acetic acid. The methodology lab experiment consisted of three steps. In the first step, the oxidation behavior of finely ground licorice meal (particle size < 0.1 mm) was investigated using an aqueous hydrogen peroxide solution and acetic acid at mass ratios relative to the organic fraction of the licorice meal in the range of H_2O_2: CH_3COOH = 100 : (10–20) : (0.1–1). In the second step, the phosphate rock was decomposed by 92% sulfuric acid, requiring 30-80% equivalent amounts for monocalcium phosphate. In the third step, the resulting products were mixed with the oxidized licorice paste at a ratio of 100:10:1. This paper evaluates the optimal conditions for processing the phosphorus-humus fertilizer, also producing flowcharts for processing, such as phosphate, provided by each resource. The efficiency of this new technology is presented. The results suggest that low rock phosphate and waste licorice root are environmentally friendly and can be recommended as an alternate tool to reduce the use of high-consumption chemical fertilizers or time consuming conventional composting process.

Keywords: licorice meal, hydrogen peroxide, phosphorite, extractive substances, sulfuric acid, oxidation.

Information about authors:

Azamat Orakbayev — *Doctor of Philosophy in Technical Sciences, junior researcher of the Institute of General and Inorganic Chemistry of the Academy of Sciences of the Republic of Uzbekistan, 100170, Mirzo Ulugbek St., 77, Tashkent, Uzbekistan. Email: a_orakbayev@mail.ru; ORCID ID: https://orcid.org/0009-0004-4635-4012*

Ogulnur Jumaewa — *Head of laboratory at the Institute of Chemistry of the Turkmen Academy of Sciences, Ashgabat, Turkmenistan. Email: jumayewa.ogulnur@mail.ru; ORCID ID: https://orcid.org/0009-0003-3748-7182*

Najimuddin Usanbayev — *Doctor of Technical Sciences, professor at the Institute of General and Inorganic Chemistry, Academy of Sciences of the Republic of Uzbekistan, 100170, Mirzo Ulugbek St., 77, Tashkent, Uzbekistan. Email: najim70@mail.ru*

Hallymyrat Ataew — *Candidate of Chemical Sciences, Director of the Institute of Chemistry of the Turkmen Academy of Sciences, Ashgabat, Turkmenistan. Email: himiyainstituty.tm@gmail.com; ORCID ID: https://orcid.org/0009-0009-7172-793X*

Shafoat Namazov — *Doctor of Technical Sciences, academition, head of laboratory at the Institute of General and Inorganic Chemistry, Academy of Sciences of the Republic of Uzbekistan, 100170, Mirzo Ulugbek St., 77, Tashkent, Uzbekistan. Email: diana-ye@yandex.com; ORCID ID: https://orcid.org/0000-0002-0040-2048*

Umarbek Alimov — *Doctor of Technical Sciences, professor at the Institute of General and Inorganic Chemistry, Academy of Sciences of the Republic of Uzbekistan, 100170, Mirzo Ulugbek St., 77, Tashkent, Uzbekistan. Email: umaralihonalimov@mail.ru; ORCID ID: https://orcid.org/0000-0001-5608-5304*

Rejepowa Maýa — *Junior researcher of the Chemistry of the Turkmen Academy of Sciences, Ashgabat, Turkmenistan. Email: jumayewa.ogulnur@mail.ru*

Sanjarbek Shamuratov — *Doctor of Philosophy in Technical Sciences, Associate Professor at the Faculty of Chemical Technology, Urgench State University named after Abu Rayhon Biruni, 220100, H. Olimjon Street 14, Urgench, Uzbekistan. Email: shamuratovsx@gmail.com; ORCID ID: https://orcid.org/0000-0002-1040-1807*

Introduction

Worldwide experience in sustainable agriculture development and agro-chemical research proves the efficacy of organic and organo-mineral fertilizer use for maintaining soil fertility and obtaining higher plant yields. Thus, for example, organo-mineral fertilizer application was proven to enhance the efficiency of nitrogen use, soil, and corn yield [1]. Also, the prolonged use of organic manure along with mineral fertilizer increased soil organic carbon, availability of nutrients, and crop yield under the pearl-millet/wheat rotation system [2]. Therefore, the production and usage of such fertilizers from organic materials, phosphate materials, and agricultural ores, providing all essential nutrients for plant development, play an important role in improving agricultural productivity and sustainability.

In worldwide agricultural practices, soil fertility is assessed on the basis of three large categories of indicators: agrophysical, agrochemical, and biological. These components are intricately interlinked and contribute significantly to the ability of the soil to support the growth of plants in the surrounding environment. Agrophysical indicators are used to describe the physical state of the soil and consist of structure, particle size distribution, mineralogical constitution, porosity, air and water-holding capacity, and water permeability. These properties are generally much slower to change and can only be restored to their former state after a significant amount of time and difficult efforts when degraded [3]. The agrochemical component is used to describe the quantity and availability of vital nutrients like nitrogen, phosphorus, potassium, and other macronutrients and micronutrients. This property plays a pivotal role in defining the availability of nutrients for plants and directly affects the productivity of crops and their growth rate [4]. Biological components can be associated with the quantity, quality, and type of soil organic matter and microbial activity, along with the general phytosanitary status of the soil. However, in a large number of cases, the general standard of soil fertility can be attributed to the quality and quantity of the existing organic matter. Organic matter plays a highly significant role in defining the distinct characteristics of the soil, acting as the principal connecting link that defines the general state of soil fertility. Moreover, acting as a reservoir of carbon, nitrogen, phosphorus, potassium, and other nutrients, the role of soil organic matter can help ensure optimal fertility for plant development and can counterbalance the effects of toxic substances present in the surrounding soil and environment [[5], [6]].

Humification and mineralization of residue C in the soil by the microflora result in nutrient release. Data indicate that residue addition augments the concentration of C by 10-12% and that of N by 7-9% compared to fertilizer addition alone [[7], [8]]. Long-term studies indicate that when residue addition is coupled with the addition of mineral nutrients, about 5.5 t of C/ha carbon sequestration is possible in five years [[7], [8], [9]]. Moreover, residue addition to soils and subsequent microbial decomposition have been found to enhance carbon and nutrient cycling [[9], [10]]. It has been found that a meta-analysis of residue addition is effective in augmenting soil organic carbon concentration [[7], [11]]. Thus, organic matter addition to soils through residue addition is essential to maintain soil fertility and nutrient cycles [11].

According to [11], organomineral fertilizers promoted considerable increases in yield. The greatest values in terms of grain, straw, and sheaf weights were recorded with dung-lignin mixture at 60 t/ha, reaching 20.04, 23.60, and 43.89 g/vessel, respectively; this is a significant increase by 65-79% compared with the control. More or less similar yields (44-46 g/vessel) were recorded with semi-rotted manure at 60-80 t/ha and with dung-lignin mixture at 40 t/ha. At higher doses (80 t/ha), dung-lignin mixture and lignin-sludge mixture at 40 t/ha slightly lowered the oat grain yield, while straw and sheaf weight increased by 28-62%; thus, there is a tendency towards vegetative development. A limitation of this method is that the large volumes of fertilizer produced lead to substantial transportation costs.

The use of humic substances (HS) together with mineral fertilizers improves soil agrochemical properties and helps maintain long-term fertility. HS interacts with mineral particles to form stable organomineral complexes that effectively absorb moisture and dissolved nutrients. By binding soil particles, HS promotes the development of a water-resistant, loose, granular structure, which enhances both water infiltration and nutrient retention. As a result, nutrients remain available to plants rather than becoming fixed by soil minerals or lost through leaching [[12], [13]].

Paper [14] presents a method for producing phosphorus organomineral fertilizers with high resistance to nutrient leaching. Aspen bark is impregnated with KH_2PO_4 and converted into $Ca(H_2PO_4)_2$, resulting in a water-resistant product that can also be enriched with microelements. The improved resistance ensures a prolonged fertilizer

effect, and pot experiments confirmed its positive influence on plant growth. The preparation process has multiple stages, and generating effluent is not a term of an environmentally friendly approach.

In [15], phosphorus biocomposite fertilizers were produced by impregnating porous birch bast and bark with aqueous K_2HPO_4. The most effective conditions for reducing phosphate leaching were heating at 100 °C for 2 h, drying at 200 °C, and treating with 0.1 N HNO_3. The resulting materials, containing 3.5–4.0 wt.% P, released only ~35% of their phosphorus over 72 h, demonstrating prolonged nutrient release. Phosphorus loadings above 4 wt.% decreased water resistance. Overall, these birch-based biocomposites showed much higher resistance to leaching than standard granular fertilizers. Low concentration and time-consuming processing restrict the product's application on a wider scale.

Phosphorus has long been a key focus in agricultural chemistry because most soils contain little of it and its low mobility makes it poorly available to plants. At the same time, global reserves of phosphate raw materials are limited, and many are unsuitable for producing water-soluble fertilizers. Ensuring future food security requires more efficient phosphorus use and better understanding of its cycling in soil–plant systems, including the interactions between soil physics, chemistry, biology, and plant traits [[16], [17]].

Phosphate fertilizers are derived from natural phosphate ores—primarily phosphorites (≈85%), while apatite accounts for only about 6% of the estimated 75.1 billion tonnes of global proven reserves. In both ore types, the principal phosphorus-bearing mineral is calcium fluorapatite ($Ca_5(PO_4)_3F$), occurring mainly as fluorapatite and hydroxyapatite. The physical and chemical characteristics of phosphate ores vary depending on their mineral composition and impurity levels. One of the world's richest and most industrially significant apatite–nepheline deposits is located on the Kola Peninsula [[18], [19]].

Ten countries, such as Morocco, the United States, China, Russia, Mexico, Kazakhstan, Peru, South Africa, Western Sahara, and Tunisia, hold around 61,015.4 million tonnes of P_2O_5, or 87% of global phosphate reserves. Significant additional deposits have also been identified on the seabed and continental shelves [20].

The Kyzylkum phosphorite basin covers an estimated 65,000 km². Assuming that only 5% of this area contains industrially significant phosphorite beds, and using an average ore layer thickness of 2.5 m, the predicted geological reserves would amount to approximately 16.25 billion tonnes of phosphorite, or about 1.95 billion tonnes of P_2O_5 (based on an average P_2O_5 content of 12%) [68]. Phosphorite deposits occur in several regions of Uzbekistan, with the Central Kyzylkum area considered the most promising for industrial development. Four deposits have been identified: Jeroy-Sardara, Jetymtau, Tashkurin, and Karakatin. The best-studied is the Jeroy-Sardara deposit, which includes the Jeroy South, Kurukkuduk, and Tashkura sites. Total reserves are estimated at 384.4 million tonnes of ore, containing about 73.9 million tonnes of P_2O_5 [[21], [22]].

The most widely used phosphorus fertilizer globally is simple superphosphate (SSP), which consists primarily of water-soluble calcium dihydrogen phosphate, $Ca(H_2PO_4)_2$. It is produced by treating phosphate rock with sulfuric acid.

$$2Ca_5(PO_4)_3F_{(s)} + 7H_2SO_{4(l)} \rightarrow 3Ca(H_2PO_4)_{2(aq)} + 7CaSO_{4(s)} + 2HF_{(g)} \quad 1$$

However, after application SSP to neutral or calcareous soils, the readily soluble $Ca(H_2PO_4)_2$ is rapidly transformed into less soluble forms such as $CaHPO_4$ and $Ca_3(PO_4)_2$, which gradually supply phosphorus to plants as follows:

$$Ca(H_2PO_4)_{2(aq)}+Ca(HCO_3)_{2(aq)} \rightarrow 2CaHPO_4{\cdot}2H_2O_{(s)}+2CO_{2(g)} \quad 2$$

$$Ca(H_2PO_4)_{2(aq)}+2Ca(HCO_3)_{2(aq)} \rightarrow Ca_3(PO_4)_{2(s)} +4H_2O_{(l)} + 4CO_{2(g)} \quad 3$$

In that case, poorly soluble minerals such as hydroxyapatite or fluorapatite may form in the soil, making phosphorus unavailable for plant uptake [23].

In acidic soils (pH < 5.5), Al^{3+} is released from aluminosilicate minerals (e.g., clay minerals like kaolinite, gibbsite). Ferric iron (Fe^{3+}) released from geotite is the dominant form in well-drained acidic soils. Ferrous iron (Fe^{2+}) occurs in reducing or waterlogged conditions (wüstite, olivine, pyroxene, and troilite) and is more soluble [[24], [25]].

Therefore, in acidic soils rich in sesquioxides such as Al^{3+} and Fe^{2+}/Fe^{3+}, poorly soluble and difficult-to-utilize phosphorus compounds can form, reducing phosphorus availability to plants.

A simplified overall reaction:

$$Ca(H_2PO_4)_{2(aq)} + Al^{3+} \rightarrow 2H^+ + Ca^{2+} + AlPO_4 \downarrow \quad 4$$

$$Ca(H_2PO_4)_{2(aq)} + Fe^{2+} \rightarrow 2H^+ + Ca^{2+} + FeHPO_4 \downarrow \quad 5$$

$Ca(H_2PO_4)_{2(aq)} + Fe^{3+} \rightarrow 2H^+ + Ca^{2+} + FePO_4 \downarrow$ 6

Consequently, the application of phosphate rarely exceeds ~ 10–25 % efficiency, leading to the consumption of water-soluble phosphate fertilizers at rates significantly higher than the actual phosphorus demand [[26], [27]].

The significance and mode of action of organomineral fertilizers in agricultural production have been extensively discussed [[28], [29], [30], [31]]. Humic substances present in these fertilizers enhance the uptake of essential nutrients by plants. They prevent the retrogradation of readily assimilable phosphates, provide microelements and physiologically active compounds, improve soil structure, create favorable conditions for beneficial microorganisms, and ultimately stimulate plant growth and development. Organic and/or organomineral fertilizer raw materials may comprise manure, peat, lignin, sapropel, brown coal, and/or various plant organic materials. Composted agricultural by-products, including olive waste sludge compost, humic-rich organic materials, and/or other stabilized organic by-product materials, are also used extensively, besides being productive additives in the formulation of organomineral fertilizers [[28], [29], [30], [31]].

Naked licorice meal is a potential raw material for the production of humic fertilizers due to its high concentration of biologically active compounds. Licorice refers to a Glycyrrhiza species that is an herbaceous perennial and a legume family member. The licorice leaf is recognized for making medicinal preparations and decompositions, and the licorice hay, which has high protein nutrients, is used as animal feed [[32], [33]]. However, the root is considered the most pharmacologically significant part of the plant. Licorice root contains organic acids (malic, citric, and succinic), β-carotene, a broad spectrum of vitamins, and essential macro- and microelements including potassium, calcium, iron, phosphorus, and magnesium. The principal biologically active constituents are triterpenoid compounds, notably glycyrrhizic acid, along with a diverse group of flavonoids, which may constitute up to 25% of the root's chemical composition.

In Uzbekistan, more than thirty enterprises of various ownership types are involved in the procurement and processing of licorice root, primarily in the Khorezm and Bukhara regions and the Republic of Karakalpakstan. Licorice naturally grows in the Amu Darya and Syr Darya river deltas, where it thrives in tugai forest ecosystems, along irrigation networks, and on saline soils and fallow lands [34].

Turkmenistan is also a significant regional producer. In 2021, the country produced 680 tons of dry licorice extract; the Buýan agro-industrial complex alone generated 680 tons of dry and 610 tons of thick extract from 2,960 tons of purified licorice root. According to 'Turkmenistan: Golden Age,' the enterprise exceeded its production plan by 118.7%. Buýan is located in Turkmenabat and is involved in making licorice-based teas, extracts, balms, and capsules. It has been processing 17,500 tons of licorice root annually as of 2020 and 19,000 tons in 2022. These figures show enhanced processing capacities and their significance for the economy.

It is worth mentioning that after industrial processing of licorice root, a significant amount of licorice meal is obtained, namely, over 80% of raw material, with a yearly output exceeding 100,000 tons in Karakalpakstan alone, which is actually treated as industrial waste. Also, during the process, a liquid ammonium sulphate solution with a concentration of (0.5-1%) of 400,000 tons is obtained, with a significant amount of physiologically active compounds [[35], [36], [37], [38]].

The above-mentioned methods for producing organic and organo-mineral humus and/or humic-containing fertilizers based on composting are time-consuming and limited in their applicability to large-scale agricultural production. Moreover, the use of commercial fertilizers such as mono- and diammonium phosphate and triple superphosphate increases the final product cost. In contrast, the use of an aqueous hydrogen peroxide solution in the presence of acetic acid to accelerate the humification of licorice meal waste, combined with low sulfuric acid consumption for processing low-grade phosphate rock, has both academic and practical significance for applied chemistry and agrochemistry.

It has been found that the available literature provides no effective means to date to utilize the insoluble part of the licorice meal to produce valuable compounds like Humic Acids, Fulvic Acids, or Humic-Like Substances, the role of which is very important in increasing the fertility of the soil. It is important to note that no other similar work has been carried out on the licorice-root meal, the largest solid waste generated in the pharmaceutical industries, for the extraction of glycyrrhizic acid or other biologically active compounds.

Within this framework, the purpose of this study is to find and introduce a new method involving the oxidation of licorice meal by hydrogen peroxide in acetic acid solution and to make use of the resultant

oxidation substance in conjunction with the by-product derived from the decomposition of phosphate raw material with sulfuric acid for phosphorus-humus fertilizer production.

Experimental part

Licorice root meal served as the primary raw material for the study. The material was air-dried and subsequently ground to a particle size of 0.25 mm. Following drying and grinding, a composite representative sample exceeding 10 kg was prepared for analytical characterization and experimental work. Subsamples were collected to determine moisture content, ash content, and the amounts of water-soluble and alkali-soluble extractives.

The extractable organic fraction (EOF) of the initial and oxidized meal was determined using a procedure analogous to the standard method for isolating humic substances. Weighed sample of the meal was placed in a 250-mL flask A. 100 mL of a 1% alkaline sodium hydroxide solution is added, and the mixture is heated for 2 hours in a boiling water bath. After cooling, the contents of Flask A are centrifuged for 15 minutes at 210 $s^{-1,}$ and the supernatant is decanted. The residue was washed twice with 100 mL NaOH; all alkaline extracts were combined and filtered into a 500-mL volumetric flask B and made up to volume.

A 100-mL aliquot of this extract was acidified with 60 mL of HCl to precipitate high-molecular-weight organic acids. The precipitate was centrifuged, washed with water to the onset of peptization, and treated with an additional 5 mL of HCl to ensure complete precipitation. The precipitate was collected on a pre-dried ashless filter and dried to constant mass at 90 ± 5°C. The filter was then transferred to a crucible, ignited at 600 ± 25°C to constant mass, and weighed to determine both organic and ash fractions.

The mass fraction of soluble organic acids (SOA), recalculated to a dry ash-free basis, was calculated as:

$$\mathrm{SOA} = \frac{100 \cdot V(m_1 - m_2)}{V_1 \cdot m} \qquad 7$$

where m_1 and m_2 are the masses of the dried and ashed precipitate of SOA, respectively, g; V is the total extract volume, mL; V_1 is the volume of an aliquot of the alkaline solution taken for SOA precipitation, mL; m is the mass of the meal sample on a dry ash-free basis, g, calculated using the formula:

$$m = m_3 \cdot \frac{100 - (W + A)}{100} \qquad 8$$

where m_3 is the mass of the meal sample, g, W, and A are the moisture and ash contents of the meal.

The organic portion (substance) (OS) of both liquid and solid phases represents the oxidized meal. Its yield was calculated from the organic content of the initial raw meal [[39], [40]].

The total content of phenolic and carboxyl functional groups in high-molecular-weight organic acids isolated from oxidized meal (0–0.25 mm fraction) was determined by alkalimetric titration. A 0.5 g sample was weighed with an accuracy of ±0.0002 g and treated with 50 mL of 0.1 N NaOH. The suspension was kept for 24 h with intermittent shaking, after which the solid phase was separated using paper filtration. An aliquot of the filtrate was transferred to a conical titration flask and titrated with 0.1 N HCl in the presence of phenolphthalein until the disappearance of the crimson color. A blank test (without oxidized meal) was performed under identical conditions.

The total acidity (phenolic + carboxyl groups) in mg-eq/g was calculated using:

$$N_{\mathrm{OH+COOH}} = \frac{(V - V_1)V_3 N_{\mathrm{HCl}}}{G\,V_2} \qquad 9$$

where: V is volume of HCl used for the blank, mL; V_1 is volume of HCl used for the sample of SOA, mL; V_2 is aliquot volume, mL; V_3 is volume of 0.1 N NaOH added to the sample, mL; NHCl is normality of HCl; G is sample mass of SOA, g.

Determination of carboxyl groups was performed analogously. A 0.5 g sample was treated with 0.1 N $NaHCO_3$, kept for 24 h, filtered, and an aliquot was titrated with 0.1 N HCl using methyl orange (yellow → crimson). Carboxyl group content was calculated using the formula above. The concentration of phenolic hydroxyl groups was determined as the difference between total acidity and carboxyl group content.

For the determination of carbonyl groups, a 0.5 g sample was treated with 50 mL of 0.1 N hydroxylamine hydrochloride, mixed, and left for 24 h. After filtration, an aliquot was titrated with 0.1 N NaOH in the presence of phenolphthalein until a stable crimson color appeared. Carbonyl group content was calculated as:

$$N_{\mathrm{C=O}} = \frac{(V - V_1)V_3 N_{\mathrm{NaOH}}}{G\,V_2} \qquad 10$$

where: V is NaOH volume for blank, mL; V_1 is VNaOH volume for used for titration of the solution with SOA, mL; V_2 is aliquot volume, mL; V_3 is volume of 0.1 N hydroxylamine hydrochloride added to the test sample, mL; N_{NaOH} is normality of NaOH; G is sample mass, g.

Phosphorite raw materials from Uzbekistan (Kyzylkum) and Turkmenistan (Durnals) were used in this study. The first sample was phosphate rock from the Kyzylkum deposit (Uzbekistan), characterized by the following chemical composition (%, by mass): P_2O_5 – 17.54; citric-acid-soluble P_2O_5 – 3.15; Trilon-B-soluble P_2O_5 – 3.76; CaO – 47.75; MgO – 1.79; Al_2O_3 – 0.90; Fe_2O_3 – 0.73; F – 1.70; CO_2 – 16.50; SO_3 – 4.06.

The proportion of plant-available phosphorus relative to total P_2O_5 amounted to 17.96% (citric acid) and 21.44% (Trilon-B).

The second raw material was phosphate rock from the Durnals deposit (Turkmenistan), with the following composition (%, by mass): P_2O_5 – 13.73; citric-acid-soluble P_2O_5 – 6.18; Trilon-B-soluble P_2O_5 – 2.96; CaO – 28.21; MgO – 1.10; Al_2O_3 – 1.10; Fe_2O_3 – 9.01; F – 1.08; CO_2 – 1.70; SO_3 – 21.55. Plant-available P_2O_5 relative to total P_2O_5 was 45.04% (citric acid) and 21.58% (Trilon-B or EDTA).

At the initial stage of the study, the oxidation behavior of finely ground licorice meal (particle size <0.1 mm) was investigated using an aqueous hydrogen peroxide solution in the presence of acetic acid. The reagents were applied in the following mass ratios relative to the organic fraction of the licorice meal:

$$H_2O_2: CH_3COOH = 100: (10–20): (0.1–1).$$

The experiments were performed in a cylindrical glass reactor with a thermostatic jacket and equipped with mechanical stirring. The oxidizing solution was first fed into the reactor, the set temperature was reached, and the stirrer was switched on. A weighed amount of the crushed licorice meal was then introduced to start the oxidation process.

After the reaction was complete, the mixture was dried to an air-dry condition. The obtained material was tested for ash content, moisture, organic matter, and extractable substances yield by 1% solution of sodium hydroxide. All analytical procedures were carried out by the methodologies given in references [[39], [40]].

The subsequent stage of the research was devoted to the preparation of phosphorus-humus fertilizers by decomposing phosphate rock of Uzbekistan and Turkmenistan with sulfuric acid. To activate the phosphate raw material, 92% sulfuric acid was used as the decomposing agent, ensuring effective dissolution of the reactive mineral phases and formation of the target phosphate–sulfate mixture suitable for subsequent incorporation with the oxidized licorice meal.

The first stage in producing phosphorus–humus fertilizers consisted of decomposing the phosphate raw material with sulfuric acid to convert the insoluble form of P_2O_5 into plant-available forms. The amount of sulfuric acid was varied and set to 10, 20, 30, 40, and 80% of the stoichiometric requirement for the formation of monocalcium phosphate, according to the following reaction:

$$CaO_{\text{in phosphorite}} + 2H_2SO_{4(aq)} \rightarrow Ca(H_2PO_4)_2 \cdot H_2O_{(s)} \quad 11$$

At a sulfuric acid dosage corresponding to 70% of the stoichiometric requirement, 50.58 g of 92% H_2SO_4 was needed to process 100 g of phosphate rock from the Uzbekistan deposit. In contrast, at 40% of the stoichiometric requirement, 5.84 g of 92% H_2SO_4 was sufficient to treat 100 g of phosphate rock from the Turkmenistan deposit.

The phosphate rock was decomposed with sulfuric acid for 60 min. Upon completion of decomposition, the oxidized licorice meal was introduced into the reaction mixture at a weight ratio of phosphorite: meal (organic portion) = 1: (0.20–1.00). The mixture was then stirred for 30 min and subsequently neutralized with 25% aqueous ammonia to a pH of 4.0–4.5. Drying was performed at 80 °C, and granulation was carried out by the pelleting method during the ammoniation and drying stages.

The chemical composition and mechanical strength of the resulting fertilizer granules were determined. The compressive strength of 2–3 mm granules was measured using an IPG-1M granule strength meter, yielding average values of 2.3–2.7 MPa.

All forms of P_2O_5 were quantified gravimetrically by precipitating phosphate ions with a magnesia mixture as magnesium ammonium phosphate, followed by calcination of the precipitate at 1000–1050 °C, in accordance with GOST 20851.2-75. Nitrogen was determined in accordance with GOST 26715-85. SO_3 was measured by precipitation as barium sulfate, and CaO was determined by titration with 0.05 N Trilon B using flurexon as the indicator.

X-ray diffraction (XRD) analysis was performed using a Shimadzu XRD-6100 diffractometer equipped with a CuKα radiation source (λ = 1.5406 Å), operated at 40 kV and 30 mA. Diffraction patterns were recorded in the 2θ range of 5–70° with a scan speed of 2°/min. Phase identification was conducted using standard domestic reference catalogs and the ASTM Powder Diffraction File (PDF) database [[41], [42], [43]].

Elemental analysis of the licorice meal ash was performed using an Agilent 7900 ICP-MS (Agilent Technologies, USA). Samples were introduced through a micro-mist nebulizer and quartz spray chamber under standard plasma conditions (RF power 1550 W). Helium collision mode (He-CRC) was used to suppress polyatomic interferences for elements such as Fe, Ca, Mg, and Ti. The instrument provides a full mass range (m/z 7–238), allowing accurate determination of all measured elements (Li, Be, B, Na, Mg, Al, P, K, Ca, Cr, Mn, Fe, Co, Ni, Cu, Zn, Mo, Ag, Ba, Ti). Calibration was performed using multi-element standards with Rh and In as internal standards for drift correction.

Results and Discussion

The analytical characteristics of the initial licorice meal are summarized in Table 1.

Table 2 presents the results of the mass spectrometric (ICP-MS) analysis of the ash obtained from licorice meal. The data indicate that licorice meals contain a diverse range of microelements that are essential for plant growth and physiological development.

Under the optimal oxidation conditions, the degree of oxidation of the licorice meal reached 70.94%. The resulting oxidation product consisted of 87.78% organic matter, including 35.88% humic acids, 26.39% fulvic acids, and 29.06% residual unoxidized meal. This wet, dense oxidized mass was subsequently used as the starting material for processing the decomposition products of phosphate raw materials.

The functional groups of the initial licorice meal, the oxidized meal, the residual unoxidized fraction, and the humic acids (HA) isolated from both the original and oxidized material were determined. The analytical results are summarized in Table 3.

Table 1 - Chemical composition of the original licorice root meal

Humidity, %	**Ash content, %**	**Content of extractive substances extracted by 1% NaOH solution, %**	**Content of extractive substances extracted by water, %**	**Insoluble organic matter, %**
5.41	4.66	5.87	15.78	68.28

Table 2 - Results of mass spectrometric analysis of licorice meal ash

Name and content of elements, in g/t									
Li	Be	B	Na	Mg	Al	P	K	Ca	Cr
59	1.80	16	12000	14000	80000	770	21000	65000	55
Mn	Fe	Co	Ni	Cu	Zn	Mo	Ag	Ba	Ti
1200	34000	16	40	75	100	3.30	0.490	440	3600

Table 3 - Active functional groups of the original licorice meal and its oxidation products

Substance	Moisture, %	Ash, %	Functional groups		
			COOH+OH, mg-eq/g	COOH, mg-eq/g	OH, mg-eq/g
Original meal	5.41	4.66	5.75	2.56	3.19
Oxidized meal	4.60	1.18	8.41	3.4	5.01
Humic acids of original meal	2.01	0.69	9.79	5.0	4.79
Humic acids of oxidized meal	3.83	0.63	10.66	5.02	5.64
Residual organic matter of original meal	5.34	6.04	2.53	1.18	1.35
Residual organic matter of oxidized meal	5.11	6.76	2.99	1.18	1.81

As shown in Table 3, oxidation of licorice meal with hydrogen peroxide in the presence of acetic acid significantly increased the content of active functional groups in both the oxidized material and the humic acids derived from it. In the original meal, the carboxyl group content was 2.56 mg-eq/g and the phenolic hydroxyl content was 3.19 mg-eq/g. After oxidation, these values increased to 3.40 mg-eq/g and 5.01 mg-eq/g, respectively. Even more pronounced changes were observed in the humic acids isolated from the oxidized meal, in which the carboxyl and phenolic hydroxyl group contents reached 5.00 mg-eq/g and 4.79 mg-eq/g, respectively. These results confirm that oxidative treatment enhances the reactivity and functional group enrichment of licorice-derived organic matter, improving its potential suitability for producing humic fertilizers.

The analytical results are presented in Tables 4–5.

Table 4 - Composition of phosphorus-humus fertilizers obtained based on oxidized meal with hydrogen peroxide and phosphorite powder from the Kyzylkum deposit in Uzbekistan

Ratio of Phosphorite: meal	P_2O_5 total, %	P_2O_5 accep by 2% citric acid, %	P_2O_5 accep. 0.2 M EDTA%	CaO total, %	$\frac{P_2O_{5accep.}}{P_2O_{5total}}$, %	SO_3 total, %	N total, %	OS, %	ES, %
Stoichiometric consumption of H_2SO_4 requirement for $Ca(H_2PO_4)_2$ formation (40%)									
1 : 0	14.75	5.93	4.40	41.52	40.26	30.34	0.60	0	0
1 : 0.2	13.02	5.67	4.14	37.08	43.58	26.80	0.77	14.35	10.18
1 : 0.4	11.35	5.30	3.87	32.26	46.75	24.11	0.89	25.07	17.78
1 : 0.6	9.68	4.71	3.20	28.67	48.62	21.37	1.10	33.11	23.48
1 : 0.8	8.83	4.46	2.76	25.54	50.53	19.56	1.24	39.31	27.88
1 : 1.0	7.91	4.15	2.38	22.89	52.44	17.32	1.37	44.16	31.32
Stoichiometric consumption of H_2SO_4 requirement for $Ca(H_2PO_4)_2$ formation (50%)									
1 : 0	14.19	7.08	5.87	40.00	49.89	29.88	1.10	0	0
1 : 0,2	12.57	6.57	5.38	35.66	52.27	26.23	1.36	13.90	9.86
1 : 0,4	10.98	6.05	4.96	31.25	55.14	23.75	1.54	24.72	17.53
1 : 0,6	9.33	5.26	4.18	27.53	56.48	20.96	1.66	32.76	23.24
1 : 0,8	8.35	4.83	3.70	24.38	57.87	19.12	1.83	38.91	27.60
1 : 1,0	7.68	4.56	3.21	22.27	59.41	16.80	1.98	43.85	31.10
Stoichiometric consumption of H_2SO_4 requirement for $Ca(H_2PO_4)_2$ formation (60%)									
1 : 0	13.47	8.02	6.34	38.04	59.56	29.37	1.50	0	0
1 : 0.2	11.93	7.33	5.97	33.85	61.44	25.78	1.83	13.38	9.49
1 : 0.4	10.52	6.67	5.23	30.25	63.58	23.04	1.97	24.11	17.03
1 : 0.6	9.05	5.84	4.38	26.20	64.52	20.26	2.12	31.93	22.46
1 : 0.8	7.84	5.13	3.86	23.57	65.49	18.66	2.29	38.44	27.26
1 : 1.0	7.45	4.94	3.35	21.64	66.42	16.39	2.45	43.38	30.77
Stoichiometric consumption of H_2SO_4 requirement for $Ca(H_2PO_4)_2$ formation (70%)									
1 : 0	12.94	8.93	7.41	36.58	69.05	28.77	2.21	0	0
1 : 0.2	11.76	8.31	6.98	31.65	70.66	24.96	2.37	12.92	9.16
1 : 0.4	10.25	7.38	5.85	29.27	72.00	22.45	2.56	23.75	16.59
1 : 0.6	8.77	6.56	4.67	25.62	72.48	19.80	2.72	31.44	21.95
1 : 0.8	7.53	5.49	4.11	22.76	72.93	18.06	2.98	37.91	26.89
1 : 1.0	6.96	5.11	3.72	21.02	73.45	15.93	3.14	42.84	30.39
Stoichiometric consumption of H_2SO_4 requirement for $Ca(H_2PO_4)_2$ formation (80%)									
1 : 0	12.41	10.14	8.56	35.20	78.54	28.12	2.48	0	0
1 : 0.2	11.38	9.06	7.43	30.33	79.61	24.56	2.65	12.43	8.82
1 : 0.4	9.89	8.36	6.27	28.28	80.46	21.87	2.83	23.11	16.39
1 : 0.6	8.33	6.73	5.04	24.57	80.87	19.36	2.99	30.89	21.91
1 : 0.8	7.11	5.78	4.68	22.06	81.34	17.68	3.14	37.21	26.40
1 : 1.0	6.49	6.12	4.11	20.39	81.72	15.56	3.32	41.93	29.74

Table 5 - Composition of phosphorus-humus fertilizers obtained on the basis of oxidized meal with hydrogen peroxide and phosphorite powder from the Durnals deposit in Turkmenistan

Ratio of Phosphorite : meal	P_2O_5 total, %	P_2O_5 accep by 2% citric acid, %	P_2O_5 accep. 0.2 M EDTA%	CaO total, %	$\frac{P_2O_{5accep.}}{P_2O_{5total}}$, %	SO_3 total, %	N total, %	OS, %	ES, %
Stoichiometric consumption of H_2SO_4 requirement for $Ca(H_2PO_4)_2$ formation (10%)									
1 : 0	13.46	6.47	4.39	28.01	48.08	22.88	0.61	0	0
1 : 0.2	11.52	5.77	3.93	22.63	50.13	18.75	0.68	17.93	12.72
1 : 0.4	9.93	5.20	3.64	19.57	52.35	15.62	0.76	28.37	20.12
1 : 0.6	9.25	5.01	3.35	17.11	54.17	13.14	0.87	36.51	25.90
1 : 0.8	8.57	4.84	3.11	15.38	56.53	11.42	0.95	43.15	30.61
1 : 1.0	7.86	4.57	2.88	14.23	58.19	9.79	1.08	47.82	33.92
Stoichiometric consumption of H_2SO_4 requirement for $Ca(H_2PO_4)_2$ formation (20%)									
1 : 0	13.34	6.90	4.85	27.75	51.77	23.91	1.01	0	0
1 : 0.2	11.28	5.99	4.06	22.32	53.18	19.46	1.12	17.36	12.31
1 : 0.4	9.61	5.32	3.69	19.24	55.32	16.28	1.23	27.73	19.67
1 : 0.6	8.42	4.85	3.27	16.85	57.61	13.87	1.31	35.85	25.43
1 : 0.8	7.91	4.73	3.15	14.97	59.83	12.02	1.39	42.32	30.02
1 : 1.0	7.53	4.64	2.97	13.86	61.58	10.45	1.51	47.06	33.38
Stoichiometric consumption of H_2SO_4 requirement for $Ca(H_2PO_4)_2$ formation (30%)									
1 : 0	13.18	7.96	5.15	27.56	60.43	25.17	1.45	0	0
1 : 0.2	11.05	6.92	4.28	22.07	62.66	20.05	1.61	16.68	11.83
1 : 0.4	9.37	6.03	3.91	18.92	64.37	16.92	1.70	27.10	19.22
1 : 0.6	8.22	5.48	3.52	16.51	66.75	14.56	1.82	35.12	24.91
1 : 0.8	7.81	5.35	3.28	14.75	68.51	12.73	1.93	41.77	29.63
1 : 1.0	7.27	5.12	3.11	13.56	70.44	11.15	2.07	46.36	32.89
Stoichiometric consumption of H_2SO_4 requirement for $Ca(H_2PO_4)_2$ formation (40%)									
1 : 0	12.96	9.09	5.27	27.25	70.17	26.04	2.10	0	0
1 : 0.2	10.77	7.83	4.60	21.62	72.68	20.72	2.19	15.87	11.26
1 : 0.4	9.02	6.70	4.22	18.51	74.32	17.64	2.32	26.20	18.64
1 : 0.6	7.84	6.13	3.82	16.12	78.17	15.30	2.40	34.28	24.32
1 : 0.8	7.43	5.93	3.47	14.38	79.83	13.44	2.55	40.85	28.98
1 : 1.0	6.82	5.56	3.20	12.93	81.52	11.88	2.66	45.62	32.36
Stoichiometric consumption of H_2SO_4 requirement for $Ca(H_2PO_4)_2$ formation (50%)									
1 : 0	12.73	10.20	5.69	26.98	80.17	27.04	2.46	0	0
1 : 0.2	10.40	8.56	4.94	21.38	82.35	21.42	2.58	15.16	10.75
1 : 0.4	8.91	7.51	4.47	18.31	84.32	18.34	2.75	25.46	18.41
1 : 0.6	7.76	6.79	3.95	15.94	87.53	15.95	2.84	33.91	23.99
1 : 0.8	6.87	6.12	3.58	14.11	89.07	14.14	2.96	40.01	28.38
1 : 1.0	6.16	5.58	3.21	12.65	90.64	12.68	3.11	44.85	31.82

The results obtained for both types of phosphate raw materials demonstrated similar trends. As the sulfuric acid dosage increased and the proportion of phosphate raw material decreased, the total P_2O_5 content (P_2O_{5total}) of the final product decreased; however, the relative proportion of plant-available phosphorus ($P_2O_{5assimilable}$) increased. This indicates that higher acidification promotes deeper decomposition of the phosphate phase and conversion of P_2O_5 into more soluble forms.

At a meal-to-phosphorite ratio of 1: 0.2 and a sulfuric acid rate of 40% of the stoichiometric requirement for monocalcium phosphate formation, the resulting phosphorus–humus fertilizer contained (wt.%):P_2O_{5total} – 13.02; $P_2O_{5citric\text{-}soluble}$ – 5.67; $P_2O_{5byTrilon\ B\text{-}soluble}$ – 4.14; organic

substance (OS) – 14.35; extractive substance (ES) – 10.18; nitrogen – 0.77; CaO_{total} – 37.08. The relative content of citric-soluble P_2O_5 was 43.58% of P_2O_{5total}.

Increasing the acid dosage to 80% of stoichiometry at the same meal-to-phosphorite ratio resulted in a fertilizer with the following composition (wt.%): P_2O_{5total} – 11.38; $P_2O_{5citric\text{-}soluble}$ – 9.06; $P_2O_{5byTrilon\ B\text{-}soluble}$ – 7.43; OS – 12.43; ES – 8.82; nitrogen – 2.65; CaO_{total} – 30.33. The relative content of P_2O_5 available to plants, determined using citric acid, is 79.61, indicating that the relative available form of phosphorus increases by approximately 2-fold.

Based on the data presented in Tables 4 and 5, it can be observed that the presence of humic acids in the oxidized meal increases the relative content of plant-available P_2O_5 by 1.5–10% compared with phosphate rock digestion carried out in the absence of oxidized organic matter. Unlike previous studies, the present research clearly demonstrates that humic substances significantly enhance the relative availability of phosphorus in the resulting products, which in turn enables a reduction in sulfuric acid consumption and decreases the amount of phosphogypsum waste generated per ton of finished fertilizer.

From the data in Table 4, it can be seen that with an increase in the amount of oxidized meal, plant-available phosphorus increases. When the phosphorus to meal ratio is 1 : 0 and with 40% stoichiometric dosage of sulfuric acid for monocalcium phosphate, the content of P_2O_5 in digestible form increases to 40.26%. When the phosphorus-to-meal ratio is altered to 1:1 with continued use of 40% stoichiometric dosage of sulfuric acid, this content increases to 52.44%, solidifying the fact that oxidized organic matter has a positive influence on phosphorus solubilization.

Similar observations were also realized when phosphate rock from the Turkmenistan Deposit was used (Table 5). For example, at a meal-to-phosphorite ratio of 1: 0.4 and a sulfuric acid rate of 10% of stoichiometry, the resulting humic superphosphate exhibited the following composition (wt.%): P_2O_{5total} – 9.93; $P_2O_{5citric\text{-}soluble}$ – 5.20; $P_2O_{5\ byTrilon\ B\text{-}soluble}$ – 3.64; OS – 28.37; ES – 20.12; nitrogen – 0.76; CaO_{total} – 19.57.

Under these conditions, the relative proportion of citric-soluble P_2O_5 reached 52.35%.

Increasing the sulfuric acid dosage to 50% of stoichiometry at the same meal-to-phosphorite ratio yielded a product with the following composition (wt.%):

P_2O_{5total} – 8.91; $P_2O_{5citric\text{-}soluble}$ – 7.51; $P_2O_{5\ byTrilon\ B\text{-}soluble}$ – 4.47; OS – 25.46; ES – 18.41; nitrogen – 2.75; CaOtotal – 18.31.

The relative content of citric-soluble P_2O_5 increased sharply to 84.32%, demonstrating a substantial improvement in phosphorus availability at higher degrees of phosphate decomposition.

These results collectively confirm that both the oxidized organic component and the acid decomposition level are key factors governing the formation of readily assimilable phosphorus forms in phosphorus–humus fertilizers.

Figures 1–4 present the X-ray diffraction (XRD) patterns of the initial phosphate raw materials from the Central Kyzylkum Desert (Uzbekistan) and Turkmenistan, along with the diffraction profiles of the phosphorus–humus fertilizers produced at a phosphorite-to-meal ratio of 1: 1 and a sulfuric acid dosage of 50% of the stoichiometric requirement for monocalcium phosphate formation. The comparative XRD analysis enables identification of phase transformations occurring during acid decomposition and subsequent interaction with oxidized organic matter.

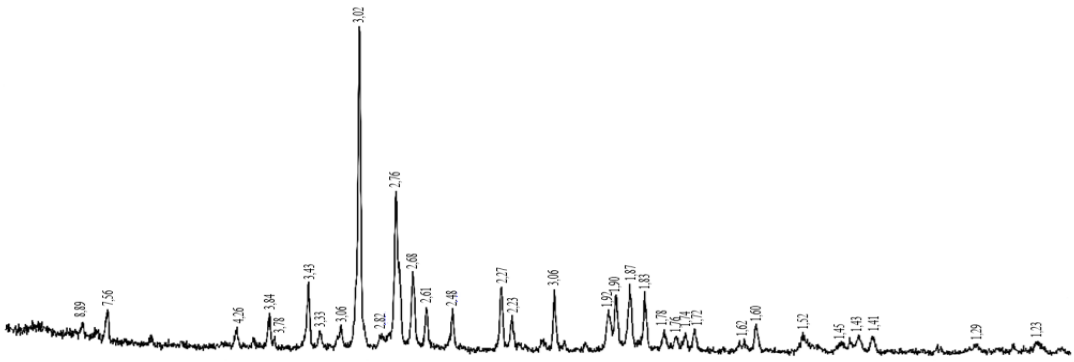

Figure 1 - XRD of phosphate rock from the Kyzylkum deposit in Uzbekistan

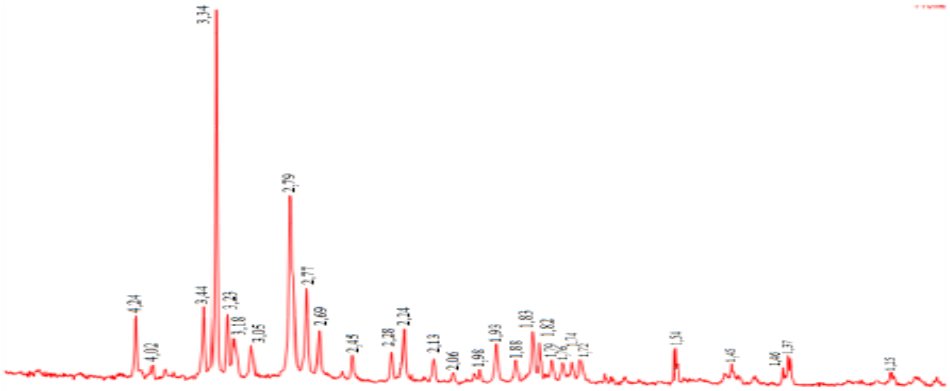

Figure 2 - XRD of phosphate rock from the Durnals deposit in Turkmenistan

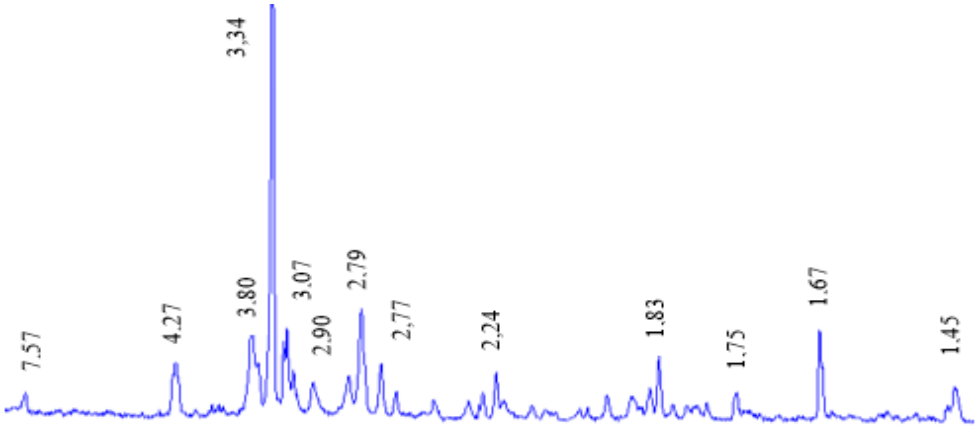

Figure 3 - XRD of phosphorus-humus fertilizer obtained from phosphate raw materials of the Kyzylkum deposit in Uzbekistan

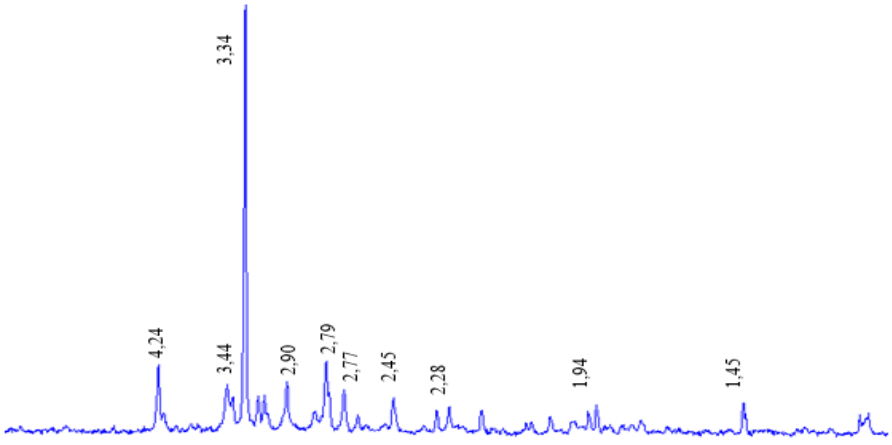

Figure 4 - XRD of phosphorus-humus fertilizer obtained from phosphate raw materials of the Durnals deposit in Turkmenistan

In the XRD of phosphate rock from the Kyzylkum deposit (Uzbekistan) (Fig. 1), the characteristic reflections at 1.72, 1.74, 1.79, 1.83, 1.93, 2.24, 2.69, 2.77, 2.79, 3.18, and 3.44 Å correspond to fluorocarbonate–apatite, the principal phosphate-bearing phase. The presence of calcite is confirmed by diffraction lines at 1.88, 2.28, and 3.05 Å, while reflections at 1.37, 1.54, and 4.02 Å indicate dolomite. Strong peaks at 1.82, 1.98, 2.13, 2.45, 3.23, 3.34, and 4.24 Å reflect a significant contribution from silicon oxide (SiO_2). Additional bands at 1.37 and 1.94 Å are attributed to calcium

fluoride (CaF_2), whereas lines at 2.06, 2.45, and 3.23 Å can be assigned to calcium silicate ($CaSiO_3$).

In the XRD of phosphate rock from the Turkmenistan deposit (Fig.2), the reflections at 1.72, 1.74, 1.79, 1.83, 1.93, 2.24, 2.69, 2.77, 2.79, 3.18, and 3.44 Å correspond to fluorocarbonate apatite, confirming its role as the primary phosphate mineral. The presence of calcite is indicated by peaks at 1.88, 2.28, and 3.05 Å, while reflections at 1.37, 1.54, and 4.02 Å signify dolomite. Strong peaks at 1.82, 1.98, 2.13, 2.45, 3.23, 3.34, and 4.24 Å confirm a high concentration of silicon oxide (SiO_2). Peaks at 1.37 and 1.94 Å are characteristic of calcium fluoride (CaF_2). Peaks at 2.06, 2.45, and 3.23 Å confirm the presence of calcium silicate ($CaSiO_3$)

In the XRD pattern of the phosphorus-humus fertilizer based on the Kyzylkum phosphate rock phosphates (Fig. 3), the process of chemical degradation with sulfuric acid and the addition of oxidized meal led to the occurrence of distinct changes in the structure. This pattern shows the characteristic peaks of monocalcium phosphate at 3.80, 2.79, and 2.21 Å; and those of dicalcium phosphate and tricalcium phosphate at 3.50 and 2.66 Å and 3.44 Å, respectively. Peaks due to ammonium sulfate appear at 2.32 Å, and gypsum at 1.45 Å.

The XRD pattern of the phosphorus-humus fertilizer obtained from the phosphate rock in Turkmenistan (Fig.4) has the same mineral composition. The peaks due to monocalcium phosphate are present at 7.57 Å, 2.90 Å, 1.83 Å, and 1.65 Å, while for dicalcium phosphate at 1.75 Å. The peaks due to ammonium sulfate at 2.32 Å and gypsum at 1.45 Å have also been identified. The diffraction pattern shows that the acidification process and the formation of humus have resulted in the formation of soluble phosphate materials in all phosphate rocks.

Worth noting here is that, during the manufacture of phosphate fertilizers, the ammoniation and drying stages usually entail a corresponding decline in available P_2O_5 content due to phosphorus retrogradation. Nevertheless, adding the oxidized meal to the phosphate raw materials significantly raises the level of available P_2O_5 content. This appears to be related to the presence of organic acids in the oxidized meal, which, when reacting with monocalcium phosphate and other phosphates in the acidic superphosphate mixture, retard phosphorus retrogradation reactions (Eqs 2-6). As such, contrary to expectations, rather than decreasing, there would be a substantially augmented level of available phosphorus content following the ammoniation stage instead.

According to contemporary agriculture requirements, the comparative number of phosphoric acids in complex fertilizer should not be lower than 50% as compared to the total amount of fertilizer. Using this data, the best conditions for processing phosphate rock from the Kyzylkum deposit (Uzbekistan) were calculated. The best results were attained for sulfuric acid amount 70% from stoichiometry for monocalcium phosphate and ratio of phosphorite to oxidized meal 1 to 0.6.

Under these optimized conditions, the resulting granular fertilizer exhibited the following composition (wt.%): P_2O_{5total} – 8.77; $P_2O_{5citric\text{-}acid\text{-}soluble}$ – 6.56; OS – 31.44; HA – 21.95; nitrogen – 2.72; CaO_{total} – 25.62; relative content of citric-acid-soluble P_2O_5 – 72.48%; moisture – 5.17; and total SO_3 – 19.80. The mechanical strength of the granules reached 2.3 MPa, which is sufficient for storage, transportation, and field application. These results confirm that the introduction of oxidized meal under the selected process conditions allows for the production of a phosphorus–humus fertilizer with a high proportion of assimilable P_2O_5 and improved physical properties.

For the processing of phosphate rock from Turkmenistan, the optimal technological parameters were established as follows: a sulfuric acid dosage equal to 40% of the stoichiometric requirement for monocalcium phosphate formation and a phosphorite-to-oxidized-meal mass ratio of 1:0.6. Under these conditions, the resulting phosphorus–humus fertilizer had the following composition (wt.%): P_2O_{5total} – 7.84; $P_2O_{5citric\text{-}acid\text{-}soluble}$ – 6.13; OS – 34.28; HA – 24.32; nitrogen – 2.40; CaO_{total} – 16.12; relative content of citric-acid-soluble P_2O_5 – 78.17%; moisture – 5.62; and total SO_3 – 15.30. The granules exhibited a mechanical strength of 2.4 MPa, indicating sufficient durability for handling, transport, and field application.

These results demonstrate that the selected conditions for Turkmenistan phosphate rock ensure a high proportion of plant-available P_2O_5 and enhanced fertilizer quality, comparable to or exceeding typical requirements for complex fertilizers.

Based on the conducted research, the key technological parameters for the production of phosphorus–humus fertilizers from phosphate rock of the Kyzylkum deposit (Uzbekistan) and Durnals deposit (Turkmenistan) were established, and the material flows and a basic technological scheme were developed (Figs. 5–7).

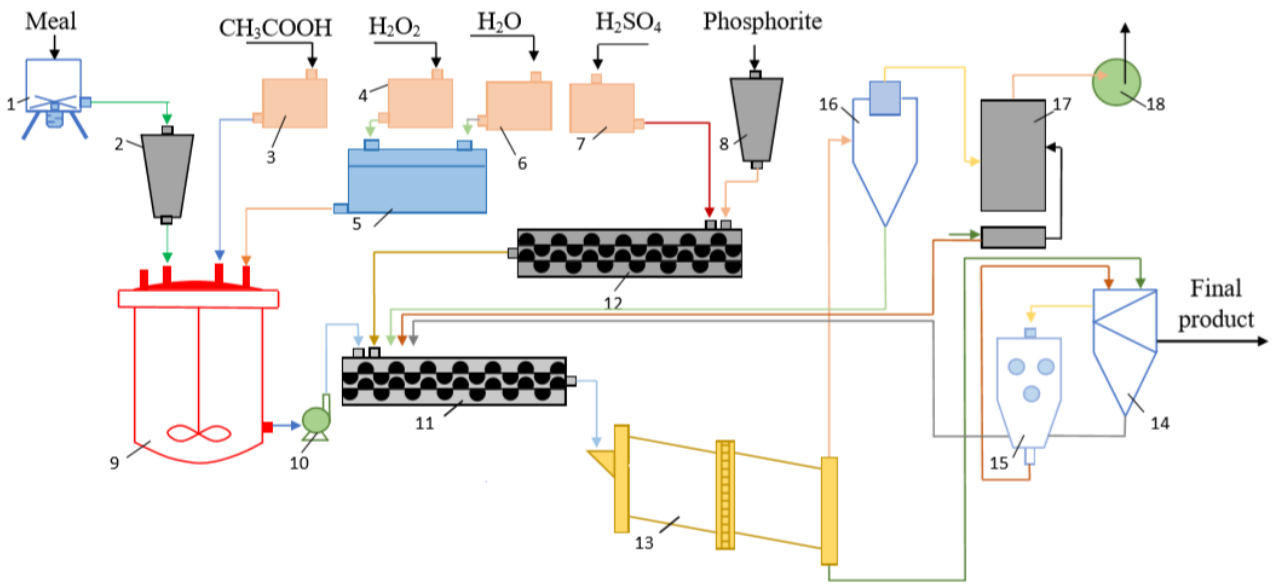

Figure 5 - Basic technological flow sheet for the production of phosphorus–humus fertilizer: 1 – knife crusher; 2,8 - feeder hopper; 3,4,6,7- tanks; 5 - automatic concentrator; 9 - reactor; 10 -pump; 11, 12 - auger mixer; 13 - drum dryer; 14 – classifier; 15-crusher 16 -cyclone; 17-scrubber; 18 – fan.

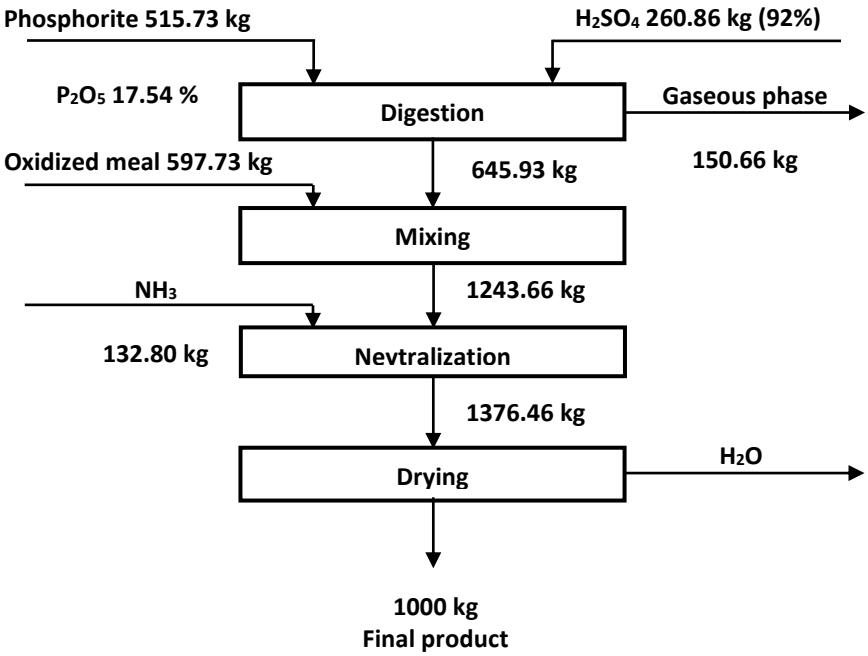

Figure 6 - Material balance for the production of phosphorus–humus fertilizer from phosphate rock sourced from the Kyzylkum deposit, Uzbekistan.

The optimal process conditions for producing humic simple superphosphate are as follows: grinding of licorice meal to a particle size below 0.25 mm; hydrogen peroxide concentration of 10%; mass ratio of the organic portion of licorice meal to H_2O_2 and acetic acid of 100:1:0.1; sulfuric acid dosage for decomposition of Kyzylkum phosphate rock to $Ca(H_2PO_4)_2$ of 60% of the stoichiometric requirement, and for Turkmenistan phosphate rock, 40% of the stoichiometric requirement; mass ratio of organic meal to phosphorite of 1:0.4; oxidation temperature of 60°C and duration of 60 min; phosphorite decomposition time of 30 min; neutralization of the resulting pulp with ammonia to pH 4.5 for 20 min; and drying of the final product at 80–100°C.

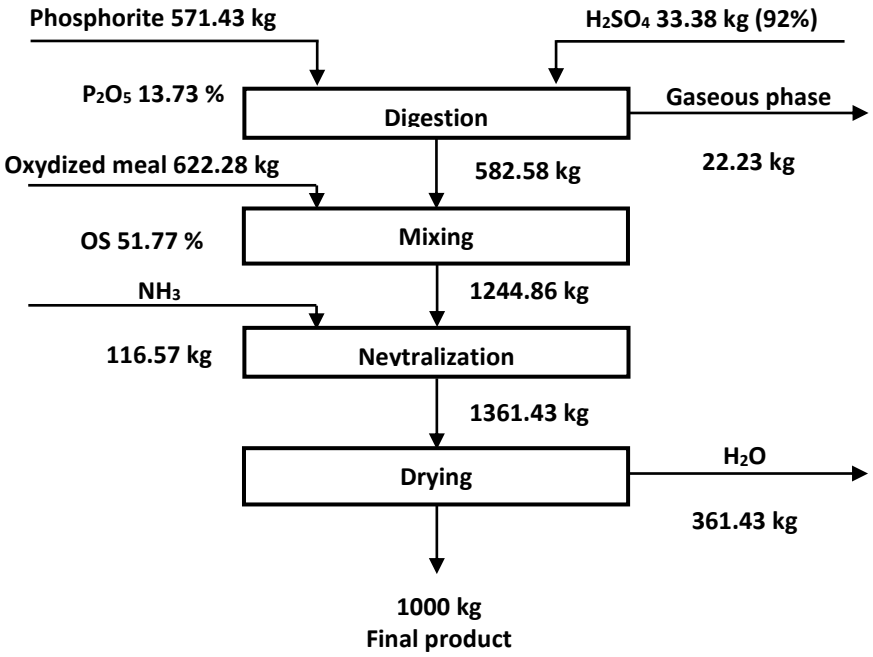

Figure 7 - Material balance for the production of phosphorus–humus fertilizer from phosphate rock sourced from the Durnals deposit, Turkmanistan.

Hydrogen peroxide (60%) is pumped from the storage tank (1) to the pressure tank (3) and subsequently to the automatic concentrator (5), where it is diluted to 10% with water. The diluted oxidizer is then fed to the reactor (8) together with crushed licorice meal (2) for oxidation.

The phosphate rock is treated with sulfuric acid in the two-shaft screw reactor (10). The obtained acid superphosphate is passed on to the screw mixer (11), where it is mixed with the oxidized licorice meal, recycled, and the 25% ammonia solution for neutralization.

The homogeneous mixture is then moved to the drum dryer (12) for drying and then to the screening unit (16) for granule classification. Off-gases with ammonia and dust are purified in a cyclone (13) and a water scrubber (14) and then emitted into the atmosphere.

Finally, dried and screened granules are transported to the classification unit and subsequently warehoused in the finished product warehouse.

Compared with these existing methods, the present technology combines partial sulfuric acid decomposition of low-grade phosphate rock with oxidized licorice meal, achieving high proportions of plant-available P_2O_5 (up to 78–84%) while reducing sulfuric acid consumption to 40–60% of the stoichiometric requirement. In addition, the resulting granular fertilizers exhibit sufficient mechanical strength for storage and field application, addressing both agronomic efficiency and logistical practicality.

Overall, by overcoming the high material demand, long processing time, and technological complexity associated with previously reported methods [[11], [12], [13],[14], [15]], the proposed approach offers a more efficient and scalable route for producing phosphorus–humus fertilizers suitable for modern agricultural systems.

Conclusion

The effects of oxidizer concentration, temperature, and the weight ratio of the organic portion of the meal to anhydrous hydrogen peroxide were taken into consideration for improving the humic substances and organic acids content in licorice meal through oxidation with hydrogen peroxide in the presence of acetic acid. The oxidized meal was characterized by its humic substance content and functional groups. A technology has also been developed in this work on the production of phosphorus–humus fertilizers by incorporating the oxidized meal into the acidic superphosphate mass before ammoniation and drying. This treatment simultaneously increases the relative content of digestible P_2O_5 forms and decreases the sulfuric acid requirement for phosphate decomposition. The application of such fertilizers in

agriculture is expected to improve the soil humus content and to ameliorate the structure and physical–mechanical properties of the soil, ensuring the complete supply of all essential plant nutrients, which will result in increased yields, improved crop quality, and an enhancement in resistance to diseases.

Conflicts of interest. On behalf of all authors, the corresponding author states that there is no conflict of interest.

CRediT author statement: **U. Alimov**: Conceptualization, Methodology, Software; **A. Orakbayev**: Data curation, Writing draft preparation; H. **Ataew, U. Alimov, N. Usanbayev**: Visualization, Investigation; **S. Namazov**: Supervision **O. Jumaewa**: Software, Validation **M. Rejepowa**: Reviewing and Editing.

Formatting of funding sources. This research did not receive any specific grant from funding agencies in the public, commercial, or not-for-profit sectors.

Cite this article as: Kurayazov Z, Ollaberganova A, Jabbarov M, Matnazarov U, Babajanova R. Reduction of Fluoride in Central Kyzylkum Phosphate Waste in an Acidic Environment: Experimental and Mathematical Study Based on the Langmuir Model. Kompleksnoe Ispolzovanie Mineralnogo Syra = Complex Use of Mineral Resources. 2027; 343(4):77-94. https://doi.org/10.31643/2027/6445.42

Тотыққан мия ұнтағы және фосфатты шикізат негізіндегі фосфор-қарашірінді тыңайтқыштар

[1] Оракбаев А., [2] Жумаева О. , [1] Усанбаев Н., [2]Атаев Х., [1] Намазов Ш., [1]Алимов У., [2]Режепова М., [3] Шамуратов С.

[1]Өзбекстан Республикасы Ғылым академиясының Жалпы және бейорганикалық химия институты, Ташкент, Узбекистан
[2]Химия институты, Түрікменстан Ғылым академиясы, Ашхабад, Түрікменстан
[3]Әбу Райхан Беруни атындағы Үргеніш мемлекеттік университеті, Үргеніш, Өзбекстан

Мақала келді: *17 желтоқсан 2025*
Сараптамадан өтті: *10 қаңтар 2026*
Қабылданды: *10 наурыз 2026*

АННОТАЦИЯ

Гумус құрамды органикалық және органо-минералдық тыңайтқыштар жоғары су ұстау қабілетінің, жақсартылған су өткізгіштігінің, сондай-ақ карбонатты топырақтарда кальций мен магний иондарының және қышқыл топырақтарда сесквиоксидтердің әсерінен фосфордың фиксациясын төмендету қасиетінің арқасында топырақ құнарлылығын арттыруда маңызды рөл атқарады. Мал шаруашылығы қалдықтарынан, шымтезектен және қоңыр көмірден алынған органикалық заттар тыңайтқыштарды гумуспен байытуға мүмкіндік береді. Алайда өсімдік қалдықтары, атап айтқанда көктерек қабығы, ауыл шаруашылығы қалдықтарының қауыздары және мия тамырының ұны, органикалық тыңайтқыштар өндіру үшін ең тиімді қоспалардың қатарына жатады. Бұл зерттеуде Түрікменстандағы Қызылқұм кен орнынан табылған индикаторлы фосфориттер мен сутек асқын тотығы және сірке қышқылымен өңделген тотықтырылған мия пастасын пайдалана отырып, түйіршіктелген фосфор-гумусты тыңайтқыштарды синтездеу бағаланды. Зертханалық эксперимент әдістемесі үш кезеңнен тұрды. Бірінші кезеңде бөлшек өлшемі < 0,1 мм болатын ұсақталған мия ұнының тотығу қасиеттері судағы сутек асқын тотығы ерітіндісі мен сірке қышқылы арқылы, мияның органикалық фракциясына қатысты H_2O_2 : CH_3COOH = 100 : (10–20) : (0,1–1) массалық қатынастарында зерттелді. Екінші кезеңде фосфорит 92%-дық күкірт қышқылымен монокальцийфосфат түзілуіне қажетті стехиометриялық мөлшердің 30–80%-ы көлемінде ыдыратылды. Үшінші кезеңде алынған өнімдер тотықтырылған мия пастасымен 100:10:1 қатынасында араластырылды. Жұмыста фосфор-гумусты тыңайтқыштарды өндеудің оңтайлы шарттары бағаланып, әрбір шикізат көзіне сәйкес технологиялық ағындық сызбалар әзірленді. Ұсынылған жаңа технологияның тиімділігі көрсетілді. Алынған нәтижелер төмен сапалы фосфориттер мен мия тамыры қалдықтарының экологиялық тұрғыдан қауіпсіз екенін және жоғары шығынды химиялық тыңайтқыштарды қолдануды немесе уақытты көп қажет ететін дәстүрлі компосттау процестерін азайту үшін баламалы құрал ретінде пайдалануға болатынын көрсетті.

Түйін сөздер: мия тамыры ұны, сутек асқын тотығы, фосфорит, экстрактивті заттар, күкірт қышқылы, тотығу

Авторлар туралы ақпарат:

Азамат Оракбаев
Техника ғылымдарының философия докторы, Өзбекстан Республикасы Ғылым академиясының Жалпы және бейорганикалық химия институтының кіші ғылыми қызметкері, 100170, Мирзо Улугбек, 77, Ташкент, Өзбекстан. Email: a_orakbayev@mail.ru; ORCID ID: https://orcid.org/0009-0004-4635-4012

Огульнур Жумаева
Түрікменстан Ғылым академиясының Химия институтының зертхана меңгерушісі, Ашхабад, Түрікменстан. Email: jumayewa.ogulnur@mail.ru; ORCID ID: https://orcid.org/0009-0003-3748-7182

Нажимуддин Усанбаев	*Өзбекстан Республикасы Ғылым академиясы Жалпы және бейорганикалық химия институтының профессоры, техника ғылымдарының докторы, 100170, Мирзо Улугбек, 77, Ташкент, Өзбекстан.Email: najim70@mail.ru*
Халлимйрат Атаев	*Химия ғылымдарының кандидаты, Түрікменстан Ғылым академиясының Химия институтының директоры, Ашхабад, Түрікменстан, Email: himiyainstituty.tm@gmail.com; ORCID ID: https://orcid.org/0009-0009-7172-793X*
Шафоат Намазов	*Техника ғылымдарының докторы, академик, Өзбекстан Республикасы Ғылым академиясының Жалпы және бейорганикалық химия институтының зертхана меңгерушісі, 100170, Мирзо Улугбек, 77, Ташкент, Өзбекстан. Email: diana-ye@yandex.com; ORCID ID: https://orcid.org/0000-0002-0040-2048*
Умарбек Алимов	*Техника ғылымдарының докторы, Өзбекстан Республикасы Ғылым академиясының Жалпы және бейорганикалық химия институтының жетекші ғылыми қызметкері, 100170, Мирзо Улугбек, 77, Ташкент, Өзбекстан. Email: umaralihonalimov@mail.ru; ORCID ID: https://orcid.org/0000-0001-5608-5304*
Режепова Мая	*Түрікменстан Ғылым академиясының химия жөніндегі кіші ғылыми қызметкері, Ашхабад, Түрікменстан. Email: jumayewa.ogulnur@mail.ru*
Санжарбек Шамуратов	*Техника ғылымдарының философия докторы, Әбу Райхан Беруни атындағы Үргеніш мемлекеттік университетінің химия-технология факультетінің доценті, 220100, Х.Олимжон көшесі 14, Үргеніш, Өзбекстан. Email: shamuratovsx@gmail.com; ORCID ID: https://orcid.org/0000-0002-1040-1807*

Фосфорно-гумусовые удобрения на основе окисленного солодкового шрота и фосфатного сырья

[1] Оракбаев А., [2] Жумаева О. , [1] Усанбаев Н., [2]Атаев Х., [1] Намазов Ш., [1]Алимов У., [2]Режепова М., [3] Шамуратов С.

[1]Институт общей и неорганической химии Академии наук Республики Узбекистан, Ташкент, Узбекистан
[2]Институт химии Академии наук Туркменистана, Ашхабад, Туркменистан
[3]Ургенчский государственный университет имени Абу Райхана Беруни, Ургенч, Узбекистан

Поступила: *17 декабря 2025*
Рецензирование: *10 января 2026*
Принята в печать: *10 марта 2026*

АННОТАЦИЯ

Гумуссодержащие органические и органо-минеральные удобрения играют ключевую роль в повышении плодородия почв благодаря их высокой влагоудерживающей способности, улучшенной водопроницаемости, а также способности снижать фиксацию фосфора ионами кальция и магния в карбонатных почвах и сесквиоксидами в кислых почвах. Органическое вещество, получаемое из отходов животноводства, торфа и бурого угля, может обогащать удобрения гумусом. Однако растительные остатки, такие как кора осины, сельскохозяйственные шелухи и мука из корня солодки, относятся к числу наиболее эффективных добавок для производства органических удобрений. В настоящем исследовании оценивался синтез фосфорно-гумусных удобрений в гранулированной форме с использованием индикаторных фосфоритов, обнаруженных в месторождении Кызылкум (Туркменистан), а также окисленной пасты корня солодки, обработанной перекисью водорода и уксусной кислотой. Лабораторная методика эксперимента включала три этапа. На первом этапе изучалось окислительное поведение тонкоизмельчённой муки солодки (размер частиц < 0,1 мм) с использованием водного раствора перекиси водорода и уксусной кислоты при массовых соотношениях по отношению к органической фракции солодки в диапазоне H_2O_2 : CH_3COOH = 100 : (10–20) : (0,1–1). На втором этапе фосфорит подвергался разложению 92%-ной серной кислотой в количестве 30–80 % от стехиометрически необходимого для образования монокальцийфосфата. На третьем этапе полученные продукты смешивали с окисленной пастой солодки в соотношении 100:10:1. В работе оценены оптимальные условия переработки фосфорно-гумусных удобрений, а также разработаны технологические схемы переработки, включая фосфатное сырьё, поступающее из каждого источника. Представлена эффективность новой технологии. Полученные результаты показывают, что низкосортные фосфориты и отходы корня солодки являются экологически безопасными и могут быть рекомендованы в качестве альтернативного инструмента для снижения использования высокозатратных химических удобрений или трудоёмких традиционных процессов компостирования.

Ключевые слова: мука из корня солодки, перекись водорода, фосфорит, экстрактивные вещества, серная кислота, окисление

Информация об авторах:

Азамат Оракбаев	*Доктор философии по техническим наукам, младший научный сотрудник Института общей и неорганической химии Академии наук Республики Узбекистан, 100170, ул. Мирзо Улугбека, 77, Ташкент, Узбекистан. Email: a_orakbayev@mail.ru; ORCID ID: https://orcid.org/0009-0004-4635-4012*
Огульнур Жумаева	*Руководитель лаборатории Института химии Академии наук Туркменистана, Ашхабад, Туркменистан. Email: jumayewa.ogulnur@mail.ru; ORCID ID: https://orcid.org/0009-0003-3748-7182*

Нажимуддин Усанбаев	*Доктор технических наук, профессор Института общей и неорганической химии Академии наук Республики Узбекистан, 100170, ул. Мирзо Улугбека, 77, Ташкент, Узбекистан. Email: najim70@mail.ru*
Халлимйрат Атаев	*Кандидат химических наук, директор Института химии Академии наук Туркменистана, Ашхабад, Туркменистан. Email: himiyainstituty.tm@gmail.com; ORCID ID: https://orcid.org/0009-0009-7172-793X*
Шафоат Намазов	*Доктор технических наук, академик, заведующий лабораторией Института общей и неорганической химии Академии наук Республики Узбекистан, 100170, ул. Мирзо Улугбека, 77, Ташкент, Узбекистан. Email: diana-ye@yandex.com; ORCID ID: https://orcid.org/0000-0002-0040-2048*
Умарбек Алимов	*Доктор технических наук, ведущий научный сотрудник Института общей и неорганической химии Академии наук Республики Узбекистан, 100170, ул. Мирзо Улугбека, 77, Ташкент, Узбекистан. Email: umaralihonalimov@mail.ru; ORCID ID: https://orcid.org/0000-0001-5608-5304*
Режепова Мая	*Младший научный сотрудник химии Академии наук Туркменистана, Ашхабад, Туркменистан. Email:jumayewa.ogulnur@mail.ru*
Санжарбек Шамуратов	*Доктор философии по техническим наукам, доцент химико-технологического факультета Ургенчского государственного университета имени Абу Райхана Беруни, 220100, улица Х. Олимджона, 14, Ургенч, Узбекистан. Email: shamuratovsx@gmail.com; ORCID ID: https://orcid.org/0000-0002-1040-1807*

References

[1] Uddin MK, Yeasmin S, Mohiuddin KM, Chowdhury MAH, Saha BK. Peat-Based Organo-Mineral Fertilizer Improves Nitrogen Use Efficiency, Soil Quality, and Yield of Baby Corn (Zea mays L.). Sustainability. **2023;** 15:9086. https://doi.org/10.3390/su15119086

[2] Sunita Sheoran, Dhram Prakash, Dev Raj, Parmod Kumar Yadav, Rameshwar Singh, Rajeev Kumar Gupta, Saud Alamri, Manzer H. Siddiqui and Shahbaz Khan. Sheoran et al. BMC Plant Biology. 2025; 25:117. https://doi.org/10.1186/s12870-025-06128-2

[3] Usman S, Jayeoba JO. Evaluation of soil structural quality and soil fertility indicators of dryland and fadama milieus based on soil profile description at 0–20 cm soil depth. Discov. Soil. 2025; 2:24. https://doi.org/10.1007/s44378-025-00049-0

[4] Shamuratov S, Baltaev U, Achilova S, Alimov U, Namazov S, & Usanbaev N. Enhancement of availability of high calcareous phosphorite by neutralization of acid effluent and composting of cattle manure. E3S Web of Conferences. 2023; 377. https://doi.org/10.1051/e3sconf/202337703004

[5] Audette Y, Congreves KA, Schneider K, et al. The effect of agroecosystem management on the distribution of C functional groups in soil organic matter: A review. Biol Fertil Soils. 2021; **57:**881–894. https://doi.org/10.1007/s00374-021-01580-2

[6] Trukhachev VI, Belopukhov SL, Grigoryeva M, Dmitrevskaya II. Study of the Sustainability of Ecological and Chemical Indicators of Soils in Organic Farming. Sustainability. **2024;** 16(2):665. https://doi.org/10.3390/su16020665

[7] Liu J, Qiu T, Peñuelas J, Sardans J, Tan W, Wei X, Cui Y, Cui Q, Wu C, Liu L, Zhou B, He H, Fang L. Crop residue return sustains global soil ecological stoichiometry balance. Glob Chang Biol. 2023; 29(8):2203-2226. https://doi.org/10.1111/gcb.16584

[8] Kirkby CA, Richardson AE, Wade LJ, Conyers M, Kirkegaard JA. Inorganic Nutrients Increase Humification Efficiency and C-Sequestration in an Annually Cropped Soil. PLoS One. 2016; 4;11(5):e0153698. https://doi.org/10.1371/journal.pone.0153698

[9] Zhao SC, Huang SW, Qiu SJ, He P. Response of soil organic carbon fractions to increasing rates of crop residue return in a wheat–maize cropping system in north-central China. Soil Research. 2018; 56:856–864. https://doi.org/10.1071/SR18123

[10] Wang X, He C, Liu B, Zhao X, Liu Y, Wang Q, Zhang H. Effects of Residue Returning on Soil Organic Carbon Storage and Sequestration Rate in China's Croplands: A Meta-Analysis. Agronomy. **2020;** 10:691. https://doi.org/10.3390/agronomy10050691

[11] Badamaeva SE, Evtushenko SV. Efficiency of application of complex organomineral fertilizers on different types of soils. Epoch of science. 2015; 4:482-486. https://cyberleninka.ru/article/n/effektivnost-primeneniya-kompleksnyh-organo-mineralnyh-udobreniy-na-raznyh-tipah-pochv

[12] Jaya Tiwari, Al Ramanathan, Kuldeep Bauddh, John Korstad. Humic substances: Structure, function and benefits for agroecosystems—a review. Pedosphere. 2023; 33(2):237-249. https://doi.org/10.1016/j.pedsph.2022.07.008

[13] Šimanský V, Wójcik-Gront E, Bordoloi S, et al. Biochar and its combination with nitrogen fertilisation altered soil organic matter, humic substances, and soil structure: short-term versus long-term changes. Environ Geochem Health. 2025; **47:**532. https://doi.org/10.1007/s10653-025-02853-7

[14] Sotimboev I, Baltaev U, Shamuratov S, Shamsiddin R, Alimov U, & Saporboyev M. Technical and economic efficiency of processing acidic wastewater from the oil and fat industry into necessary agricultural products. E3S Web of Conferences. 2024; 563. https://doi.org/10.1051/e3sconf/202456303072

[15] Veprikova E V, Fetisova O Yu, Chesnokov N V, Kuznetsov B N. Study of Resistance of Phosphorus Biocomposite Fertilizers Based on Birch Bark to Washing-out of the Active Components. Chemistry for Sustainable Development. 2017; 25:460–468. https://doi.org/10.15372/CSD20170504

[16] Ogwu MC, Patterson ME, Senchak PA. Phosphorus mining and bioavailability for plant acquisition: environmental sustainability perspectives. Environ Monit Assess. 2025; 197:572. https://doi.org/10.1007/s10661-025-14012-7

[17] Bindraban PS, Dimkpa CO, & Pandey R. Exploring phosphorus fertilizers and fertilization strategies for improved human and environmental health. Biol Fertil Soils. 2020; **56:**299–317. https://doi.org/10.1007/s00374-019-01430-2

[18] Gilyarova AA. Phosphate mineral res: reserves, production and mining projects. Russian Mining Industry. 2023; 5:72-77. https://doi.org/10.30686/1609-9192-2023-5-72-77

[19] Phosphate Mineral. https://www.sciencedirect.com/topics/agricultural-and-biological-sciences/phosphate-mineral?utm_source=chatgpt.com

[20] Yuldasheva A P K, Shamuratov S K U, Kurambayev S R, & Radjabov M F. Mathematical Analysis of CaO Content Variation in Acidic Wastewater and Mineralized Mass Mixture from Central Kyzylkum Phosphorite Based on Exponential Decay Model. Kompleksnoe Ispolzovanie Mineralnogo Syra = Complex Use of Mineral Resources. 2026; 339(4):79–86. https://doi.org/10.31643/2026/6445.42

[21] Popov VS, Konnov LP. Phosphorite-bearing basins of Central Asia. Proceedings of the Central Asian Research Institute of Geology and Mineral Resources. Tashkent. 1981; 3:49-60.

[22] Khaitov OG, Dzhuraev SDz, Bekmurodov AO, Ravshanov ZYa. Features of development of a reservoir phosphorite deposit. Globus. 2020; 5 (51). https://cyberleninka.ru/article/n/osobennosti-razrabotki-plastovogo-mestorozhdeniya-fosforitov

[23] Schultheiss S, Sethmann I, Schlosser M, Kleebe H-J. Pseudomorphic transformation of Ca/Mg carbonates into phosphates with focus on dolomite conversion. Mineralogical Magazine. 2013; 77(6):2725-2737. https://doi.org/10.1180/minmag

[24] Gypser S, Schütze E, Freese D. Single and Binary Fe- and Al-hydroxides Affect Potential Phosphorus Mobilization and Transfer from Pools of Different Availability. Soil Syst. **2021;** 5:33. https://doi.org/10.3390/soilsystems5020033

[25] Yi C, Zhu J, Chen L, Huang X, Wu R, Zhang H, Dai X, Liang J. Speciation of Iron and Aluminum in Relation to Phosphorus Sorption and Supply Characteristics of Soil Aggregates in Subtropical Forests. Forests. **2023**; 14:1804. https://doi.org/10.3390/f14091804

[26] Edward Johnston A, Paul R Poulton, Paul E Fixen, Denis Curtin. Chapter Five - Phosphorus: Its Efficient Use in Agriculture. Editor(s): Donald L Sparks. Advances in Agronomy. Academic Press. 2014; 123:177-228. https://doi.org/10.1016/B978-0-12-420225-2.00005-4

[27] Govil BP, Prasad R. Effects of the amounts of phosphate fertilizer, and of the proportions of water-soluble phosphate in the fertilizers tested on the phosphorus nutrition of sorghum. The Journal of Agricultural Science. 1974; 83(1):177-179. https://doi.org/10.1017/S0021859600047158

[28] Xiong Q, Wang S, Lu X, Xu Y, Zhang L, Chen X, Xu G, Tian D, Zhang L, Jing J, et al. The Effective Combination of Humic Acid Phosphate Fertilizer Regulating the Form Transformation of Phosphorus and the Chemical and Microbial Mechanism of Its Phosphorus Availability. Agronomy. **2023;** 13:1581. https://doi.org/10.3390/agronomy13061581

[29] Bouhia Y, Hafidi M, Ouhdouch Y, Zeroual Y, Lyamlouli K. Organo-Mineral Fertilization Based on Olive Waste Sludge Compost and Various Phosphate Sources Improves Phosphorus Agronomic Efficiency, Zea mays Agro-Physiological Traits, andWater Availability. Agronomy. **2023;** 13:249. https://doi.org/10.3390/agronomy 13010249

[30] Jing J, Zhang S, Yuan L, Li Y, Chen Cand Zhao B. Humic Acid Modified by Being Incorporated Into Phosphate Fertilizer Increases Its Potency in Stimulating Maize Growth and Nutrient Absorption. Front. Plant Sci. 2022; 13:885156. https://doi.org/10.3389/fpls.2022.885156

[31] Canellas LP, Olivares FL. Physiological responses to humic substances as plant growth promoter. Chem. Biol. Technol. Agric. 2014; 1:3. https://doi.org/10.1186/2196-5641-1-3

[32] He C, Cui J, Chen X, Wang W, & Hou J. Effects of enhancement of liquorice plants with dark septate endophytes on the root growth, glycyrrhizic acid and glycyrrhizin accumulation amended with organic residues. Current Plant Biology. 2020; 23:100154. https://doi.org/10.1016/j.cpb.2020.100154

[33] Jayakumar M, Prabhu SV, Abo LD, Daba BJ, Periyasamy S, & Jabesa A. Microbial conversion of agricultural residues into organic fertilizers. In Agricultural Waste to Value-Added Products. Springer, Singapore. 2023. https://doi.org/10.1007/978-981-99-4472-9_6

[34] Wahab S, Annadurai S, Abullais S S, Das G, Ahmad W, Ahmad M F, Kandasamy G, Vasudevan R, Ali M S, & Amir M. Glycyrrhiza glabra (Licorice): A Comprehensive Review on Its Phytochemistry, Biological Activities, Clinical Evidence and Toxicology. Plants (Basel, Switzerland). 2021; 10(12):2751. https://doi.org/10.3390/plants10122751

[35] Shamuratov S, Baltaev U, Myachina O, Alimov U, Atashev E, & Kuramboev T. Agrochemical efficiency of slow release phosphate fertilizers derived on the base of phosphorite activation. E3S Web of Conferences. 2023; 434. https://doi.org/10.1051/e3sconf/202343403014

[36] Sharma V, Katiyar A, Agrawal RC. Glycyrrhiza glabra: Chemistry and Pharmacological Activity. In: Mérillon, JM., Ramawat, K. (eds) Sweeteners. Reference Series in Phytochemistry. Springer, Cham. 2018. https://doi.org/10.1007/978-3-319-27027-2_21

[37] Pastorino G, Cornara L, Soares S, Rodrigues F, & Oliveira M B P P. Liquorice (Glycyrrhiza glabra): A phytochemical and pharmacological review. Phytotherapy research: PTR. 2018; 32(12):2323–2339. https://doi.org/10.1002/ptr.6178

[38] Azamat Orakbayev, Hallymyrat Ataew, Najimuddin Usanbayev, Ogulnur Jumaewa, Umarbek Alimov, Oraz Charyew, Shafoat Namazov / Development of organic fertilizer pellets technology using licorice meal and hydrogen peroxide technology. New Materials Compounds and Applications. 2025; 9(1):209-221. https://doi.org/10.62476/nmca.91209

[39] Zhao Z, Wang S, Li X, Huang H, & Lu Y. Cyclic oxidation behavior and microstructural evolution of the Ni-16Mo-7Cr alloy from 700 °C to 800 °C using in molten salt reactors. Materials Characterization. 2025; 229:115656. https://doi.org/10.1016/j.matchar.2025.115656

[40] Saber D, Emam I S, & Abdel-Karim R. High temperature cyclic oxidation of Ni based superalloys at different temperatures in air. Journal of Alloys and Compounds. 2017; 719:133–141. https://doi.org/10.1016/j.jallcom.2017.05.130

[41] Lamar RT, Monda H. Quantification of Humic and Fulvic Acids in Humate Ores, DOC, Humified Materials and Humic Substance-Containing Commercial Products. J. Vis. Exp. 2022; 181:e61233. https://doi.org/10.3791/61233

[42] Alphabetikal and Group Numerical Index of X-Ray Diffraction Data. American Society for Testing and Materials. New York. 1973.

[43] Mikheev VI. X-ray diffraction guide to minerals. In 2 volumes. Moscow. 1957; 1:868.

[44] Giller YaL. Tables of interplanar distances. In 2 volumes. Moscow: Nedra. 1966, 330.

Crossref
DOI: 10.31643/2027/6445.43
Mining & Mineral Processing

Geopolymer porous concrete: formation and performances

Miryuk O.A.

Rudny Industrial University, Rudny, Kazakhstan

Corresponding author email: psm58@mail.ru

Received: *January 6, 2026*
Peer-reviewed: *March 4, 2026*
Accepted: *March 11, 2026*

ABSTRACT
The article presents the results of geopolymer technology development and a study of the performance of lightweight concrete based on a porous aggregate. The purpose of the study is to identify the transformations in composition and structure during the formation and operational testing of porous geopolymer concrete. The porous aggregate and binder are synthesized from molding mixtures of related composition containing sodium liquid glass and finely dispersed from thermal power plants' waste (fly ash and aluminosilicate microsphere). A thermal curing mode for concrete is proposed to ensure the formation of a porous structure with satisfactory resistance to mechanical stress and water. Phase transformations are studied during thermal synthesis of geopolymer material, with prolonged exposure of concrete to water and solutions of magnesium sulfate and sodium. Preliminary economic calculations are performed, indicating the advantages of porous geopolymer concrete compared to cement concrete based on expanded clay. The porous concrete based on geopolymer binder is intended for the production of energy-efficient wall products.

Keywords: Geopolymerization, liquid glass, large-porous concrete, fly ash, salt aggression.

Miryuk Olga Aleksanrovna

Information about authors:
Doctor of Technical Sciences, Professor, Rudny Industrial University, 111500, 50 let Oktyabrya str., 38, Rudny, Kazakhstan. Email: psm58@mail.ru; ORCID ID: https://orcid.org/0000-0001-6892-2763

Introduction

The widespread use of concrete in construction is due to the possibility of regulating the composition and structure of concrete mixtures, using raw materials of various origins. The predominance of cement concretes is due to the deep study of the technology of production of concrete products, high construction and technical properties, and long-term observations of the performance of cement paste [[1], [2], [3]].

The cement industry is a major consumer of raw materials, fuel, and energy. Cement production accounts for about 5% of global CO_2 emissions [[4], [5]]. To solve this problem, the development of low-carbon concrete technologies is relevant. The use of low-clinker and cement-free binders contributes to achieving carbon neutrality of concrete [[6], [7], [8]].

Geopolymer concretes based on cementless binders obtained from powdered aluminosilicate and/or silicate material and a liquid alkaline component are very promising. Finely ground materials are used as a powder base for geopolymer binder, such as blast furnace slag, ash from fuel combustion, and agricultural waste, red mud, man-made glass [[9], [10], [11], [12], [13], [14]]. Hardening of geopolymer binders is based on chemical reactions between aluminosilicates and/or silicates and an alkali solution. Sodium (potassium) hydroxide and sodium (potassium) silicate or their combinations are used for alkaline activation of the powdered component of geopolymer binders [[15], [16], [17]].

The mechanism of geopolymerization is due to the processes of dissolution-hydrolysis and hydrolysis-polycondensation. Alkaline activation leads to the dissolution of silicon and alumina from powdered materials with subsequent orientation, polycondensation, and the formation of a three-dimensional rigid network and a ring structure with Si-O-Al-O bonds [[18], [19]]. Hydrates of various structures are involved in the formation of three-dimensional rigid networks: amorphous phase (geopolymer gel), semi-crystalline phases, and crystalline zeolites. The main gel-like hydration products of geopolymer binder are calcium aluminosilicate hydrate (C-A-S-H) and sodium aluminosilicate hydrate (N-A-S-H) [20]. High

mechanical properties of geopolymer concrete are achieved by selecting a rational proportion of sodium silicate and sodium hydroxide in the liquid component of the binder, as well as the ratio of silica and alumina in its solid part [[18], [19], [20]]. For example, geopolymer systems characterized by molar ratios of SiO_2/Al_2O_3 = 3.5 – 4.5; Na_2O/Al_2O_3 = 0.8 – 1.6; Na_2O/SiO_2 = 0.20 – 0.48 and H_2O/Na_2O = 10 – 25 have high strength and durability [21]. To ensure the required SiO_2/Al_2O_3 ratios in the geopolymer binder, combined powdered aggregates are used, for example, fly ash, blast furnace slag, and nickel slag with a high magnesium content [6]; liquid crystal glass waste and metakaolin [10]; glass powder, fly ash, and metallurgical slag [22]. The choice of the H_2O/Na_2O ratio determines the hardening capabilities of the binder, for example, for some systems at H_2O/Na_2O exceeding 25, polycondensation does not occur and the material does not harden [21]. The use of liquid glass with a high silica modulus, for example, 2.92, improves the rheological (fresh) and mechanical properties of self-compacting geopolymer concrete [23]. Along with the binder material composition, the curing conditions affect the geopolymerization reaction. When the curing temperature increases from 20 to 50 – 80°C, the activation of the binder accelerates, and the strength of the concrete increases twofold. Geopolymer binder containing metakaolin and subjected to multi-hour heat treatment at a temperature of 80°C, at the age of 56 days is characterized by a compressive strength of 67 MPa [13]. According to [23], geopolymer concrete based on fly ash demonstrates higher strength at temperatures of 150°C and 450°C.

The results of numerous studies confirm that geopolymer concrete can serve as a worthy alternative to cement concrete [[10], [13], [23]]. The widespread use of technogenic materials in geopolymerization processes indicates the resource-saving and environmental focus of cement-free concrete activated by alkali. Compared to Portland cement, the production of geopolymer binder emits 5 – 7 times less CO_2 [10].

Liquid glass is an alkaline component of many geopolymer binders. Liquid glass is an aqueous solution of alkali silicates. Sodium liquid glass ($Na_2O{\cdot}mSiO_2 + nH_2O$) is often used in geopolymer binders. Changing the ratios $(mSiO_2)/Na_2O$ and $(Na_2O{\cdot}mSiO_2)/H_2O$ allows to regulate the chemical activity and density of liquid glass.

High thermal sensitivity to thermal effects is an advantage of liquid glass [[23], [24]]. Solid foam with a density of 50 – 150 kg/m^3 is formed when liquid glass is heated to a temperature of 120 – 500°C. The combination of liquid glass with powder aggregates allows the creation of highly porous materials. The main driving force of the process of thermal porization of liquid glass compositions is an increase in the water vapor pressure with an increase in the temperature inside the liquid glass mass. According to [24], porization consists of three stages, the duration and nature of which depend on the type and amount of moisture. At the first stage (temperatures of 100 – 120°C), the original mass partially passes into a pseudopyroplastic state and begins to deform with an increase in volume. At the second stage (temperatures of 130 – 150°C), free and adsorbed moisture are vigorously released, and intensive porization of the material is observed. At the final stage (temperature above 150°C), the constitutional moisture is removed, the final restructuring of the structure occurs, and the physical and chemical processes are completed. The greatest contribution to the formation of the porous structure is made by the constitutional water, which begins to be removed at temperatures above 150°C. The unique properties of liquid glass form the basis of porous concrete technologies, granulated materials for various purposes [[25], [26]]. The multifunctionality of liquid glass is realized in the production of geopolymer concrete components: for alkaline activation of cementless binders and as part of the raw mix for porous granulated aggregates [[26], [27], [28]].

The diversity of the composition of binders and structures of geopolymer concretes predetermines their widespread use in energy-efficient construction. This requires the expansion of scientific understanding of the formation and stability of porous geopolymer concretes in various conditions [[29], [30], [31]].

The aim of the work is to study the transformations of the composition and structure during the formation and operational testing of porous geopolymer concrete.

The object of the study is geopolymer concrete based on a porous aggregate.

The idea of the study is the formation of a stable highly porous structure of geopolymer material due to components contributing to the directed creation of pores and voids.

Experimental part

To implement the idea, molding mixtures of liquid glass and fine-dispersed hollow waste from thermal power engineering were used. The use of

fine-dispersed waste from thermal power engineering in the composition of concrete is known and confirmed by positive experience [[9], [28]].

Geopolymer binder and porous concrete were synthesized from molding mixtures of related composition (Table 1). Sodium liquid glass with a silicate modulus n = $mSiO_2/Na_2O$ = 2.8 and a density of 1350 kg/m^3 was used in the experiments. Liquid glass is a binding base for molding compositions. When liquid glass is heated, steam is formed, which causes the pyroplastic raw material to swell.

Table 1 – Composition of molding mixtures

Raw materials	Content in molding mixture, kg/m^3	
	for geopolymer binder	***for porous aggregate***
Sodium liquid glass	200.0	136.0
Fly ash	85.0	40.8
Aluminosilicate microsphere	85.0	95.2

Chemical composition of thermal power plant fly ash, %: SiO_2 – 51; Al_2O_3 – 27; Fe_2O_3 – 4; CaO – 7; MgO – 2; Na_2O – 1; SO_3 – 2; LOI – 6. The material composition of fly ash includes aluminosilicate glass, quartz, mullite, and particles of unburned coal. The fly ash bulk density is 720 kg/m^3. The specific surface area of fly ash is 300 m^2/kg and does not require preliminary preparation of the material when introducing it into the molding mixture. The fly ash regulates the consistency of liquid glass molding mixtures and is active in geopolymerization processes. The low bulk density of fly ash is favorable for obtaining porous concrete. The use of fly ash helps to reduce thermal conductivity and increase the fire resistance of the material.

Chemical composition of ash aluminosilicate microsphere, %: SiO_2 – 68; Al_2O_3 – 25; Fe_2O_3 – 2; CaO – 5. Aluminosilicate microsphere consists of hollow glass-crystalline particles with a diameter of 50 – 200 μm. The microsphere is predominantly composed of aluminosilicate glass, and anorthite, mullite, and quartz are also present. Bulk density is 400 kg/m^3. Aluminosilicate microsphere serves as an elementary cell for the formation of a homogeneous porous structure of materials. The use of microsphere as an aggregate in concrete is due to its high dispersion, low density, high strength, increased resistance to thermal and aggressive effects.

The generally accepted methods were used to study the materials. A FSH-6K photosedimentometer was used to assess the dispersion of thermal energy waste. A hydrometer was used to determine the density of the liquid glass. To assess the overall porosity of the granules, the average density of both the starting material and the burnt granules was determined. The splitting method, taking into account the maximum force and the granule splitting area, was used to assess the strength of the fired granules. The arithmetic mean of the results of 10 tests on a PGM-1000MG4 hydraulic press was used to evaluate the granules' compressive strength.

The mass of the initial sample and the sample soaked in water for 1 day was compared to assess the water absorption of concrete.

The effect of liquids on the strength of the concrete under study was characterized by the coefficient of water resistance. For this purpose, the strength of concrete samples exposed to liquids was compared with the strength of concrete samples hardened in air.

Compressive strength of concrete was determined on testing samples measuring 70×70×70 mm by a PGM-1000MG4 hydraulic press.

The thermal conductivity coefficient of concrete was estimated using an ITP-MG4 device on samples measuring 100×100×10 mm.

Physical and mechanical tests of concrete were conducted on seven samples from each series. The range of test results was 4.2 – 5.8%.

To determine the phase composition of the materials, a modernized DRON-3M diffractometer with a BSV-24 X-ray tube with CuK α-radiation was used. The microstructure of the concrete was studied using a JSM-649OLV scanning electron microscope.

Porous aggregate is the basis of lightweight concrete. The fractional composition and porosity of the aggregate determine the density, thermal conductivity, and strength of lightweight concrete. Using computer modeling of the structure of large-pore geopolymer concrete, the fraction of granulated aggregate was adopted as 10 – 12 mm [32]. Hexagonal packing of aggregate particles with minimal separation of granules represents a stable framework.

The binding matrix holds the aggregate granules together at the contact points and partially fills the intergranular space (Figure 1). To obtain an aggregate of a given size, granules with a diameter of 8 – 10 mm and an average density of 970 kg/m^3 were molded from a liquid glass mixture.

Granules were porousized by thermal swelling. The effect of processing temperature on the composition, structure, and properties of granules was studied (Figure 2, Tables 2 and 3).

Temperatures of 150, 250, and 350°C with isothermal exposure for 60 minutes were selected for firing pellets. The formation of granules of a regular spherical shape was achieved as a result of swelling.

At the same time, the temperature of 150°C made it possible to achieve the optimal swelling coefficient of the granules – 1.20. With a subsequent increase in temperature, the diameter of the granules remained virtually unchanged (Table 2).

Firing granules at a temperature of 150°C ensures the greatest porosity.

The compressive strength and water resistance of granules are very sensitive to the firing temperature (Table 3). An increase in the firing temperature from 150 to 250 and 350°C is accompanied by an increase in the compressive strength of the granules by 1.7 and 1.5 times, respectively, and an increase in the water resistance of the granules by 3.0 and 3.5 times, respectively.

The increased compressive strength and water resistance of granules fired at temperatures of 250 and 350°C are due to the presence of crystalline compounds.

During heat treatment of a liquid glass mixture with the participation of anorthite and aluminosilicate amorphous phases, calcium and sodium hydroalumosilicates are formed, mainly hydrogelenite C_2ASH_8 and hydrosodalite NAS_2H_2 (Table 3).

The hardening of the material and an increase in its water resistance are achieved as a result of an increase in the proportion of crystalline compounds with increasing temperature.

To bind the porous aggregate in the concrete mixture, a binder with a similar composition to the granules is used. On the one hand, genetic kinship ensures reliable bonding of the concrete components and helps to increase the compressive strength of the material. On the other hand, liquid glass, having high adhesion to the porous aggregate, gives the concrete matrix a pronounced binding capacity. Thirdly, the related composition of raw mixes for the aggregate and binder of geopolymer concrete will allow organizing integrated production and reducing the firing temperature of granules to 150 – 200°C.

The low-temperature firing method makes it possible to ensure the strength of the granules is sufficient to preserve their integrity during further processing. Further firing of geopolymer concrete at a temperature of 350°C will make it possible to ensure the hardening of the binder and the hardening of the porous aggregate.

In the studied molding mixture, the ratio of the aggregate and binder volumes equal to 9:1 ensured the distribution of the binder matrix around the granules and partial placement in the intergranular space. To prepare the molding mixture, liquid glass was mixed with fly ash and an aluminosilicate microsphere.

The resulting suspension was mixed with porous granules, evenly distributing the binder between the aggregate. The flowability of the molding mixture was characterized by 2 – 3 cm of slump of the Abrams cone. Concrete curing mode: 1 hour – preliminary curing, 2 hours – heating to a temperature of 350°C; 2 hours – isothermal holding, 1 hour – cooling. The choice of the maximum temperature of concrete processing is made taking into account the thermal transformations during firing of the granulated liquid glass mixture (Table 3).

The results of tests of large-pore concrete are presented in Table 4.

The compressive strength of the structure of large-pore concrete is ensured by reliable adhesion of the aggregate to the binder in the interfacial transition zones (Figure 3).

The operational resistance of geopolymer concrete to the impact of water, magnesium sulfate, and sodium sulfate solutions was studied.

Concrete samples were kept in liquid media for 24 months, and visual studies were carried out (Figure 4). The concrete resistance coefficient was determined after 3, 6, 12, and 24 months (Table 5).

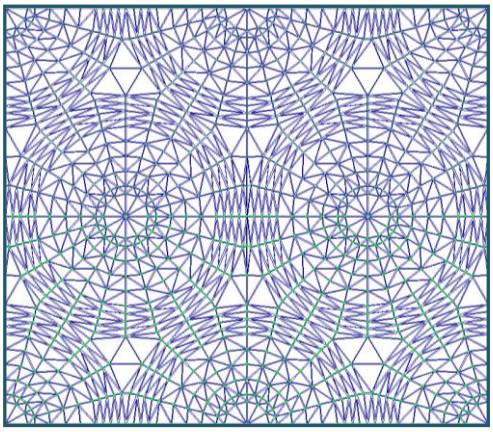

Figure 1 – Model of the structure of large-pore concrete

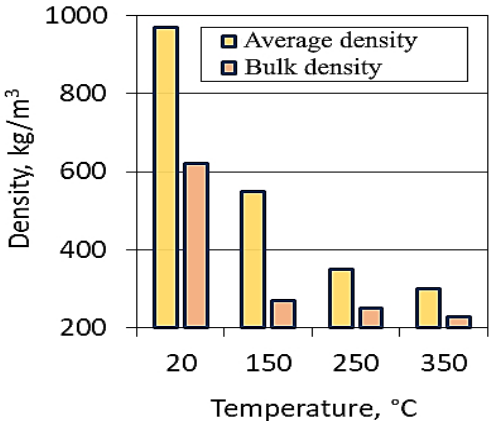

Figure 2 – Effect of processing temperature on granule density

Table 2 – Effect of firing temperature on granule structure

Firing temperature, °C	Swelling coefficient	Porosity, %	Granule structure mm	Microstructure
150	1.20	73.2		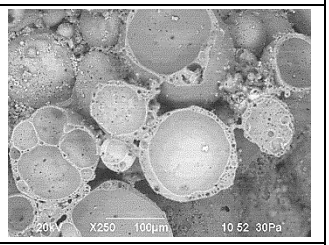
250	1.20	76.0		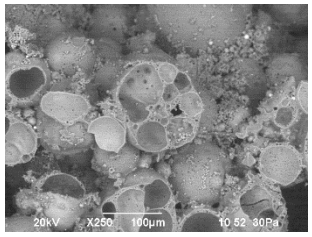
350	1.20	78.1		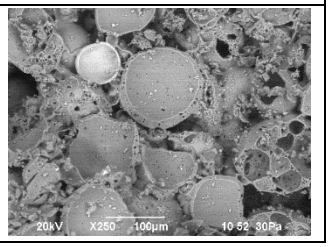

Discussion of results

The concrete samples that were in water did not show any external signs of change (Figure 4).

The decrease in concrete strength should be associated with a decrease in the proportion of the amorphous component, as indicated by the decrease in the spectrum against the background of the XRD pattern in the range of angles of 16 – 38 degrees.

Concrete samples were observed to transform a magnesium sulfate solution (3% concentration) starting from 2 months.

The structure and components of the concrete retained their stability. At the same time, white amorphous clusters of magnesium hydroxide appeared in the intergranular space, which increased in size and became denser by 12 months (Figure 4).

Table 3 – Effect of firing temperature on the granules' composition and properties

XRD pattern *A – anorthite, K – quartz, M – mullite, H – hydrogelenite, N – hydrosodalite*	Compressive strength, MPa	Water resistance coefficient
Unfired		
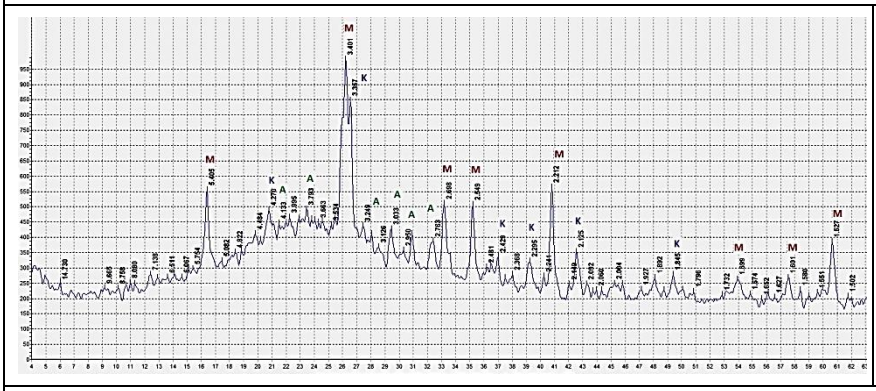	No determined	
150°C		
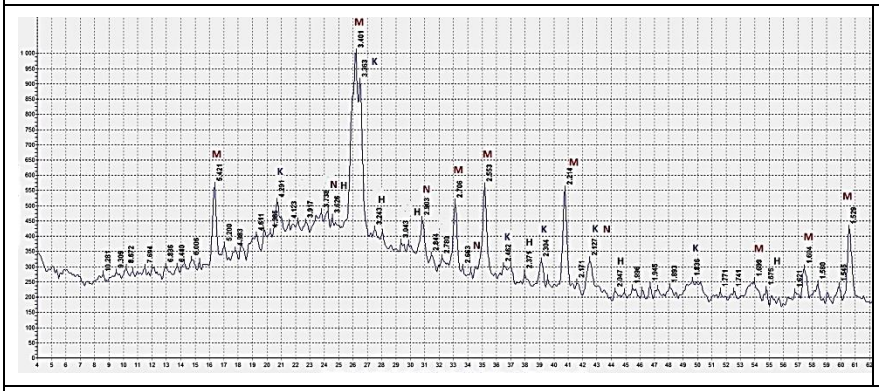	1.9	0.25
250°C		
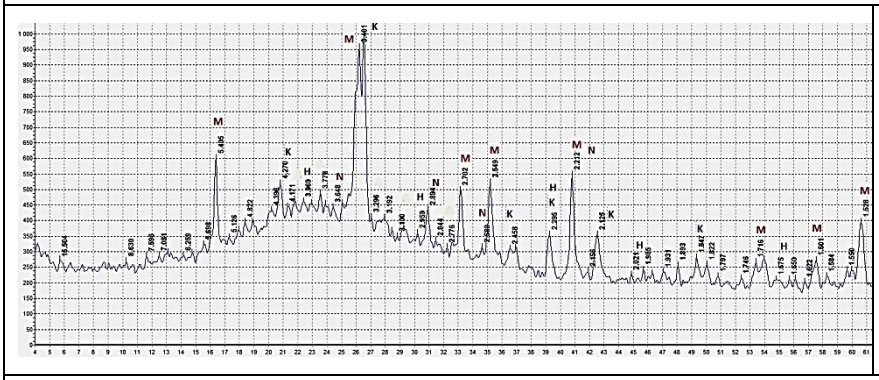	3.3	0.75
350°C		
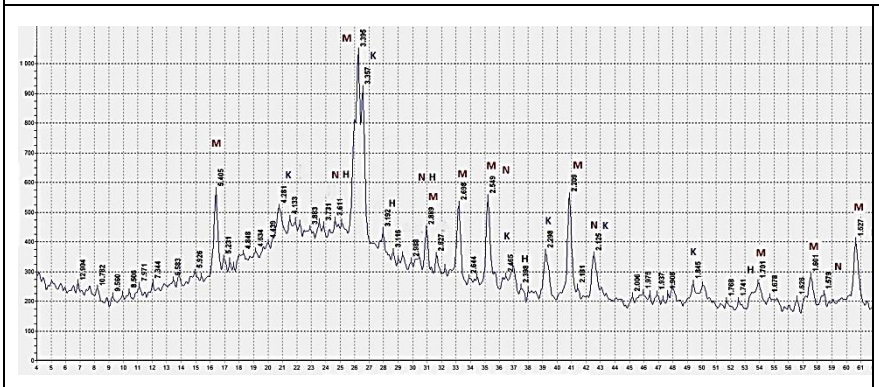	2.9	0.87
Intensity, pulse/s		
2Θ, degree		

General appearance | **Nature of destruction under compression by a press** | **Microstructure (red line – interfacial transition zone)**

Figure 3 – Structure of large-pore geopolymer concrete

Table 4 – Properties of large-pore geopolymer concrete

Properties	Values
Average density, kg/m^3	480
Compressive strength, MPa	4.7
Water absorption, %	31.0
Water resistance coefficient	0.87
Thermal conductivity coefficient, W/(m·°C)	0.095

The samples' state was stable from 12 to 24 months of exposure to a magnesium sulfate solution. The intensity of hydrate reflections changed in the concrete diffraction pattern (Figure 4): hydrosodalite reflections increased (d/n = 3.678; 2.671; 2.106 Å), and hydrogelenite reflections decreased (d/n = 3.576; 2.37; 1.734 Å).

The presence of geopolymer concrete in a sodium sulfate solution (concentration 5%) is accompanied by significant transformations of the composition and structure. After 2 months of exposure to an aggressive environment, thinning and destruction of the binder shells around the granules was observed.

This phenomenon is the result of the leaching of hydrate compounds from the geopolymer binder. This is confirmed by the data of diffractometric analysis: the «elevation» in the spectrum in the range of 16 – 38 degrees decreases.

Over the time of exposure of concrete to the sodium sulfate solution, gel-like masses appeared in the intergranular space and on the surface of the aggregate, released from the aggressive solution saturated with amorphous phases (Figure 4). The increased resistance of the granules compared to the binder matrix of concrete is due to the greater vulnerability of the matrix to external influences and the quantitative difference in the composition (Table 5).

For the economic assessment of large-pore geopolymer concrete, calculations of material and energy costs for the production of 1 m^3 of concrete were carried out.

For comparison, the indicators of cement expanded clay concrete of a similar structure, characterized by a thermal conductivity coefficient of 0.155 W/(m·°C), were used. The costs of the components of the molding mix of geopolymer concrete, according to preliminary calculations, are 84.5 U.S. dollars/m^3, which is 4.9 U.S. dollars/m^3 less than for cement expanded clay concrete.

The estimated energy costs for obtaining geopolymer concrete are 2.2 U.S. dollars/m^3, which is 1.4 times higher than the same indicator for cement expanded clay concrete.

This is due to the proposed mode of heat treatment of geopolymer concrete. Total costs of materials and energy for geopolymer concrete are 86.7 U.S. dollars/m^3, which is 4.3 U.S. dollars/m^3 less than for expanded clay concrete.

Large-pore geopolymer concrete is effective as thermal insulation. For the thermal resistance of the enclosing structure equal to 3.279 (m^2·°C)/W, the required thickness of the thermal insulation layer is: made of geopolymer concrete, a = [3.279 (m^2·°C)/W]·[0.095 W/(m·°C)] = 0.311 m; made of cement expanded clay concrete, a = [3.279 (m^2·°C)/W]·[0.155 W/(m·°C)] = 0.508 m.

The use of porous geopolymer concrete allows for a 1.63 – fold reduction in the consumption of materials for thermal insulation of wall structures.

The prospects for the implementation of the developed geopolymer porous concretes lie in their ability to give impetus to the development of small businesses in various regions [33].

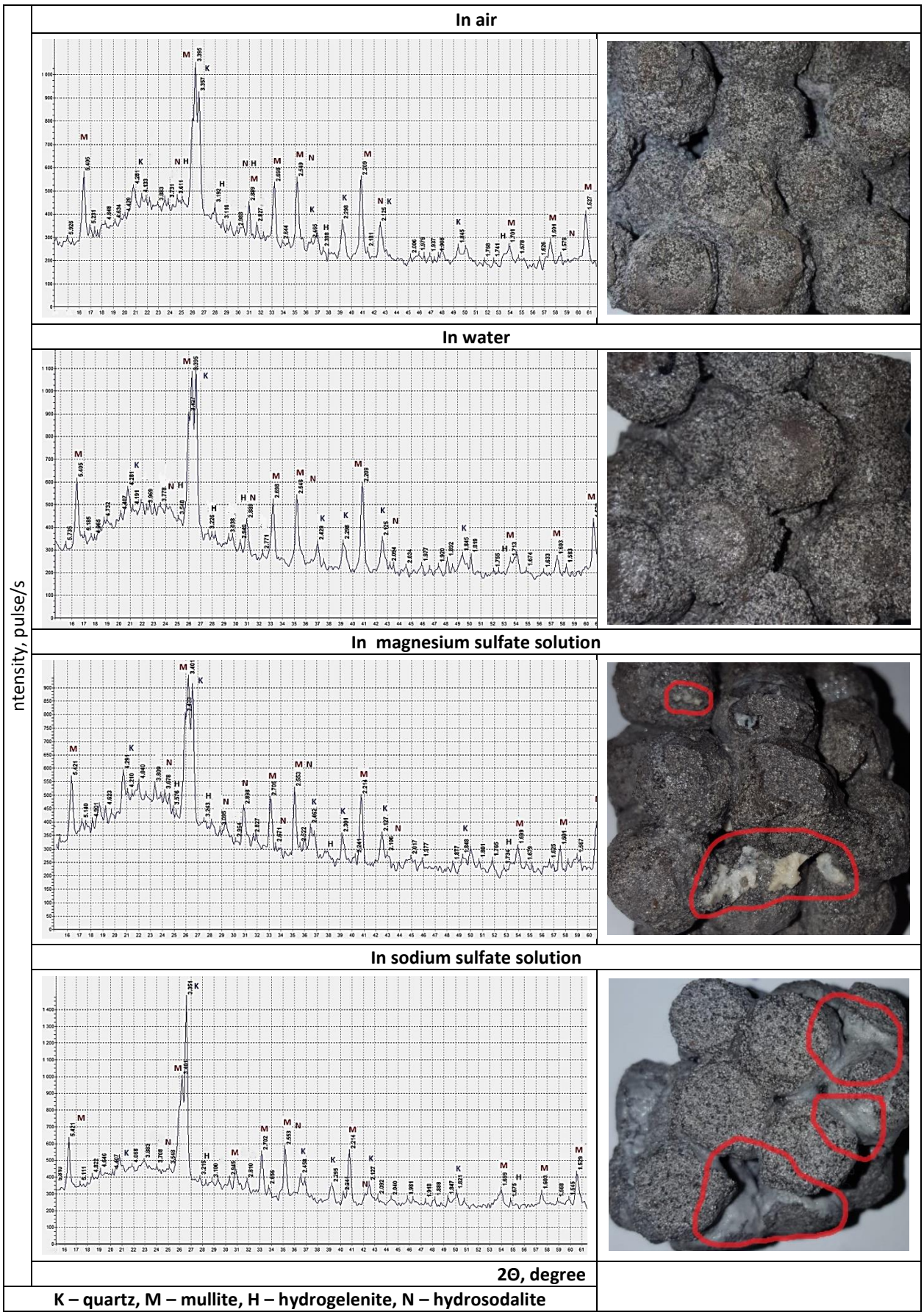

Figure 4 – XRD patterns (1) and appearance (2) of geopolymer concrete after 24 months of exposure to various environments

Table 5 – Resistance of geopolymer concrete to aggressive environments

Duration of the test, months	Resistance coefficient of geopolymer concrete		
	in water	*in magnesium sulfate solution (concentration 3%)*	*in sodium sulfate solution (Concentration 5%)*
3	0.82	0.76	0.52
6	0.78	0.73	0.48
12	0.76	0.70	0.45
24	0.75	0.69	0.40

Conclusions

Large-pore concrete has been developed, in which the binder and aggregate are formed as a result of geopolymerization processes.

The following main results were obtained.

Liquid-glass activation of thermal energy waste in combination with thermal treatment ensures the formation of a water-resistant composition and a stable porous structure of geopolymer concrete.

The use of raw mixes of related composition for the synthesis of porous aggregate and binder allows integrating technological processes, ensuring reliable adhesion of the components of geopolymer concrete.

The results of studies of phase transformations of geopolymer material under the influence of water and salt solutions indicate the prospects for further improvement of the technology of porous geopolymer concrete and the expansion of its scope of application.

Conflicts of interest. The author states that he has no conflicts of interest to disclose.

Gratitude: This research has been funded by the Science Committee of the Ministry of Science and Higher Education of the Republic of Kazakhstan (Grant No. AP26199493).

Cite this article as: Miryuk OA. Geopolymer porous concrete: formation and performances. Kompleksnoe Ispolzovanie Mineralnogo Syra = Complex Use of Mineral Resources. 2027; 343(4):95-105. https://doi.org/10.31643/2027/6445.43

Геополимерлі кеуекті бетон: қалыптастыру және пайдалану сипаттамалары

Мирюк О.А.

Рудный индустриялық университеті, Рудный, Қазақстан

Мақала келді: *6 қаңтар 2026*
Сараптамадан өтті: *4 наурыз 2026*
Қабылданды: *11 наурыз 2026*

ТҮЙІНДЕМЕ

Мақалада геополимерлік технологияны әзірлеу және кеуекті толтырғыш негізінде жеңіл бетонның сипаттамаларын зерттеу нәтижелері ұсынылған. Зерттеудің мақсаты – кеуекті геополимерлік бетонды қалыптастыру және пайдалану сынақтары процесінде құрамы мен құрылымының өзгерістерін анықтау. Кеуекті толтырғыш пен байланыстырушы зат ұқсас құрамдағы қалыптау қоспаларынан синтезделген, олардың құрамында сұйық натрий шынысы мен жылу электр станцияларынан алынған ұсақ дисперсті қалдықтар (ұшпа күл мен алюмосиликатты микросфера) бар. Механикалық жүктемеге және судың әсеріне қанағаттанарлық төзімділігі бар кеуекті құрылымды қалыптастыруды қамтамасыз ететін бетонды қатайтудың жылу режимі ұсынылды. Геополимерлік материалдың термиялық синтезі кезінде жүретін фазалық түрленулер, бетонға суға және магний мен натрий сульфатының ерітінділеріне ұзақ уақыт әсер ету кезіндегі өзгерістер зерттелді. Керамзит негізіндегі бетонмен салыстырғанда кеуектелген геополимерлік бетонның артықшылықтарын растайтын алдын ала экономикалық есептеулер жүргізілді. Әзірленген кеуекті геополимерлік бетондар энергия үнемдейтін қабырға бұйымдарын өндіруге арналған.

Түйін сөздер: Геополимерлеу, сұйық шыны, ірі кеуекті бетон, күл-тасу, тұз агрессиясы.

Мирюк Ольга Александровна

Авторлар туралы ақпарат:
Техника ғылымдарының докторы, профессор, Рудный индустриялық университеті, 111500, Октябрге 50 жыл көшесі, 38, Рудный, Қазақстан. E-mail: psm58@mail.ru; ORCID ID: https://orcid.org/0000-0001-6892-2763

Геополимерный пористый бетон: формирование и эксплуатационные характеристики

Мирюк О.А.

Рудненский индустриальный университет, Рудный, Казахстан

Поступила: *6 января 2026*
Рецензирование: *4 марта 2026*
Принята в печать: *11 марта 2026*

АННОТАЦИЯ

В статье представлены результаты разработки геополимерной технологии и исследования характеристик легкого бетона на основе пористого заполнителя. Цель исследования – выявление преобразований состава и структуры в процессе формования и эксплуатационных испытаний пористого геополимерного бетона. Пористый заполнитель и вяжущее синтезированы из формовочных смесей родственного состава, содержащих жидкое натриевое стекло и мелкодисперсные отходы тепловых электростанций (зола-уноса и алюмосиликатная микросфера). Предложен тепловой режим отверждения бетона, обеспечивающий формирование пористой структуры, которая имеет удовлетворительную стойкость к механической нагрузке и воздействию воды. Исследованы фазовые превращения при термическом синтезе геополимерного материала, при продолжительном воздействии на бетон воды и растворов сульфата магния и натрия. Выполнены предварительные экономические расчеты, свидетельствующие о преимуществах поризованного геополимерного бетона по сравнению с цементным бетоном на основе керамзита. Разработанные геополимерные поризованные бетоны предназначены для энергоэффективных стеновых изделий.

Ключевые слова: Геополимеризация, жидкое стекло, крупнопористый бетон, зола-уноса, солевая агрессия.

Мирюк Ольга Александровна

Информация об авторах:
Доктор технических наук, профессор, Рудненский индустриальный университет, 111500, улица 50 лет Октября, 38, Рудный, Казахстан. E-mail: psm58@mail.ru; ORCID ID: https://orcid.org/0000-0001-6892-2763

References

[1] Khawaja SA, Javed U, Zafar T, Riaz M, Zafar MS, Khan MK. Eco-friendly incorporation of sugarcane bagasse ash as partial replacement of sand in foam concrete. Cleaner Engineering and Technology 2021; 4:100164. https://doi.org/10.1016/j.clet.2021.100164

[2] Nurbayeva M, Aruova L, Lukpanov R, Vainberger S, Gunasekaran M. Fine-grained fiber concreteusing polypropyleneand basalt fibers. Kompleksnoe Ispolzovanie Mineralnogo Syra = Complex Use of Mineral Resources. 2023; 326(3):32-40. https://doi.org/10.31643/2023/6445.26

[3] Miryuk OA. Magnesia composite materials for layered products. Kompleksnoe Ispolzovanie Mineralnogo Syra = Complex Use of Mineral Resources. 2024; 328(1):5-12. https://doi.org/10.31643/2024/6445.01

[4] Benhelal E, Shamsaei E, Rashid MI. Challenges against CO_2 abatement strategies in cement industry: A review. Journal of Environmental Sciences. 2021; 104:84–101. https://doi.org/10.1016/j.jes.2020.11.020

[5] Tang Y, Qiu J. CO_2-sequestering ability of lightweight concrete based on reactive magnesia cement and high-dosage biochar aggregate. Journal of Cleaner Production. 2024; 451:141922. https://doi.org/10.1016/j.jclepro.2024.141922

[6] Bouaissi A, Li L, Abdullah MM, Bui Q. Mechanical properties and microstructure analysis of FA-GGBS-HMNS based geopolymer concrete. Construction and Building Materials. 2019; 210:198–209. https://doi.org/10.1016/j.conbuildmat.2019.03.202

[7] Jeon IK, Qudoos A, Woo BH, Yoo DH, Kim HG. Effects of nano-silica and reactive magnesia on the microstructure and durability performance of underwater concrete. Powder Technology. 2022; 398:116976. https://doi.org/10.1016/j.powtec.2021.11.020

[8] Miryuk OA. The effect of waste on the formation of cement clinker. IOP Conference Series: Materials Science and Engineering. 2019; 510(1):012012. https://doi.org/10.1088/1757-899X/510/1/012012

[9] Javed U, Shaikh FUA, Sarker PK. Microstructural investigation of lithium slag geopolymer pastes containing silica fume and fly ash as additive chemical modifiers. Cement and Concrete Composites. 2022; 134:104736. https://doi.org/10.1016/j.cemconcomp.2022.104736

[10] Arslan S, Öz A, Benli A, Bayrak B, Kaplan G, Aydın AC. Sustainable use of silica fume and metakaolin in slag/fly ash-based self-compacting geopolymer composites: Fresh, physico-mechanical and durability properties. Sustainable Chemistry and Pharmacy. 2024; 38:101512. https://doi.org/10.1016/j.scp.2024.101512

[11] Du J, Liu Z, Christodoulatos C, Conway M, Bao Y, Meng W. Utilization of off-specification fly ash in preparing ultra-high-performance concrete (UHPC): Mixture design, characterization, and life-cycle assessment. Resources, Conservation and Recycling. 2022; 180:106136. https://doi.org/10.1016/j.resconrec.2021.106136

[12] Lee SW, You I, Oh T, Kim GW, Banthia N, Yoo DY. Effect of liquid crystal display glass powder to blast furnace slag ratio on the microstructure and mechanical properties of ultra-high-performance alkali-activated concrete. Construction and Building Materials. 2024; 444:137755. https://doi.org/10.1016/j.conbuildmat.2024.137755

[13] Serelis E, Vaitkevicius V. Effect of waste glass powder and liquid glass on the Physico-Chemistry of Aluminum-Based Ultra-Lightweight concrete. Construction and Building Materials. 2023; 390:131615. https://doi.org/10.1016/j.conbuildmat.2023.131615

[14] Juengsuwattananon K, Winnefeld F, Chindaprasirt P, Pimraksa K. Correlation between initial SiO_2/Al_2O_3, Na_2O/Al_2O_3, Na_2O/SiO_2 and H_2O/Na_2O ratios on phase and microstructure of reaction products of metakaolin-rice husk ash geopolymer. Construction and Building Materials. 2019; 226:406–417. https://doi.org/10.1016/j.conbuildmat.2019.07.146

[15] Samarakoon MH, Ranjith PG, De Silva VRS. Effect of soda-lime glass powder on alkali-activated binders: Rheology, strength and microstructure characterization. Construction and Building Materials. 2020; 241:118013. https://doi.org/10.1016/j.conbuildmat.2020.118013

[16] Tan Y, He Y, Cui X, Liu L. The influence of different water glass moduli on the chemical corrosion resistance of alkali-activated porous concrete. Construction and Building Materials. 2024; 415:134971. https://doi.org/10.1016/j.conbuildmat.2024.134971

[17] Singh RP, Mohanty B. Effect of waste glass powder on the durability and microstructural properties of fly ash-GGBS based alkali activated concrete containing 100% recycled concrete aggregate. Construction and Building Materials. 2024; 447:138024. https://doi.org/10.1016/j.conbuildmat.2024.138024

[18] Pacheco-Torgal F, Castro-Gomes J, Jalali S. Alkali-activated binders: A review. Part 2. About materials and binders manufacture. Construction and Building Materials. 2008; 22:1315–1322. https://doi.org/10.1016/j.conbuildmat.2007.03.019

[19] Ozer I, Soyer-Uzun S. Relations between the structural characteristics and compressive strength in metakaolin based geopolymers with different molar Si/Al ratios. Ceramics International. 2015; 41:10192–10198. https://doi.org/10.1016/j.ceramint.2015.04.125

[20] Singh B, Ishwarya G, Gupta M, Bhattacharyya SK. Geopolymer concrete: A review of some recent developments. Construction and Building Materials. 2015; 85:78–90. https://doi.org/10.1016/j.conbuildmat.2015.03.036

[21] Buchwald A, Zellmann HD, Kaps Ch. Condensation of aluminosilicate gels – model system for geopolymer binders. Journal of Non-Crystalline Solids. 2011; 357(5):1376–1382. https://doi.org/10.1016/j.jnoncrysol.2010.12.036

[22] Yoo DY, Lee Y, You I, Banthia N, Zi G. Utilization of liquid crystal display (LCD) glass waste in concrete: A review. Cement and Concrete Composites. 2022; 130:104542. https://doi.org/10.1016/j.cemconcomp.2022.104542

[23] Thatikonda N, Mallik M, Sarella VR, Dubey S. Evaluation of self-compacting geopolymer concrete properties containing different water glass solutions. Sustainable Chemistry and Pharmacy. 2024; 41:101680. https://doi.org/10.1016/j.scp.2024.101680

[24] Mukhametkaliyev T, Ali MH, Kutugin V, Savinova O, Vereschagin V. Influence of Mixing Order on the Synthesis of Geopolymer Concrete. Polymers. 2022; 14:4777. https://doi.org/10.3390/polym14214777

[25] Zhao Z, Qu X, Li Z, He T, Li F. Preparation and characterization of geopolymer foamed concrete based on coal gangue and slag. Construction and Building Materials. 2024; 455:139187.https://doi.org/10.1016/j.conbuildmat.2024.139187

[26] Miryuk O, Fediuk R, Amran M. Foam Glass Crystalline Granular Material from a Polymineral Raw Mix. Crystals. 2021; 11:1447. https://doi.org/10.3390/cryst11121447

[27] Mohammed Al-Saudi SK, Géber R. Production of lightweight geopolymer concrete with foam glass aggregate derived from cathode-ray glass waste. Case Studies in Construction Materials. 2024; 21:e03888. https://doi.org/10.1016/j.cscm.2024.e03888

[28] Miryuk O, Fediuk R, Amran M. Porous Fly Ash/AluminosilicateMicrospheres-Based CompositesContaining Lightweight Granules Using Liquid Glass as Binder. Polymers. 2022; 14:3461. https://doi.org/10.3390/polym14173461

[29] Gopalakrishna B, Dinakar P. The evaluation of the life cycle and corrosion properties of recycled aggregate geopolymer concrete incorporating fly ash and GGBS. Journal of Building Engineering. 2024; 94:109977. https://doi.org/10.1016/j.jobe.2024.109977

[30] Singh RP, Vanapalli KR, Jadda K, Mohanty B. Durability assessment of fly ash, GGBS, and silica fume based geopolymer concrete with recycled aggregates against acid and sulfate attack. Journal of Building Engineering. 2024; 82:108354. https://doi.org/10.1016/j.jobe.2023.108354

[31] Shafiei S, Mohammadi Y. Effect of AR-glass fibers and natural micronized zeolite on mechanical and permeability properties of concrete exposed to normal, sodium chloride, and magnesium sulfate environments. Construction and Building Materials. 2024; 457:139288. https://doi.org/10.1016/j.conbuildmat.2024.139288

[32] Miryuk O, Oleinik A, Akhmedov K. Influence of packaging of discrete fillers on elastic characteristics of lightweight concrete. AIP Conference Proceedings. 2022; 2657:020040. https://doi.org/10.1063/5.0106705

[33] Levkina EV, Titova NY. The Analysis of the Financial Condition of Small Business and the Ways of its Development in the Primorsky Territory. IOP Conference Series: Earth and Environmental Science. 2019; 272(3):032185 https://doi.org/10.1088/1755-1315/272/3/032185

Crossref
DOI: 10.31643/2027/6445.44
Mining & Mineral Processing

Exponential modeling of Al_2O_3 reduction during activation of Navbahor alkaline-earth bentonite

[1*]Boyjanov N.I., [2]Otajonova G.M., [3]Kendjayev B.B., [1]Matyakubova M.X., [1]Sabirova N.K., [4]Masharipov A.T., [1]Boyjanov I.R., [5]Serkayev Q.P.

[1]Urgench State University named after Abu Rayhon Beruni, Urgench, Uzbekistan
[2]Mamun University, Khiva, Uzbekistan
[3]Urgench Innovation University, Urgench, Uzbekistan
[4]Academic Lyceum of Urgench State University, Urgench, Uzbekistan
[5]Tashkent Chemical-Technological Institute, Tashkent, Uzbekistan

**Corresponding author email: b.nodirbek@urdu.uz*

Received: *February 9, 2026*
Peer-reviewed: *February 27, 2026*
Accepted: *March 16, 2026*

ABSTRACT
In this study, using mathematical modeling, the change in Al2O3 content as a function of acid concentration during hydrochloric acid activation of alkaline-earth bentonite from the Navbahor deposit is investigated. During the experiment, the HCl concentration varied from 5% to 20%, and the change in Al2O3 content was nonlinear. To describe the experimental data obtained during hydrochloric acid activation of alkaline-earth bentonite from the Navbahor deposit, an exponential decay model was proposed, and its parameters were estimated by regression analysis. The accuracy of this approach is supported by the coefficient of determination (R^2 = 0.964) and the root mean square error (RMSE = 0.231%), indicating high accuracy and stability. The results obtained show that the decrease in Al_2O_3 content under acid activation conditions exhibits a nonlinear dependence on hydrochloric acid concentration rather than on time, and they enable formulation of a mathematical expression for the quantitative description of the process and for evaluating the effect of concentration.

Keywords: bentonite, acid, activation, relative area, modelling, exponential decay, coefficient of determination (R^2).

Information about authors:

Boyjanov Nodirbek Ilxomovich — *Doctor of Philosophy in Technical Sciences, Associate Professor at the Faculty of Chemical Technology, Urgench State University named after Abu Rayhon Beruni, 220100, H. Olimjon Street 14, Urgench, Uzbekistan. Email: b.nodirbek@urdu.uz; ORCID ID: https://orcid.org/0009-0002-1454-9478*

Otajonova Gulkhayo Maqsud kizi — *Teacher at Mamun University, Khiva, Khorezm, Uzbekistan. Email: otajonovagulhayo1508@gmail.com; ORCID ID: https://orcid.org/0009-0008-7529-9656*

Kendjayev Bunyod Bahtiyor ugli — *Teacher, Urgench Innovation University, Khorezm region, Urgench, Uzbekistan. Email: bun0401kbb@gmail.com; ORCID ID: https://orcid.org/0009-0002-3235-5159*

Matyakubova Mavlyuda Xudayberganovna — *Doctor of Philosophy in Technical Sciences, Associate Professor at the Faculty of Chemical Technology, Urgench State University named after Abu Rayhon Beruni, 220100, H. Olimjon Street 14, Urgench, Uzbekistan. Email: matyaqubovamavluda2010@gmail.com; ORCID ID: https://orcid.org/0009-0000-2961-3626*

Sabirova Nadira Kamiljanovna — *Doctor of Philosophy in Technical Sciences, Associate Professor at the Faculty of Chemical Technology, Urgench State University named after Abu Rayhon Beruni, 220100, H. Olimjon Street 14, Urgench, Uzbekistan. Email: nodira.sob11@gmail.com; ORCID ID: https://orcid.org/0000-0001-9685-9861*

Masharipov Azamat Tursunboyevich — *Doctor of Philosophy in Chemical Sciences, Teacher Academic Lyceum of Urgench State University, Fayozov 27, Urgench, Uzbekistan. Email: yadrokimyo1@gmail.com; ORCID ID: https://orcid.org/0009-0003-3537-3130*

Boyjanov Islom Rajabboyevich — *Candidate of Technical Sciences, Associate Professor of the Faculty of Chemical Technology, Urgench State University named after Abu Rayhon Beruni, 220100, H. Olimjon Street 14, Urgench, Uzbekistan. Email: rajrajrajradju@gmail.com; ORCID ID: https://orcid.org/0000-0002-8416-5472*

Serkayev Qamar Pardayevich — *Professor at the Tashkent Institute of Chemical Technology, Navoi Street, 32, Tashkent, Uzbekistan. Email: serkayev@mail.ru; ORCID ID: https://orcid.org/0009-0009-8316-4994*

Introduction

At present, the development of adsorbents for the chemical and food industries, along with their technological enhancement, is recognized as one of the most pressing scientific and technical challenges. In this regard, a lot of research has been conducted to create modified adsorbents with micro-, meso-, and macroporous structures, along with their capacity to perform processes such as ion

exchange and chemical bonding, to improve their technological efficiency under actual conditions [[1], [2], [3], [4]].

Activation methods for bentonite clays are applied under different conditions, depending on their mineral composition, structure, chemical composition, and intended use.

Acid activation is a chemical modification process wherein H^+ ions replace exchangeable metal ions, such as K^+, Na^+, Ca^{2+}, and Mg^{2+}. The removal of metal ions, located within the interlayer space, results in a silica-rich structure. At the same time, a variety of active sites are created during the process of acid activation, which increases the sorption potential of the clay material [5].

Natural pigments like chlorophyll, xanthophyll, carotenoids, gossypol, soapstock, and other soap-like compounds, free fatty acids, and peroxides, etc., present in vegetable oils, vary in nature due to their physicochemical properties. Depending upon the nature of the compounds present, the process of refining vegetable oils is carried out, either completely or partially, through processing cycles. The quality of the oil produced by various methods is evaluated based on the physicochemical properties of the oil produced by various methods. The properties include phospholipid, moisture, and volatile matter content, iodine value, color index, refractive index, and saponification value, etc. Improvement of these properties is not only related to the reagents used but is also associated with the application of advanced technology in the production process [[6], [7], [8], [9], [10], [11], [12]].

The mathematical modeling of any production process allows, in advance, the formulation of well-founded forecasts regarding the term of the technological process, the amount of consumed raw materials, and the quantity and quality of the obtained products. This allows the improvement of the stability and efficiency of the production process. Industrial and processing processes require the construction of mathematical models that allow the identification and quantification of the interaction between the technological parameters, such as moisture, temperature, concentration, pH, and others [[6], [7], [8], [9], [10]].

Mathematical modeling can also have an important methodological impact on the process of acid activation of bentonite clays, making it possible to describe changes in chemical composition during experiments in a unified and generalized form, which would allow us to speak of a controlled and predictable process. In particular, mathematical modeling can significantly inform the description of processes of interaction with mineral acids, including the specific leaching of Al^{3+} ions from the mineral's octahedral layer and the formation of an amorphous SiO_2-rich phase [11].

The selection of exponential decay models is substantiated by the high accuracy that can be obtained with a small number of parameters and also by the robustness to errors in experiments. In these models, the rate constant serves as a universal criterion for kinetic analysis, enabling comparative studies of different raw materials and processes. Experimental evidence from a wide range of investigations published in the literature confirms that, for bentonite clays, an increase in acid concentration results in a substantial increase in leaching rate for Al^{3+}, Mg^{2+}, and other cations from the octahedral layer. The complex kinetic character of the process requires the use of non-linear regression models for adequate description [[12], [13]].

The mathematical modeling allows for a quantitative description of the overall kinetic trend detected during the process of acid activation of bentonite clays. It was detected that the decrease in Al_2O_3 content has a non-linear dependence on the acid concentration during the process, being rapid at the initial stages and slowing down with time, which can be described by a general kinetic pattern. An exponential decay model has been used as a simplified model from a statistical point of view. Its adequacy is checked based on the experiment [[14], [15]].

One of the key benefits of modeling is the possibility of a formal definition of product quality-oriented objective functions (such as the consistent decrease or stabilization of the Al_2O_3 content over a certain range), thereby creating the necessary basis for the calculation of the optimal acid concentration [16].

While the results of polynomial regression models can describe experimental points with a high degree of accuracy, they do not necessarily reflect real physicochemical processes. On the other hand, the exponential model naturally describes the process of Al_2O_3 depletion, the deceleration of which with increasing HCl concentration is quite logical, and yields stable results in prediction [[17], [18]].

The physical meaning of the selective leaching of Al^{3+} ions while preserving the structural framework is logically consistent with the exponential decay-type kinetic law. In making a justified choice between two or more models, the

coefficient of determination (R^2) value alone is not enough; rather, a detailed analysis including the root mean square error (RMSE) is needed [[19], [20], [21]].

The kinetic methods used in acid leaching processes provide a fundamental scientific tool for quantitative measurement and control of rate. They describe the rate of leaching with respect to time using mathematical expressions, which helps to determine the rate-controlling step of a chemical reaction [[22], [23]].

If, after such treatment by acid, there are no changes in the position of the peaks corresponding to the Si-O bonds, it is considered that these changes are mainly related to the selective leaching of Al, Mg, and Fe cations from the octahedral layer. It is then considered that the initial structure of tetrahedral Si-O bonds remains stable [[24], [25], [26], [27], [28], [29]]. Due to this process, the crystal lattice of clay minerals is preserved, and the main framework is kept intact. At the same time, the leaching of cations from the octahedral layer enhances the surface area and porosity of the material. Hence, this modified form of clay can be utilized effectively in adsorption and catalytic purposes [[30], [31], [32], [33], [34], [35]].

The mathematical way of understanding this activation process allows for the quantitative prediction of the sorption properties of the clay, which reduces the number of experiments and optimizes this process. With this approach, it is possible to plan the consumption of acid and water at a rational level, and it is possible to determine in advance the probable amount of additional reagents to be used. Thus, this activation process not only becomes scientifically understandable and controllable but also becomes an important tool for making efficient use of resources, for improving energy efficiency, and for reducing technological costs.

In this study, a new approach to summarizing experimental data was developed, which is based on a table, graph, and model sequence, thus facilitating the identification of a continuous governing relationship of the process from discrete experimental points. This new approach allows one to consider changes in Al_2O_3 content not only from a statistical point of view, but also in relation to the physicochemical nature of the acid activation process. Therefore, this study presents a new scientific and methodological basis for a deeper understanding of the acid activation of bentonites, the effective conditions of this process, and a predictive assessment of further stages of this process.

In this work, an exponential decay model is proposed for describing the variation of Al_2O_3 content as a function of hydrochloric acid concentration. Using this model, it is possible to represent quantitatively the non-linear and strictly decreasing trend of the experimental data.

Materials and Methods

As the object of the study, the alkaline earth (calcium-type) bentonite from the Navbahor deposit was chosen. In the chemical composition of the natural bentonite clay, Al_2O_3 makes up 12.60% as the main exchangeable component. The SiO_2 content is 61.54%, which shows that this mineral has a silica-based structure. The high percentage of SiO_2 ensures the stability of the mineral layers and acts as a non-degradable framework during the acid activation process.

Additionally, the chemical composition of the bentonite clay contains small amounts of other oxides, and their composition is shown in Table 1. The chemical composition was not used as an initial parameter for the simulation of the kinetics of the reduction of Al_2O_3 during hydrochloric acid activation, as the simulation is based on the process that begins after the onset of acid activation.

Table 1 - Chemical composition of natural alkaline-earth bentonite from the Navbahor deposit

Sample	Content, %							
	SiO_2	Al_2O_3	Fe_2O_3	TiO_2	CaO	MgO	Na_2O	K_2O
Natural bentonite clay	61.54	12.60	6.23	0.56	0.75	3.98	0.82	2.11

Bentonite clay with a sample mass of 100 g was activated with different concentrations of HCl solution (5%, 10%, 15%, and 20%) with a ratio of 1:2.5 and a temperature of 373 K for 2 hours with continuous stirring in a water bath. After activation, the suspension was washed with distilled water until a pH value of 4 was reached. Then it was dried at 473 K and sieved through a 56 µm mesh sieve. The content of Al_2O_3 in clay was analyzed by a chemical method according to GOST 21216-2014.

Three experiments were carried out in parallel, and their average values were calculated. Based on the experimental results, the relationship between

the increase in the hydrochloric acid content and the change in the Al_2O_3 content was investigated. A mathematical model for the decrease in the Al_2O_3 content as a function of increasing hydrochloric acid content was created based on the experimental results obtained.

The composition of the non-activated bentonite, as presented in the table, was described as the initial state; however, since the mathematical modeling is focused on the changes that occur during the acid activation in the concentration range of HCl from 5% to 20%, this value was not considered as a model parameter.

It was determined that the relationship between the decrease in Al2O3 content and hydrochloric acid concentration can be modeled by an exponential regression equation (1).

$$Al_2O_3 = A \cdot exp^{-k \cdot HCL} \quad (1)$$

where

Al_2O_3 - dependent variable, %

HCl - independent variable, %

A and k - determined parameters after regression analysis

To test the goodness of the model, the coefficient of determination (R^2) was calculated. The graphical analysis presented in Figure 1 was obtained by utilizing the Origin 2021 Pro software. This graphical representation demonstrates the agreement between the predictions and the experimentally obtained data.

The agreement between the data and the selected mathematical model was assessed using the coefficient of determination (R^2) and the root mean square error (RMSE). The RMSE was calculated with the help of the following formula (2).

$$RMSE = \sqrt{\frac{1}{n}} \sum_{i=1}^{n} (y_i - \acute{y}i)^2 \quad (2)$$

where

yi - Al_2O_3 content determined experimentally,

ŷi - value calculated by the model,

n - number of experimental data points.

To further validate the model's adequacy, a residual analysis was conducted. In this case, residuals were defined as differences between experimental and calculated values. Additionally, the absence of systematic deviations and a specific pattern in the residuals indicates that the chosen model adequately describes the experimental data.

Results and Discussion

The changes in Al_2O_3 content in samples activated with HCl solutions of different concentrations (5, 10, 15, and 20%) at a solid-liquid ratio of 1:2.5 are shown in Table 2.

Table 2 - Al_2O_3 content % in clay samples activated at different concentrations of hydrochloric acid

Acid concentration, %	Al_2O_3 content, %
5	12.26
10	11.81
15	10.34
20	9.64

The experimental results, as represented in Table 2, show the decreasing trend of the parameter with increasing acid concentration. No abrupt changes were observed between the four measured data points. At the same time, the results represented in the table are not enough to show the exact nature of the relationship between the parameter and the acid concentration.

To achieve a more accurate interpretation of the dependence of the investigated parameter on the concentration of the acid, as well as to assess the mathematical nature of the observed dependence, the experimental points were represented in a graphical form. The graphical representation of the data revealed a nonlinear dependence, thereby supporting the use of an exponential model.

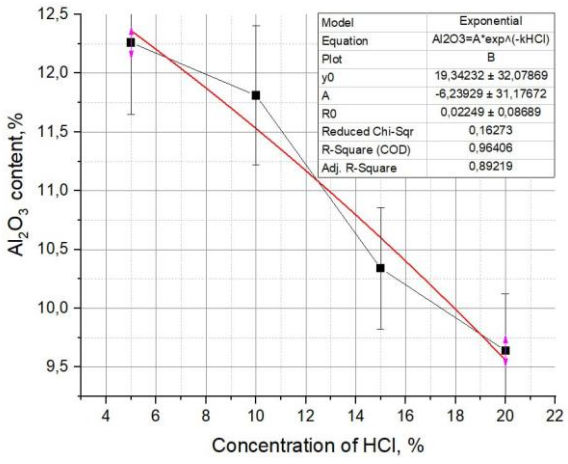

Figure 1 - Exponential decrease in Al_2O_3 content in clay with an increase in HCl concentration

As shown in the graph, the experimental data points follow an exponential curve, indicating that this mathematical model is appropriate for describing the phenomenon. There is no linear

distribution of points, indicating that the decrease is not linear with increasing HCl concentration.

Based on the modeling results, the high coefficient of determination (R^2 = 0.964) indicates strong agreement with the experimental data.

To generalize the experimental data, the relationship was described by an exponential decay model. Thus, the dependence of the Al_2O_3 content on the HCl concentration was expressed by equation (3).

$$Al_2O_3 = 13.3 \cdot exp^{-0.01685 \cdot HCL} \quad (3)$$

This equation also demonstrates the fact that with an increase in the HCl solution concentration, the content of Al_2O_3 decreases rapidly and then slows down, which corresponds to the main physicochemical features of the selective leaching process.

The goodness of fit of the model is high, indicating a close and stable relationship between the experimental and calculated data, thereby demonstrating the high quality of the selected exponential method. The calculated value of the exponential coefficient k shows that the decrease in the content of Al_2O_3 does not occur at a constant rate but depends on the amount of the substance remaining in the system at a given time, which is typical for a kinetic process of selective leaching.

In the following sections, the mechanism of dissolution of Al_2O_3 during the acid activation of bentonite clay will be schematically illustrated step by step (Figure 2).

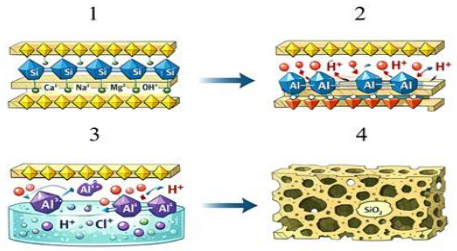

Figure 2 - Schematic illustration describing the selective dissolution of Al_2O_3 during activation of bentonite with HCl

It is possible to visualize the preservation of the SiO_2 network and the creation of porosity through this figure. In its natural state, this clay mineral is known as montmorillonite and is characterized by a layered-type crystalline structure. In this structure, aluminum ions are predominantly located in the octahedral layer. The interlayer space is occupied by exchangeable cations such as Na^+, Ca^{2+}, and Mg^{2+}, which maintain this structure in a relatively stable state. The removal of these ions leads to the creation of micropores and mesopores inside this clay structure. This increases the specific surface area of the clay and its adsorption properties.

In general, the exponential model captures the behavior of the change in Al2O3 content as a function of acid concentration in an appropriate mathematical form, thereby enabling accurate characterization of the process.

The following table facilitates a scientific analysis of the comparison between the experimentally obtained Al_2O_3 contents and those calculated using the exponential model as a function of HCl concentration (Table 3).

Table 3 - Experimental and modeled values of the decrease in Al_2O_3 content in the clay

HCl concentration, %	Al_2O_3 (experimental), %	Al_2O_3 (model), %	Residual ($\Delta = y - \hat{y}$)	Relative error (RE), %
5	12.26	12.46	-0.20	-1.63
10	11.81	11.46	0.35	+2.96
15	10.34	10.55	-0.21	-2.03
20	9.64	9.72	-0.08	-0.83

The root mean square error (RMSE) between the experimental and model values is 0.231%.

The results obtained in Table 3 show that the Al_2O_3 content in the clay decreases with an increase in the concentration of hydrochloric acid in a non-linear manner. The differences between the experimental results and the results obtained by the model are low, with the maximum relative error not being more than 2.96%, thus confirming the high accuracy of the selected exponential model. The positive and negative residual values being distributed in a balanced manner confirm that there are no systematic errors in the model. The low value of the total root mean square error also confirms that the exponential model can be used with good accuracy to quantitatively define the relationship between the Al_2O_3 content and the concentration of HCl.

RMSE makes it possible to quantitatively estimate the average deviation between calculated and experimental Al_2O_3 values with the same unit (%). Although the coefficient of determination (R^2) is a measure of the quality of the model, RMSE was used because it directly represents the actual accuracy of the model.

These results confirm that the reduction of Al_2O_3 content occurs without destruction of the aluminosilicate framework of bentonite and that

this process occurs under conditions of preservation of its structure. Thus, the suggested method of modeling can be considered a scientifically grounded tool for quantitative evaluation of Al_2O_3 content variation during the acid activation process, characterizing the process's intensity, optimizing the process conditions, and making a predictive assessment of this process.

In this study, structural methods such as FTIR and XRD were not used as research objectives. Still, they were employed as theoretical tools to substantiate the results of the kinetic research and the mathematical modeling. According to literature data, under low and moderate conditions of acid activation, the main aluminosilicate structure of bentonites, especially the Si-O bonds, is not destroyed. Therefore, the decrease in the Al_2O_3 content cannot be explained by the destruction of the structure under low and moderate conditions of acid activation. Thus, the main emphasis of this research has been on the mathematical and statistical substantiation of the results.

Conclusions

The scientific contribution of this study lies in the quantitative description of the change in Al_2O_3 content as a function of hydrochloric acid concentration for bentonite from the Navbahor deposit using a mathematical model, as well as its analysis through graphical and statistical criteria.

The acid activation of bentonites in previous studies was often studied in relation to adsorption properties and an increase in specific surface area, and the change in aluminum oxide content in relation to acid concentration was not always analyzed from a mathematical point of view. The decrease in Al_2O_3 content in this study is analyzed as a selective leaching process that preserves the structural framework, and the nonlinear, continuously decreasing nature of this phenomenon is demonstrated through experimental and graphical analyses.

The model developed on the basis of experimental results clearly showed that the change in Al_2O_3 content has a regular, non-linear, and stable decreasing trend with an increase in acid concentration. The results of graphical analysis and statistical evaluation have proved that the selected model can adequately describe the general trend of experimental results with a high degree of accuracy.

As shown by the results of the modeling, a high adequacy of the model was attained. In particular, a large value of the coefficient of determination (R^2 = 0.964) suggests that a significant portion of the variation in the content of Al_2O_3 is explained by the variation of the hydrochloric acid concentration. The above results allow one to proceed from a set of discrete points of the experiment to a continuous description of the process, ensuring the quantitative reliability of the obtained relationship.

The scientific novelty of the research lies in the fact that the variation of the content of Al_2O_3 during the acid activation process has been mathematically and consistently substantiated as a selective chemical process under conditions of structural framework preservation.

The value of this approach is based on the possibility of calculating the increase in the specific surface area of the clay material during the activation process based on the decrease in the Al_2O_3 content using mathematical modeling. This, in turn, allows us to decrease the number of economically expensive analysis techniques, such as the BET method.

Conflicts of interest. On behalf of all authors, the corresponding author states that there is no conflict of interest.

CRediT author statement: **N. Boyjanov and Q. Serkayev**: Conceptualization, Methodology, Software, Data curation, Writing draft preparation; **I. Boyjanov**, **M. Matyakubova, and N. Sabirova**: Visualization, Investigation; **A. Masharipov**: Supervision; **B. Kenjayev and G. Otajanova**: Software, Validation; **Q. Serkayev**: Reviewing and Editing.

Formatting of funding sources. This research did not receive any specific grant from funding agencies in the public, commercial, or not-for-profit sectors.

Cite this article as: Boyjanov NI, Otajonova GM, Kendjayev BB, Matyakubova MX, Sabirova NK, Masharipov AT, Boyjanov IR, Serkayev QP. Exponential modeling of Al_2O_3 reduction during activation of Navbahor alkaline-earth bentonite Kompleksnoe Ispolzovanie Mineralnogo Syra = Complex Use of Mineral Resources. 2027; 343(4):106-115. https://doi.org/10.31643/2027/6445.44

Навбахор кен орнының сілтілі жер бентонитін белсендіру кезінде Al_2O_3 мөлшерінің төмендеуін экспоненциалды модельдеу

[1]Бойжанов Н.И., [2]Отажонова Г.М., [3]Кенжаев Б.Б., [1] Матяқубова М.Х, [1]Сабирова Н.К., [4]Машарипов А.Т., [1]Бойжанов И.Р., [5]Серкаев К.П.

[1]Әбу Райхон Беруни атындағы Үргеніш мемлекеттік университеті, Үргеніш, Өзбекстан
[2]Мамун университеті, Хива, Өзбекстан
[3] Үргеніш инновациялық университеті, Үргеніш, Өзбекстан
[4]Үргеніш мемлекеттік университетінің академиялық лицейі, Үргеніш, Өзбекстан
[5]Ташкент химия-технология институты, Ташкент, Өзбекстан

Мақала келді: *9 ақпан 2026*
Сараптамадан өтті: *27 ақпан 2026*
Қабылданды: *16 наурыз 2026*

ТҮЙІНДЕМЕ
Осы зерттеуде математикалық модельдеу әдістерін қолдана отырып, тұз қышқылын пайдалана, Навбахор кен орнының сілтілі топырақ бентонитінің қышқыл белсенділігі процесіндегі қышқыл концентрациясына тәуелді өзгерісі зерттелді. Тәжірибе барысында HCl концентрациясы 5–20 % аралығында өзгерді, бұл ретте Al_2O_3 мөлшерінің өзгеруі сызықтық емес сипатқа ие екені анықталды. Көрсетілген бентониттің қышқылдық белсендіру кезінде алынған эксперименттік деректерді сипаттау үшін оның параметрлері регрессиялық талдау негізінде айқындалған экспоненциалдық кему моделі ұсынылған. Осы тәсілдің дәлдігі мен тиімділігі детерминация коэффициентінің ($R^2 \approx 0.964$) және орташа квадраттық қатенің (RMSE = 0.231 %) мәндерімен расталған, бұл модельдің жоғары дәлдігі мен тұрақтылығы дәлелденді. Алынған нәтижелер қышқылдық белсендіру жағдайында Al_2O_3 мөлшерінің төмендеуі уақыт факторына емес, тұз қышқылы концентрациясына сызықтық емес тәуелділік көрсететінін дәлелдейді және бұл процесті сандық тұрғыдан сипаттайтын математикалық өрнек құруға, сондай-ақ концентрацияның әсерін бағалауға мүмкіндік береді.

Түйін сөздер: бентонит, қышқыл, белсендіру, салыстырмалы бет ауданы, модельдеу, экспоненциалдық азаю, детерминация коэффициенті (R^2).

Авторлар туралы ақпарат:

Бойжанов Нодирбек Илхомович — *Техника ғылымдары бойынша философия докторы, Әбу Райхон Беруни атындағы Үргеніш мемлекеттік университетінің химиялық технология факультетінің қауымдастырылған профессоры, 220100, Х. Әлімжан көшесі, 14, Үргеніш, Өзбекстан. Email: b.nodirbek@urdu.uz; ORCID ID: https://orcid.org/0009-0002-1454-9478*

Отажонова Гүлхайо Мақсудтың қызы — *Мамун университетінің оқытушысы, Хива, Хорезм, Өзбекстан. Email: otajonovagulhayo1508@gmail.com; ORCID ID: https://orcid.org/0009-0008-7529-9656*

Кенджаев Бунёд Бахтиёр угли — *Үргеніш инновациялық университетінің оқытушысы, Хорезм облысы, Үргеніш, Өзбекстан. Email: bun0401kbb@gmail.com; ORCID ID: https://orcid.org/0009-0002-3235-5159*

Матяқубова Мавлуда Худайберганoвна — *Техника ғылымдарының кандидаты, Әбу Райхон Беруни атындағы Үргеніш мемлекеттік университетінің Тағам технологиясы кафедрасының меңгерушісі, 220100, Х. Әлімжан көшесі, 14, Үргеніш, Өзбекстан. Email: matyaqubovamavluda2010@gmail.com; ORCID ID: https://orcid.org/0009-0000-2961-3626*

Сабирова Надира Камилжановна — *Техника ғылымдары бойынша философия докторы, Әбу Райхон Беруни атындағы Үргеніш мемлекеттік университетінің химиялық технология факультетінің қауымдастырылған профессоры, 220100, Х. Әлімжан көшесі, 14, Үргеніш, Өзбекстан. Email: nodira.sob11@gmail.com; ORCID ID: https://orcid.org/0000-0001-9685-9861*

Машарипов Азамат Турсунбоевич — *Химия ғылымдарының философия докторы (PhD), Үргеніш мемлекеттік университеті академиялық лицейінің оқытушысы, Фаёзов к-сі, 27, Үргеніш, Өзбекстан. Email: yadrokimyo1@gmail.com; ORCID ID: https://orcid.org/0009-0003-3537-3130*

Бойжанов Ислом Ражаббоевич — *Техника ғылымдарының кандидаты, Әбу Райхон Беруни атындағы Үргеніш мемлекеттік университеті, Химия-технология факультетінің доценті, 220100, Х.Олимжон көшесі 14, Үргеніш, Өзбекстан. Email: rajrajrajradju@gmail.com; ORCID ID: https://orcid.org/0000-0002-8416-5472*

Серкаев Камар Пардаевич — *Ташкент химиялық технология институтының профессоры, Навои көшесі, 32, Ташкент, Өзбекстан. Email: serkayev@mail.ru; ORCID ID: https://orcid.org/0009-0009-8316-4994*

Экспоненциальное моделирование снижения содержания Al_2O_3 при активации щёлочноземельного бентонита Навбахорского месторождения

[1]Бойжанов Н.И., [2]Отажонова Г.М., [3]Кенжаев Б.Б., [1]Матяқубова М.Х., [1]Сабирова Н.К., [4]Машарипов А.Т., [1]Бойжанов И.Р., [5]Серкаев К.П.

[1]Ургенчский государственный университет имени Абу Райхона Беруни, Ургенч, Узбекистан
[2]Университет Мамуна, Хива, Узбекистан
[3]Ургенчский инновационный университет, Ургенч, Узбекистан
[4]Академический лицей Ургенчского государственного университета, Ургенч, Узбекистан
[5]Ташкентский химико-технологический институт, Ташкент, Узбекистан

Поступила: *9 февраля 2026*
Рецензирование: *27 февраля 2026*
Принята в печать: *16 марта 2026*

АННОТАЦИЯ

В настоящем исследовании с применением методов математического моделирования изучено изменение содержания Al_2O_3 в зависимости от концентрации кислоты в процессе кислотной активации щёлочноземельного бентонита Навбахорского месторождения с использованием соляной кислоты. В ходе эксперимента концентрация HCl изменялась в диапазоне 5–20 %, при этом установлено, что изменение содержания Al_2O_3 носит выраженный нелинейный характер. Для описания экспериментальных данных, полученных при кислотной активации указанного бентонита, предложена модель экспоненциального убывания, параметры которой определены на основе регрессионного анализа. Достоверность и эффективность данного подхода подтверждены значениями коэффициента детерминации ($R^2 \approx 0,964$) и среднеквадратичной ошибки (RMSE = 0,231 %), что свидетельствует о высокой точности и устойчивости модели. Полученные результаты показывают, что снижение содержания Al_2O_3 в условиях кислотной активации проявляет нелинейную зависимость от концентрации соляной кислоты, а не от временного фактора, и позволяют сформулировать математическое выражение для количественного описания процесса и оценки влияния концентрации.

Ключевые слова: Бентонит, кислота, активация, удельная поверхность, моделирование, экспоненциальное убывание, коэффициент детерминации (R^2).

Информация об авторах:

Бойжанов Нодирбек Илхомович *Доктор технических наук, доцент факультета химической технологии Ургенчского государственного университета имени Абу Райхона Бируни, 220100, ул. Х. Олимжон, 14, Ургенч, Узбекистан. Email: b.nodirbek@urdu.uz; ORCID ID: https://orcid.org/0009-0002-1454-9478*

Отажонова Гульхаё Максуд кизи *Преподаватель университета Мамун, Хива, Хорезм, Узбекистан. Email: otajonovagulhayo1508@gmail.com; ORCID ID: https://orcid.org/0009-0008-7529-9656*

Кенджаев Бунёд Бахтиёр угли *Преподаватель Ургенчского инновационного университета, Хорезмская область, Ургенч, Узбекистан. Email: bun0401kbb@gmail.com; ORCID ID: https://orcid.org/0009-0002-3235-5159*

Матякубова Мавлуда Худайберганoвна *Кандидат технических наук, заведующий кафедрой технологии пищевых продуктов Ургенчского государственного университета имени Абу Райхона Беруни, Ургенч, улица Х. Олимжона, 14, 220100, Узбекистан. Email: matyaqubovamavluda2010@gmail.com; ORCID ID: https://orcid.org/0009-0000-2961-3626*

Сабирова Надира Камилжановна *Доктор технических наук, доцент факультета химической технологии Ургенчского государственного университета имени Абу Райхона Бируни, 220100, ул. Х. Олимжон, 14, Ургенч, Узбекистан. Email: nodira.sob11@gmail.com; ORCID ID: https://orcid.org/0000-0001-9685-9861*

Машарипов Азамат Турсунбоевич *Доктор философии по химии, преподавательский академический лицей Ургенчского государственного университета, Фаёзов 27, Ургенч, Узбекистан. Email: yadrokimyo1@gmail.com; ORCID ID: https://orcid.org/0009-0003-3537-3130*

Бойжанов Ислом Ражаббоевич *Кандидат технических наук, доцент химико-технологического факультета Ургенчского государственного университета имени Абу Райхона Беруни, 220100, ул. Х. Олимжон, 14, Ургенч, Узбекистан. Email: rajrajrajradju@gmail.com; ORCID ID: https://orcid.org/0000-0002-8416-5472*

Серкаев Камар Пардаевич *Профессор Ташкентского института химической технологии, улица Навои, 32, Ташкент, Узбекистан. Email: serkayev@mail.ru; ORCID ID: https://orcid.org/0009-0009-8316-4994*

References

[1] Zubair NA, Moawia RM, Nasef MM, et al. A Critical Review on Natural Fibers Modifications by Graft Copolymerization for Wastewater Treatment. J Polym Environ. 2022; 30:1199-1227. https://doi.org/10.1007/s10924-021-02269-1

[2] Boyjanov N, Radjabov M, Serkayev Q, Boyjanov I, & Yaxshimuradov N. Activation and comparison of indicators of bentonite clay of the Navbakhor deposit. E3S Web of Conferences. 2024; 563:02018. https://doi.org/10.1051/e3sconf/202456302018

[3] Haidar Abbas, Sarmad Jaafar Mohammed Alrubaye, Ali Fawzi Al-Hussainy, Basim Mohammed Saadi, Mohannad Abdulrazzaq Gati, Talib Kh. Hussein, Boyjanov Nodirbek Ilxomovich, Nafaa Farhan Muften. Role of Carrageenan and Health Approach for Adsorption of Safranin-T Dye from Aqueous Solution by Using Polymer/CNT Surface. Journal Nanostruct. 2025; 15(4): 1798-1807.

[4] Hussein U A-R, Alalwan D H K, Qabel H A, Abid F M, Hamza H H, Ilxomovich B N, Aljeboree A M, & Alkaim A F. Green synthesis and characterization of guar gum/polyacrylamide/activated carbon hydrogel for efficient methylene blue removal. Journal of Nanostructures. 2025; 15(4):1849-1860.

[5] Hussin F, Aroua M K, Daud W M A W. Textural characteristics, surface chemistry and activation of bleaching earth: A review. Chemical Engineering Journal. 2011; 170(1):90-106. https://doi.org/10.1016/j.cej.2011.03.065

[6] Shamuratov Sanzharbek, Umid Baltaev, Umarbek Alimov, Namazov Shafoat, Sherzod Kurambaev, and Bazar Ibadullaev. Utilization Process Research of the Soap Industry Acid Waste Water with High Carbonate Phosphorite of Central Kyzylkum.E3S Web of Conferences. EDP Sciences. 2021. https://doi.org/10.1051/e3sconf/202126404079

[7] Shamuratov Sanjarbek, Umid Baltaev, Sanobar Achilova, Umarbek Alimov, Shafoat Namazov, and Najimuddin Usanbaev. Enhancement of Availability of High Calcareous Phosphorite by Neutralization of Acid Effluent and Composting of Cattle Manure. E3S Web of Conferences. EDP Sciences. 2023. https://doi.org/10.1051/e3sconf/202337703004

[8] Shamuratov Sanjarbek, Umid Baltaev, Olga Myachina, Umarbek Alimov, Elyor Atashev, and Tokhir Kuramboev. Agrochemical Efficiency of Slow Release Phosphate Fertilizers Derived on the Base of Phosphorite Activation. E3S Web of Conferences. EDP Sciences. 2023. https://doi.org/10.1051/e3sconf/202343403014

[9] Sotimboev Ilgizarbek, Umidbek Baltaev, Sanjarbek Shamuratov, Ruzimov Shamsiddin, Umarbek Alimov, and Mirzabek Saporboyev. Technical and Economic Efficiency of Processing Acidic Wastewater from the Oil and Fat Industry into Necessary Agricultural Products. E3S Web of Conferences. EDP Sciences. 2024. https://doi.org/10.1051/e3sconf/202456303072

[10] Turatbekova Aidai, Malokhat Abdukadirova, Sanjarbek Shamuratov, Bakhodir Latipov, Mirzabek Saporboyev, Jafar Shamshiyev, and Yusuf Makhmudov. Investigation of the Effect of Fertilizers on the Biochemical and Physical Characteristics of Carrots (Daucus Carota L.). E3S Web of Conferences. EDP Sciences. 2024. https://doi.org/10.1051/e3sconf/202456303074

[11] Shamuratov S, Alimov U, Rifky M, Baltaev U, Ibragimova M, Kurambaev S, & Radjabov M. Investigation of the Kinetics of Cotton Soapstock Saponification under Ultrasonic Illumination. Eurasian Chemico-Technological Journal. 2025; 27(4):323–335. https://doi.org/10.18321/ectj1679

[12] Boyjanov NI, Rakhimov UB, Ataullaev ZM, Boltayev MA, Serkayev QP, Khamidova MO. Mathematical analysis of the linear increase in SIO_2 content during the activation of Navbakhor alkaline bentonite with hydrochloric acid. Kompleksnoe Ispolzovanie Mineralnogo Syra = Complex Use of Mineral Resources. 2027; 342(3):90-99. https://doi.org/10.31643/2027/6445.33

[13] Yuldasheva A P, Shamuratov S Kh, Kurambayev Sh R, & Radjabov M F. Mathematical analysis of CaO content variation in acidic wastewater and mineralized mass mixture from Central Kyzylkum phosphorite based on exponential decay model. Kompleksnoe Ispolzovanie Mineralnogo Syra = Complex Use of Mineral Resources. 2026; 339(4):79-86. https://doi.org/10.31643/2026/6445.42

[14] Baltayev U S, Shamuratov S X, Alimov U K, Madaminov A E, & Jabbarov M E. Extraction of P_2O_5 from the mineralized mass of the Central Kyzylkum using acidic wastewater generated from cotton soapstock processing: Scientific analysis based on equilibrium principles. Kompleksnoe Ispolzovanie Mineralnogo Syra = Complex Use of Mineral Resources. 2027; 341(2):83-96. https://doi.org/10.31643/2027/6445.20

[15] Shamuratov SX, Baltaev US, Alimov UK, Jabbarov ME, Madaminov AE. Sigmoid Neutralization Response of Acidic Soapstock Waste by Mineralized Phosphorite Residues: A 4-Parameter Logistic Approach. Kompleksnoe Ispolzovanie Mineralnogo Syra = Complex Use of Mineral Resources. 2027; 342(3):80-89. https://doi.org/10.31643/2027/6445.32

[16] Palvan K, et al. Information and Measuring System for Monitoring the Moisture Content of Grain and Grain Materials, 2025 IEEE 26th International Conference of Young Professionals in Electron Devices and Materials (EDM), Altai, Russian Federation. 2025, 2260-2265. https://doi.org/10.1109/EDM65517.2025.11096667

[17] Komadel P, & Madejová J. Acid activation of clay minerals. In Bergaya F, Theng B K G, & Lagaly G. (Eds.), Handbook of clay science. Elsevier. 2006; 5:263–287. https://doi.org/10.1016/B978-0-08-098258-8.00013-4

[18] Balci S. Structural property improvements of bentonite with sulfuric acid activation and a test in catalytic wet peroxide oxidation of phenol. International Journal of Chemical Reactor Engineering. 2019; 17(6):121776. https://doi.org/10.1515/ijcre-2018-0167

[19] Terzić A, Pezo L, Andrić L, Pavlović V B, & Mitić V V. Optimization of bentonite clay mechano-chemical activation using artificial neural network modeling. Ceramics International. 2017; 43(6):4994–5004. https://doi.org/10.1016/j.ceramint.2016.11.058

[20] Rouhani H, Farhadi F, Akbari Kenari M, Eskandari E, & Ramakrishna S. Selection of suitable bentonite and the influence of various acids on the preparation of a special clay for the removal of trace olefins from aromatics. Clay Minerals. 2021; 56(3):185. https://doi.org/10.1180/clm.2021.32

[21] Aziz B K, Abdullah M A, & Kaufhold S. Kinetics of oil extraction from clay used in the lubricating oil re-refining processes and re-activation of the spent bleaching clay. Reaction Kinetics, Mechanisms and Catalysis. 2021; 132(1):1–18. https://doi.org/10.1007/s11144-020-01904-7

[22] Didi M A, Makhoukhi B, Azzouz A, Villemin D. Colza oil bleaching through optimized acid activation of bentonite: A comparative study. Applied Clay Science. 2009; 42(3-4):336-344. https://doi.org/10.1016/j.clay.2008.03.014

[23] Arfaoui S, Frini-Srasra N, & Srasra E. Modelling of the adsorption of the chromium ion by modified clays. Desalination. 2008; 222(1-3):474-481. https://doi.org/10.1016/j.desal.2007.03.014

[24] Christidis G E, Scott P W, & Dunham A C. Acid activation and bleaching capacity of bentonites from the islands of Milos and Chios, Aegean, Greece. Applied Clay Science. 1997; 12(1-2):57-75. https://doi.org/10.1016/S0169-1317(97)00017-3

[25] Foletto E L, Volzone C, & Porto L M. Clarification of cottonseed oil: How structural properties of treated bentonites by acid affect bleaching efficiency**.** Latin American Applied Research. 2006; 36(1):37–42.

[26] Noyan H, Önal M, & Sarıkaya Y. The effect of sulphuric acid activation on the crystallinity, surface area, porosity, surface acidity and bleaching power of a bentonite. Food Chemistry. 2007; 105(1):156-163. https://doi.org/10.1016/j.foodchem.2007.03.060

[27] Chanturia V A, Minenko V G, Samusev A L, et al. Adsorption of rare earth elements at modified saponite. Journal of Mining Science. 2024; 60:485–493. https://doi.org/10.1134/S1062739124030153

[28] Karimi L, & Salem A. Analysis of bentonite specific surface area by kinetic model during activation process in presence of sodium carbonate. Microporous and Mesoporous Materials. 2011; 141(1–3):81–87. https://doi.org/10.1016/j.micromeso.2010.10.031

[29] Crundwell F K. The dissolution and leaching of minerals: Mechanisms, myths and misunderstandings. Hydrometallurgy. 2013; 139:132-148. https://doi.org/10.1016/j.hydromet.2013.08.003

[30] Madejová J, & Komadel P. Baseline studies of the Clay Minerals Society source clays: Infrared methods. In CMS Workshop Lectures. Clay Minerals Society. 1998; 9:99-139.

[31] Tyagi B, Chudasama C D, & Jasra R V. Determination of structural modification in acid activated montmorillonite clay by FT-IR spectroscopy. Spectrochimica Acta Part A: Molecular and Biomolecular Spectroscopy. 2006; 64(2):273–278. https://doi.org/10.1016/j.saa.2005.07.018

[32] Shattar SFA, et al. One-step acid activation of bentonite derived adsorbent for effective removal of contaminants. Scientific Reports. 2020; 10:20053. https://doi.org/10.1038/s41598-020-76723-w

[33] Yaghmaeiyan N, Mirzaei M, & Delghavi R. Montmorillonite clay: Introduction and evaluation of its applications in different organic syntheses as catalyst: A review. Results in Chemistry. 2022; 4:100549. https://doi.org/10.1016/j.rechem.2022.100549

[34] Tsakiri D, Douni I, & Taxiarchou M. Structural and surface modification of oxalic-acid-activated bentonites in various acid concentrations for bleaching earth synthesis-A comparative study. Minerals. 2022; 12(6):764. https://doi.org/10.3390/min12060764

[35] Ayati B, Newport D, Wong H, Cheeseman C. Acid activated smectite clay as pozzolanic supplementary cementitious material. Cement and Concrete Research. 2022; 162:106969. https://doi.org/10.1016/j.cemconres.2022.106969

Crossref
DOI: 10.31643/2027/6445.45
Earth and Planetary Sciences: Earth-Surface Processes

Application of a Numerical Model for Forecasting the Consequences of an Explosion

[1]Bakhtybayev N.B., [1*]Atageldiyev K.T., [1]Abil O.A., [2]Bakhtybayeva A.S., [2]Suiintayeva S.Ye.

[1]Mining Research Group LLP, Karaganda, Kazakhstan
[2] Abylkas Saginov Karaganda Technical University, Karaganda, Kazakhstan

** Corresponding author email: kobeyatageldiyev@gmail.com*

Received: *January 12, 2026*
Peer-reviewed: *February 25, 2026*
Accepted: *March 16, 2026*

ABSTRACT

The study presents an investigation of the consequences of explosive impacts during blasting operations at the Zhairem deposit using numerical modeling in the Ansys LS-DYNA software package. Based on literature data and the physico-mechanical properties of rock materials, two modeling scenarios were implemented: the explosion of a single blast hole and a group of blast holes. Dependencies of internal and kinetic energies, displacements, velocities, and accelerations of the rock mass, as well as the distribution of stresses and pressures within the rock, were obtained. It was shown that the maximum equivalent stress during the explosion of a single hole reaches 923.73 MPa, corresponding to the zone of intensive rock mass destruction. For a group of blast holes, energy release increases by several orders of magnitude, reaching 1.2×10^9 J. Characteristic phases of energy transformation and blast wave dynamics were identified, allowing the assessment of hazardous zones and potential consequences of unauthorized explosions. The results of the study can be used to improve the safety of blasting operations and to predict the impact of air-blast overpressure on buildings and structures.

Keywords: blasting operations; numerical modeling; Ansys LS-DYNA; single blast hole; group of boreholes; air-blast wave; overpressure; equivalent stresses; blast dynamics; explosion consequences prediction.

Information about authors:

Bakhtybayev N.B. — *Candidate of Technical Sciences, director of the Mining Research Group LLP, Karaganda, Kazakhstan. E-mail: bakhtybayev@minrg.com; ORCID ID: http://orcid.org/0000-0002-9816-9765*

Atageldiyev K.T. — *Research Scientist of the Mining Research Group LLP, Karaganda, Kazakhstan. E-mail: kobeyatageldiyev@gmail.com; ORCID ID: https://orcid.org/0000-0002-1902-0170*

Abil O.A. — *Associate Director of the Mining Research Group LLP, Karaganda, Kazakhstan. E-mail: orazabil@minrg.com; ORCID ID: https://orcid.org/0000-0001-9939-9039*

Bakhtybayeva A.S. — *PhD, senior lecturer, Abylkas Saginov Karaganda Technical University, N. Nazarbayev Ave., 56, Karaganda, Kazakhstan. E-mail: bahtybaeva18@gmail.com; ORCID ID: https://orcid.org/0000-0001-7163-6274*

Suiintayeva S.Ye. — *PhD student, Abylkas Saginov Karaganda Technical University, N. Nazarbayev Ave., 56, Karaganda, Kazakhstan. E-mail: suiintayevas@mail.ru; ORCID ID: https://orcid.org/0000-0003-1362-2493*

Introduction

As part of the literature review, modern domestic and foreign studies on the modeling, analysis, and prediction of explosion consequences were examined. The studied materials range from empirical relationships and regulatory methods to numerical models.

In their article [1], Qiang W. et al., based on collected data from accidental explosions (at a US plant in 2013, at the Tianjin port in China in 2015, and at the Beirut port in Lebanon in 2020), studied the consequences and effects of ammonium nitrate (AN) explosions based on the Chinese national standard GB6722-2014. The main focus is on calculating the TNT equivalent of various explosives and assessing the impact of the blast wave, considering distance and scaling.

In studies [2], the authors focused on the blast wave propagating from the source to the object. The article analyzes different mathematical models used to determine the magnitude of explosion pressure. Two cases of their application were analyzed. In the first case, the distance to the explosive was varied while the explosive weight was constant. In the second case, the explosive mass was varied at the same distance. The results showed that the difference in calculations for different cases is least noticeable at large distances.

Work [[3], [4], [5]] examines the propagation of hydrogen combustion products in numerical modeling. The model accounts for pressure

distribution and made it possible to determine the maximum overpressure at control points. It was found that with an increase in explosion power, the maximum overpressure increases. This increase is associated with the combustion radius and the amount of destroyed materials.

Based on the literature analysis, it has been established that explosion parameters (pressure, radius, impulse) significantly depend on:

- physicochemical properties of the explosive materials (EM);
- density of the medium;
- cloud shape (in the case of a gas or vapor-air mixture);
- initiation mode;
- conditions of wave propagation.

Based on the relevance of the topic, the aim of this work is to determine the scale and nature of possible consequences using numerical sumalation.

Experimental part

The object of study in this research work is the Zhairem barite-polymetallic deposit, specifically the Dalnezapadny open-pit mine, where mining is carried out by open-pit method. It is located in the Zhan-Arka district of the Karaganda region within the Atasu ore district. The geographical coordinates of the deposit are: 48°17′ N latitude and 70°20′ E longitude (Figure 1).

The main activity of JSC "Zhairem Mining and Processing Plant" is the extraction and processing of polymetallic, manganese, and iron ores, as well as the production of zinc and lead concentrates. The leading economic sector in the region is represented by the Kazzinc company, which is controlled by the Glencore group [6].

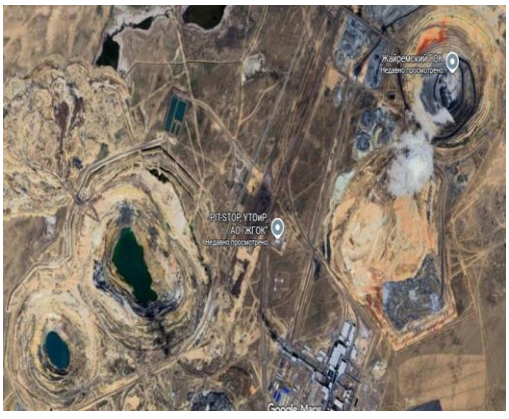

Figure 1 – Overview map of the study area

The collected data on drilling and blasting operations formed the initial basis for this scientific research. According to the drilling and blasting records, a consistent blast hole pattern of 5.2 x 5.7 m and a vertical drilling angle (90°) were used across the horizons.

In accordance with the deposit development plan, the following explosives are used in open-pit blasting operations: ANFO, Explo P, and Explo E 70. The effective energy relative to ANFO at a density of 0.8 g/cm³ is 2.30 MJ/kg, according to the stated characteristics [[7], [8], [9]]. These energy values are based on ideal detonation calculations at a limiting pressure of 100 MPa [[10], [11]].

To analyze the impact of explosions on the environment and structures, the LS-DYNA software package is used based on the aforementioned data. These methods allow for considering the complex geometry of objects and the heterogeneity of the medium, providing visualization of the dynamics of shock wave propagation in space and time.

In the numerical simulation, calculations were performed to analyze the physical processes of the explosion using the physico-mechanical characteristics of the rock from the deposit (Table 1).

Table 1 – Initial Parameters

Rock type	Rock mass
Rock density, kg/m³	2400
Young's modulus, MPa	19360
Poisson's ratio	0.25
Compressive strength, MPa	94.2
Explosive type	Anfo
Charge length, m	9.2
Stemming length, m	3.3
Explosive charge mass in the borehole, kg	150
Explosive density, g/cm³	0.8
Detonation velocity (D), m/s	42
Borehole diameter, mm	171
Effective energy, MJ/kg	2.30

Two variants of geometric models were considered in this study for a comprehensive assessment of blasting effects: a single borehole model for investigating the effect of an individual charge and a full block model for analyzing the interaction of charges and their overall impact on the rock mass (Figures 2–3). According to the drilling and blasting design parameters, the borehole diameter was 171 mm, with a spacing pattern of 5.5 × 5.5 m. The charge configuration consisted of 9.2 m of explosive column and 3.3 m of stemming.

The mathematical description of rock mass behavior was implemented using the MAT_PLASTIC_KINEMATIC (Type No. 3) material model. This model was selected because it effectively describes the elastoplastic behavior of the medium, taking into account isotropic and kinematic hardening. In addition, the model is computationally efficient for solid elements and allows consideration of strain rate effects.

To simulate the expansion process of detonation products of the explosive material (ANFO), the JWL (Jones–Wilkins–Lee) equation of state was used [[12], [13], [14], [15]]:

$$p = A\left(1 - \frac{\omega}{R_1 V}\right)e^{-R_1 V} + B\left(1 - \frac{\omega}{R_2 V}\right)e^{-R_2 V} + \frac{\omega E}{V}$$

In this equation, the parameters A, B, and E have the dimension of pressure, while R_1, R_2, ω, and V are dimensionless quantities. For modeling processes involving explosives, it is recommended to use the 'gram-centimeter-microsecond' unit system. Within this coherent unit system, pressure is expressed in megabars (Mbar) [[16], [17], [18]].

Option 1. Single-borehole model

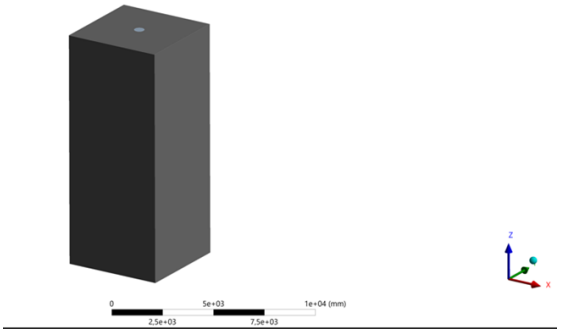

Figure 2 – Single borehole model

Option 2. Model of the entire block for analyzing the interaction of charges and the overall impact on the rock mass. According to the deposit's blast pattern passport, this model studied boreholes arranged in a staggered pattern with a 5.5 × 5.5 m grid and a delay interval of 42 ms (Figure 3).

The model shows dimension lines and values indicating the parameters of the block and the design of the blast holes. The block with a staggered arrangement of blast holes has the following dimensions:

- Length: 20 m;
- Width: 15 m;
- Height: 12 m;

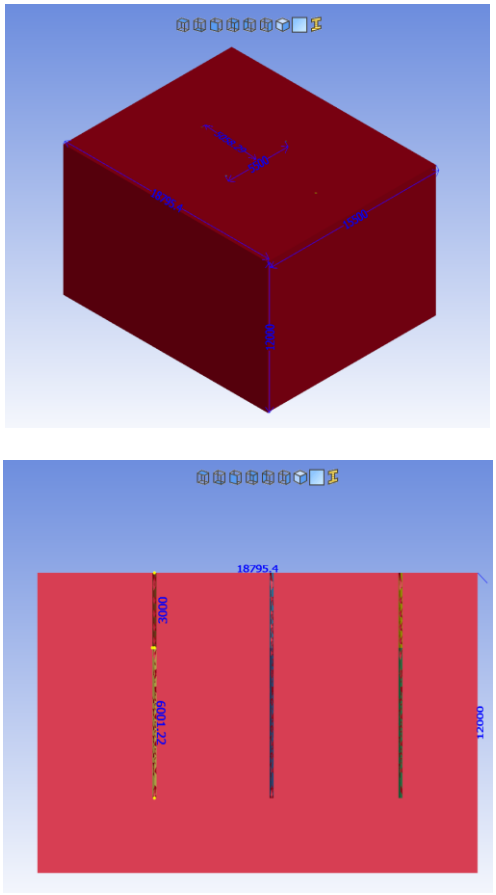

Figure 3 – Model of a full block of blast holes.

Results and Discussion

From the numerical modeling for Option 1, graphs of the internal energy, the kinetic energy of the system, and the velocity of the destroyed materials versus time were obtained (Figures 4-11).

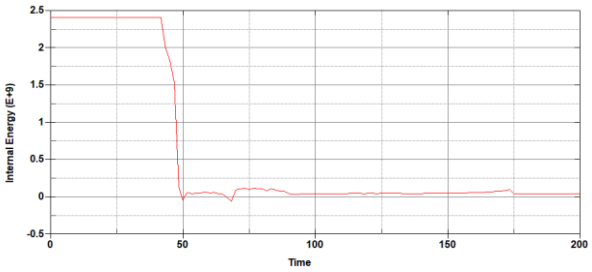

Figure 4 – Graph of internal energy variation

Analysis of the internal energy graph shows that characteristic phases of energy transformation can be identified. At the initial moment, a positive value of internal energy is observed. The main stage of energy absorption occurs in the interval from 0 to 50 ms, where the internal energy monotonically increases to a maximum value of 2.5×10^6 J, indicating an intensive process of plastic deformation and damage accumulation in the

material. The subsequent phase from 50 to 200 ms is characterized by a monotonic decrease in internal energy to near-zero values. These internal energy dynamics correspond to a typical scenario of intense dynamic loading.

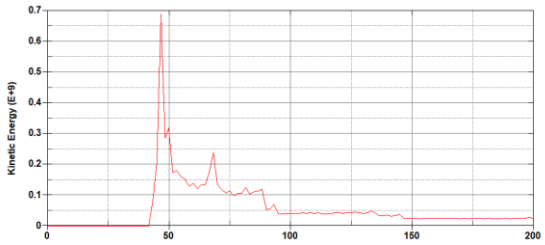

Figure 5 – Graph of kinetic energy variation

Based on the analysis of the kinetic energy dependence, a characteristic dynamic process of energy transformation under impulse loading is revealed. At the initial stage, an intensive increase in kinetic energy from zero to a maximum level of 0.65×10^9 J at T ≈ 42 ms is observed, which corresponds to the phase of active energy input and the transformation of external impact energy into mechanical motion. The subsequent monotonic decrease in kinetic energy continues in the interval of 50-200 ms.

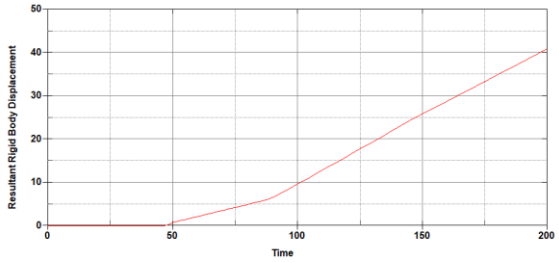

Figure 6 – Total displacement vs. time

From the graph of the velocity parameter versus time, a characteristic nonlinear development of the dynamic process under impulsive loading is observed. In the initial period, an intensive increase is recorded under the action of the external load.

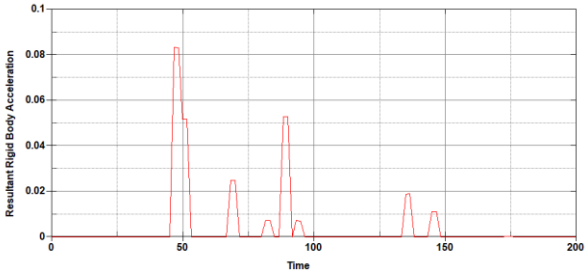

Figure 7 – Dependence of total acceleration on time

At the initial stage of the process, the acceleration remains near zero, indicating the absence of significant external influences. A sharp increase in acceleration, observed at T ≈ 40 ms, reaches an extreme value of $a_{max} \approx 0.083–0.084 m/s^2$ at T = 50 ms, corresponding to the primary impulsive loading on the structure. The subsequent dynamics are characterized by rapid attenuation, manifested as distinct peaks at T ≈ 90 ms (a ≈ 0.055) and T ≈ 140 ms (a ≈ 0.018). The amplitude of successive peaks decreases within the interval 100–150 ms.

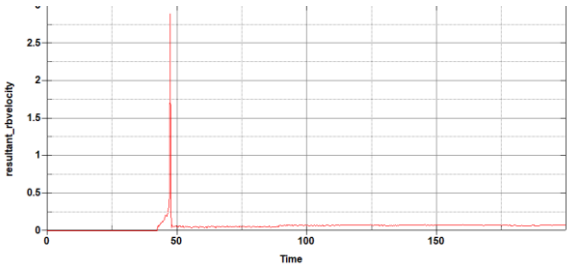

Figure 8 – Dependence of total velocity on time

The seismic effect is characterized by a sharp increase to a maximum value at the moment of detonation, followed by attenuation, manifested as a decrease in peak amplitudes within the 100–150 ms interval.

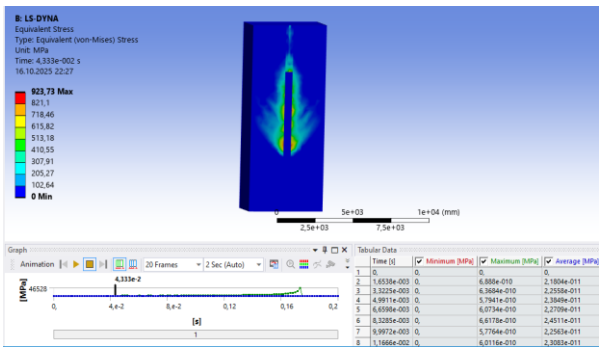

Figure 9 - Equivalent stress distribution in the rock mass after the blast

Also, from the simulation results, it was found that the maximum equivalent stresses under the blast impact at 42 ms reach 923.73 MPa near the borehole axis, which corresponds to the zone of greatest destruction of the rock mass. As the distance from the explosion source increases, the stresses decrease, reflecting the attenuation of the shock wave. Analysis of the destruction process allows for determining the boundaries of intensive impact zones for designing safe blasting operation parameters.

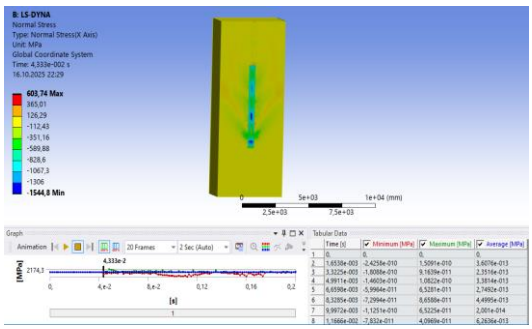

Figure 10 – Equivalent stress distribution in the rock mass after the blast

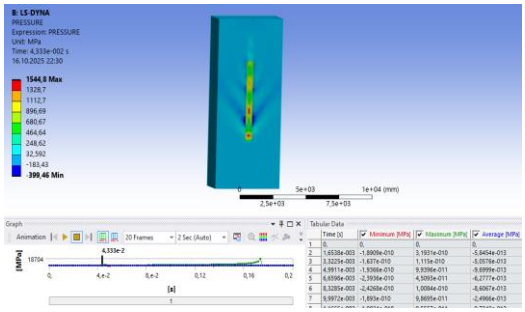

Figure 11 – Distribution of stress pressure in the massif after detonation

Analysis of normal stresses showed that during an explosion in the axial direction, alternating zones of compression and tension are observed with extreme values ranging from –1544.8 to 603.74 MPa. The main impact is concentrated along the borehole axis, where maximum rock compression occurs. The stress distribution indicates the formation of cracks as a result of tensile stresses in the peripheral zones.

When processing the results of Option 2, graphs of the energy, displacement, velocity, acceleration, as well as the distribution of stresses and pressure in the rock mass were obtained (Figure 12).

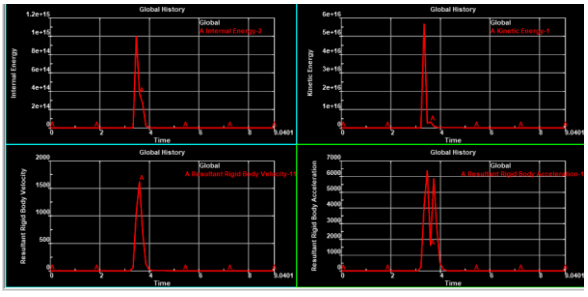

Figure 12 – Parameters of the rock mass under blast loading

The graphs from option 2 of the numerical simulation allow the following key features to be highlighted:

Graph No. 1. The main part of the explosion energy (J) is converted into internal energy over a very short period of time, which corresponds to the phase of intensive plastic deformation and rock fracture. After the shock wave passes, the system quickly stabilizes.

Graph No. 2. The peak of kinetic energy (J) occurs slightly later than the peak of internal energy, which is associated with the transition from deformation to movement of the rock mass.

Graph No. 3. The velocity impulse (m/s) confirms the development of high-speed movement of rock mass fragments at the moment of explosion. Rapid attenuation indicates the absence of prolonged displacement; the main response is impulsive, which is typical for the impact of a shock wave.

Graph No. 4. The acceleration (m/s²) confirms the presence of a powerful short-term impulse corresponding to the passage of the shock wave and the transfer of maximum force to the rock mass. Secondary oscillations indicate high-frequency vibration of the rock after the primary impact, which is characteristic of the seismic response during an explosion.

All four graphs demonstrate a typical picture of a short-term but extremely powerful dynamic process. In 2–3 ms, the main transfer of explosion energy to the rock mass occurs. Internal energy increases → then the energy transitions to kinetic → the rock acquires high velocities → and maximum accelerations.

The pressure distribution in the rock mass model at time t = 2.8722 ms after the 42 ms detonation time is shown (Figure 13). The pressure contours applied to the elements of the mass are displayed.

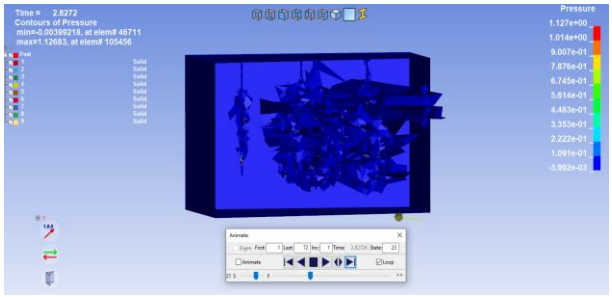

Figure 13 - Distribution of pressure in the rock mass

The distribution scale shows pressure amplitudes in the range: max = 1.127e+00 Pa, min = –3.992e–03 Pa. At a time of about 2.87 ms, the shock wave has already formed a region of high pressure in the central zone. At the periphery, the pressure remains low, indicating incomplete propagation of the wave at the early stage of the process.

The summarized simulation results for both options are presented in Table 2.

Table 2 – Comparative analysis of simulation results

Parameter of comparison	Single borehole (Option 1)	Group of boreholes (Option 2)
Total energy release	1.2×10^3 J	$1,2\times10^9$ J
Max. internal energy	2.5×10^6 J	Several orders of magnitude higher (intensive plastic deformation)
Max. kinetic energy	0.65×10^9 J	Exceeds the values of a single borehole (transition to mass movement)
Max. equivalent stresses	923.73 MPa	Characterized by the interaction of stress fields of adjacent charges
Max. acceleration of the rock mass (a_max)	≈0.084 m/s²	Short-term impulse and force transfer to the entire block
Max. pressure	Concentrated along the borehole axis	Up to 1.127 Pa (at time t = 2.87 ms)

The analysis of the results allows for a well-founded practical interpretation to be formulated:

- seismic safety and vibration impact;
- stability of structures and failure zones;
- assessment of hazardous zones based on flyrock and pressure;

The quantitative indicators obtained in Ansys LS-DYNA are the basic data for designing safe blasting operation parameters and developing measures for the protection of buildings and structures [[19], [20]].

Conclusion

Based on the conducted research on forecasting the possible consequences of an explosion of a single borehole and an entire block, the following conclusions can be drawn:

The analysis of the equivalent stress distribution and plastic deformation zones (up to 923.73 MPa) makes it possible to optimize the blast hole pattern. The obtained data on the crushing zone radius provide the opportunity to reasonably change the distance between charges to achieve the required quality of rock mass fragmentation while simultaneously reducing the specific consumption of explosives.

The obtained dependences of peak accelerations and displacement velocities of the rock mass serve as a tool for assessing seismic safety. This makes it possible to predict the degree of vibration impact on buildings and structures located near the work zone and, if necessary, to adjust the mass of simultaneously blasted charges.

Modeling the dynamics of the air shock wave and rock flyout zones allows for establishing the boundaries of hazardous areas. This is critically important for protecting mining and transport equipment and personnel, as well as for preventing the impact of overpressure on infrastructure facilities.

Thus, the developed numerical model is an effective tool for the operational management of blasting operation parameters, ensuring a balance between blast productivity and industrial safety.

CRediT author statement: **B. Bakhtybayev:** Conceptualization, Methodology, Software, Data curation, Writing draft preparation, Reviewing and Editing; **A. Bakhtybayeva, S. Suiintayeva:** Visualization, Investigation, Supervision; **K. Atageldiyev** and **O. Abil:** Software, Validation.

Formatting of funding sources. This research was carried out within the framework of research and development work (R&D) under Contract No. 3110/2025–2043 dated August 8, 2025, on the topic: "Forecasting the possible consequences of a potential hazard arising from an unauthorized explosion at blasting operation sites in zones ranging from the explosion of a single borehole to the explosion of an explosive material storage site and an entire block containing the maximum possible number of explosive materials.".

Cite this article as: Bakhtybayev NB, Atageldiyev KT, Abil OA, Bakhtybayeva AS, Suiintayeva SYe. Application of a Numerical Model for Forecasting the Consequences of an Explosion. Kompleksnoe Ispolzovanie Mineralnogo Syra = Complex Use of Mineral Resources. 2027; 343(4):116-123. https://doi.org/10.31643/2027/6445.45

Жарылыс салдарын болжау үшін сандық модельді қолдану

[1]Бахтыбаев Н.Б., [1]Атагелдиев К.Т., [1]Әбіл О.А., [2]Бахтыбаева А.С., [2]Сүйінтаева С.Е.

[1]Mining Research Group ЖШС, Қарағанды, Қазақстан
[2] Әбілқас Сағынов атындағы Қарағанды техникалық университеті, Қарағанды, Қазақстан

Мақала келді: *12 қаңтар 2026*
Сараптамадан өтті: *25 ақпан 2026*
Қабылданды: *16 наурыз 2026*

ТҮЙІНДЕМЕ

Ғылыми жұмыста Ansys LS-DYNA бағдарламалық кешенінде сандық модельдеуді қолдана отырып, Жәйрем кен орнында жарылыс жұмыстары кезіндегі жарылыс әсерінің салдарын зерттеу ұсынылған. Әдеби деректер мен тау жыныстарының физика-механикалық қасиеттері негізінде екі модельдеу нұсқасы орындалды: жеке ұңғыманың жарылысы және ұңғымалар тобының жарылысы. Ішкі және кинетикалық энергиялардың, қозғалыстарына, жылдамдықтары мен массивтің үдеулері, сондай-ақ тау жыныстарындағы кернеулер мен қысымдардың таралуына тәуелділіктер алынды. Жеке ұңғыманың жарылысы кезінде эквивалентті кернеудің ең жоғарғы мәні 923,73 МПа-ға жететіні көрсетілді, бұл массивтің қарқынды бұзылу аймағына сәйкес келеді. Ұңғымалар тобы үшін энергия бөлінуі бірнеше есе артып, $1{,}2\times10^9$ Дж шамасына дейін жетеді. Энергияның түрлену фазалары және соққы толқынының динамикасы анықталып, қауіпті аймақтарды және рұқсат етілмеген жарылыстардың ықтимал салдарын бағалауға мүмкіндік береді. Зерттеу нәтижелері жарылыс жұмыстарының қауіпсіздігін арттыруға және соққы ауа толқынының ғимараттар мен құрылыстарға әсерін болжауға қолданылуы мүмкін.

Түйін сөздер: жарылыс жұмыстары; сандық модельдеу; Ansys LS-DYNA; жеке ұңғыма; ұңғымалар тобы; соққы ауа толқыны; артық қысым; эквивалентті кернеулер; жарылыс динамикасы; жарылыс салдарын болжау.

Авторлар туралы ақпарат:

Бахтыбаев Н.Б. *Т.ғ.к., Mining Research Group ЖШС директоры, Қарағанды, Қазақстан. E-mail: bakhtybayev@minrg.com; ORCID ID: http://orcid.org/0000-0002-9816-9765*

Атагелдиев К.Т. *Mining Research Group ЖШС ғылыми қызметкері, Қарағанды, Қазақстан. E-mail: kobeyatageldiyev@gmail.com; ORCID ID: https://orcid.org/0000-0002-1902-0170*

Әбіл О.А. *Mining Research Group ЖШС директорының орынбасары, Қарағанды, Қазақстан. E-mail: orazabil@minrg.com; ORCID ID: https://orcid.org/0000-0001-9939-9039*

Бахтыбаева А.С *PhD, аға оқытушы, Әбілқас Сағынов атындағы Қарағанды техникалық университеті, Н. Назарбаев даңғылы, 56, Қарағанды, Қазақстан. E-mail: bahtybaeva18@gmail.com; ORCID ID: https://orcid.org/0000-0001-7163-6274*

Сүйінтаева С.Е. *Докторант, Әбілқас Сағынов атындағы Қарағанды техникалық университеті, Н. Назарбаев даңғылы, 56, Қарағанды, Қазақстан. E-mail: suiintayevas@mail.ru; ORCID ID: https://orcid.org/0000-0003-1362-2493*

Применение численной модели для прогнозирования последствий взрыва

[1]Бахтыбаев Н.Б., [1]Атагелдиев К.Т., [1]Абиль О.А., [2]Бахтыбаева А.С., [2]Сүйінтаева С.Е.

[1] ТОО Mining Research Group, Караганда, Казахстан
[2] Карагандинский технический университет имени Абылкаса Сагинова, Караганда, Казахстан

Поступила: *12 января 2026*
Рецензирование: *25 февраля 2026*
Принята в печать: *16 марта 2026*

АННОТАЦИЯ

В научной работе представлено исследование последствий взрывных воздействий при ведении взрывных работ на Жайремском месторождении с использованием численного моделирования в программном комплексе Ansys LS-DYNA. На основе литературных данных и физико-механических свойств горных пород выполнено моделирование двух вариантов: взрыва одиночной скважины и группы скважин. Получены зависимости внутренних и кинетических энергий, перемещений, скоростей и ускорений массива, а также распределения напряжений и давлений в горной породе. Показано, что максимальные эквивалентные напряжения при взрыве одиночной скважины достигают 923,73 МПа, что соответствует зоне интенсивного разрушения массива. Для группы скважин энерговыделение возрастает на несколько порядков, достигая $1{,}2\times10^9$ Дж. Установлены характерные фазы преобразования энергии и динамики ударной волны, что позволяет оценить опасные зоны и возможные последствия несанкционированных взрывов. Результаты исследования могут быть использованы для повышения безопасности взрывных работ и прогнозирования влияния ударной воздушной волны на зданий и сооружени.

Ключевые слова: взрывные работы; численное моделирование; Ansys LS-DYNA; одиночная скважина; группа скважин; ударная воздушная волна; избыточное давление; эквивалентные напряжения; динамика взрыва; прогнозирование последствий взрыва.

	Информация об авторах:
Бахтыбаев Н.Б.	*Кандидат технических наук, директор ТОО Mining Research Group, Караганда, Казахстан. E-mail: bakhtybayev@minrg.com; ORCID ID: http://orcid.org/0000-0002-9816-9765*
Атагелдиев К.Т.	*Научный сотрудник ТОО Mining Research Group, Караганда, Казахстан. E-mail: kobeyatageldiyev@gmail.com; ORCID ID: https://orcid.org/0000-0002-1902-0170*
Әбіл О.А.	*Заместитель директора ТОО Mining Research Group, Караганда, Казахстан. E-mail: orazabil@minrg.com; ORCID ID: https://orcid.org/0000-0001-9939-9039*
Бахтыбаева А.С	*PhD, старший преподаватель, Карагандинский технический университет имени Абылкаса Сагинова, пр. Н. Назарбаева, 56, Караганда, Казахстан. E-mail: bahtybaeva18@gmail.com; ORCID ID: https://orcid.org/0000-0001-7163-6274*
Суйінтаева С.Е.	*Докторант, Карагандинский технический университет имени Абылкаса Сагинова, пр. Н. Назарбаева, 56, Караганда, Казахстан. E-mail: suiintayevas@mail.ru; ORCID ID: https://orcid.org/0000-0003-1362-2493*

References

[1] Wang Q, Zhang L, Wang L, Bu L. A practical method for predicting and analyzing the consequences of ammonium nitrate explosion accidents adjacent to densely populated areas. Heliyon. 2023; 9(5). https://doi.org/10.1016/j.heliyon.2023.e15616

[2] Jankura R, Zvaková Z, & Boroš M. Analysis of mathematical relations for calculation of explosion wave overpressure. Proceedings of CBU in Natural Sciences and ICT. 2020; 1:21-27. https://doi.org/10.12955/pns.v1.116

[3] Mkrtychev OV, Savenkov AYu. Chislennoye modelirovaniye fronta vozdushnoy udarnoy volny pri vzryve v vozdukhe i nad zemley v programmnom komplekse LS-DYNA [Numerical simulation of the air shock wave front during an explosion in the air and above the ground in the LS-DYNA software package]. Stroitel'naya mekhanika inzhenernykh konstruktsiy i sooruzheniy [Structural Mechanics of Engineering Constructions and Buildings]. 2018; 14(6):467-474. (in Russ.). https://doi.org/10.22363/1815-5235-2018-14-6-467-474

[4] Hong X, Li W, Xu H, Wang B, Xiao W. Experimental study on the explosion dispersion process of a multilayer composite charge under different initiation modes. Defence Technology. 2020; 16(4):883-892. https://doi.org/10.1016/j.dt.2019.11.002

[5] Skob Y, Yakovlev S, Pichugina O, Kalinichenko M, Kartashov O. Numerical assessment of harmful consequences after an accidental explosion at a hydrogen refueling station. Environmental and Climate Technologies. 2024; 28(1):181-194. https://doi.org/10.2478/rtuect-2024-0015

[6] Brusnitsyn I, Perova EN, Vereshchagin OS, Britvin SN, Letnikova EF, Shkolnik SI, Ivanov AV. Barite–lead–zinc and iron–manganese deposits of the zhairem ore district: a geological field trip to central Kazakhstan. Minerals. 2018; 4(3).

[7] Magreth S, Yashar P. The Influence of Explosive and Rock Mass Properties on Blast Damage in a Single-Hole Blasting. Mining, 2024; 4(1):168-188. https://doi.org/10.3390/mining4010011

[8] Widodo S, Anwar H, Syafitri NA. Comparative analysis of ANFO and emulsion application on overbreak and underbreak at blasting development activity in underground Deep Mill Level Zone (DMLZ) PT Freeport Indonesia. Earth and Environmental Science. 2019; 279:012001. https://doi.org/10.1088/1755-1315/279/1/012001

[9] Magdalena F, Tomasz J. Improving ANFO: Effect of Additives and Ammonium Nitrate Morphology on Detonation Parameters. Materials. 2021; 14(19):5745. https://doi.org/10.3390/ma14195745

[10] Uranchimeg E, Narantsetseg M, Purev L. Modification of ANFO detonation parameters by biowaste addition. In IOP Conference Series: Materials Science and Engineering; IOP Publishing: Bristol, UK. 2021; 1019:012040. https://doi.org/10.1088/1757-899X/1019/1/012040

[11] Biessikirski A, Barański K, Pytlik M, Kuterasiński Ł, Biegańska J, Słowiński K. Application of silicon dioxide as the inert component or oxide component enhancer in ANFO. Energies. 2021; 14(8):2152. https://doi.org/10.3390/en14082152

[12] Zhang Y, Xu M, Liu S, Liu F, Wang Q. Rate-dependent constitutive modelling blasting crack initiation and propagation in rock masses. International Journal of Coal Science & Technology. 2023; 10:83. https://doi.org/10.1007/s40789-023-00633-1

[13] Zhixian Hong, Ming Tao, Shurong Feng, Hao Liu, Wenhong Wu, Xudong Li, Shuai Liu. Experimental study of the impact of deck-charge structure on blast-induced fragmentation. Geomech. Geophys. Geo-energ. Geo-resour. 2025; 11:3. https://doi.org/10.1007/s40948-024-00915-1

[14] Li X, Liu K, Sha Y, Yang J, Ma S, Hong Z Investigation on radial fracturing around borehole under combined static stress and blasting. Theoret Appl Fract Mech. 2023; 127:104038. https://doi.org/10.1016/j.tafmec.2023.104038

[15] Lan R., Cheng R., Zhou Z., Chen L., Wang P., Wang Z. Damage and Fragmentation of Rock Under Multi Long Hole Blasting with Large Empty Holes // Rock Mechanics and Rock Engineering. – 2024. – Vol. 57. – P. 7603–7622. https://doi.org/10.1007/s00603-024-03942-2.

[16] Castedo R, Natale M, López LM, Sanchidrián JA, Santos AP, Navarro J, Segarra P. Estimation of Jones-Wilkins-Lee parameters of emulsion explosives using cylinder tests and their numerical validation. International Journal of Rock Mechanics and Mining Sciences. 2018; 112:290-301. https://doi.org/10.1016/j.ijrmms.2018.10.027

[17] Lu Liu, Jinhui O, Wencheng Y, and Sijing Wang. Strain Rate Effects on Characteristic Stresses and Dynamic Strength Criterion in Granite Under Triaxial Quasi-Static Compression. Appl. Sci. 2025; 15(11):6214. https://doi.org/10.3390/app15116214

[18] He M, Cheng T, Qiao Y, Li H. A Review of Rockburst: Experiments, Theories, and Simulations. J. Rock Mech. Geotech. Eng. 2023; 15(5):1312–1353. https://doi.org/10.1016/j.jrmge.2022.07.014

[19] Kamyansky VN. Modelirovaniye vzryva skvazhinnykh zaryadov v srede ANSYS [Borehole blasting simulation using ANSYS software]. Problemy ispol'zovaniya nedr [Problems of Subsoil Use]. 2017; 1:119-125. (in Russ.). https://doi.org/10.18454/2313-1586.2017.01.119

[20] Kozyrev SA, Kamyanskiy VN. Razrabotka chislennykh modeley dlya vzryva skvazhinnykh zaryadov v gornoy porode [Development of numerical models of borehole charges blasting in rock massif]. Vestnik Kol'skogo nauchnogo tsentra Rossiyskoy akademii nauk [Bulletin of the Kola Science Centre of the Russian Academy of Sciences]. 2019; 11(2):34-44. (in Russ.). https://doi.org/10.25702/KSC.2307-5228.2019.11.2.34-44

Crossref
DOI: 10.31643/2027/6445.46
Earth and Planetary Sciences: Earth-Surface Processes

Polyurethane Sorbents with Optimized Open-Pore Structure for Efficient Oil Spill Cleanup Produced in a Mobile Manufacturing Complex

[1*]Iskalieva A.Z., [2]Kenzhaliyev O.B., [1]Ibray D., [1]Sakhnov S.

[1] School of Chemical Engineering, Kazakh-British Technical University, Almaty, Kazakhstan
[2] Karaganda Industrial University, Temirtau, Kazakhstan

** Corresponding author email: asylzat@bk.ru*

Received: *January 28, 2026*
Peer-reviewed: *March 12, 2026*
Accepted: *March 30, 2026*

ABSTRACT
Oil spill cleanup is one of the major environmental issues facing the world today; this problem is often compounded by the delayed response of emergency teams in the supply of sorbents for cleanup operations. Although sorption is considered the preferred method of cleanup, its success is often hindered by the centralized production of synthetic sorbents. In this paper, we report on the development of a mobile manufacturing container to produce polyurethane-based oil sorbents. The system has been optimized for the entire production process of polyurethane-based sorbents through the precise measurement of polyether polyol, isocyanate, and water ratios in the mixture to produce an open-cell foam with a density of 16 kg/m³ and a special pore structure in which 80% of the pores are less than 50 µm in diameter. From the experimental results obtained using this sorbent, it was evident that it was capable of fully absorbing 100 mL of crude oil on the surface of water within 10 minutes; in addition, this sorbent was able to maintain its high performance after 5-10 cycles of mechanical regeneration. The transition from a centralized production system to one of decentralized production of sorbents for cleanup operations is a major step towards solving the problems of delayed response in cleanup operations.

Keywords: polyurethane sorbent; oil spill response; mobile manufacturing complex; open-cell foam; sorption capacity; reusable sorbents.

Information about authors:

Iskalieva Asylzat — *Ph.D, School of Chemical Engineering, Kazakh-British Technical University, Str. Tole bi, 59, 050000, Almaty, Kazakhstan. Email: asylzat@bk.ru; ORCID ID: https://orcid.org/0000-0003-4806-4137*

Kenzhaliyev Olzhas — *Ph.D., Karaganda Industrial University, Republic Ave. 30, 101400, Karaganda region, Temirtau, Kazakhstan. Email: o.kenzhaliyev@tttu.edu.kz; ORCID ID: https://orcid.org/0000-0002-3776-9724*

Ibray Danat — *School of Chemical Engineering, Kazakh-British Technical University, Str. Tole bi, 59, 050000, Almaty, Kazakhstan. Email: danat.ibray@gmail.com; ORCID ID: https://orcid.org/0009-0007-4549-5229*

Sakhnov Sergey — *School of Chemical Engineering, Kazakh-British Technical University, Str. Tole bi, 59, 050000, Almaty, Kazakhstan. Email: sakhnov67@gmail.com; ORCID ID: https://orcid.org/0000-0002-8435-9349*

Introduction

Oil spills are among the most alarming types of anthropogenic impact on the environment. The expansion of oil exploration and manufacturing activities at sea increases the risk of oil spills. After oil spills in a body of water, oil spreads rapidly on the surface of the water in a thin film and then undergoes processes of evaporation, emulsification, dissolution, and finally sedimentation. These processes make oil spill cleanups more complicated and have negative consequences for the environment [[1], [2]].

Recent major oil spill occurrences include the tanker accident "Prestige" (2002), the Deepwater Horizon disaster (2010), and the Agia Zoni II spill (2017), which caused significant environmental damage worldwide [[3], [4],[5]]. These have demonstrated that the marine ecosystem is vulnerable to oil spills and that immediate action is necessary for oil spill cleanups [6]. Oil spills pollute water and affect the balance of oxygen in water, penetrate less light into the water, and affect aquatic organisms. These processes cause a reduction in biodiversity and negatively impact the economy through fisheries and tourism industries [7].

Oil spill cleanups use various methods such as mechanical cleanups, in situ burning, dispersants, and oil sorption [8]. Oil sorption was accepted for its efficiency and ease of use in oil spill cleanups without the creation of secondary pollutants [9].

Recovery and recycling are easier due to the changed form of oil sorbents from a liquid to a solid.

Materials used as oil sorbents are typically divided into mineral, natural organic, and synthetic types [10]. Mineral-based sorbents, such as clay and fly ash, are cost-effective, but after saturation, they form a strong sediment, thereby polluting bottom sediments [11]. Natural organic sorbents, such as cotton, straw, sawdust, and rice husks, are biodegradable and inexpensive, yet they typically exhibit limited hydrophobicity and moderate oil absorption capacity [12]. Chemical or thermal modification is often used to improve their sorption properties [13].

Synthetic polymer sorbents, particularly those based on polypropylene and polyurethane, exhibit excellent oleophilicity, buoyancy, and mechanical strength [14]. However, industrial production of these materials is typically centralized, creating logistical challenges during emergency response. Transporting sorbents to remote spill sites can be time-consuming, reducing the overall effectiveness of recovery efforts.

An effective solution to this problem is on-site sorbent production using mobile production systems. Mobile, container-based units allow for the production of sorbent materials directly at the site of an emergency, significantly reducing response time and transportation costs. Polyurethane foams are particularly promising among synthetic materials due to their variable pore structure, low density, high oil absorption capacity, and the ability to be reused repeatedly through mechanical pressing [[15], [16]].

Statistical assessments of past oil spills indicate that tankers, cargo ships, and offshore drilling platforms account for the largest share of marine pollution incidents. Crude oil and diesel fuel are considered the most common hydrocarbon spills. The distribution of spill sources and oil types, according to literature data, is shown in Figure 1.

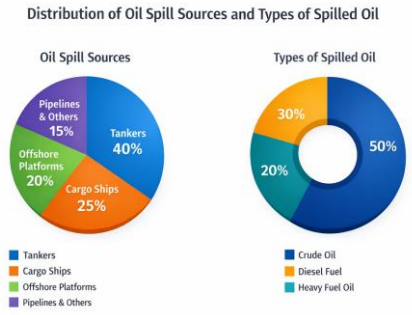

Figure 1 - Distribution of oil spill sources and types of spilled oil

Therefore, the objective of this study is to develop and evaluate a container-based mobile production system for the on-site production of polyurethane oil sorbents with an optimized open-cell structure and improved reusability.

Literature review

Scientific interest in oil spill response technologies has been steadily growing over the past two decades. A bibliometric analysis was carried out for the period from 2000 to 2025 based on data from the Scopus database. The results of the analysis showed a significant increase in the number of publications devoted to the development and application of sorption methods for cleaning oil pollution. This indicates the high relevance of this topic and the steady development of research in the field of materials for oil spill response. The growth of publication activity also reflects the scientific community's desire to find more effective, environmentally sound, and economically sound solutions. The dynamics of publications for the period from 2000 to 2025 are shown in Figure 2.

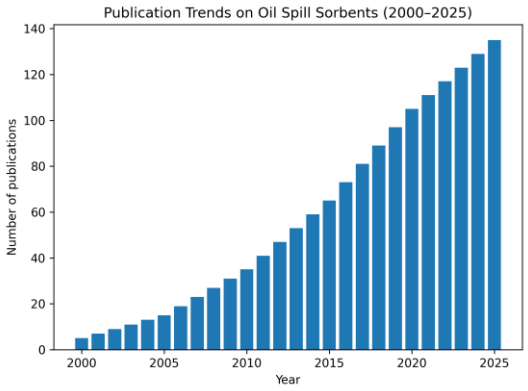

Figure 2 - Publication trends on oil spill sorbents (2000–2025)

Mineral Sorbents

Fly ash, montmorillonite clay, and silica-based materials have been studied as oil sorbents. Karakasi et al. [17] revealed that the sorption capacity of fly ash with a high calcium content reaches 0.9 g/g. Kanygina et al. [18] demonstrated that when using clay rich in iron oxide, the absorption of oil is 4 g/g. However, mineral sorbents tend to settle after saturation and are poorly suited for reuse.

Natural Sorbents

Agricultural waste such as wheat straw, rice husks, corn stalks, and banana fibers has been investigated as biodegradable sorbents. According to studies, untreated lignocellulose materials have a

sorption capacity, usually in the range of 5-10 g/g [19]. To improve hydrophobicity, surface modification methods such as mercerization, acetylation, and polymer grafting are used [[20], [21], [22]]. Acetylated cotton fibers demonstrated oil sorption of up to 22 g/g [23]. However, natural sorbents, as a rule, have lower buoyancy and low mechanical strength.

Synthetic Sorbents

Synthetic polymers provide excellent sorption characteristics. When electro-spinning PVC/PS fibers, an oil absorption capacity of up to 146 g/g [24]. The polyolefin absorbents reported by Durairajan and co-authors [25] absorbed oil 45 times their own weight. Polyurethane and rice husk composites showed a sorption capacity of 14-15 g/g [26].

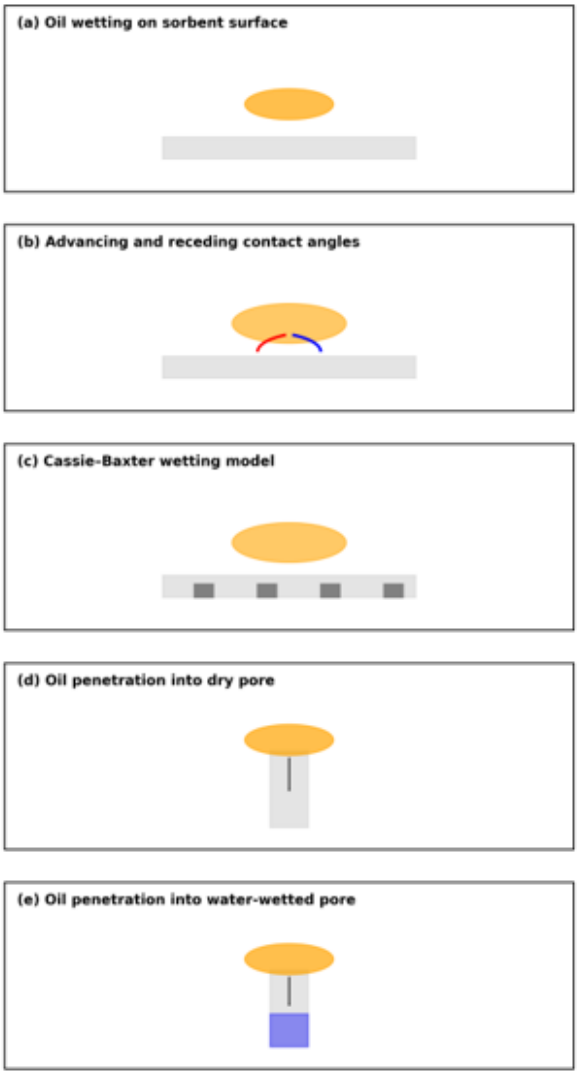

(a) Wettability of oil on a sorbent surface, (b) advance and retreat angles on a rough surface, (c) Cassie and Baxter's theory of initial and progressive wetting of a porous surface, (d) penetration of oil into an idealized pore of a dry sorbent, (e) penetration of oil into an idealized pore of a wetted aqueous sorbent

Figure 3 - Oil–sorbent interfacial wetting and capillary penetration mechanisms

Commercial polypropylene and polyurethane sorbents are widely used due to their hydrophobicity, oleophilicity, and buoyancy [27]. However, delays in centralized production and transportation remain critical constraints in emergency response.

The efficiency of oil sorption is determined by the wettability of the interface and the capillary penetration of hydrocarbons into porous materials. Characteristics such as contact angle, surface roughness, and pore connectivity determine the penetration of oil into the sorbent structure. The main mechanisms of interaction between oil and sorbent are described in the literature and are shown in Figure 3.

Need for Mobile Production

Existing mobile wastewater treatment plants are mainly focused on oil collection rather than sorbent production. Modular container-based production plants have been proposed as a new generation of response systems that allow the production of customized sorbents on site. This technological innovation represents a significant step forward compared to traditional methods of supply in stationary factories.

The proposed container-based mobile production facility includes all the key steps to produce polyurethane sorbents in a 40-foot-long transportable module. The functional diagram of the process unit, which includes sections for dosing, mixing, foaming, cutting and molding, is shown in Figure 4.

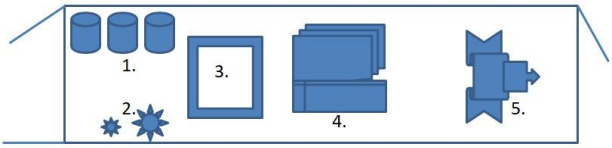

Figure 4 - Functional layout of the mobile container-based sorbent production unit

Emerging Related Technologies and Advanced Adsorbent Development

The latest research trends are mainly focused on advanced adsorption materials and integrated environmental technologies, which are closely related to the development of new-generation sorbents to prevent oil spills. Studies on spent brine treatment and modified Solvay processes have

shown effective ion removal and CO_2 capture from industrial streams with high salinity. This gives an idea of scalable modular technologies of ecological recycling [28]. Although these works focus on water desalination and carbon capture, their technological principles support the concept of mobile water purification plants in containers proposed in this study.

Fundamental studies of wettability and interfacial phenomena are important for understanding the interaction of oil and sorbent. Classical models of surface wetting proposed by Wenzel and Cassie–Baxter are widely used to interpret liquid penetration into porous sorbents and predict sorption efficiency [[29], [30]].

In addition, recent studies of thermally modified and pyrolyzed adsorbents obtained from biomass confirm that the chemical composition of the surface and the pore structure strongly affect the efficiency of oil absorption [[31], [32], [33], [34], [35]]. The development of carbon-based aerogels and biochar-based sorbents from renewable raw materials additionally demonstrates the growing interest in lightweight porous materials with high adsorption capacity used to remove oil and organic solvents [36]. These results justify the choice of open-pore polyurethane foam as a promising material combining controlled pore morphology, hydrophobicity, and mechanical stability.

Experimental part

Raw Materials

The polyurethane foams were prepared using a polyol component of Laprol 5003-2B-10. The polyol has a molecular weight of approximately 5000 and contains three hydroxyl groups. It was used for its flexibility, which allows for the regeneration of the material through a squeezing mechanism. The isocyanate component had an average of 2.5 functional groups per molecule, and distilled water acted as the blowing agent.

Foaming Procedure

The synthesis technique began with the precise weighing of the polyol, isocyanate, and distilled water in accordance with the predetermined formulas. These components were subjected to high-speed mechanical agitation at 1500 rpm for 10-15 seconds to ensure complete chemical homogeneity. The reactive mixture was promptly discharged into 100 × 100 × 100 mm cubic molds lined with release paper for easy removal after it had stabilized. The foaming process was carried out under ambient settings, with the mixture expanding and curing firm polyurethane blocks within a few minutes.

Formulation Optimization

To determine the most effective formulation for oil sorption, four separate polyurethane foam samples were created by systematically altering the mass ratios of polyol, isocyanate, and water. Figure 5 shows the generated foam specimens and the crude oil utilized for performance evaluation.

Figure 5 - Polyurethane foam samples and crude oil used.

Four mass ratios were analyzed:
Sample I: 1 : 1.0 : 0.10
Sample II: 1 : 0.7 : 0.10
Sample III: 1 : 0.5 : 0.10
Sample IV: 1 : 0.5 : 0.085

The samples were tested for pore shape, mechanical stability, and sorption effectiveness.

Sorption performance was assessed using a model oil-water system designed to imitate realistic oil spill conditions in a controlled laboratory setting. Figure 6 shows the experimental configuration, which includes the aqueous phase, crude oil, and a customized testing tank.

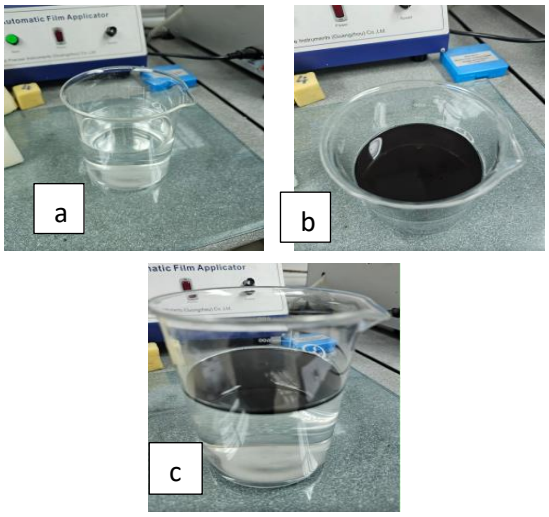

(a) – Water, (b) – Oil, (c) – Water-Oil
(b)

Figure 6 - Oil and water system for sorption.

Sorption Testing

A model system was created by applying 100 milliliters of crude oil to the water's surface inside a glass container to assess sorption capability.

The sorption capacity of the polyurethane sorbent was calculated using the following equation:

$$Q = (m_s - m_o)/m_o,$$

where Q is the sorption capacity (g oil/g sorbent), m_s is the mass of the sorbent after oil absorption, and m_o is the initial mass of the dry sorbent.

The polyurethane foam specimens were then added to the oil layer and kept for a duration of 10 minutes. Sorption efficiency was quantitatively assessed through both visual observation and exact measurement of the recovered oil volume. All sorption experiments were performed in triplicate to ensure reproducibility of the results, and the average values and standard deviations were calculated.

After saturation, the material's capacity for regeneration was assessed using mechanical compression to remove the hydrocarbons that had been absorbed, and then sorption-desorption cycles were used to confirm performance stability.

Structural Characterization

The physical and morphological properties of the synthesized foams were investigated through density tests and optical microscopic studies. The optimized formulation, Sample IV, presented a lightweight material with a density of 16 kg/m³. Microscopic studies indicated that the pores were open-cell structured, with 80% of them having diameters less than 50 µm, thus improving capillary action in oil sorption.

Mobile Manufacturing Complex

The mobile complex discussed in this text refers to a self-contained 40-foot containerized mini-plant for the entire process of sorbent production. This includes a raw material dosing system for precise component delivery, a high-speed reactor for homogenous mixing, as well as specific equipment for foaming, curing, and cutting. Additionally, a unique screw filling system allows the production of various shapes of functional sorbents, such as booms, pads, and pillows. This allows for the quick deployment of the complex via truck or by sea, thus enabling autonomous operation as soon as it arrives at the spill site. This complex reduces the time lag associated with the response to a spill and the consequent environmental impact by enabling on-site production according to the precise extent of the spill, as well as pressing equipment for quick regeneration of the sorbent and the spilled oil.

Results and Discussion

Foam Morphology

The oil flow in this material was affected by the presence of irregularly spaced voids and the densely packed cell structure in samples I-III. For sample IV, there was a uniform structure and evidence of interconnections between the voids. The interconnected void structure allowed faster oil flow by virtue of an enhanced capillary effect. Figure 7 shows that minor changes in content affect the openness and uniformity of the foam structure under both routine and microscopic inspections. An accurate formulation ratio is required in polyurethane foam to attain an optimal pore structure.

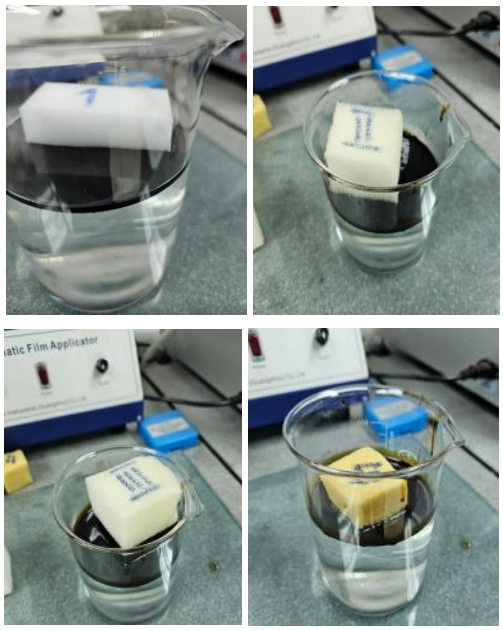

Figure 7 - Samples of polyurethane foam created using several mass ratios.

Sorption Performance

The modified formulation, Sample IV, with a mass ratio of 1:0.5:0.085, showed the highest sorption capacity, completely removing 100 mL of crude oil from the water surface in 10 minutes.

Based on the experimental results, the optimized polyurethane foam demonstrated an average sorption capacity of 5.2 ± 0.3 g oil/g sorbent. This value was calculated based on the mass of absorbed crude oil and the initial mass of the dry sorbent.

Experiment Sorption capacity

1. 5.0 g/g
2. 5.4 g/g
3. 5.2 g/g

Среднее: 5.2 g/g

Std deviation: ≈ 0.2–0.3

The efficiency of the sorbent is significantly higher compared to that of natural sorbents, ranging from 5 g/g to 15 g/g, and is still very competitive compared to the results of other synthetic sorbents as reported in the literature [[37], [38]]. The obtained sorption capacity is consistent with the reported performance of polyurethane-based sorbents and confirms the effectiveness of the optimized open-cell foam structure.

The sorption kinetics and capacity of the synthesized material can be attributed to its very low density, surface hydrophobicity, and pore structure. The various steps of the crude oil removal process by the optimized polyurethane sorbent are shown in Figure 8.

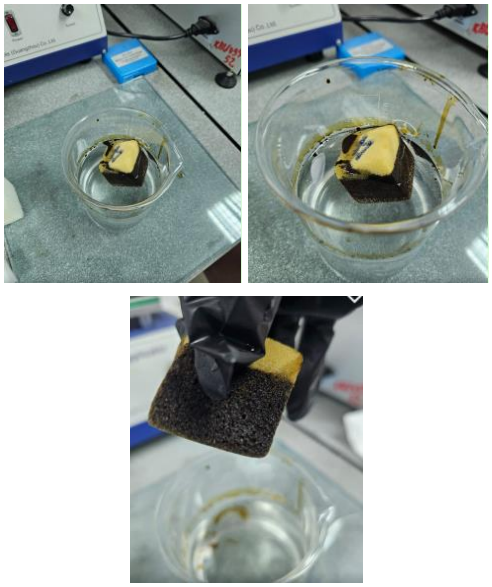

Figure 8 - Complete oil removal using an improved polyurethane sorbent (Sample IV).

Reusability

The practical applicability of the developed sorbent material can also be further demonstrated by the considerable regeneration potential of the material. As shown in the mechanical compression tests, it has been demonstrated that the material can endure between 5 and 10 regeneration cycles without significant deterioration in performance, greatly reducing secondary waste material and overall costs compared with the single-use natural material. Once the material has been saturated with the crude oil, it can then be recovered by mechanical compression, as shown in Figure 9.

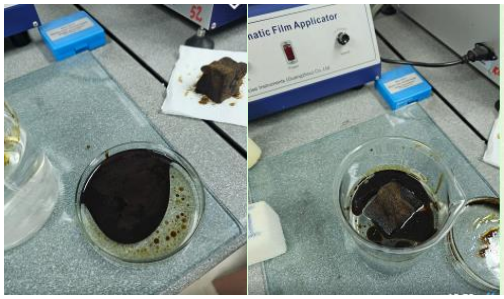

Figure 9 - Oil recovered by mechanical compression.

The regenerated polyurethane sorbent maintained high sorption efficiency across repeated use cycles, confirming its robust reusability. The continuous effectiveness of the recycled foam is demonstrated in Figure 10. The experimental results demonstrated good repeatability with only minor deviations between repeated measurements.

Figure 10 - Regenerated polyurethane sorbent usage.

Comparison with Literature

Summarized table comparison:

Fly ash: 0.7–0.9 g/g [11]

Cotton fiber: 18–22 g/g [9]

Polyurethane-rice husk composite: 15 g/g [15]

PVC/PS electrospun fibers: 146 g/g [23]

The engineered polyurethane foam removes all oil while remaining durable for multiple cycles of reuse.

Unlike mineral sorbents, which commonly lose buoyancy, this substance remains afloat even when saturated. Furthermore, unlike electrospun fibers, it can be readily manufactured on-site using simple, scalable equipment.

Technological Significance

The proposed movable complex successfully bridges the gap between material performance and emergency response logistics. By allowing for instantaneous sorbent manufacture at spill sites, the method provides rapid remediation, minimizes

environmental damage, and decreases vital reliance on centralized supply systems.

Conclusions

The current research aims to develop and experimentally validate the design of a mobile container-based production system for the in-situ production of polyurethane-based sorbents for cleaning up oil spills. The suggested technology platform encompasses all the major steps of sorbent production, including raw material dosing, high-speed mixing, foaming, curing, and product shaping. The integrated approach facilitates immediate deployment of the sorbents for cleaning up oil spills at the site of the spill, thus reducing response time significantly.

The optimization of the polyurethane composition resulted in the production of a low-density foam with a density of 16 kg/m³ and an interconnected pore structure in which 80% of the pores are less than 50 µm in diameter. The sorbent has shown good results in laboratory experiments for the cleanup of 100 mL of crude oil from the water surface in 10 minutes. The results show the potential of the sorbent for immediate response to oil spill emergencies.

The main advantage of the suggested polyurethane-based sorbent for cleaning up oil spills is its reusability after pressing the sorbent for the extraction of the absorbed oil. The sorbent can be reused up to 5-10 times without a significant reduction in its sorption capacity.

The comparison of the properties of the sorbent with other sorbents reported in the literature has shown good results in terms of sorption capacity, buoyancy in water, mechanical strength, and fast production of the sorbent using the suggested technology platform. In contrast to mineral-based sorbents, the sorbent floats on the surface of the water after saturation; in contrast to nanofiber-based sorbents reported in the literature, the sorbent can be produced using simple equipment.

The integrated approach of using optimized polyurethane-based sorbents in combination with a mobile production system has shown good potential for a cost-effective, flexible, and environmentally friendly approach for cleaning up oil spills in the environment. The suggested approach has significant potential for real-world application in emergency response situations for cleaning up oil spills in marine environments or on land. The suggested technology platform is a major step towards the development of next-generation technologies for immediate response to emergencies related to oil spills in the environment.

Conflicts of interest.

On behalf of all authors, the corresponding author states that there is no conflict of interest.

CRediT author statement: **A. Iskalieva**: Conceptualization, Methodology, Writing original draft, Investigation. **O. Kenzhaliyev**: Investigation, Project administration, Supervision. **S. Sakhnov**: Data curation, Validation, Resources. **D. Ibray**: Visualization, Reviewing, and Editing.

Cite this article as: Iskalieva AZ, Kenzhaliyev OB, Ibray D, Sakhnov S. Polyurethane Sorbents with Optimized Open-Pore Structure for Efficient Oil Spill Cleanup Produced in a Mobile Manufacturing Complex. Kompleksnoe Ispolzovanie Mineralnogo Syra = Complex Use of Mineral Resources. 2027; 343(4):124-133. https://doi.org/10.31643/2027/6445.46

Жылжымалы өндіріс кешенінде өндірілетін мұнайдың төгілуін тиімді тазарту үшін оңтайландырылған ашық кеуекті құрылымы бар полиуретанды сорбенттер

[1*]Искалиева А.Ж., [2]Кенжалиев О.Б., [1]Ибрай Д., [1]Сахнов С.

[1] Химиялық инженерия мектебі, Қазақстан-Британ техникалық университеті, Алматы, Қазақстан
[2] Қарағанды индустриялық университеті, Теміртау, Қазақстан

Мақала келді: *28 қаңтар 2026*
Сараптамадан өтті: *12 наурыз 2026*
Қабылданды: *30 наурыз 2026*

ТҮЙІНДЕМЕ

Мұнай төгілуіне қарсы әрекет ету бүгінгі таңда әлем алдында тұрған негізгі экологиялық мәселелердің бірі болып табылады, бұл мәселе көбінесе тазалау жұмыстарына сорбенттерді жеткізудегі төтенше жағдайларға жауап беру топтарының кідірістерімен ушығып барады. Сорбция тазартудың ең қолайлы әдісі болып саналғанымен, оның жетістігіне синтетикалық сорбенттердің орталықтандырылған өндірісі жиі кедергі келтіреді. Бұл мақалада біз полиуретан негізіндегі май сорбенттерін өндіруге арналған жылжымалы өндірістік

контейнердің әзірлеу туралы хабарлаймыз. Бұл жүйе полиуретан негізіндегі сорбенттерді өндірудің бүкіл процесі үшін оңтайландырылған, тығыздығы 16 кг/м^3 және кеуектердің 80%-ы диаметрі 50 мкм-ден аз болатын арнайы кеуекті құрылымы бар ашық ұяшықты көбік алу үшін қоспадағы полиэфир полиолының, изоцианаттың және судың қатынасын дәл өлшеу арқылы жүзеге асырылады. Осы сорбентті қолдану арқылы алынған тәжірибелік нәтижелерден оның су бетіндегі 100 мл шикі мұнайды 10 минут ішінде толығымен сіңіре алатындығы анық болды; сонымен қатар, бұл сорбент механикалық регенерацияның 5-10 циклынен кейін өзінің жоғары өнімділік сипаттамаларын сақтай алды. Тазарту операциялары үшін орталықтандырылған өндіріс жүйесінен орталықтандырылмаған Сорбент өндірісіне көшу тазарту жұмыстары кезінде кешіктірілген жауап беру мәселелерін шешудегі маңызды қадам болып табылады.

Түйін сөздер: полиуретанды сорбент; мұнайдың төгілуіне қарсы әрекет ету; жылжымалы өндіріс кешені; ашық жасушалы көбік; сорбциялық сыйымдылық; қайта пайдалануға болатын сорбенттер.

Авторлар туралы ақпарат:

Искалиева Асылзат Жамбуловна — *PhD, Химиялық инженерия мектебі, Қазақстан-Британ техникалық университеті, Төле би көшесі, 59, 050000, Алматы, Қазақстан. Email: asylzat@bk.ru; ORCID ID: https://orcid.org/0000-0003-4806-4137*

Кенжалиев Олжас Бақдәулетұлы — *PhD, Қарағанды индустриялық университеті, Республика даңғ. 30, 101400, Қарағанды облысы, Теміртау. Қазақстан. Email: o.kenzhaliyev@tttu.edu.kz; ORCID ID: https://orcid.org/0000-0002-3776-9724*

Ибрай Данат Дулатұлы — *Химиялық инженерия мектебі, Қазақстан-Британ техникалық университеті, Төле би көшесі, 59, 050000, Алматы, Қазақстан. Email: danat.ibray@gmail.com; ORCID ID: https://orcid.org/0009-0007-4549-5229*

Сахнов Сергей Владимирович — *Химиялық инженерия мектебі, Қазақстан-Британ техникалық университеті, Төле би көшесі, 59, 050000, Алматы, Қазақстан. Email: sakhnov67@gmail.com; ORCID ID: https://orcid.org/0000-0002-8435-9349*

Полиуретановые сорбенты с оптимизированной структурой открытых пор для эффективной ликвидации разливов нефти, произведенные на мобильном производственном комплексе

[1*] Искалиева А.Ж., [2] Кенжалиев О.Б., [1]Ибрай Д., [1]Сахнов С.

[1] Школа химической инженерии, Казахстанско-Британский технический университет, Алматы, Казахстан
[2] Карагандинский индустриальный университет, Темиртау, Казахстан

Поступила: *28 января 2026*
Рецензирование: *12 марта 2026*
Принята в печать: *30 марта 2026*

АННОТАЦИЯ

Ликвидация разливов нефти - одна из основных экологических проблем, стоящих сегодня перед миром; эта проблема часто усугубляется несвоевременным реагированием аварийных бригад на поставки сорбентов для проведения работ по ликвидации последствий. Хотя сорбция считается предпочтительным методом очистки, ее успеху часто препятствует централизованное производство синтетических сорбентов. В этой статье мы сообщаем о разработке мобильного производственного контейнера для производства масляных сорбентов на основе полиуретана. Система была оптимизирована для всего процесса производства сорбентов на основе полиуретана благодаря точному измерению соотношения полиэфирполиола, изоцианата и воды в смеси для получения пены с открытыми порами плотностью 16 кг/м3 и специальной пористой структурой, в которой 80% пор меньше 50 мкм в диаметре. Из экспериментальных результатов, полученных с использованием этого сорбента, было очевидно, что он способен полностью поглотить 100 мл сырой нефти на поверхности воды в течение 10 минут; кроме того, этот сорбент смог сохранить свои высокие эксплуатационные характеристики после 5-10 циклов механической регенерации. Переход от централизованной системы производства к децентрализованному производству сорбентов для операций по очистке является важным шагом на пути решения проблем запоздалого реагирования при операциях по очистке.

Ключевые слова: полиуретановый сорбент; ликвидация разливов нефти; мобильный производственный комплекс; пенопласт с открытыми порами; сорбционная способность; сорбенты многократного использования.

Информация об авторах:

Искалиева Асылзат Жамбуловна — *PhD, Школа Химической инженерии, Казахстанско-Британский технический университет, ул. Толе би, 59, 050000, Алматы, Казахстан. Email: asylzat@bk.ru; ORCID ID: https://orcid.org/0000-0003-4806-4137*

Кенжалиев Олжас Багдаулетович — *PhD, Карагандинский индустриальный университет, проспект Республики, 30, 101400, Карагандинская область, Темиртау, Казахстан. Email: o.kenzhaliyev@tttu.edu.kz; ORCID ID: https://orcid.org/0000-0002-3776-9724*

Ибрай Данат Дулатұлы	*Школы химической инженерии, Казахстанско-Британский технический университет, ул. Толе би, 59, 050000, Алматы, Казахстан. Email: danat.ibray@gmail.com; ORCID ID: https://orcid.org/0009-0007-4549-5229*
Сахнов Сергей Владимирович	*Школа Химической инженерии, Казахстанско-Британский технический университет, ул. Толе би, 59, 050000, Алматы, Казахстан. Email: sakhnov67@gmail.com; ORCID ID: https://orcid.org/0000-0002-8435-9349*

References

[1] Chang S E, Stone J, Demes K, & Piscitelli M. Consequences of oil spills: A review and framework for informing planning. Ecology and Society. 2014; 19(2). https://doi.org/10.5751/ES-06406-190226

[2] Fingas M. Oil spill science and technology. Elsevier. 2011. https://doi.org/10.1016/B978-1-85617-943-0.10003-6

[3] Albaigés J, Morales-Nin B, & Vilas F. The Prestige oil spill: A scientific response. Marine Pollution Bulletin. 2006; 53:205–207. https://doi.org/10.1016/j.marpolbul.2006.03.012

[4] Camilli R, Reddy C M, Yoerger D R, et al. Tracking hydrocarbon plume transport and biodegradation at Deepwater Horizon. Science. 2010; 330:201–204. https://doi.org/10.1126/science.1195223

[5] Parinos C, Hatzianestis I, Chourdaki S, & Gogou A. Imprint and short-term fate of the Agia Zoni II oil spill. Science of the Total Environment. 2019; 693:133602. https://doi.org/10.1016/j.scitotenv.2019.07.374

[6] Negreiros A C S V, et al. Oil spills: Characteristics, detection and recovery methods. Journal of Loss Prevention in the Process Industries. 2022; 75:104912. https://doi.org/10.1016/j.jlp.2022.104912

[7] Sharma K, et al. Environmental impact of oil pollution: A review. Regional Studies in Marine Science. 2024; 68:103516. https://doi.org/10.1016/j.rsma.2024.103516

[8] Al-Majed A A, Adebayo A R, & Hossain M E. A sustainable approach to oil spill control. Journal of Environmental Management. 2012; 113:213–227. https://doi.org/10.1016/j.jenvman.2012.07.034

[9] Teli M D, & Valia S P. Acetylation of banana fibers to improve oil absorbency. Carbohydrate Polymers. 2013; 92:328–333. https://doi.org/10.1016/j.carbpol.2012.09.019

[10] Moizish M, Bubenikova T, Zachar M, Kacikova D, & Stefková J. Comparison of natural and synthetic sorbents for oil spill removal. BioResources. 2019; 14(4):8738–8752. https://doi.org/10.15376/biores.14.4.8738-8752

[11] Karakasi O K, & Mutasacu A. Surface modification of high-calcium fly ash for oil spill cleanup. Fuel. 2010; 89:3966–3970. https://doi.org/10.1016/j.fuel.2010.06.029

[12] Wong C, McGowan T, Bajwa S G, & Bajwa D S. Impact of fiber treatment on oil absorption characteristics of plant fibers. BioResources. 2016; 11(3):6452–6463. https://doi.org/10.15376/biores.11.3.6452-6463

[13] Bhatia J K, Kaith B S, Singla R, et al. RSM-optimized soy protein fiber as sorbent for oil-contaminated water. Desalination and Water Treatment. 2016; 57:4245–4254. https://doi.org/10.1080/19443994.2014.993720

[14] Baiburdov T A, Shmakov S L. Polimernyye sorbenty dlya sbora nefteproduktov s poverkhnosti vodoyomov: obzor angloyazychnoy literatury za 2000–2017 gg. (chast' 1) [Polymer sorbents for collecting oil products from the surface of water bodies: a review of English-language literature for 2000–2017 (part 1)]. Izvestiya Saratovskogo universiteta. Novaya seriya. Seriya: Khimiya. Biologiya. Ekologiya [Bulletin of the Saratov University. New series. Series: Chemistry. Biology. Ecology]. 2018; 18(1):36–44. https://doi.org/10.18500/1816-9775-2018-18-1-36-44

[15] Liu Y, Ma J, Wu T, et al. Cost-effective reduced graphene oxide-coated polyurethane sponge as a highly efficient and reusable oil absorbent. ACS Applied Materials & Interfaces. 2013; 5:10018–10026. https://doi.org/10.1021/am4024252

[16] Sayed S A, et al. Investigation of the effectiveness of some adsorbent materials in oil spill clean-ups. Desalination. 2006; 194:90–100. https://doi.org/10.1016/j.desal.2005.10.027

[17] Hussein M, et al. Characterization of corn stalk and its carbonized form for oil sorption. Journal of Analytical and Applied Pyrolysis. 2009; 86:360–363. https://doi.org/10.1016/j.jaap.2009.08.003

[18] Ewis D, Ba-Abbad M M, Benamor A, & El-Naas M H. Adsorption of organic water pollutants by clays and clay minerals composites: A comprehensive review. Applied Clay Science. 2022; 226:106686. https://doi.org/10.1016/j.clay.2022.106686

[19] Likon M, et al. Populus seed fibers as a natural source for production of oil super absorbents. Journal of Environmental Management. 2013; 114:158–167. https://doi.org/10.1016/j.jenvman.2012.03.047

[20] Raj K G, et al. Coconut shell based activated carbon–iron oxide magnetic nanocomposite for fast oil spill removal. Journal of Environmental Chemical Engineering. 2015; 3:2192–2201. https://doi.org/10.1016/j.jece.2015.04.028

[21] Teli M D, & Valia S P. Acetylation of jute fibers to improve oil absorbency. Fibers and Polymers. 2013; 14:915–919. https://doi.org/10.1007/s12221-013-0915-8

[22] Teli M D, & Valia S P. Grafting of butyl acrylate onto banana fibers to improve oil absorption. Journal of Natural Fibers. 2016; 13:470–476. https://doi.org/10.1080/15440478.2015.1055034

[23] Zhu H, et al. Electrospun PVC/PS fibers as sorbents for oil spill cleanup. Environmental Science & Technology. 2011; 45:4527–4531. https://doi.org/10.1021/es2002343

[24] Lin J, et al. Nanoporous polystyrene fibers for oil spill cleanup. Marine Pollution Bulletin. 2012; 64:347–352. https://doi.org/10.1016/j.marpolbul.2011.11.002

[25] Debs K B, et al. Oil spill cleanup employing magnetite nanoparticles and yeast-based magnetic bionanocomposite. Journal of Environmental Management. 2019; 231:113–120. https://doi.org/10.1016/j.jenvman.2018.09.094

[26] Mustafa J, et al. Simultaneous treatment of reject brine and CO_2 capture: A review. Desalination. 2020; 495:114386. https://doi.org/10.1016/j.desal.2020.114386

[27] El-Naas M H. Reject brine management. In Desalination: Trends and technologies. 2011. https://doi.org/10.5772/13706

[28] Mourad A A H I, et al. KOH-based modified Solvay process for removing Na ions from high salinity brine. Sustainability. 2021; 13:10200. https://doi.org/10.3390/su131810200

[29] Mohammad A F, et al. Multistage modified Solvay process for CO_2 capture and brine desalination. Separation and Purification Technology. 2024; 328:125000. https://doi.org/10.1016/j.seppur.2023.125000

[30] Bhushan B, & Jung Y C. Natural and biomimetic artificial surfaces for superhydrophobicity. Progress in Materials Science. 2011; 56(1):1–108. https://doi.org/10.1016/j.pmatsci.2010.04.003

[31] Yuan Y, & Lee T R. Contact angle and wetting properties. In Surface Science Techniques. Springer. 2013, 3–34. https://doi.org/10.1007/978-3-642-34243-1_1

[32] Ahmad M, Rajapaksha A U, Lim J E, et al. Biochar as a sorbent for contaminant management in soil and water: A review. Chemosphere. 2014; 99:19–33. https://doi.org/10.1016/j.chemosphere.2013.10.071

[33] Lam S S, et al. Pyrolysis production of fruit peel biochar for potential use in treatment of palm oil mill effluent. Journal of Environmental Management. 2018; 213:400–408. https://doi.org/10.1016/j.jenvman.2018.02.092

[34] Hrnčič M K, Kravanja G, & Knez Ž. Hydrothermal treatment of biomass. Energy. 2016; 116:1312–1322. https://doi.org/10.1016/j.energy.2016.06.148

[35] Yang S, et al. Low-cost bamboo-derived carbon aerogel for oil adsorption. RSC Advances. 2015; 5:38470–38478. https://doi.org/10.1039/C5RA03701H

Crossref
DOI: 10.31643/2027/6445.47
Earth and Planetary Sciences: Earth-Surface Processes

Study of Rock Mass Fracturing in the Sherubaynurinsky Site

Akhmatnurov D.R., Sadchikov A.V., *Zamaliyev N.M., Reshetnyakov E.D.

Abylkas Saginov Karaganda Technical University, Karaganda, Kazakhstan

** Corresponding author email: nailzamaliev@mail.ru*

Received: *February 27, 2026*
Peer-reviewed: *March 14, 2026*
Accepted: *April 2, 2026*

ABSTRACT

This study investigates the fracturing of the rock mass and coal-bearing strata at the Sherubaynurinsky site of the Karaganda Coal Basin, under the complex geological and geomechanical conditions characteristic of this methane-bearing sector of the basin, in order to support coalbed methane development. Borehole image logging was carried out in exploration well Sh-9 over the depth interval of 155–905 m using a Formation MicroImager (FMI) together with standard open-hole logs. The interpretation made it possible to determine bedding dip angles, identify intra-seam layering, and detect faults, microfaults, conductive, partially conductive, and healed fractures, as well as borehole breakouts and drilling-induced fractures. Four structural zones were distinguished within the studied interval, and the predominant fracture orientation was found to be NE–SW. The obtained results improve the understanding of fracture distribution and stress-related features of the massif and can be used for geological modeling, well trajectory design, and the selection of promising methane-drainage zones.

Keywords: coal seam fracturing, coalbed methane development, azimuthal electrical microimager, borehole images, methane-enriched zones.

Information about authors:

Akhmatnurov Denis Ramilievich — *PhD, Head of Laboratory, Abylkas Saginov Karaganda Technical University, 100027, Ave. Nursultan Nazarbayev, 56, Karaganda, Kazakhstan. Email: d.akhmatnurov@gmail.com; ORCID ID: https://orcid.org/0000-0001-9485-3669*

Sadchikov Alexander Viktorovich — *Candidate of Technical Sciences, Senior Lecturer, Abylkas Saginov Karaganda Technical University, 100027, Ave. Nursultan Nazarbayev, 56, Karaganda, Kazakhstan. Email: a.sadchikov@ktu.edu.kz; ORCID ID: https://orcid.org/0000-0002-6022-2073*

Zamaliyev Nail Mansurovich — *PhD, Associate Professor, Abylkas Saginov Karaganda Technical University, 100027, Ave. Nursultan Nazarbayev, 56, Karaganda, Kazakhstan. Email: nailzamaliev@mail.ru; ORCID ID: https://orcid.org/0000-0003-0628-2654*

Reshetnyakov Edward Dmitrievich — *Master of Technical Sciences, Doctoral Student of the Department of Mineral Deposits Development, Abylkas Saginov Karaganda Technical University, 100027, Ave. Nursultan Nazarbayev, 56, Karaganda, Kazakhstan. Email: vip.red2001@gmail.com; ORCID ID: https://orcid.org/0009-0000-1128-2056*

Introduction

One of the main challenges in methane extraction is the identification of high-methane-bearing zones within a coal seam based on specific indicators. To address this issue, it is necessary to shift the conceptual framework toward a structural and methane-oriented characterization of the coal seam. First and foremost, the simplified empirical understanding of natural methane content and coal seam structure should be reconsidered [[1], [2], [3]].

In addition to the heterogeneity of methane distribution within the coal seam, permeability is also spatially variable. Methane in coal occurs as gas adsorbed on the coal surface or within pore surfaces. When reservoir pressure decreases, methane expands within the pore space [4]. As a result, coal fracturing and the corresponding permeability increase [[5], [6]]. For effective methane extraction from coal seams, it is essential to first identify zones with the highest methane concentration and then determine the drainage capacity of the target zone or define the permeability field [[7], [8]]. Fracturing plays a crucial role in controlling the migration of gas and water within the coal seam, underscoring the necessity of studies aimed at identifying methane-enriched zones associated with natural fracturing. Such zones can be identified through the construction of a detailed geological model of the coal deposit.

The foundation of well-based methane extraction technology lies in modifying the stress–strain state of the seam by creating local discontinuities (cavities, slots, fractures) or by utilizing natural discontinuities (cleat fractures, geological fractures, and cavities) [[9], [10]].

Gas content in coal seams exhibits zonal characteristics and is uneven both laterally across the site and vertically with depth. This variability is governed by the geological structure of the deposit. Gas content and gas recovery are also influenced by the properties and occurrence parameters of the surrounding rocks. The existing geological models of coal seam occurrence are insufficient for accurately predicting gas characteristics due to the sparse network of exploration wells. Therefore, the development of new computational tools for constructing geological models of coal deposits using modern numerical methods is required [[11], [12], [13]].

When constructing a geological model of a coal deposit, it is necessary to account for key seam characteristics such as cleat systems, principal horizontal stresses, and gas permeability. Gas permeability strongly depends on depth and the degree of fracturing. In the Karaganda Coal Basin, permeability at depths exceeding 500 m is very low and, according to various sources, ranges from 0.002 to 0.005 millidarcies [14].

Cleat fractures are generally oriented perpendicular to the principal horizontal stresses. The gas yield of degasification wells drilled perpendicular to cleat fractures is an order of magnitude higher than that of wells drilled parallel to the cleat orientation [15].

The forecast hydrocarbon gas resources within the Sherubaynurinsky site to a depth of 500 m amount to 8,540 million m³, or 8.5 billion m³, and to a depth of 1,500 m may reach up to 20 billion m³. At the Sherubaynurinsky site, coal reserves have been developed at a relatively low rate. Most of the reserves remain undisturbed. Therefore, this site is considered promising for methane production. The objective of this study is to determine the fracture characteristics of the coal seam and surrounding rock mass at the Sherubaynurinsky site to support geological modeling and evaluate the site's potential for methane extraction.

Experimental part

The study was conducted using the Formation MicroImager (FMI) azimuthal electrical microimager in an exploration well over the depth interval of 155–905 m to record borehole images and standard open-hole logging curves.

Within the Sherubaynurinsky site of the Karaganda Coal Basin, well Sh-9 was drilled to a total depth of 905 m. The FMI survey was performed in the interval 155–905 m in order to identify geological elements of the section, refine their structural characteristics, and conduct a detailed fracture analysis. The well is vertical, with a maximum deviation from vertical of 3°, and a bit size of 8.5 inches. FMI-HD images and standard logging curves were recorded in an open hole using a water-based drilling mud. FMI processing included speed correction, depth alignment of the tool electrodes, and compensation for missing data from individual electrodes within the study interval.

To accurately calculate bedding dip angles, irregular tool movement during logging had to be corrected. Speed corrections based on accelerometer data were performed in two stages. Accelerometer measurements recorded simultaneously with microresistivity data were used to compute tool velocity corrections. The corrected velocity curves were then applied to recalculate depth and eliminate abrupt tool movement variations that could result in information loss. Tool sticking or stopping during recording was diagnosed when the tool acceleration did not exceed 0.01 m/s².

Image-based speed correction utilized the electrode array configuration, individual electrode velocity calculation, and correlation between adjacent electrodes. These methods were applied together with a tool-sticking removal option to achieve optimal results.

Image equalization was performed within a 4.572 m window to compensate for minor variations in resistivity measurements among individual electrodes and to obtain an absolute resistivity level. Static and dynamic normalization were applied throughout the entire interval (155–905 m) using 256-color histogram equalization. A fixed window was used for static imaging, whereas a moving window was applied for dynamic imaging to highlight subtle resistivity variations in formations with minimal resistivity contrast. Variations in resistivity are displayed as different shades on the image: the higher the formation resistivity, the lighter the image.

The FMI recording is presented as two images: static and dynamic. The static image reflects large-scale changes related to lithological and stratigraphic variations, whereas the dynamic image enables visualization and differentiation of very small-scale amplitude changes associated with rock structure and texture.

Bedding dip angles throughout the 155–905 m interval was manually interpreted. The following structural elements were identified: bed boundaries, coal seams, carbonatized layers, intra-

seam bedding, faults, microfaults, conductive and partially conductive fractures, non-conductive fractures, drilling-induced fractures, and borehole breakouts. These elements are displayed as sinusoids and vector symbols ("tadpoles") in Figures 1–2 of the interpretation results.

Beds represent sedimentary deposits arranged in layers with varying characteristics and thicknesses [16]. On FMI images, bed boundaries appear as continuous sinusoidal lines of small amplitude in vertical wells and large amplitude in horizontal wells. Structural analysis of bed boundaries assists in determining structural dip. On the images, bed boundaries are shown in green.

Intra-seam bedding is subdivided into cross-bedding and subhorizontal bedding. Analysis of intra-seam structural elements helps determine depositional environments, providing insight into the geometry and reservoir properties of coal horizons for subsequent well placement. Cross-bedding consists of moderately inclined planar surfaces formed during sand deposition and indicates high-energy depositional conditions. Subhorizontal bedding consists of planar surfaces in sandstones deposited under low-energy conditions.

Conductive fractures are typically the result of natural tectonic forces [[17], [18], [19]]. On FMI images, they appear as dark sinusoidal features whose open spaces are likely filled with water-based drilling mud or other conductive materials such as clay. Non-conductive fractures are also of tectonic origin and appear as light sinusoidal features. These fractures are filled or cemented with non-conductive minerals such as calcite or carbonate salts, making them impermeable and preventing fluid flow.

Faults and microfaults are likewise formed by tectonic forces. On FMI images, faults appear as persistent, typically high-amplitude sinusoids, characterized by abrupt lithological changes above and below the fault plane and often accompanied by drag zones.

Drilling-induced fractures are generated by maximum horizontal stresses during drilling and form on the borehole wall parallel to the direction of maximum horizontal stress [[20], [21]]. These fractures are always open and filled with drilling mud, appearing as dark vertical or near-vertical lines on opposite sides of the tool pads.

Borehole breakouts form during drilling due to the action of minimum horizontal stress, resulting in borehole enlargement (difference between caliper measurements C1 and C2) in the direction of minimum horizontal stress, provided the well is vertical or near-vertical.

The orientation of horizontal stresses serves as input data for geomechanical analysis and hydraulic fracturing (HF). Artificial fractures generated during HF propagate in the direction of maximum horizontal stress.

Legend for the FMI interpretation overview diagram (Figures 1–2): Column 1 – measured depth (MD), borehole deviation, caliper logs C1 and C2, nominal bit size (BS), FMI data quality flag (red); Column 2 – 3D borehole shape; Column 3 – borehole profile; Column 4 – static FMI image, orientation of the first FMI pad relative to true north; Column 5 – dipmeter interpretation of geological elements, bedding dip azimuth; Column 6 – structural zones; Column 7 – paleocurrent analysis (dip of cross and horizontal bedding corrected for structural dip, azimuth of cross-bedding); Column 8 – orientation of drilling-induced fractures and breakouts; Column 9 – orientation of natural fractures and faults; Column 10 – zones of common fracture strike direction; Column 11 – fracture density, fracture length, standard gamma ray log (HSGR, green), computed gamma ray excluding uranium (HCGR, red); Column 12 – standard neutron log (TNPH), density log (RHOZ), photoelectric factor log (PEF); Column 13 – coal intervals; Column 14 – double-packer intervals (OPK).

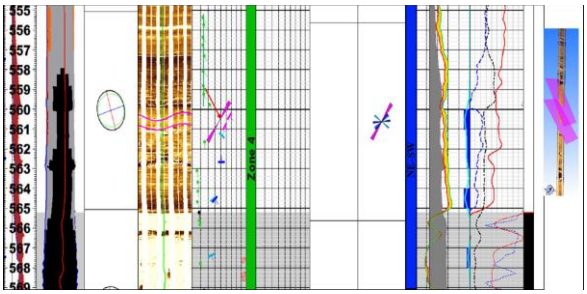

Figure 1 - FMI image showing microfaults identified at depths of 560.5 m and 561.0 m, striking NE–SW

A high fracture density and minor drag (indicated by the red arrow) are observed near the fault zone.

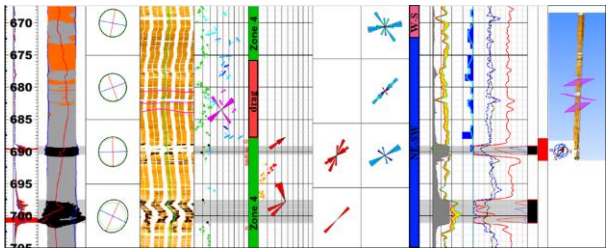

Figure 2 - FMI image showing microfaults identified at depths of 680.7 m and 683.7 m, striking NE–SW, and at a depth of 682.4 m, striking NW–SE

A high fracture density and a zone of fault drag are observed near the fault.

Structural dip analysis includes the identification of the main structural features of the deposits, such as bed boundaries and faults, as well as their statistical analysis, the distribution of dip angles, and the orientation of structural elements.

As a result of the interpretation, bedding dip angles were determined within the studied interval of 155–905 m. The dip angles range from 1° to 60°. The average bedding dip is 9.7°, with a predominant dip toward the southeast and a secondary direction toward the northeast.

Within the 155–905 m interval, four structural zones were identified:

1) zone 1: 155–183 m, 48° toward the NW;
2) zone 2: 183–371 m, 4.6° toward the NNW;
3) zone 3: 371–549 m, 6.6° toward the SE;
4) zone 4: 549–905 m, 13.7° toward the SE.

For coal seam mapping and the planning of subsequent wells, it is recommended to conduct a facies analysis based on borehole images (Figure 3). The borehole image represents a significant complement to core-based facies analysis and enables three-dimensional reservoir modeling.

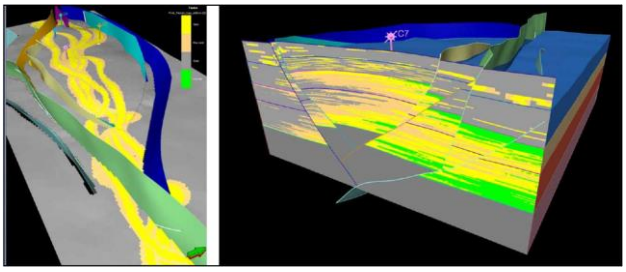

Figure 3 - Three-dimensional model of the deposit constructed from facies analysis results

The input data for such an analysis include sandstone layers identified within the studied interval that exhibit cross-bedding and subhorizontal bedding. The orientation of these structures indicates the direction of paleowater flow during sedimentation and, consequently, the direction of sand body development. Knowing the spatial distribution of sand bodies makes it possible to predict the location of potential flooding zones where coal formation may occur.

To determine the paleoflow direction and assess the depositional environment, a correction for the structural dip angle was applied. Before correction, the dip angle of intra-seam bedding ranged from 1° to 35°, with a predominant dip azimuth toward the southeast and a secondary direction toward the northwest (Figure 4).

After applying the structural dip correction, intra-seam bedding can be subdivided into cross-bedding and subhorizontal bedding. The paleoflow direction is determined by cross-bedding, which shows multidirectional orientations, indicating frequent changes in depositional conditions within the studied interval.

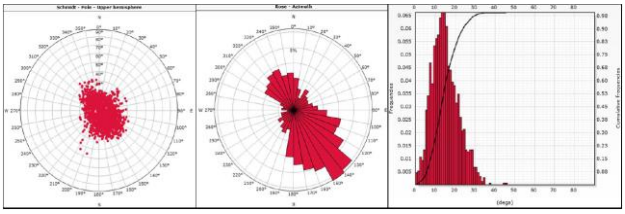

Figure 4 - Distribution, orientation, histogram, and strike directions of intra-seam bedding before structural dip correction

The dip angle of intra-seam bedding varies from 1 to 35 degrees, with a predominant dip azimuth toward the southeast and a secondary direction toward the northwest.

Fractures identified on FMI images are represented by high-amplitude sinusoids in vertically drilled wells and low-amplitude sinusoids in horizontal wells. In the presence of fractures in the section, unlike faults, the correlation of geological horizons is not disrupted. Within the studied interval, conductive, partially conductive, and non-conductive (healed) fractures were identified. Partially conductive fractures are visible only on 2–3 tool pads. Conductive fractures are likely filled with water-based drilling mud. This type of fracture may also be healed by any electrically conductive mineral, for example, clay. Healed fractures exhibit high resistivity on FMI images due to infilling with high-resistivity minerals (primarily calcite)

The strike of conductive fractures predominantly trends NE–SW and N–S. The strike of partially conductive fractures is NW–SE and NE–SW. The predominant strike of non-conductive (healed) fractures is NE–SW.

Fracture strike varies by interval (Figure 5): NE–SW zone: 155–195 m, 840–905 m; multidirectional strike zone: 195–265 m; NNW–SSE zone: 265–315 m, 465–525 m; NW–SE zone: 575–673 m; NE–SW and NW–SE zone: 315–465 m, 755–840 m.

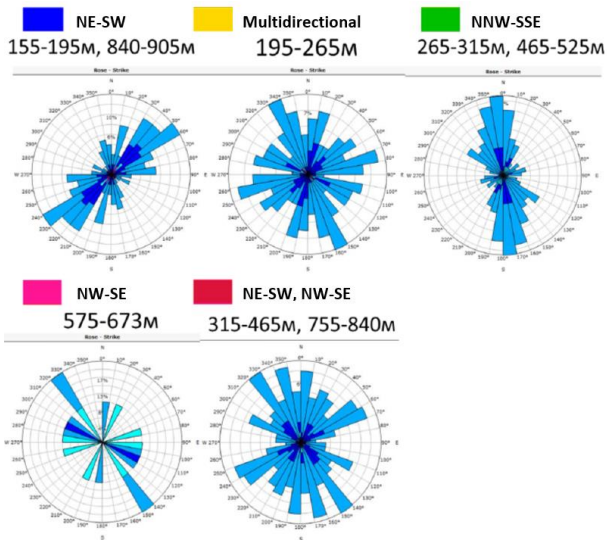

Figure 5 - Distribution of fracture strike directions by structural zones

Results and Discussion

As a result of the interpretation, the dip angles of the layers in the research interval of 155-905 m were determined. The dip angles vary from 1 to 60 degrees. The average dip angle of the layers is 9.7 degrees, with a predominant dip to the southeast and a secondary dip to the northeast.

In the research interval of 155-905 m, four structural zones were calculated: zone 1: 155-183 m, 48 degrees to the northwest; zone 2: 183-371 m, 4.6 degrees to the west-northwest; zone 3: 371-549 m, 6.6 degrees to the southeast; zone 4: 549-905 m, 13.7 degrees to the southeast. In the studied interval, intra-layer stratification was identified. To determine the direction of paleoflow and assess the sedimentary environment, a correction for the structural angle was introduced.

In the FMI image, fault planes were highlighted at depths of 262.1 m and 307.8 m, with strike directions of northwest-southeast, at depths of 382.5 m and 383 m with strike directions of northeast-southwest and north-south, respectively. Changes in lithology or filtration reservoir properties along the fault plane, increased fracture density, and slight displacement of the layers (fault at a depth of 262.1 m) confirm the fault interpretation [[22], [23]].

In the FMI image, microfracture planes were highlighted at depths of 560.5 m, 561 m, 680.7 m, and 683.7 m with a strike of northeast-southwest, and at a depth of 682.4 m with a strike of northwest-southeast. Along the microfracture planes, slight displacement of the layers is observed, and areas of dragging are also visible near the microfracture planes.

In the studied interval, conducting, semi-conducting, and non-conducting (healed) fractures were identified on the FMI-HD images. The strike directions of the conducting fractures predominantly follow the northeast-southwest and north-south directions. The strike of the semi-conducting fractures follows the northwest-southeast and northeast-southwest directions. The predominant strike of the non-conducting (healed) fractures follows the northeast-southwest direction. The strike of the fracture changes by interval:

- zone northeast-southwest: 155-195 m, 840-905 m;
- zone of opposite strikes: 195-265 m;
- zone west-northwest-southeast: 265-315 m, 465-525 m;
- zone northwest-southeast: 575-673 m;
- zone northeast-southwest, northwest-southeast: 315-465 m, 755-840 m.

In the research interval, collapses and technogenic fractures were identified. The predominant direction of collapses (minimum horizontal stress) is northeast-southwest. The predominant direction of technogenic fractures (maximum horizontal stress) is northwest-southeast.

Conclusions

The interpretation of FMI data in the 155–905 m interval made it possible to identify the main structural features of the studied rock mass, including bedding dip, intra-seam layering, faults, microfaults, conductive, semi-conductive, and healed fractures, as well as borehole breakouts and drilling-induced fractures. The results showed that the interval is structurally heterogeneous and consists of several zones with different fracture orientations and deformation characteristics.

The study confirmed that natural fracturing plays an important role in the spatial distribution of methane-bearing zones at the Sherubaynurinsky site, since fracture systems control permeability and gas migration pathways. The obtained structural data can therefore be used to refine the geological model of the site and to support the planning of coalbed methane extraction, including well placement and the selection of intervals with higher drainage potential.

Further research should focus on integrating the identified fracture systems into a 3D geological and geomechanical model of the site and on evaluating the relationship between fracture parameters and

methane productivity using additional logging, core, and production data.

Conflicts of interest. On behalf of all authors, the corresponding author states that there is no conflict of interest.

CRediT author statement: **D. Akhmatnurov:** Conceptualization, Methodology, Software; **A. Sadchikov:** Data curation, Writing draft preparation, Visualization; **N. Zamaliyev:** Investigation, Supervision; **E. Reshetnyakov:** Software, Validation, Reviewing and Editing.

Acknowledgements. This study was supported by the Science Committee of the Ministry of Science and Higher Education of the Republic of Kazakhstan as part of the program-targeted funding for the implementation of the scientific and scientific-technical program IRN BR28712407.

Cite this article as: Akhmatnurov DR, Sadchikov AV, Zamaliyev NM, Reshetnyakov ED. Study of Rock Mass Fracturing in the Sherubaynurinsky Site. Kompleksnoe Ispolzovanie Mineralnogo Syra = Complex Use of Mineral Resources. 2027; 343(4):134-141. https://doi.org/10.31643/2027/6445.47

Шерубайнурин учаскесіндегі тау жыныстарының жарықшақтылығын зерттеу

Ахматнуров Д.Р., Садчиков А.В., *Замалиев Н.М., Решетняков Э.Д.

Ә. Сағынов атындағы Қарағанды техникалық университеті, Қарағанды, Қазақстан

Мақала келді: *27 ақпан 2026*
Сараптамадан өтті: *14 наурыз 2026*
Қабылданды: *2 сәуір 2026*

ТҮЙІНДЕМЕ

Бұл зерттеу Қарағанды көмір бассейнінің Шерубай-Нұра учаскесіндегі тау жыныстары массиві мен көмірлі қабаттардың жарықшақтануын зерттеуге арналған және көмір қабаттарынан метан өндіруді ғылыми тұрғыдан негіздеуге бағытталған. Зерттеулер осы метанды аймаққа тән күрделі геологиялық құрылым және кернеулі геомеханикалық жағдайында ескеріле отырып жүргізілді. Геофизикалық зерттеулер Ш-9 барлау ұңғымасында 155–905 м тереңдік диапазонында жүргізілді, стандартты ашық ұңғымаларды каротаждау әдістерімен бірге кешенді түрде Formation MicroImager (FMI) ұңғымаларын микросканерлеу әдісін қолдану арқылы жүргізілді. Алынған материалдарды интерпретациялау қабаттардың құлау бұрыштарын анықтауға мүмкіндік берді, қабатішілік қабаттасуларды ерекшелеу, сондай-ақ жарылымдарды, микробұзылуларды, өткізгіш, жартылай өткізгіш және бітіп қалған жарықшақтарды анықтауға мүмкіндік берді. Сонымен қатар, ұңғыма қабырғаларының опырылу аймақтары мен бұрғылау әсерінен қалыптасқан жарықтар анықталды, бұл массивтің кернеулік жағдайын бағалауға мүмкіндік берді. Зерттелген аралықта төрт құрылымдық аймақ анықталды Жарықшақтардың басым бағыты солтүстік-шығыс - оңтүстік-батыс екені анықталды. Зерттеу нәтижелері жарықшақтанудың таралу заңдылықтарын тереңірек түсінуге мүмкіндік береді және оларды геологиялық модельдеуде, ұңғыма траекториясын жобалау мен перспективалы дегазация аймақтарын таңдауда пайдалануға болады.

Түйін сөздер: көмір қабатының жарықшақтылығы, көмір қабаттары метанын игеру, азимуттық электрлік микросканер, ұңғымалық кескіндер, метанға байытылған аймақтар.

Авторлар туралы ақпарат:

Ахматнуров Денис Рамильевич — *PhD докторы, зертхана жетекшісі, Әбілқас Сағынов атындағы Қарағанды техникалық университеті, 100027, Нұрсұлтан Назарбаев даңғ. 56, Қарағанды, Қазақстан. Email: d.akhmatnurov@gmail.com; ORCID ID: https://orcid.org/0000-0001-9485-3669*

Садчиков Александр Викторович — *Техникалық ғылымдар кандидаты, профессор, Әбілқас Сағынов атындағы Қарағанды техникалық университеті, 100027, Нұрсұлтан Назарбаев даңғ. 56, Қарағанды, Қазақстан. Email: a.sadchikov@ktu.edu.kz; ORCID ID: https://orcid.org/0000-0002-6022-2073*

Замалиев Наиль Мансурович — *PhD докторы, қауымдастырылған профессор, Әбілқас Сағынов атындағы Қарағанды техникалық университеті, 100027, Нұрсұлтан Назарбаев даңғ. 56, Қарағанды, Қазақстан. Email: nailzamaliev@mail.ru; ORCID ID: https://orcid.org/0000-0003-0628-2654.*

Решетняков Эдвард Дмитриевич — *Т.ғ.м., Пайдалы қазбалар кен орындарын өндіру кафедрасының докторанты, Әбілқас Сағынов атындағы Қарағанды техникалық университеті, 100027, Нұрсұлтан Назарбаев даңғ. 56, Қарағанды, Қазақстан. Email: vip.red2001@gmail.com; ORCID ID: https://orcid.org/0009-0000-1128-2056*

Исследование трещиноватости массива горных пород Шерубайнуринского участка

Ахматнуров Д.Р., Садчиков А.В., *Замалиев Н.М., Решетняков Э.Д.

Карагандинский технический университет имени А. Сагинова, Караганда, Казахстан

Поступила: *27 февраля 2026*
Рецензирование: *14 марта 2026*
Принята в печать: *2 апреля 2026*

АННОТАЦИЯ

Данное исследование посвящено изучению трещиноватости горного массива и угленосных толщ на Шерубай-Нуринском участке Карагандинского угольного бассейна с целью научного обоснования разработки метана угольных пластов. Исследования выполнены в условиях сложного геологического строения и напряжённого геомеханического состояния, характерных для данного метаноносного района. Геофизические исследования проводились в разведочной скважине Ш-9 в интервале глубин 155–905 м с применением метода микросканирования стенок скважины Formation MicroImager (FMI) в комплексе со стандартными методами каротажа в открытом стволе. Интерпретация полученных материалов позволила определить углы падения пластов, выделить внутрипластовую слоистость, а также выявить разломные нарушения, микронарушения, проводящие, частично проводящие и залеченные трещины. Кроме того, были зафиксированы зоны разрушения стенок скважины и трещины, индуцированные бурением, отражающие особенности напряжённого состояния массива. В пределах исследуемого интервала выделены четыре структурные зоны. Установлено, что преобладающее направление трещиноватости имеет северо-восточное - юго-западное простирание. Полученные результаты расширяют представления о закономерностях распределения трещиноватости и могут быть использованы при геологическом моделировании, проектировании траекторий скважин и выборе перспективных зон дегазации.

Ключевые слова: трещиноватость угольного пласта, освоение метана угольных пластов, азимутальный электрический микросканер, скважинные изображения, зоны, обогащённые метаном.

Информация об авторах:

Ахматнуров Денис Рамильевич — *PhD, руководитель лаборатории, Карагандинский технический университет имени А. Сагинова, 100027, пр. Нурсултана Назарбаева, 56, Караганда, Казахстан. Email: d.akhmatnurov@gmail.com; ORCID ID: https://orcid.org/0000-0001-9485-3669*

Садчиков Александр Викторович — *Кандидат технических наук, старший преподаватель, Карагандинский технический университет имени А. Сагинова, 100027, пр. Нурсултана Назарбаева, 56, Караганда, Казахстан. Email: a.sadchikov@ktu.edu.kz; ORCID ID: https://orcid.org/0000-0002-6022-2073*

Замалиев Наиль Мансурович — *PhD, Ассоциированный профессор, Карагандинский технический университет имени А. Сагинова, 100027, пр. Нурсултана Назарбаева, 56, Караганда, Казахстан. Email: nailzamaliev@mail.ru; ORCID ID: https://orcid.org/0000-0003-0628-2654*

Решетняков Эдвард Дмитриевич — *М.т.н., докторант кафедры Разработка месторождений полезных ископаемых, Карагандинский технический университет имени А. Сагинова, 100027, пр. Нурсултана Назарбаева, 56, Караганда, Казахстан. Email: vip.red2001@gmail.com; ORCID ID: https://orcid.org/0009-0000-1128-2056*

References

[1] Kamarov RK, Zamaliyev NM, Akhmatnurov DR, Musin RA. Setting the volume and location of gas collectors of abandoned coal mines. Naukovyi Visnyk Natsionalnoho Hirnychoho Universytetu = Scientific Bulletin of National Mining University. 2018; 2:5-11. https://doi.org/10.29202/nvngu/2018-2/2

[2] Duan H. Present situation and optimization strategy of coalbed methane development technology. Modern Chemical Research. 2021; 5:7-8.

[3] Zhang Y, Tu Y, Dong Y. Permeability variation of tectonic coal under microwave radiation. Journal of Taiyuan University of Technology. 2022; 53(6):1004-1013.

[4] Hu X. Research and application of coal bed methane logging technology. Value Engineering. 2021; 16:239-240.

[5] Drizhd NA, Dauletzhanova ZhT, Zamaliyev NM, Dauletzhanov AZh. Influence of technological process parameters on qualitative characteristics of coal thermolysis products. Naukovyi Visnyk Natsionalnoho Hirnychoho Universytetu = Scientific Bulletin of National Mining University. 2021; 1:39-46.

[6] Drizhd NA, Dauletzhanov AZh, Zamaliyev NM, Dauletzhanova ZhT. Efficiency of application of antipyrogenic materials for coating coals and coke. Naukovyi Visnyk Natsionalnoho Hirnychoho Universytetu = Scientific Bulletin of National Mining University. 2019; 6:112-116. https://doi.org/10.29202/nvngu/2019-6/16

[7] Zhou X, Li G, Li C. Ground development technology and engineering application of CBM in coal mine goafs: A case study of Jincheng mining area in Qinshui Basin. Coal Geology and Exploration. 2022; 50(5). https://doi.org/10.12363/issn.1001-1986.21.09.0533

[8] Li S, Wang C, Wang H. Reservoir forming characteristics and favorable area evaluation of deep coalbed methane in Daning-Jixian Block. Coal Geology and Exploration. 2022; 50(9):59-67.

[9] Matayev AK, Kainazarova AS, Arystan ID, Abeuov Ye, Kainazarov AS, Baizbayev MB, Demin VF, Sultanov MG. Research into rock mass geomechanical situation in the zone of stope operations influence at the 10th Anniversary of Kazakhstan's Independence mine. Mining of Mineral Deposits. 2021; 15(1):1-10. https://doi.org/10.33271/mining15.01.042

[10] Matayev AK, Lozynskyi VH, Musin A, Abdrashev RM, Kuantay AS, Kuandykova AN. Substantiating the optimal type of mine working fastening based on mathematical modeling of the stress condition of underground structures. Naukovyi Visnyk Natsionalnoho Hirnychoho Universytetu = Scientific Bulletin of National Mining University. 2021; 3:57-63. https://doi.org/10.33271/nbngu/2021-3/057

[11] Korchak SA, Abaturova IV, Savintsev IA, Storozhenko AA. Assessment of the degree and nature of fracturing of rock masses for constructing a predictive engineering-geological model of the deposit. Izvestiya UGGU = News of the Ural State Mining University. 2022; 67(3):90-99. https://doi.org/10.21440/2307-2091-2022-3-90-99

[12] Zhuravlev AB, Karev VI, Kovalenko YuF, Ustinov KB. The influence of filtration on the stressed-deformed state of rock in the vicinity of a well. Applied Mathematics and Mechanics. 2014; 1:86-97.

[13] Zhuravkov MA, Chumak NG. Deterministic-probabilistic approaches to studying the behavior of macrofractures in layered rock masses. Mining Mechanics. 2007; 1:54-59.

[14] Drizhd NA, Rabatuly M, Alexandrov AYu, Balniyazova G, Junis G. Results of testing pilot industrial wells in the Sherubainur section of the Karaganda coal basin. Ugol = Russian Coal Journal. 2020; 6:36-40. https://doi.org/10.18796/0041-5790-2020-6-36-40

[15] Niu X, Niu Y, Suo Y. Microbial community structure and function prediction of in-situ coal samples. Coal Engineering. 2022; 54(8):149-156.

[16] Maiorov AE, Abramov IL, Kulik DP. Assessment of fracturing and filtration properties of rock masses. Vestnik NC VostNII = Bulletin of VostNII Research Center. 2021; 2:12-21. https://doi.org/10.25558/VOSTNII.2021.90.58.002

[17] Zamaliyev NM, Zhalburov ZhD, Valiev NG, Akhmatnurov DR, Zhanseytov AT. Development of proposals for improving cyclic-flow technology for the Bozshakol deposit. Ugol = Russian Coal Journal. 2024; 2:58-64. https://doi.org/10.18796/0041-5790-2024-2-58-64

[18] Yeremenko AA, Koltyshev VN, Uzun EE, Khristolyubov EA. Assessment of the structure of rock mass based on the state of the surface of unloading wells in the rock core at the Sheregesh mine. Mountain Information and Analytical Bulletin. 2023; 11:91-101.

[19] Jiang Y, Song C, Wang S. Study on desorption and diffusion characteristics of coalbed methane under ultrasonic excitation. Coal Science and Technology. 2020; 48(3):174-179.

[20] Yang Z, Yuan J, Zhu J. Thermal injection stimulation to enhance coalbed methane recovery. Reservoir Evaluation and Development. 2022; 12(4):617-625.

[21] Wei B, Li X, Tian J. Underground coal gasification trials at home and abroad and its enlightenment to Xinjiang underground coal gasification. Coal Science and Technology Magazine. 2022; 43(4):27-35.

[22] Pat. 37803 KZ. Method for extracting ore reserves in interchamber pillars. Abeuov EA, Zamaliyev NM, Demin VF, Akhmatnurov DR, Mussin RA, Ganyukov NY. Publ. 06.02.2026. Applicant: JSC Abylkas Saginov Karaganda Technical University.

[23] Pat. 37836 KZ. Method for degasification of gas-bearing strata. Akhmatnurov DR, Zamaliyev NM, Mussin RA, Schmidt-Fedotova IM, Demin VF, Reshetnyakov ED. Publ. 20.02.2026. Applicant: JSC Abylkas Saginov Karaganda Technical University.

МАЗМҰНЫ
СОДЕРЖАНИЕ
CONTENTS

METALLURGY AND METALLURGICAL ENGINEERING

MINING & MINERAL PROCESSING

EARTH AND PLANETARY SCIENCES: EARTH-SURFACE PROCESSES

Техникалық редакторлар:
Г.К. Қасымова, Н.М.Айтжанова, Т.И. Қожахметов

Компьютердегі макет:
Г.К. Қасымова

Дизайнер:
Г.К. Қасымова, Н.М.Айтжанова

“Металлургия және кен байыту институты” АҚ
050010, Қазақстан Республикасы, Алматы қаласы, Шевченко к-сі, 29/133

Жариялауға 02.04.2026 жылы қол қойылды

Технические редакторы:
Г.К. Касымова, Н.М. Айтжанова, Т.И. Кожахметов

Верстка на компьютере:
Г.К. Касымова

Дизайнер:
Г.К. Касымова, Н.М.Айтжанова

АО “Институт металлургии и обогащения”
050010, г. Алматы, Республика Казахстан. ул. Шевченко, 29/133

Подписано в печать 02.04.2026 г.

Technical editors:
G.K. Kassymova, N.M. Aitzhanova, T.I. Kozhakhmetov

The layout on a computer:
G.K. Kassymova

Designer:
G.K. Kassymova, N.M. Aitzhanova

“Institute of Metallurgy and Ore Beneficiation” JSC
050010, Almaty city, the Republic of Kazakhstan. Shevchenko str., 29/133

Signed for publication on 02.04.2026